

UNSUPERVISED UNMIXING ANALYSIS BASED ON MULTISCALE REPRESENTATION

By

Maria Constanza Torres-Madroño

A dissertation submitted in partial fulfillment of the requirements for the degree of
DOCTOR OF PHILOSOPHY
in
COMPUTING AND INFORMATION SCIENCE AND ENGINEERING

University of Puerto Rico
MAYAGUEZ CAMPUS
May 2013

Approved by:

Shawn Hunt, Ph.D
President, Graduate Committee

Date

Miguel Veléz-Reyes, Ph.D
Co-president, Graduate Committee

Date

Nayda G. Santiago, Ph.D
Member, Graduate Committee

Date

James Goodman, Ph.D
Member, Graduate Committee

Date

Wilson Rivera, Ph.D
Program Coordinator

Date

Elsie I. Parés Matos, Ph.D
Graduate School Representative

Date

Abstract of dissertation presented to the Graduate School of the
University of Puerto Rico in partial fulfillment of the requirements
for the Degree of Doctor of Philosophy.

UNSUPERVISED UNMIXING ANALYSIS BASED ON MULTISCALE REPRESENTATION

By

Maria Constanza Torres-Madroño

May 2013

Chair: Miguel Veléz-Reyes, Ph.D

Ph.D Major: Computing and Information Science and Engineering

ABSTRACT

Unsupervised unmixing analysis aims to extract the basic materials, the so called endmembers, and their abundances from a hyperspectral image. Unmixing is usually performed by pixels-only techniques that do not take into account the spatial information and generally require a priori estimate of the number of endmembers. Recently, several spatial-spectral unmixing techniques have been developed. However, most of these techniques depend of spatial kernels or windows to include the spatial information in the unmixing analysis. In this work, a new unmixing approach based on multiscale representation is developed. The proposed technique extracts spectral signatures and spectral endmember classes from hyperspectral imagery in an unsupervised fashion. A multiscale representation of the hyperspectral images is obtained using nonlinear diffusion. Then, spectral endmembers are automatically identified using multigrids methods to solve the diffusion partial differential equation. The multiscale representation and multigrids allows to avoid the use of spatial kernels. Once the spectral endmembers are identified, similar spectra are clustered to build spectral endmember classes thus accounting for the spectral variability of the materials along the unmixing analysis. A comparison with other unmixing methods

shows that the proposed unsupervised unmixing approach outperforms traditional spectral techniques. Capabilities of the proposed approach were validated and assessed using simulated imagery and real imagery collected with the AVIRIS and AISA sensors over different landscapes.

Resumen de disertación presentado a la Escuela Graduada
de la Universidad de Puerto Rico como requisito parcial
para el Grado de Doctor en Filosofía.

ANALYSIS DE DESMEZCLADO NO SUPERVISADO BASADO EN REPRESENTACIONES EN MULTIESCALA

Por

Maria Constanza Torres Madroñero

Mayo 2013

Consejero: Miguel Veléz Reyes, Ph.D

Ph.D. : Ciencias e Ingeniería de la Información y la Computación

RESUMEN

El análisis de desmezclado no supervisado busca extraer los constituyentes básicos, conocidos como "*endmembers*", y sus abundancias desde una imagen hiperespectral. Comúnmente, el desmezclado es realizado a través de técnicas que no toman en consideración la información espacial de la imagen y que generalmente requieren estimar de ante mano el número de "*endmembers*". Recientemente, varias técnicas que combinan la información espacial y espectral han sido desarrolladas. Sin embargo, la mayoría de estas técnicas dependen de ventanas o vecindarios para incluir la información espacial en el desmezclado. Un nuevo método de desmezclado basado en las representaciones en múltiples escalas fue desarrollado para este trabajo. El método propuesto extrae los "*endmembers*" espectrales y las clases espectrales de "*endmembers*" desde una imagen hiperespectral de una manera no supervisada. Una representación en multiescala es obtenida por difusión no lineal. Los "*endmembers*" espectrales son automáticamente identificados usando métodos de "*multigrids*" para solucionar la ecuación diferencial de difusión. La representación en multiescala y el "*multigrad*" evitan el uso de ventanas espaciales. Una vez los "*endmembers*" espectrales son identificados, espectros similares son agrupados para formar las clases

espectrales de "*endmembers*" manteniendo la variabilidad espectral de los materiales a lo largo del proceso de desmezclado. Una comparación entre el método basado en las representaciones en múltiples escalas y otras técnicas de desmezclado demuestran que el método desarrollado supera las técnicas tradicionales. Las capacidades del algoritmo fueron validados y evaluados usando imágenes sintéticas e imágenes reales capturadas con los sensores AVIRIS y AISA sobre diferentes paisajes.

To my little girl: *Maria Camila*.

ACKNOWLEDGMENTS

I would like to express my very great appreciation to Dr. Miguel Velez-Reyes. This work had not taken place without his advice. I also thank him for his support to my career, and the great opportunity to work with him. I would also like to thank to my graduate committee: Dr. Shawn Hunt, Dr. Nayda Santiago and Dr. James Goodman for their valuable comments and suggestions, these helped to make of this document a great work.

Furthermore, I am grateful for the assistance given by IRISE staff: Maribel, Soliris, and Evelyn. I also thanks to the Laboratory for Applied Remote Sensing and Image Processing (LARSIP). In this place, I did not only develop my research but also I found great people and valuable friends. Thanks Victor and Samuel for your support. And thanks to all my friends in the lab that have been part of this rich experience. Special thanks to my friends Diego Aponte, Maider Marin, Leidy Dorado, Andrea Santos, Miguel Goenaga, Maria Fernanda Cordoba, Ana Medina and their families. They had done my days in Puerto Rico very pleasant and fun.

Finally, I thank with all my heart to my family. I thank to my little girl Maria Camila for lending your time to develop this work. She is the driving force of my life and the inspiration of each of my days. I thank to David for your support and company. I also thanks to my brother Jose Luis and my sister Esperanza to fill my life with a lot of fun and insanities. Thanks to my great family: my grandfather, uncles, and cousins who have been with me from Colombia and provided me with their support to develop my career. Thanks to Elkin for your friendship all these years. Special thanks to my parents: Eduardo y Esperanza for believing in me, I owe them all that I am.

This work was supported by the NASA EPSCoR Program under Grant NNX09AV03A, and used facilities of the Center for Subsurface Imaging Systems (CenSSIS) a Na-

tional Science Foundation Engineering Research Center sponsored under Award EEC-9986821, and additional support of the US Forest Service International Institute of Tropical Forestry. Any opinions, findings, and conclusions or recommendations expressed in this material are those of the authors and do not necessarily reflect the views of NASA, NSF, or USDA.

CONTENTS

ABSTRACT	ii
RESUMEN	iv
ACKNOWLEDGMENTS	vii
TABLE OF CONTENTS	xi
LIST OF FIGURES	xii
LIST OF TABLES	xvi
1 INTRODUCTION	1
1.1 Justification	1
1.2 Rationale	4
1.3 Technical Approach	7
1.4 Research Design and Objectives	10
1.4.1 Specific Objectives	11
1.4.2 Validation and Assessment	12
1.5 Thesis Contributions	15
1.5.1 Contributions to CISE	16
1.6 Thesis Outline	17
2 LITERATURE REVIEW	19
2.1 Hyperspectral Imagery	20
2.2 Linear Mixing Model	21
2.3 Endmember Extraction Algorithms	23
2.3.1 Geometric Methods	23
2.3.2 Parametric Methods	28
2.3.3 Spectral - Spatial Methods	29
2.4 Abundance Estimation Algorithms	36
2.4.1 Least Square Methods	36
2.4.2 Sparse Regression	37
2.5 Estimation of the Number of Endmembers	39
2.6 Scale Spaces and Multiscale Representations	41
2.7 Summary	44
3 SPECTRAL ENDMEMBER EXTRACTION BASED ON MULTISCALE REPRESENTATION	46
3.1 Multiscale Representation of Hyperspectral Imagery	47

3.1.1	Input Parameters	52
3.2	Spectral Endmember Extraction	52
3.2.1	Scale Selection	55
3.3	Experiments	59
3.3.1	Scale Effects	63
3.3.2	Analysis of Results	68
3.4	Summary	72
4	SPECTRAL ENDMEMBER CLASS EXTRACTION USING CLUSTERING	74
4.1	Cluster Analysis	75
4.1.1	Similarity Metrics	76
4.1.2	Clustering Algorithms	76
4.1.3	Validity Indexes	82
4.2	Spectral Endmember Classes	87
4.3	Experiments	88
4.3.1	Test Data Set	88
4.3.2	Comparison of Clustering Algorithms	91
4.3.3	Estimation of the Number of Spectral Endmember Classes	96
4.3.4	Discussion of Results	108
4.4	Summary	109
5	EXPERIMENTS WITH SYNTHETIC DATA	111
5.1	Synthetic Data Sets	112
5.2	Assessment Metrics	114
5.3	Unmixing Analysis of Synthetic Data	117
5.3.1	Experiments with Grid Synthetic Data	117
5.3.2	Experiments with Synthetic Data Including Spatial Complexity	123
5.3.3	Analysis of Results	134
5.4	Summary	137
6	EXPERIMENTS WITH REAL HYPERSPECTRAL IMAGE	139
6.1	Data Sets	139
6.1.1	A.P. Hill	140
6.1.2	Cuprite	142
6.1.3	Guanica Dry Forest	142
6.2	Assessment Methodology	145
6.2.1	Qualitative Evaluation	146
6.2.2	Quantitative Assessment of Detected Classes	147
6.2.3	Agreement Assessment of Classification Maps	149
6.3	Unmixing Analysis of A.P. Hill and Cuprite	149
6.3.1	Multiscale Representation and Scale Selection	150
6.3.2	Spectral Endmember and Spectral Endmember Class Extraction	151
6.3.3	Assessment of Unmixing Results	155
6.3.4	Analysis of Results	181

6.4	Spatial Resolution Effects	183
6.4.1	Analysis of Results	188
6.5	Summary	190
7	COMPARISON OF UNMIXING METHODS	192
7.1	Unmixing Analysis of A.P. Hill	193
7.1.1	Unmixing using SMACC, VCA, and RBSPP for A.P. Hill	193
7.1.2	Assessment of Unmixing Results	200
7.2	Unmixing Analysis of Cuprite	215
7.2.1	Unmixing using SMACC, VCA, and RBSPP for Cuprite	215
7.2.2	Assessment of Unmixing Results	216
7.3	Further Analysis	241
8	A COMPUTING SYSTEM FOR UNMIXING ANALYSIS	244
8.1	Implementation Description	244
8.2	Complexity Analysis	250
8.3	Summary	251
9	ETHICAL CONSIDERATIONS ABOUT REMOTE SENSING IMAGING	252
10	CONCLUSIONS AND FUTURE WORK	255
10.1	Conclusions	255
10.2	Future Work	259
	BIBLIOGRAPHY	261

LIST OF FIGURES

Figure 1.1	Spectral endmember classes concept.	5
Figure 1.2	Example of nonlinear diffusion.	7
Figure 1.3	Multigrid structure.	8
Figure 1.4	Schematic of proposed approach for unmixing.	10
Figure 1.5	False Leaf image.	12
Figure 2.1	Hyperspectral imagery.	20
Figure 2.2	Geometric models for mixed pixels.	24
Figure 2.3	Piece-wise convex approach.	29
Figure 2.4	Automated morphology endmember extraction algorithm.	31
Figure 2.5	Scale concept.	42
Figure 2.6	Isotropic diffusion and scale space.	44
Figure 3.1	Example of nonlinear diffusion.	49
Figure 3.2	Example of representative spectra for False Leaf image.	54
Figure 3.3	Spectral endmember extraction methodology.	54
Figure 3.4	Test images for comparison of stopping criteria.	60
Figure 3.5	Comparison of scale selection criteria.	62
Figure 3.6	Comparison of selected scales for the False Leaf image.	65
Figure 3.7	Comparison of selected scales for the AP Hill subset image.	66
Figure 3.8	Comparison of selected scale for Guanica subset image.	67
Figure 3.9	Example of spectral endmembers from False Leaf image.	69
Figure 3.10	Example of spectral endmembers from AP Hill subset image.	70
Figure 3.11	Example of spectral endmembers from Guanica subset image.	71
Figure 4.1	Dendrogram example for hierarchical clustering algorithms.	77
Figure 4.2	Spectral endmember class extraction using clustering.	88
Figure 4.3	Localization of spectra for each spectral endmember classes of Test Data.	89
Figure 4.4	Test Data set.	90
Figure 4.5	Mixed cluster from hierarchical clustering and SAM.	95
Figure 4.6	Validity indexes for Test Data set.	98
Figure 4.7	Spectral endmember classes for Test Data with $\hat{c} = 8$	100
Figure 4.8	Validity indexes for False Leaf image.	102
Figure 4.9	Spectral endmember classes for False Leaf image with $\hat{c} = 14$ using complete linkage and SAM.	104
Figure 4.10	Spectral endmember class abundances for False Leaf image with $\hat{c} = 14$ using complete linkage and SAM.	105
Figure 4.11	Spectral endmember classes for False Leaf image with $\hat{c} = 14$ using average linkage and SAM.	106

Figure 4.12	Spectral endmember classes abundances for False Leaf image with $\hat{c} = 14$ using average linkage and SAM.	107
Figure 5.1	Synthetic Data I with a grid arrangement of four materials.	113
Figure 5.2	Synthetic Data II with 7 endmembers and abundances from real data.	115
Figure 5.3	Synthetic Data III with 8 endmembers and abundances from real data.	116
Figure 5.4	Sum of abundances used for Synthetic Data.	116
Figure 5.5	Abundances estimated from Synthetic Data I at different noise levels.	119
Figure 5.6	Spectral endmember classes extracted from Synthetic Data I at different noise levels.	121
Figure 5.7	Estimated abundances for Synthetic Data II.	125
Figure 5.8	Extracted endmembers for Synthetic Data II.	126
Figure 5.9	Additional spectral endmember classes for Synthetic Data II.	127
Figure 5.10	Histograms for the absolute errors of the estimated abundance from Synthetic Data II using the proposed approach and SMACC.	129
Figure 5.11	Estimated abundances for Synthetic Data III.	131
Figure 5.12	Extracted endmembers for Synthetic Data III.	132
Figure 5.13	Additional spectral endmember classes for Synthetic Data III.	133
Figure 5.14	Histograms for the absolute errors of the estimated abundance from Synthetic Data II using the proposed approach and RBSPP.	135
Figure 6.1	A.P. Hill hyperspectral image.	141
Figure 6.2	Spectral library for A.P. Hill	141
Figure 6.3	Cuprite hyperspectral image.	143
Figure 6.4	Classification map for Cuprite.	143
Figure 6.5	Guanica Forest hyperspectral image.	144
Figure 6.6	Composition of Guanica Forest scene.	145
Figure 6.7	Scale selection for A.P. Hill.	150
Figure 6.8	Scale selection for Cuprite.	151
Figure 6.9	Smoothed A.P. Hill and Cuprite images.	152
Figure 6.10	Validity indexes for the estimation of the number of spectral endmember classes of A.P. Hill data.	153
Figure 6.11	Validity indexes for the estimation of the number of spectral endmember classes of Cuprite data.	154
Figure 6.12	Spectral endmember classes for A.P. Hill using proposed approach with complete linkage and $\hat{c} = 14$	156
Figure 6.13	Abundances of spectral endmember classes for A.P. Hill using proposed approach with complete linkage and $\hat{c} = 14$	157
Figure 6.14	Spectral endmember classes for Cuprite using proposed approach with complete linkage and $\hat{c} = 17$	158
Figure 6.15	Abundances of spectral endmember classes for Cuprite using proposed approach with complete linkage and $\hat{c} = 17$	159

Figure 6.16	Comparison of spectral endmember classes from A.P. Hill with classification map and spectral library.	162
Figure 6.17	Evaluation of unmixing results for Cuprite: <i>kaolinite</i> and <i>chalcedony</i>	164
Figure 6.18	Evaluation of unmixing results for Cuprite: <i>calcite</i> and <i>muscovite</i>	165
Figure 6.19	Evaluation of unmixing results for Cuprite: <i>kaolinite-smectite</i> and <i>alunite</i>	166
Figure 6.20	True positives, false positives, and false negatives of <i>loblolly pine</i> , <i>summer deciduous</i> , <i>soil</i> , <i>shaded vegetation</i> classes from A.P. Hill.	169
Figure 6.21	True positives, false positives, and false negatives of <i>green field</i> , <i>grass field</i> , <i>autumn deciduous</i> , and <i>water</i> classes from A.P. Hill.	170
Figure 6.22	Histogram for the abundances of true positive and false positive pixels of A.P. Hill classes.	171
Figure 6.23	Comparison among abundances, classification map, and true positives, false positives, and false negatives of Cuprite classes.	174
Figure 6.24	Histogram for the abundances of true positive and false positive pixels of Cuprite classes.	175
Figure 6.25	Classification map from unmixing results of A.P. Hill.	178
Figure 6.26	Classification map from unmixing results of Cuprite.	180
Figure 6.27	Scale selection for Guanica images.	185
Figure 6.28	Estimation of the number of spectral endmember classes for Guanica images.	185
Figure 6.29	Abundances for extracted spectral endmember classes of Guanica images.	186
Figure 6.30	Extracted spectral endmember classes for Guanica images.	187
Figure 6.31	Comparison of vegetation spectral endmember classes from Guanica images.	189
Figure 6.32	Estimated vegetation from Guanica images.	189
Figure 7.1	Extracted endmembers from A.P. Hill using SMACC.	194
Figure 7.2	Abundances for extracted endmembers from A.P. Hill using SMACC.	195
Figure 7.3	Extracted endmembers from A.P. Hill using VCA.	196
Figure 7.4	Abundances for extracted endmembers from A.P. Hill using VCA.	197
Figure 7.5	Extracted endmembers from A.P. Hill using RBSPP combined with VCA.	198
Figure 7.6	Abundances for extracted endmembers from A.P. Hill using RBSPP combined with VCA.	199
Figure 7.7	Comparison of <i>loblolly pine</i> and <i>gravel</i> endmembers.	202
Figure 7.8	Reconstruction error from unmixing results of A.P. Hill.	203
Figure 7.9	True positives, false positives, and false negatives of <i>loblolly pine</i> , <i>summer deciduous</i> , <i>soil</i> , <i>shaded vegetation</i> classes extracted using SMACC.	204

Figure 7.10	True positives, false positives, and false negatives of <i>green field</i> , <i>grass field</i> , and <i>water</i> classes extracted using SMACC.	205
Figure 7.11	Histogram for the abundances of true positive and false positive pixels of A.P. Hill classes extracted using SMACC.	206
Figure 7.12	True positives, false positives, and false negatives of <i>loblolly pine</i> , <i>summer deciduous</i> , <i>soil</i> , <i>shaded vegetation</i> , <i>grass field</i> , and <i>water</i> classes extracted using RBSPP.	207
Figure 7.13	Histogram for the abundances of true positive and false positive pixels of A.P. Hill classes extracted using RBSPP.	208
Figure 7.14	Classification maps of A.P. Hill using unmixing results of proposed approach, SMACC, and RBSPP.	212
Figure 7.15	Extracted endmembers from Cuprite image using SMACC.	216
Figure 7.16	Abundances for extracted endmembers from Cuprite using SMACC.	217
Figure 7.17	Extracted endmembers from Cuprite image using VCA.	218
Figure 7.18	Abundances for extracted endmembers from Cuprite using VCA.	219
Figure 7.19	Extracted endmembers from Cuprite image using RBSPP combined with VCA.	220
Figure 7.20	Abundances for extracted endmembers from Cuprite using RBSPP combined with VCA.	221
Figure 7.21	Comparison of <i>kaolinite</i> and <i>alunite</i> endmembers.	224
Figure 7.22	Reconstruction error from unmixing results of Cuprite.	226
Figure 7.23	Comparison among abundances, classification map, and true positives, false positives, and false negatives of Cuprite classes extracted using SMACC.	227
Figure 7.24	Histogram for the abundances of true positive and false positive pixels of Cuprite classes extracted using SMACC.	228
Figure 7.25	Comparison among abundances, classification map, and true positives, false positives, and false negatives of Cuprite classes extracted using VCA.	229
Figure 7.26	Histogram for the abundances of true positive and false positive pixels of Cuprite classes extracted using VCA.	230
Figure 7.27	Comparison among abundances, classification map, and true positives, false positives, and false negatives of Cuprite classes extracted using RBSPP.	231
Figure 7.28	Histogram for the abundances of true positive and false positive pixels of Cuprite classes extracted using RBSPP.	232
Figure 7.29	Classification maps of Cuprite using unmixing results of proposed approach, SMACC, VCA, and RBSPP.	238
Figure 8.1	Computational system for unsupervised unmixing analysis.	245
Figure 8.2	Data structures for multigrid.	247

LIST OF TABLES

Table 2.1	Examples of hyperspectral sensors and their technical specifications.	21
Table 3.1	Optimal stopping scale for False Leaf, AP Hill subset and Guanica Subset images.	63
Table 3.2	Number of spectral endmembers for False Leaf, AP Hill subset, and Guanica Subset images.	68
Table 4.1	Similarity metrics for hyperspectral data.	76
Table 4.2	Spectral clustering algorithm.	81
Table 4.3	Number of spectra per spectral endmember class of Test Data.	89
Table 4.4	Clustering results for six spectral endmember classes from Test Data set.	93
Table 4.5	Clustering results for the seven spectral endmember classes from Test Data set.	94
Table 4.6	Confusion matrix for clustering results of average and complete linkages using SAM in Test Data set.	96
Table 4.7	Estimated number of clusters for Test Data set.	97
Table 4.8	Estimated number of clusters for False Leaf image.	101
Table 5.1	Mean square errors and standard deviations for the estimate abundance from Synthetic Data <i>I</i>	118
Table 5.2	Relative error (%) for the estimate abundance from Synthetic Data <i>I</i>	119
Table 5.3	Spectral angle and standard deviations for the extracted spectral endmembers and original endmembers for Synthetic Data <i>I</i>	120
Table 5.4	Mean square errors and standard deviations for the estimate abundance from Synthetic Data <i>I</i> using the proposed approach, SMACC, VCA, and RBSPP.	122
Table 5.5	Relative error (%) for the estimate abundance from Synthetic Data <i>I</i> using the proposed approach, SMACC, VCA, and RBSPP.	122
Table 5.6	SAM for the extracted spectral endmembers and original endmembers for Synthetic Data <i>I</i>	123
Table 5.7	Comparison of estimated number of endmembers for Synthetic Data <i>II</i> and <i>III</i>	124
Table 5.8	Mean square error and standard deviation for the estimate abundances from Synthetic Data <i>II</i>	128
Table 5.9	Spectral angle and standard deviations for the extracted spectral endmembers and original endmembers for synthetic data.	128

Table 5.10	Mean square errors and standard deviations for the estimate abundance from Synthetic Data <i>II</i>	133
Table 5.11	Spectral angle and standard deviations for the extracted spectral endmembers and original endmember for Synthetic Data <i>III</i>	134
Table 6.1	Contingent Matrix.	147
Table 6.2	Estimated number of spectral endmember classes using validity indexes for A.P. Hill and Cuprite.	155
Table 6.3	Comparison of estimated number of endmembers for A.P. Hill and Cuprite images.	155
Table 6.4	Relation between spectral endmember classes and information classes for A.P. Hill.	161
Table 6.5	Relation between spectral endmember classes and information classes for Cuprite.	167
Table 6.6	Spectral angle between spectral endmembers and reference spectra.	168
Table 6.7	True positive, false positive, and false negative rates for A.P. Hill classes.	169
Table 6.8	True positive, false positive, and false negative rates for Cuprite classes.	173
Table 6.9	Agreement matrix between reference map and generated classification map from unmixing results of A.P. Hill.	178
Table 6.10	Agreement matrix between reference map and generated classification map from unmixing results of Cuprite.	180
Table 7.1	Relation between endmembers extracted by SMACC and RB-SPP, and information classes for A.P. Hill.	201
Table 7.2	True positive, false positive, and false negative rates for A.P. Hill classes extracted using SMACC.	205
Table 7.3	True positive, false positive, and false negative rates for A.P. Hill classes extracted using RBSPP.	208
Table 7.4	Comparison of true positive and false positive rates for A.P. Hill classes extracted using the proposed approach, SMACC, and RBSPP.	210
Table 7.5	Agreement matrix between reference map and generated classification map from unmixing results of A.P. Hill using SMACC.	211
Table 7.6	Agreement matrix between reference map and generated classification map from unmixing results of A.P. Hill using RBSPP.	213
Table 7.7	Comparison agreement analysis among classification maps obtained from the proposed approach, SMACC, and RBSPP.	215
Table 7.8	Relation between endmembers extracted by SMACC, VCA, and RBSPP, and information classes for Cuprite.	223
Table 7.9	Spectral angle between extracted endmembers by SMACC, VCA, RBSPP, proposed approach, and reference spectra.	225

Table 7.10	True positive, false positive, and false negative rates for Cuprite classes extracted using SMACC.	228
Table 7.11	True positive, false positive, and false negative rates for Cuprite classes extracted using VCA.	230
Table 7.12	True positive, false positive, and false negative rates for Cuprite classes extracted using RBSPP.	232
Table 7.13	Comparison of true positive rates for A.P. Hill classes extracted using the proposed approach, SMACC, and RBSPP.	233
Table 7.14	Comparison of false positive rates for A.P. Hill classes extracted using the proposed approach, SMACC, and RBSPP.	233
Table 7.15	Agreement matrix between reference map and generated classification map from unmixing results of Cuprite using SMACC.	237
Table 7.16	Agreement matrix between reference map and generated classification map from unmixing results of Cuprite using VCA.	239
Table 7.17	Agreement matrix between reference map and generated classification map from unmixing results of Cuprite using RBSPP.	239
Table 7.18	Comparison of between-class agreement of classification maps obtained from the proposed approach, SMACC, VCA, and RBSPP.	241
Table 7.19	Comparison of assignment-class agreement of classification maps obtained from the proposed approach, SMACC, VCA, and RBSPP.	242
Table 7.20	Comparison of overall agreement of classification maps obtained from the proposed approach, SMACC, and RBSPP.	242
Table 8.1	Algorithm for scale selection.	246
Table 8.2	Algorithm for spectral endmember extraction using multigrid structure.	248
Table 8.3	Algorithm for the Davies and Bouldin validity index computation.	250

INTRODUCTION

1.1 JUSTIFICATION

Remote sensing uses spaceborne or airborne sensors to acquire information about the Earth. These data allow the characterization of the terrestrial surface, the atmosphere, and the oceans. Remote sensors are useful tools for several applications ([1, 2]) such as land cover classification, cartography, urban growth monitoring, weather, military application and even planetary exploration. One of the most promising types of remote sensing systems are hyperspectral sensors. These sensors measure the radiation reflected or emitted by a surface across of the electromagnetic spectrum, capturing spectral information in hundred of narrow contiguous bands. The spatial and spectral information collected by the hyperspectral sensors offer a unique opportunity for the remote identification of materials.

Spectral information collected by hyperspectral sensors can be the result of mixing different materials in the sensor field of the view [3]. For instance, if the ground instantaneous field of view of the sensor is larger than the objects being sensed then multiple materials occupy a single pixel in the image [1]. There are linear and nonlinear models to describe these mixed pixels. The linear mixing model (LMM) sees the pixel surface as the result of the sum of the contributions of each material or endmembers weighted by their abundances [3]. The nonlinear model assumes a more complex scenario where particles of a same material reflects the light in a non-uniform way [3]. LMM is the most used model since it is considered a good approximation to the reality especially for remote sensing applications where images

with resolution in meters are used [4]. Solving the inverse problem, i.e. *unmixing*, is of great interest in remote sensing image analysis. In unsupervised unmixing, the number of endmembers, their spectral signatures and the abundances are estimated from hyperspectral data [3]. Unmixing is a case of generalized inverse problem [3] where the model parameters are estimated from measured data. Unmixing is an ill-posed problem [3], and their results are affected by the perturbation in the measured spectral images (resulted by the interaction of the signal with the environment and the system), and the underlying assumptions of the different unmixing approaches.

Most algorithms for unmixing are based on the geometrical approach. Pixels in the hyperspectral images are points in a high-dimensional scatterplot that form a simplex where the vertices are the endmembers [5]. The problem with the geometrical methods, as well as most of the unmixing techniques, is that they only use the spectral information in the hyperspectral image (see Section 2.3 for a review of unmixing methods). In addition, most of the existing endmember extraction algorithms provide good results with the appropriate number of endmembers. However, there are no reliable methods to determine the number of endmembers (see Section 2.5). The automated estimation of the number of endmembers is still an open problem in hyperspectral image processing.

The increasing availability of high spatial and spectral resolution sensors opens new possibilities for remote exploration of materials, at the same time that new challenges are imposed for the processing of hyperspectral images. One of these challenges is the incorporation of the spatial information into the analysis. It is expected that spatial-spectral techniques will improve the results of spectral approaches, whence more algorithms that take full advantage of the spatial and spectral information captured by hyperspectral sensor should be developed. The need of spatial-spectral approaches has been recognized by several researches (e.g. [6, 7, 8]). Several algorithms that takes into account the spatial and spectral information have

been proposed for the analysis of hyperspectral imagery mainly for classification applications (e.g. [9, 10, 11, 12, 13]).

Recently, some spatial-spectral unmixing methods have been developed. For example, the Automated Morphological Endmember Extraction algorithm (AMEE [9]), the Spatial-Spectral Endmember Extraction algorithm (SSEE [14]), the Spatial Pre-Processing endmember extraction (SPP [15]), the spatially adaptive hyperspectral unmixing [16], the Region-Based Spatial Pre-Processing (RBSPP [17]), piece-wise convex spatial-spectral unmixing [18], and Weighted Non-negative Matrix Factorization (WNMF [19]) are approaches that use common techniques of image processing (e.g. morphological operation, kernel methods, segmentation) to incorporate the spatial information in the unmixing analysis. Results of AMEE, SSEE, SPP, WNMF, spatially adaptive hyperspectral unmixing and piece-wise convex spatial-spectral algorithms depend of the size of spatial kernels or windows defined into the procedures. RBSPP [17] used unsupervised clustering techniques for the segmentation of hyperspectral images into spectral uniform regions where endmembers are extracted avoiding spatial kernels. This algorithm assumes that the endmembers are in the spectrally uniform regions and mixed pixels are in the boundary of these regions. However, the RBSPP algorithm [17] is only a pre-processing step that does not perform the end-member extraction by itself. It still requires a spectral algorithm for the extraction of endmembers. A review of spatial-spectral techniques is included in Section 2.3.3.

Unmixing plays an important role in hyperspectral image processing and a wide range of applications of hyperspectral remote sensing. Fully-automated techniques that take into account the spatial and spectral information of hyperspectral image are required. In this thesis, an unsupervised unmixing algorithm that uses both the spatial and spectral information of the image for the jointly estimation of the number of endmembers and the extraction of their spectral signatures taking advantage of multiscale representation techniques based on nonlinear diffusion is presented.

1.2 RATIONALE

Endmembers are usually referred to *pure materials* in most unmixing techniques. However, it is clear that the availability of pure pixels in an image depend strongly of the spatial resolution of the sensor. Therefore, the term *spectral endmembers* in this work does not refer to pure materials. Endmembers here refer to spectral signatures representing the distinct components of an image such as uniform regions and objects. Similar endmember concepts have been employed in previous work such as in [17, 15, 18, 4].

Most unmixing techniques use a single spectrum to represent the spectral features of the basic components in an image. However, different materials in an image have spectral variability caused by factors such as topographic effects and changes of illumination (e.g. shadows). Thus, it is more appropriate to use a set of representative spectra as endmembers to account for the spectral variability. Some unmixing approaches have considered the spectral variability (e.g. [16, 20, 21, 22, 23]). For instance, the multiple endmember spectral mixture analysis (MESMA) proposed by Roberts et al. [20] allows varying the type and number of endmembers in each pixel. However, MESMA uses spectral libraries obtained from field work or laboratory spectra. Piece-wise convex (PCE) endmember extraction algorithm described in [21] and [22] builds sets of endmembers that represents the different convex regions in an image. PCE allows endmembers belonging to different sets with a grade of membership. Canham et al. [16] and Somers et al. [23] present unmixing approaches using also sets of endmembers. Both approaches employ spatial windows for endmember extraction, and then sets of endmembers are formed by clustering.

In the developed approach, the sets of spectral endmembers are named *spectral endmember classes*. The concept of spectral endmember classes can be related to the concept of information classes used in classification (see Figure 1.1) [2]. Informa-

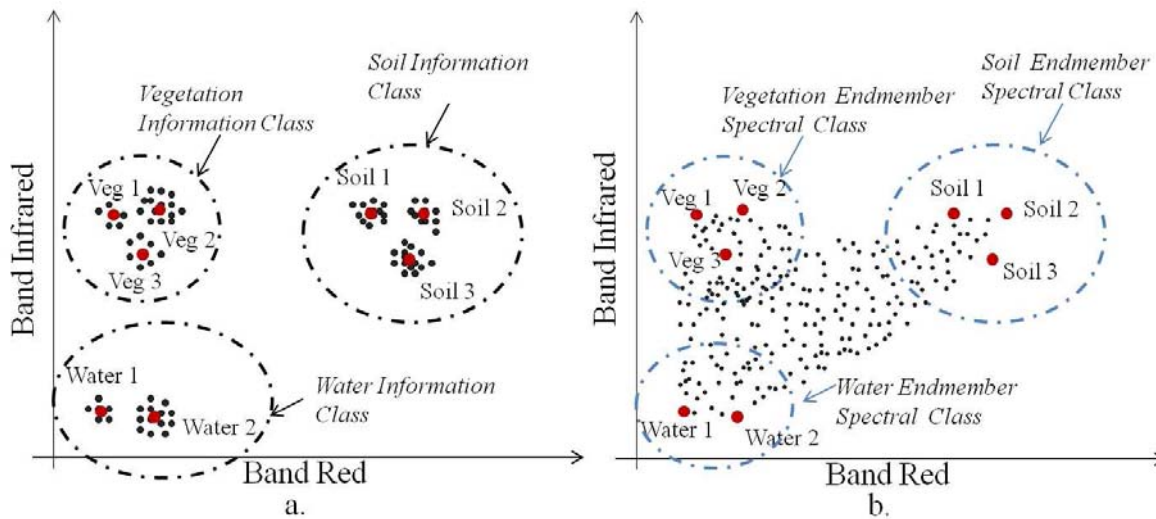


Figure 1.1: Spectral endmember classes concept: (a) Information classes for classification (Figure from [2]). (b) spectral endmember classes for unmixing analysis.

Information classes are groups of spectral classes that represent actual meaningful information classes in the image. In Figure 1.1(a), the red points represent the spectral classes (e.g. *Veg1*, *Veg2*, *Veg3*), and a set of spectral classes form an information class (e.g. $Vegetation = \{Veg1, Veg2, Veg3\}$). In unmixing, spectral endmember classes are groups of spectral endmembers (i.e. the big red points in the Figure 1.1(b)) that represent the basic components of an image while maintaining the spectral variability.

Spectral endmembers are assumed inside the spectrally uniform regions of a hyperspectral image for the developed approach. Thus, a mechanism for determining these uniform regions across an image is necessary. Spectral endmembers must be extracted from these uniform regions. RBSPP finds the uniform regions by segmentation and uses the average of the pixels within a region as the representative. However, RBSPP is a pre-processing step to include the spatial information in the unmixing analysis. The final selection of endmembers is conducted using spectral techniques such as geometrical methods. The spatial-spectral unmixing approach developed here takes advantage of multiscale representation for the determination of the spectrally uniform regions and their representative spectra avoiding the explicit segmentation of the hyperspectral image.

Multiscale representation builds a family of images where fine details are systematically removed using smoothing operations [24]. For example, a linear multiscale representation can be obtained by convolution using several linear Gaussian filters with different variances. The variances generate different levels of smoothing that define a scale space for an image. Smoothing operation using linear Gaussian filters is known as *isotropic diffusion* because it diffuses the information equally in all directions. However, isotropic diffusion reduces the noise but it also eliminates the edges in the image. In contrast, *nonlinear* diffusion seeks to smooth an image while keeping the boundaries regions or edges [24, 25]. A nonlinear diffusion partial differential equation (PDE) is solved to perform nonlinear diffusion, where the initial condition is the original hyperspectral imagery (see Section 3.1).

The spatial and spectral effects of nonlinear diffusion can be understood by looking at Figure 1.2. Parameter t represents the scale steps. Note that regions are smoother as the scale increases. The edges in the image are enhanced at the same time as that fine details are removed. In addition, scatterplots in Figure 1.2 show how the spectral variability decreases as scale increases. The scatterplots in Figure 1.2 have the same number of points (i.e. pixels). The reduction of spectral variability is due to the nonlinear diffusion.

Assuming that spectral endmember are found into the spectrally uniform regions of the image and mixed pixels are in the boundaries of these regions, then the multiscale representation based on nonlinear diffusion can be used to determine the spectral endmembers of the hyperspectral image. As multiscale representation builds a family of smoothed image where the spectrally uniform region can be distinguished (e.g. see Figure 1.2), then spectral endmembers can be selected as the representative spectra for each one of these uniform regions. A procedure based on multigrid methods is developed for the extraction of representative spectra from the smoothed images.

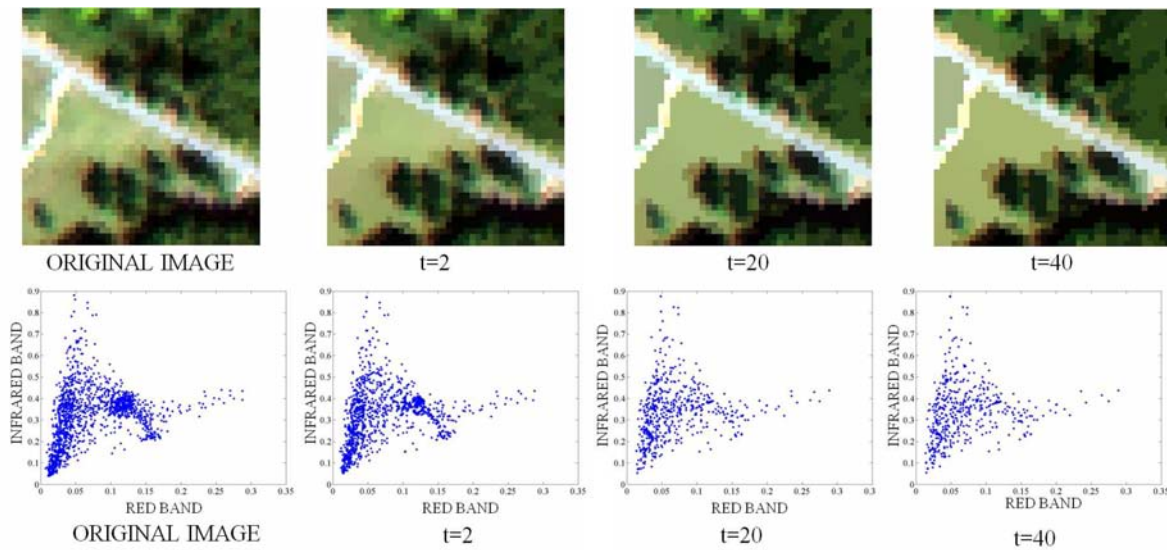


Figure 1.2: Example of nonlinear diffusion for $t = 2, 20, 40$ scale steps of an AVIRIS image of 40×40 pixels. Top row shows the RGB composition using bands 30 (650 nm), 20 (557 nm) and 9 (451 nm). Bottom row shows scatterplots between a red band (band 30: 650 nm) and a infrared band (band 43: 750 nm).

Unlike RBSPP, the unsupervised unmixing approach based on multiscale representation determines the basic constituents by itself and takes advantage of nonlinear diffusion and multigrid methods for the spectral endmember extraction avoiding segmenting the image. All representative spectra are used as spectral endmembers to consider the spectral variability. Similar spectral endmembers are grouped to build the spectral endmember classes. More details are given in Sections 3.2 and 4.2.

1.3 TECHNICAL APPROACH

Duarte et al. [26] propose an algorithm for multiscale segmentation and representation of hyperspectral imagery based on nonlinear diffusion. Duarte's algorithm uses multigrid methods to solve the nonlinear PDE. Multigrid methods are numerical techniques to solve systems of linear equations [27]. Multigrid methods build a hierarchical representation of a problem from a fine grid to a coarse grid (see Figure 1.3). In the coarsest grid, the equation system is solved exactly and then the solution

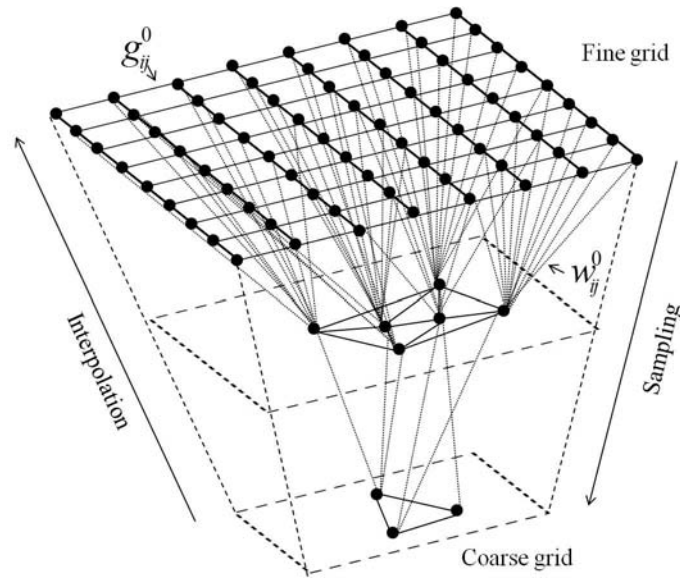


Figure 1.3: Multigrid structure. Figure from [26].

is propagated back to the finer grid. Each grid is represented by a graph. The vertices in the initial graph are the pixels in the original hyperspectral imagery and the initial edges are built using the closest neighbors. A sampling operation is responsible of building the next grids by selecting those vertices that represent a large number of vertices in the previous one (see Section 3.1).

Taking advantage of the multigrid structure, the spectral endmembers can be selected as the vertices in the coarsest grid in a given scale. These vertices are selected such that they represent the vertices in the previous grids. Then, it is expected that vertices in the last grid represent the spectral features of the image such as presented in Section 3.2. Using these spectral endmembers, the abundances can be estimated using existing methods such as least square (if the number of spectral endmembers is less or equal to the number of bands) or sparse regression (if the number of spectral endmembers is bigger that the number of bands).

Spectral endmembers represent the distinct components in a scene as well as their spectral variability. Thus, it is necessary to group spectral endmembers into sets with similar spectral features, i.e. meaningful clusters that represents the distinct materi-

als of the image. These meaningful sets of spectral endmembers are the spectral endmember classes.

A way to build the spectral endmember classes is by using clustering techniques. Clustering divides the data into subsets with similar spectra [28, 29, 30]. One of the more challenging problems in clustering analysis is to determine what an optimal partition of the data is. Clustering results depend of the definition of similarity and the metric used to measure it. In the same way, determining the number of clusters (i.e. the number of spectral endmember classes in the developed approach) is very difficult. This work used relative validity indexes to determine the number of spectral endmember classes. Validity indexes can be used to compare different clustering algorithms as well as to compare the partition obtained with different parameters such as the number of clusters [28, 31, 32]. Clustering has been used before to build set of endmembers in unmixing algorithms [16, 23]. However, there is not a clear study about how to select the method and the number of clusters for this purpose. There are several approaches for clustering, but their performance depends strongly of the data. An example using a controlled data set is conducted to determine the appropriate technique to extract the spectral endmember classes.

In summary, assuming that spectral endmembers are the representation of the spectral signatures of uniform regions and mixed pixels are found in the edges, the unmixing process can be performed as in Figure 1.4. This approach involves the three common steps for unmixing: estimation of number of endmembers, extraction of endmembers, and estimation of abundances using only the information in the hyperspectral image. The first step consists of the multiscale representation of the hyperspectral image using nonlinear diffusion. A scale is selected from the family of smoothed images to perform the spectral endmember extraction. Different scale selection methods are studied and compared in this work. Using the selected scale, the spectral endmembers are extracted by an approach based on the multigrid structure. Spectral endmembers are used to compute the abundances and these are grouped

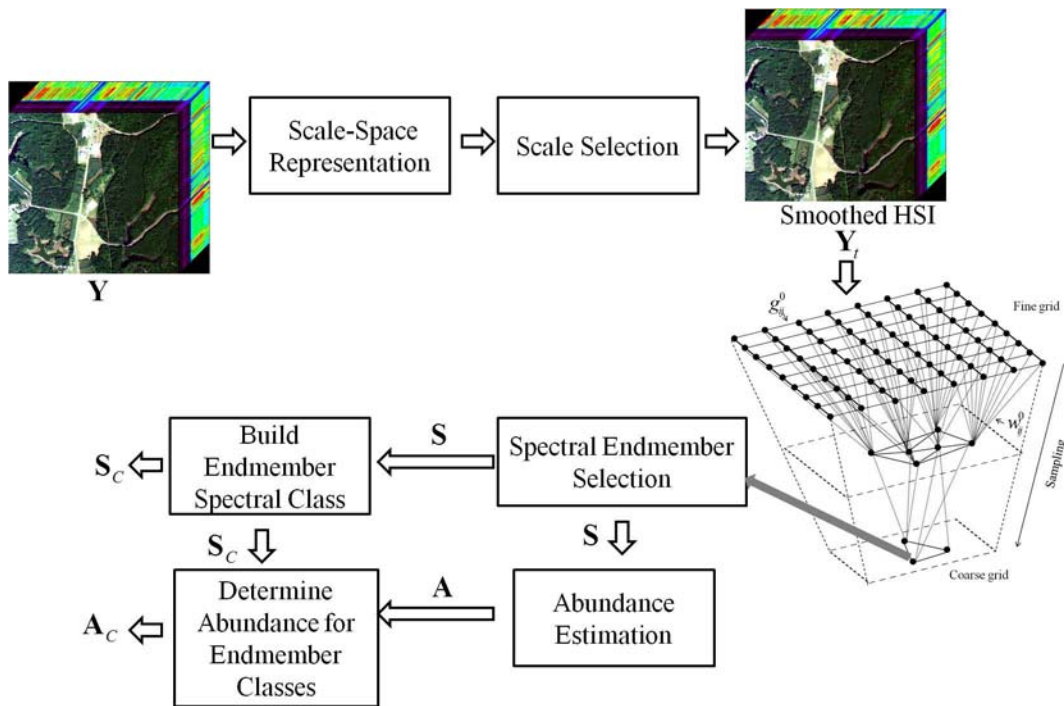


Figure 1.4: Schematic of proposed approach for unmixing.

into spectral endmember classes by clustering techniques. Finally, the abundance for an spectral endmember class will correspond to the sum of the individual abundances of the spectral endmembers that belong to the same spectral endmember class.

1.4 RESEARCH DESIGN AND OBJECTIVES

The main objective of this work was to develop a new spatial-spectral approach for unmixing analysis based on multiscale representation. Multiscale representation using nonlinear diffusion and multigrid methods is employed for spectral endmember extraction. Extracted spectral signatures are grouped into spectral endmember classes that represent both the spectral features and the spectral variability of different materials in the image. This approach is implemented in an unsupervised computing system for the analysis and processing of hyperspectral images.

1.4.1 *Specific Objectives*

The specific objectives of the work were:

- Develop a spectral endmember extraction algorithm using the multiscale representation and the multigrid structures obtained from Duarte et. al. [26] algorithm.
- Analyze the scale effects in spectral endmember extraction, and explore scale-selection methods to determine a suitable scale into the multiscale representation.
- Study the use of spectral endmember classes, instead single spectrum, for the representation of distinct components of the image.
- Compare different methods for clustering of spectral endmember class extraction. Evaluate validity indexes for the estimation of the number of spectral endmember classes.
- Validate the technical approach presented in Figure 1.4 using hyperspectral images collected over different scenarios.
- Compare the proposed approach with other unmixing techniques: VCA, SMACC, and RBSPP.
- Study the effects of spatial resolution in unsupervised unmixing analysis.
- Implement a computing system using MATLAB based on the developed unmixing approach for the unsupervised analysis of hyperspectral images.



Figure 1.5: False Leaf image.

1.4.2 Validation and Assessment

In the first part of this research, an image collected with an SOC700 hyperspectral camera is used to validate the technical approach. The *False Leaf* image was collected by Surface Optics Corporation and downloaded from their website¹. It consists of 640×640 pixels and 120 spectral bands from 402 nm to 908 nm. The image was captured under indoor lighting conditions. The image has two artificial leaves. A RGB composite using bands 57 (639 nm), 35 (548 nm) and 13 (460 nm) is presented in the Figure 1.5. The image has several regions with uniform spectral features, the basic components of this image can be easily determined, and most mixed pixels are in the edges. Because of these characteristics, the False Leaf image is used as first instance to test the different stages of the proposed approach.

A large evaluation of the unsupervised unmixing approach is presented in Chapters 5, 6, and 7. The assessment and validation of the proposed approach are performed using synthetic data sets (Section 5.1) and real hyperspectral images (Section 6.1).

¹ <http://www.surfaceoptics.net>

There is a great difficulty to simulate images with controlled condition for testing and validation of unmixing algorithms because hyperspectral images are affected by several factors such as the spectral variability of the materials, topographic and atmospheric effects, and noise. In addition, hyperspectral images do not only have spectral information, these images keep information about the spatial distribution of materials. In this work, two synthetic data sets are used for the quantitative assessment of the proposed approach (Section 5.1). The first data set has a single spatial distribution (a grid of different materials). This data set allows to simulate different noise levels, and spectral variability. The second data set seeks to simulate the spatial complexity present in real hyperspectral images. For that, abundances extracted from real data are employed to generate synthetic data (see Chapter 5). Using the synthetic data sets, the performance of the proposed approach can be quantified in term of mean square errors, and spectra angles between extracted and real endmembers.

The evaluation of the proposed approach with real data is performed using a methodology inspired by detection theory and classification accuracy analysis (see Section 6.2). In real scenes, there is no information about abundances or comparable endmembers that allow a quantitative assessment. Thus, this work proposes a methodology to assess unmixing results for two study case with hyperspectral image collected over mining and forest scenarios. First, a qualitative analysis is conducted by comparing spectral endmember classes with available spectral libraries, and comparing abundances with classification maps. Spectral endmembers are compared using the shape of the spectral signatures. The classification maps allow to know the different components of an image, and provide some information about endmember spatial distribution. The qualitative analysis provides a relation between the spectral endmembers classes and the information classes within published classification maps. The second step in the assessment methodology used these relations to perform a quantitative evaluation of the detected classes. This assessment is in-

spired in detection theory and seeks to measure how well each class is detected by the unmixing algorithm in term of true positive, false positive, and false negative rates (Section 6.2). In addition, the proposed methodology uses the estimated abundances to build a classification map. This classification map allows to understand what classes dominate the scene according to the estimated abundances. The new classification maps are compared with the published classification maps using an agreement matrix. The *between-class agreement*, *assignment-class agreement*, and the *overall agreement* allows the quantitative comparison among unmixing results and the published classification maps. The agreement matrix is inspired by the confusion matrix in classification.

Additionally, obtained results by the unsupervised unmixing approach based on multiscale representation are compared with other unmixing techniques. The Sequential Maximum Angle Convex Cone (SMACC) [33], Vertex Component Analysis (VCA) [34], and Region-Based Spatial Pre-Processing (RBSPP) [17] algorithms are selected for this comparison. SMACC and VCA are widely used geometrical methods. On other hand, RBSPP is the closest spatial-spectral method to the technique developed in this research, since both do not use spatial kernels. However, RBSPP is only a preprocessing step that does not extract the endmembers by itself. RBSPP is combined with VCA [17] to perform the endmember extraction. Methods are compared in terms of extracted signatures and abundances distributions. The assessment methodology used to evaluate the proposed approach is also used to compare the different unmixing results (see Chapter 7).

Finally, effects of spatial resolution over the proposed approach are studied using images collected at different spatial resolutions over the same scene. This study, also included in the Chapter 6, compares the spectral endmember classes and abundances obtained using the different resolutions.

1.5 THESIS CONTRIBUTIONS

The major contribution of this thesis is for the hyperspectral image processing field. The importance of unmixing for the analysis of hyperspectral imagery is evident. Unmixing algorithms that take full advantage of the spatial and spectral information of hyperspectral imagery are required. In addition, there are not reliable algorithms for the estimation of the number of endmembers. Most approaches used for the estimation of the number of endmembers are based on the estimation of the rank of a matrix which in itself is a very difficult problem and neglects spatial information. This work contributes in both directions: proposing a new approach for the estimation of the basic constituents of an image (determine the number of endmember classes using validity indexes) and using both spatial and spectral information for unmixing analysis of hyperspectral data.

On the other hand, hyperspectral imagery is an important sensing technology that is being used across different application domains. This research develops a computing system for the unsupervised unmixing analysis of hyperspectral imagery that facilitates the analysis of this type of image for several applications. The development of unsupervised techniques for hyperspectral image processing is very important. Remote sensing is usually performed for task where the acquisition of information through direct contact with the sensing objects is very difficult, too expensive or time consuming. Therefore, it is necessary to develop algorithms that allows the extraction of this information remotely, accurate, and efficiently in an unsupervised fashion. The developed computing system produces usefull abundance maps and spectral signatures that can be used in different applications of remote sensing. Although the extraction of this information is performed in an unsupervised way, the interpretation of the results require analyst intervention.

Finally, the developed assessment methodology is other important contribution of this work. It is evident the difficult to evaluate unmixing results since there are few information about the scenes and it is many times limited to classification maps and spectral libraries. The developed assessment methodology proposed a new way to perform a quantitative assessment of unmixing results using classification maps.

During the development of this work the follow publications were done:

- Miguel A. Goenaga, M. Torres-Madronero, M. Velez-Reyes, S. Van-Bloem, and J. China. "Unmixing analysis of a time-series of Hyperion images over the Guanica dry forest in Puerto Rico," *IEEE Journal of Selected Topics in Applied Earth Observations and Remote Sensing*, 2012.
- M. Torres-Madronero, and M. Velez-Reyes. "Unmixing analysis based on multiscale segmentation," in *Proceedings of 4th Workshop on Hyperspectral Image and Signal Processing Evolution en Remote Sensing WHISPERS*, Jun. 2012.
- M. Torres-Madronero, and M. Velez-Reyes, "Unsupervised unmixing analysis based on multiscale representation," in *Proceedings of SPIE Vol. 8390, Algorithms and Technologies for Multispectral, Hyperspectral, and Ultraspectral Imagery XVIII*, Apr. 2012.

1.5.1 Contributions to CISE

This work is part of the research field of Computational Signal and Image Processing inside of the concentration in Computer Science and Engineering in the *Computing and Information Science and Engineering (CISE)* doctoral program at the University of Puerto Rico [35]. CISE program seeks to integrate engineering, computing and information science components. In this research these three components can be identified. The engineering component consists in the design of the spatial-spectral

model for the unmixing analysis based on multiscale representation. The computing component is formed by the computing system for the unsupervised unmixing analysis, and the information science component is related with the information extraction process from hyperspectral imagery in which the problem of estimation of the basic components (i.e. number of spectral endmember classes) and extraction of spectral signatures are very important. The developed unmixing technique is a novel approach that takes advantage of existing techniques of image processing and data mining such as multiscale representation and clustering for the extraction of information from hyperspectral imagery.

1.6 THESIS OUTLINE

Chapter 2 presents a complete review about the state of the art in unmixing analysis of hyperspectral imagery. The linear mixing models is presented in Section 2.2, and the most widely used algorithm for endmember extraction are reviewed in Section 2.3. Section 2.3.3 is devoted to review some of the spatial-spectral methods for endmember extraction. Least square and sparse regression based methods for abundance estimation are described in Section 2.4. Some attempts to estimate the number of endmembers are presented in Section 2.5. Then, the concept of scale space and the basics of multiscale representation are introduced in Section 2.6.

Chapter 3 introduces the new spectral endmember extraction procedure. First, nonlinear diffusion and multigrid methods are reviewed in Section 3.1. Then, the spectral endmember extraction approach is described in Section 3.2 and some methods for scale selection are reviewed and compared in Section 3.2.1.

Chapter 4 aims to compare several clustering algorithms for the spectral endmember class extraction. Section 4.1 presents a review about cluster analysis. Section 4.2 shows the methodology designed for the spectral endmember class extraction and

Section 4.3 shows a comparison of several clustering algorithms and validity indexes. Section 4.3.2 compare the different techniques using a test data set, and then, validity indexes are evaluated for the estimation of the number of spectral endmember classes in Section 4.3.3.

Chapter 5 presents a quantitative assessment of the proposed unmixing approach using synthetic data. Section 5.1 describes the generation of the data used in these experiments. Section 5.2 described the metrics used for the quantitative assessment, and Section 5.3 presents the results.

Chapter 6 presents an extended validation and assessment of the proposed unmixing approach using hyperspectral images from different scenarios. Section 6.1 describes the data sets employed in these experiments. Section 6.2 describes the assessment methodology. Section 6.3 shows the unmixing analysis of two hyperspectral images and their evaluation using classification maps and spectral libraries. Finally, Section 6.4 analyzes the spatial resolution effects on the unmixing analysis based on multiscale representation.

Chapter 7 presents the comparison of the proposed approach with other unmixing techniques. Sections 7.1 and 7.2 show the comparison of SMACC, VCA, RBSPP and the proposed approach using A.P. Hill and Cuprite hyperspectral images respectively.

Chapter 8 describes the implementation and the complexity analysis for the developed unmixing algorithm. Chapter 9 aims to analyze ethical issues regarding the acquisition, processing, and interpretation of remote sensing imagery. Finally, Chapter 10 presents the conclusions of this work as well as indicates possible paths for future research.

The combined spectral-spatial information captured by hyperspectral images has a high potential for the remote identification of materials. Several hyperspectral image processing techniques have been proposed. Most of these techniques only use the spectral information captured by hyperspectral images. Spatial information has been incorporated in the hyperspectral analysis using well-known techniques of image processing such as morphological analysis, spatial kernels, and segmentation.

This chapter presents a general overview of the current state of the arte in hyperspectral image processing giving a special emphasis in the linear unmixing and methods that use both spatial and spectral information. First, an overview of hyperspectral imaging is presented. Then, the linear mixing model (LMM) is reviewed in Section 2.2, endmember extraction algorithms and abundance estimation methods are described in Sections 2.3 and 2.4 respectively. Algorithms that take advantage of both spatial and spectral information are reviewed in Section 2.3.3.

Several endmember extraction techniques assume that the number of endmembers is known a priori. However, it is difficult to determine how many endmembers there are in a scene. Some attempts to develop approaches for the estimation of the number of endmembers can be found in the literature. These techniques are reviewed in Section 2.5. Additionally, Section 2.6 introduces the concepts of scale space and multiscale representations. Both concepts are fundamental in the development of the proposed unmixing approach (Figure 1.4).

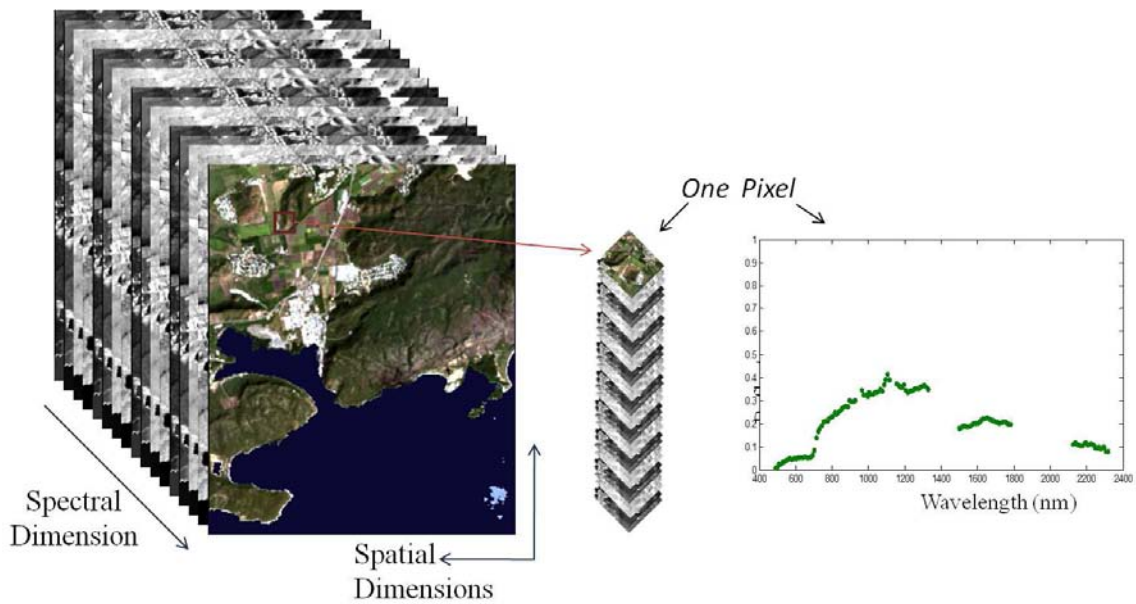


Figure 2.1: Hyperspectral imagery.

2.1 HYPERSPECTRAL IMAGERY

Multispectral and hyperspectral remote sensors measure the radiance reflected or emitted by a surface along of the electromagnetic spectrum. Multispectral remote sensors are characterized by having a relatively small number of non-contiguous bands (e.g. less than 25 bands). Instead, hyperspectral sensors capture the radiance along hundreds of narrow bands sampled continuously across the electromagnetic spectrum. Spatial and spectral information in hyperspectral images can be visualized as a cube (see Figure 2.1), where each pixel is a vector which entries correspond to the intensity of radiance along different wavelengths. The spectral signature for each material allows the characterization of the different components in a surface [2].

There are several commercial and noncommercial systems for the acquisition of hyperspectral image. Examples of hyperspectral sensors are summarized in Table 2.1. Airborne sensors such as AVIRIS, HYDICE, AISA Eagle and CASI allow the acquisition of scenes of different spatial resolution by acquiring imagery at different altitudes or using different optical configurations. AISA and CASI systems can even

Table 2.1: Examples of hyperspectral sensors and their technical specifications.

Sensor	Num. of Bands	Spectral Sampling	Spectral Range	Spatial Resolution
AVIRIS ^a	224	10 nm	380 to 2500 nm	4m
AISA Eagle ^b	256	2 nm	400 to 1000 nm	0.6 m
CASI 550 ^c	288	1.9 nm	400 to 1000 nm	0.5 m
HYPERION ^d	220	10 nm	400 to 2500 nm	30 m
HYDICE[36]	210	10 nm	400 to 2500 nm	1 m

^a<http://aviris.jpl.nasa.gov/>

^b http://galileo-gp.com/aisa_eagle.html

^c <http://www.itres.com/products/imagers/casi550/>

^d <http://edcsns17.cr.usgs.gov/eo1/sensors/hyperion>

capture sub-meter resolution imagery. Hyperion is on board NASA EO-1 satellite, and therefore, can capture imagery of a same place periodically. However, Hyperion has a low spatial resolution of 30 meters.

Pixels in hyperspectral images are the result of mixing several components or pure materials. Mixed pixels are the results of several factors such as the combination of the distinct materials that occupy a single pixel due to the spatial resolution of the sensor, the effect of the point spread function of the sensor, or the sensing of a non homogeneous surface [1][2][3]. Determining what are the materials present in an image is one of the most important problems in hyperspectral image processing. The linear mixing model and some algorithms for spectral unmixing are presented below.

2.2 LINEAR MIXING MODEL

Spectral information captured by a hyperspectral remote sensor can be modeled as the linear combination of several homogeneous materials in the sensor field of view [3]. The LMM is formulated as:

$$\mathbf{y} = \mathbf{S}\mathbf{a} + \mathbf{w} \quad (2.1)$$

where $\mathbf{y} \in \mathbb{R}^n$ is the radiance measured by the hyperspectral sensor along n spectral bands, $\mathbf{S} \in \mathbb{R}^{n \times p}$ is a collection of p signatures of basic constituents or *endmembers*, $\mathbf{a} \in \mathbb{R}^p$ is a vector whose elements represent the individual contribution of each endmember in a pixel, i.e. *abundance vector*, and $\mathbf{w} \in \mathbb{R}^n$ represents the noise. For a complete image, the mixing model can be expressed in matrix form as:

$$\mathbf{Y} = \mathbf{S}\mathbf{A} + \mathbf{W} \quad (2.2)$$

where each column of $\mathbf{Y} \in \mathbb{R}^{n \times m}$ is a pixel in the hyperspectral image, m is the number of pixels, and $\mathbf{A} \in \mathbb{R}^{p \times m}$ represents the abundances.

Unsupervised unmixing algorithms aim at estimating the number of endmembers p , their spectral signatures (i.e. the endmember matrix \mathbf{S}), and their abundances, \mathbf{A} [3]. Abundances are subject to non-negativity, $a_i \geq 0$, and full additive $\sum a_i = 1$ constraints. The full additive constraint can be relaxed to sum less or equal to one, $\sum a_i \leq 1$, to include shadow endmembers or topographic effects [37].

Several methods have been proposed to solve the unmixing problem. Many algorithms assume that endmember are known a priori. Spectral libraries obtained in laboratories or collected in the field can be used as endmembers. However in most cases endmember are unknown. This review is focused on automated unmixing algorithms that extract the endmember signatures from the hyperspectral image itself. These are known as scene-based endmembers.

Typical unmixing algorithms can be divided in two steps [3]. The first step consists of the extraction of spectral signatures of endmember from the image. The endmember extraction algorithms are classified as geometric, parametric, and spatial-spectral methods. In the second step, abundances are estimated. Once the endmembers are known, the estimation of abundances is an inversion problem. Inversion techniques based on least square and sparse regression are reviewed. Some unmixing algorithms estimate the number of endmembers together with the spectral signa-

tures. However, most endmember extraction algorithms assume that the number of endmembers is known a priori. Determining the number of endmembers in hyperspectral imagery is a challenging problem. A review of algorithms for the estimation of the number of endmembers is also included in Section 2.5.

2.3 ENDMEMBER EXTRACTION ALGORITHMS

There are several approaches for automatic endmember extraction. The most widely used algorithms are based on the relation between unmixing with convex geometry. In addition, parametric model approaches have been proposed for the endmember extraction problem. Geometric and parametric approaches are reviewed in the next sections. Techniques described in Sections 2.3.1 and 2.3.2 are per-pixel approaches that do not take into account the spatial information provided by the hyperspectral images. Section 2.3.3 is dedicated to review the state of the art of endmember extraction algorithms that use both spatial and spectral information.

2.3.1 *Geometric Methods*

The unmixing problem is related to a convex geometry problem where the spectral signatures are seen as points in an n -dimensional scatterplot [5]. Due to the non-negativity property of radiance and reflectance, spectral data lie in a convex cone [38]. When the full additive constraint is added, the spectral data lie in a simplex where the points are linear combinations of its vertices [5]. Figure 2.2 illustrates these ideas. The relation between the unmixing problem and convex geometry has been used by many researchers to develop algorithms for the extraction of endmember signatures. Algorithms such as Pixel Purity Index (PPI [39]), N-FINDR [40] [41], and Simplex Growing Algorithm (SGA [42]) are based in the simplex model. Some al-

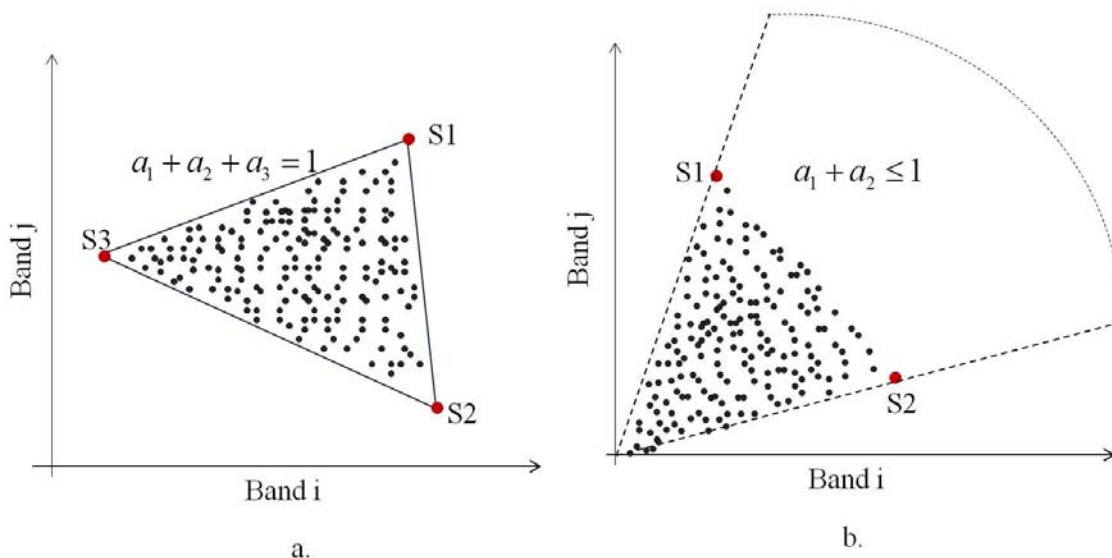


Figure 2.2: Geometric models for mixed pixels: (a) Simplex (Figure from [44]). (b) Convex cone models (Figure from [34]).

gorithms explore the convex cone approach such as Convex Cones Analysis (CCA [38]), and Sequential Maximum Angle Convex Cone (SMACC [33]). Vertex Component Analysis (VCA [34]) explores the fact that the projection of the convex cone onto a hyperplane is a simplex with the vertices corresponding to the endmembers. The unmixing problem is also related to the Non-negative Matrix Factorization (NMF) from a geometric point of view [43]. These algorithms are briefly reviewed below.

2.3.1.1 PPI

Pixel Purity Index is the first approach that explores the convex property of LMM and was proposed by Boardman in [39]. PPI determines a set of candidates for endmembers assuming that pure pixels are present in the image. This is not a fully automated technique because the final endmembers should be selected by a trained image analyst. Given a hyperspectral image, a maximum noise fraction (MNF) transform [45] is used to reduce the dimension of the data. The reduced data is projected onto random unit vectors. The numbers of times that a pixel is an extreme point in the projection are registered. The accumulated value for each pixel gives the purity

index. Pixels with the largest purity indexes are candidates for endmembers. Next, a visualizer of high dimension and experience in image analysis are required to select the final endmembers from the candidate set. PPI is included in ENVI software ¹. The PPI function in the ENVI creates an image with the purity index. The result of PPI is then an input for the ENVI n-D Visualizer where the user should select the final endmembers.

2.3.1.2 *N-FINDR*

Other widely used geometric algorithm is N-FINDR [40, 41]. N-FINDR seeks the pixels that form the simplex with the maximum volume that enclosed the data. First, the MNF [45] transform is used to reduce data dimensionality. Next, a set of pixels are randomly selected as endmembers. The volume of the simplex is calculated using the selected pixels as:

$$V(\mathbf{S}) = \frac{abs(|\mathbf{S}|)}{(p-1)!} \quad (2.3)$$

where p is the number of endmembers, $abs()$ is the absolute value and $| \cdot |$ denotes the determinant.

The algorithm iteratively replaces every endmember for each pixel in the hyper-spectral image calculating the volume. If the volume increases, then the pixel replaces the endmember. Chang et al. [42] describe the Simplex Growing Algorithm (SGA) algorithm that improves the computational complexity of N-FINDR. Similar to N-FINDR, SGA looks for pixels that form the maximum volume simplex. But, SGA begins with two endmembers, and it selects a new endmember from the hyper-spectral data such that the simplex volume increases. New endmembers are selected until the desired number of endmembers is reached. Chang et al. describe in [42] a procedure to select the initial endmembers. The main problem with the algorithms

¹ <http://www.ittvis.com/language/en-us/productservices/envi.aspx>

based in the maximum volume simplex is that results are affected by outliers. N-FINDR and SGA assume that there are pure pixels in the image.

2.3.1.3 CCA

Convex Cone Analysis (CCA) described by Ifarraguerri and Chang [38] seeks the boundaries of the convex region that circumscribe the spectral data points. The vertices of this convex region are used as endmembers for the unmixing procedure. CCA assumes that the number of endmembers is known a priori. First, CCA computes the correlation matrix \mathbf{C} of the hyperspectral data. Then, CCA selects the eigenvectors, $[\mathbf{v}_1 \dots \mathbf{v}_p]$, corresponding to the p largest eigenvalues of \mathbf{C} to form a system of equations. The boundaries of the convex cone are found solving the following equation:

$$\mathbf{x} = \begin{bmatrix} \mathbf{v}_1 & \dots & \mathbf{v}_p \end{bmatrix} \begin{bmatrix} 1 \\ a_1 \\ \vdots \\ a_{p-1} \end{bmatrix} \mathbf{V}\mathbf{a} \geq \mathbf{0} \quad (2.4)$$

where $\mathbf{V} = [\mathbf{v}_1 \dots \mathbf{v}_p]$ and a_i are the $p - 1$ free parameters. CCA seeks a set of coefficients a_i such that these produce a linear combination with $p - 1$ elements of \mathbf{x} that are exactly zero, and all of the other elements nonnegative. These points represent the corners of the convex cone [38].

2.3.1.4 SMACC

Sequential Maximum Angle Convex Cone (SMACC) algorithm [33] is also based on the convex cone model. It is a sequential algorithm that computes simultaneously both endmembers and fractional abundance maps. SMACC assumes that there are pure pixels in the image. This algorithm is also included in the ENVI software.

First, a group of extreme vectors (i.e. pixels that cannot be expressed as positive linear combination of other pixels in the image) are selected from the image. A first endmember is selected from the extreme vectors. Then, the abundance for this endmember is computed. The endmember is removed from all of the vector pixels by orthogonal projection. A new endmember is identified based on length of its residual in the actual model, where the residual is the spectral data outside of the current convex cone. The algorithm updates the abundances of previous endmember before continue to the next iteration. It terminates when all of the spectral data are within the convex cone or the number of endmembers is reached [33].

2.3.1.5 VCA

Vertex Component Analysis (VCA) [34] assumes that pure pixels are present in the hyperspectral image, similarly to other algorithms (e.g. PPI, N-FINDR, SMACC) and that the number of endmembers is known a priori. VCA exploits the fact that endmembers are the vertices of a simplex, and that the affine transformation of a simplex is also a simplex. The pixels of the hyperspectral image lie in a convex cone contained in a subspace of dimension p . VCA identifies this subspace using SVD whether the SNR (signal-to-noise ratio) of the data is higher than a given threshold, otherwise projection is obtained by PCA. The algorithm iteratively projects the data onto an orthogonal direction to the subspace spanned by the endmembers already determined, until the number of endmembers is reached. Endmember signatures correspond to the extremes of the orthogonal projections.

2.3.1.6 NMF

Non-negative Matrix Factorization (NMF) is proposed by Lee and Seung in [46]. Given a non-negative matrix $\mathbf{Y} \in \mathbb{R}_+^{n \times m}$ (e.g. a spectral image), NMF tries to find two non-negative matrixes $\mathbf{S} \in \mathbb{R}_+^{n \times p}$ and $\mathbf{A} \in \mathbb{R}_+^{p \times m}$ (e.g. spectral endmember and abundance matrix in unmixing analysis), such that $\mathbf{Y} = \mathbf{SA}$. The minimum value of p

for which the factorization exists is called the positive rank. NMF has been explored for hyperspectral image analysis in several works such as [47], [48], [49], and [50]. Donoho and Stodden [43] give the geometric interpretation of NMF and related it to finding the convex cone that contains the spectral data points. The advantage of this approach over other geometric methods is that NMF does not assume that pure pixels are present in the hyperspectral image. However, the number of endmembers or the positive rank should be known a priori.

Given p , unmixing using NMF approximation can be performed by finding $\mathbf{S} \in \mathbb{R}_+^{n \times p}$ and $\mathbf{A} \in \mathbb{R}_+^{p \times m}$ such that [49] [50]:

$$(\hat{\mathbf{S}}, \hat{\mathbf{A}}) = \arg \min_{S_{ij} \geq 0, A_{ij} \geq 0} \|\mathbf{Y} - \mathbf{S}\mathbf{A}\|_F^2 \quad (2.5)$$

Jia and Qian [49] includes smoothness and sparseness constraints in the optimization. Masalmah and Velez-Reyes [50] describe the use of constrained positive matrix factorization (cPMF) for unsupervised unmixing.

2.3.2 Parametric Methods

The algorithms described previously represent each endmember as a single spectrum. Parametric approaches model endmembers and fractional abundances as random vectors. Most parametric algorithms assume Gaussian distributions for the pure constituents [3]. Several parametric models can be found in the literature such as stochastic mixing model [51], dependent component analysis [52], endmember detection using the dirichlet process [22], Piece-wise Convex Endmember (PCE [21]), and reversible jump Markov Chain Monte Carlo algorithm [53].

Geometric models are the most used techniques for unmixing. However, researchers have demonstrated that not all hyperspectral images follow the convex hull model [21], and therefore geometric algorithms are not suitable in these cases. Zare and

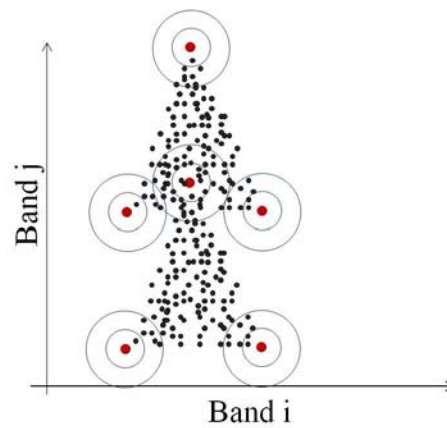


Figure 2.3: Piece-wise convex approach. Illustration from [21].

Gader [21] describe an unmixing technique based on the partitioning of spectral data into several convex regions called PCE algorithm. Figure 2.3 illustrates the approach of Zare and Gader. The curves around endmembers represent the standard deviation for each endmember distribution. Endmembers are modeled using Gaussian distributions and the priori distributions for the abundance vectors are polynomial functions. The number of convex regions are estimated using a Dirichlet process. Abundance vectors in PCE are sparse since each pixel uses only a subset of the endmembers.

2.3.3 Spectral - Spatial Methods

The algorithms described previously only take into account the spectral information in hyperspectral imagery (i.e. pixel only approaches). This section reviews some algorithms that consider both spatial and spectral information for endmember extraction.

2.3.3.1 AMEE

Automated Morphological Endmember Extraction (AMEE) is a fully automated endmember extraction algorithm proposed by Plaza et al. [9] based on mathematical

morphology operations extended to multispectral images. AMEE estimates the number of endmembers and looks for them using spatial kernels. Input parameters to the algorithm are the minimum and maximum size of the spatial kernel. The kernel K , initially with the minimum size, is moved through all image defining local neighborhoods around each pixel $\mathbf{y}(x, y)$.

Extension of morphological operators (i.e. dilation and erosion) to multispectral and hyperspectral imagery are used to define a vector ordering relation. Plaza et al. [9] describes an ordering method based on the spectral purity of a pixel. The spectrally purest pixels \mathbf{p} are related to the dilation operation and spectrally mixed pixels \mathbf{m} are related to the erosion operation. Dilation and erosion are defined for a pixel $\mathbf{y}(x, y)$ and a kernel K as:

$$\mathbf{p} = \arg \max_{(s,t) \in K} \{D(\mathbf{y}(x + s, y + t), K)\} \quad (2.6)$$

$$\mathbf{m} = \arg \min_{(s,t) \in K} \{D(\mathbf{y}(x - s, y - t), K)\} \quad (2.7)$$

where D denotes a distance metric given by:

$$D(\mathbf{h}(x, y), K) = \sum_s \sum_t \text{dist}(\mathbf{h}(x, y), \mathbf{h}(s, t)) \quad \forall (s, t) \in K \quad (2.8)$$

and $\text{dist}()$ is the spectral angle distance. The effects of dilation and erosion in spectral data are illustrated in Figure 2.4. Dilatation expands regions with pure pixels while erosion shrinks zones with pure pixels.

A morphological eccentricity index (MEI) is obtained by calculating the spectral angle distance between \mathbf{p} and \mathbf{m} . MEI is assigned to the maximum pixel in the neighborhood. This index determines the capacity of a pixel to describe other pixels in the kernel. The process is repeated for all pixels in the image using kernels of increasing size until the maximum spatial kernel size is reached. The MEI value is updated at each one of the iterations. A threshold is applied to the MEI for unsuper-

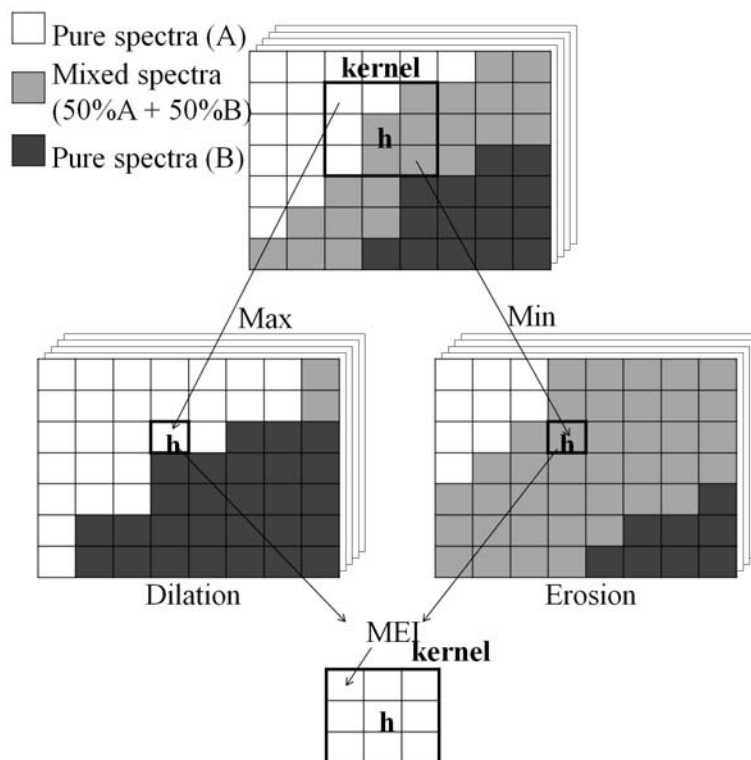


Figure 2.4: Automated morphology endmember extraction algorithm. Effects of dilation and erosion in spectral data. Figure from [9].

vised endmember selection. The number of endmembers correspond to the number of pixels that are not eliminated from the MEI. A region growing procedure is used to refine the final selection.

Kernels allow to define local neighborhoods in the search of spectral purity pixels. Thus, AMEE takes into account the spatial and spectral information of the hyperspectral data for endmember extraction. Dilation and erosion operation are extended to determine maximum and minimum spectra in term of the spectral purity of pixels. The MEI index defined by Plaza et al. [9] allows the selection of those pixels with high spectral purity (determined by the dilation operation) and few mixed (determined by the erosion operation).

2.3.3.2 *SSEE*

Spatial-Spectral Endmember Extraction (SSEE) algorithm described by Rogge et al. [14] is based on the fact that endmembers with high spectral contrast are easy to detect using any convex technique. On the other hand, the detection of endmembers with low spectral contrast with respect to the full image is a more difficult task. SSEE breaks up the full image into several subsets increasing the relative contrast of endmembers. SSEE consists of four steps. First, the largest eigenvectors from the SVD of each subset are selected. This set of eigenvectors explains most of the spectral variability of the image. Second, the full image is projected onto the selected eigenvectors. Pixels lying at the extreme are candidates for endmembers. Third, spectrally similar candidates are averaged if they are spatially related. In the last step, endmembers are ordered into a list by using the spectral angle such that the user can identify spectral endmember classes. First endmember is selected as the first spectra in the ordered list. Spectral endmember classes are determined manually by the user identifying groups of similar spectra in the ordered list.

Three parameters are required for SSEE: the pixel subset size, the threshold to select the largest eigenvectors, and the threshold to average similar endmembers in the third step. Rogge et al. [14] suggest a subset size of 20 pixels, the first threshold is fixed such that the selected eigenvectors represent the 99% of spectral variability, and the second threshold is suggested to one degree if the spectral angle distance is used.

2.3.3.3 *SPP*

Zorteza and Plaza [15] propose a spatial pre-processing (SPP) step to improve endmember extraction from hyperspectral imagery. This SPP step can be combined with any spectral endmember extraction algorithm. SPP seeks to enhance the search of endmembers based on the assumption that it is likely to find endmembers within

homogeneous regions. A scale factor $\rho(i, j)$ as function of spatial similarity between the pixel (i, j) and their neighbors is defined in [15] to improve the endmember extraction. This scale factor is used by the spectral endmember extraction algorithms to seek endmembers in spectrally uniform regions. The scale factor is defined as:

$$\rho(i, j) = \left(1 + \sqrt{\alpha(i, j)}\right)^2 \quad (2.9)$$

where:

$$\alpha(i, j) = \sum_{r=i-d}^{i+d} \sum_{s=j-d}^{j+d} \beta(r-i, s-j) \gamma(r-i, s-j) \quad (2.10)$$

and d is determined by the width of the neighborhood window of the pixel (i, j) , $\gamma(r-i, s-j)$ is a similarity measure between two pixels (r, s) and (i, j) where (r, s) is a neighbor of (i, j) , and β is a weighted factor defined such that neighbors closest to pixel (i, j) have more weight in the scale factor.

Zorteza and Plaza [15] present a simple equation to compute the scaled image \mathbf{Y}' :

$$\mathbf{Y}'(i, j) = \frac{1}{\rho(i, j)} (\mathbf{Y}(i, j) - \mu) + \mu \quad (2.11)$$

where μ is the data mean.

Once the scaled image is computed, an endmember extraction technique is applied to determine the endmembers and their positions. Then, the abundances are estimated using the spectra associated with the selected positions. The main advantage of this method is that it does not require to modify the endmember extraction procedures. However, SPP results are dependent on the neighborhood size.

2.3.3.4 *Spatially Adaptive Hyperspectral Unmixing*

Canham et al. [16] describes the spatially adaptive hyperspectral unmixing approach which divides the image into several tiles that are used to identify local endmembers. The endmember extraction in each tile is performed using per-pixel techniques. In [16], MAX-D [54] is used for the determination of local endmembers. Abundances are estimated in each tile using local endmembers and similar endmembers are clustered to determine global abundances. MAX-D requires the number of endmembers as input, for which Canham et al. use a methodology based on the Gram matrix [16]. This methodology begins by computing the volume of the convex hull formed by the endmembers extracted using MAX-D. The volume of the convex hull is computed as the determinant of the local Gram matrix expressed as:

$$\mathbf{G}(i, j) = \langle (\mathbf{Y}_k - \mathbf{Y}_i), (\mathbf{Y}_k - \mathbf{Y}_j) \rangle \quad (2.12)$$

where $\langle \rangle$ denotes the dot product, \mathbf{Y}_i and \mathbf{Y}_j are two endmembers, and \mathbf{Y}_k is the mean. The volume of the convex hull is calculated for several values of p . A property of Gram matrix is that when the vectors become linearly dependent, the determinant becomes zero. Thus, the number of endmembers is estimated when the percentage of the volume of the convex hull is close to a threshold. As the abundances are estimated locally, a tiling artifact is observed in the final abundances. The algorithms also depends of the tile size similarly to SPP, SSEE, and AMEE.

2.3.3.5 *RBSPP*

Region-Based Spatial Pre-Processing (RBSPP) [17] algorithm uses spatial information to determine the endmembers. RBSPP seeks for the most spectrally pure regions using unsupervised clustering and orthogonal subspace projection. RBSPP assumes that pure spectral signatures are presented in spatially homogenous regions and the

boundaries will contain mixed pixels. Similar to SPP, RBSPP is a pre-processing step that can be combined with per-pixel techniques for the final estimation of endmembers. Martin and Plaza [17] compare the results of RBSPP using NFINDR and VCA. The unsupervised clustering is conducted using ISODATA, k-means, and a hierarchical segmentation algorithm.

Regions are represented by their mean spectrum \mathbf{x}_k . Using these representative spectra, an orthogonal projection procedure determines those spectrally distinct regions which will be used as inputs for the per-pixel endmember extraction techniques for the final determination of endmembers. The first region is the one with the highest intensity spectrum:

$$R_1 = \arg \max_k \sum_{k=1}^r \mathbf{x}_k \mathbf{x}_k^T \quad (2.13)$$

where r is the number of regions (or segments) in the hyperspectral image. Once the first region is selected, then $\mathbf{U} = [\mathbf{x}_1]$ and iteratively other regions are selected by:

$$R_j = \arg \max_k \left\{ \left(P_{\mathbf{U}_{j-1}} \mathbf{x}_k \right)^T \left(P_{\mathbf{U}_{j-1}} \mathbf{x}_k \right) \right\} \text{ for } k = 2 \dots r \quad (2.14)$$

where $P_{\mathbf{U}_j} = \mathbf{I} - \mathbf{U}_j (\mathbf{U}_j^T \mathbf{U}_j)^{-1} \mathbf{U}_j^T$ and $\mathbf{U}_j = [\mathbf{x}_1 \dots \mathbf{x}_j]$. The orthogonal projections are repeated until $j = c$, where c is a predefined number of regions. The spectra inside the selected regions are the input for the per-pixel technique. The number of endmembers required for the per-pixel technique is determined by HYSIME [55] and c is equal to $2p$. Unlike the other spatial-spectral algorithms, RBSPP does not require kernel or spatial windows. However, it does not perform the endmember extraction by itself.

2.3.3.6 *Unmixing using Endmember Bundles*

Somers et al. [23] describes an unmixing approach to extract multiple endmembers from hyperspectral imagery using per-pixel techniques. This approach runs some spectral endmember extraction algorithms in randomly selected subsets of the image. The idea is to build a spectral library with the endmembers extracted from each subset. Once the spectral library is built, *k-means* with Euclidean distance are used to separate the endmembers into bundles (i.e. sets of endmembers that represent each ground component). The spectral library is the input for the MESMA algorithm [20] that performs the abundance estimation. Results of this methodology depend on the endmember extraction algorithm selected as well as the size and number of subsets.

2.4 ABUNDANCE ESTIMATION ALGORITHMS

Once the endmember signatures are known, the next step is abundance estimation [3]. Abundance estimation is usually performed with constrained least square methods. However, methods using sparse regression have been proposed recently. Techniques based in sparse signal representation theory are used to find the more appropriated endmembers to model each pixel when multiple spectral signatures per endmember are used. This section reviews both approaches.

2.4.1 *Least Square Methods*

Given a spectral vector \mathbf{y} and the endmember matrix \mathbf{S} , the abundance vector can be estimated by solving the least square problem:

$$\hat{\mathbf{a}} = \arg \min \|\mathbf{y} - \mathbf{S}\mathbf{a}\|_2^2 \quad (2.15)$$

The abundance represents the percentage area covered by a given endmember \mathbf{S}_i in a pixel. Therefore, abundances are subject to non-negativity and full additive constraints:

$$a_i \geq 0 \quad (2.16)$$

$$\sum a_i = 1 \quad (2.17)$$

The second constrain can be relaxed to sum less than or equal to one to take into account shadow endmembers or effects of topography [56, 37]:

$$\sum a_i \leq 1 \quad (2.18)$$

Iterative algorithms can be found in [56] and [37] to solve the constrained least square problem. For example, NNSLO solves the problem in Equation (2.15) constraining the sum of abundances to less than or equal to one (2.18). Instead, NNSTO uses the sum to one constraint (2.16) [37].

2.4.2 Sparse Regression

Recently, sparse representations have attracted the attention of the remote sensing community. Several applications of sparse representation for hyperspectral imagery can be found in the literature (e.g. [57], [58], [59], [60], [61]).

Iordache et al. [60] present a study of sparse unmixing using a spectral library and endmember extracted from the hyperspectral image with VCA and N-FINDR. When pixels in a hyperspectral image are expressed as a linear combination of a subset of endmembers from a very large spectral library \mathbf{S} , the unmixing problem can be reformulated as the problem of seeking the optimal subset of spectral signatures that

best model each mixed pixel. Under this assumption, the abundance vector becomes a sparse vector. The sparse unmixing problem can be expressed as:

$$\min_{\mathbf{a}} \|\mathbf{a}\|_0 \quad \text{subject to} \quad \|\mathbf{y} - \mathbf{S}\mathbf{a}\|_2 \leq \delta, \quad a_i \geq 0, \quad \sum a_i \leq 1 \quad (2.19)$$

where $\|\cdot\|_0$ is the zero-norm and denotes the number of nonzero elements, and δ is a fitting error threshold.

Iordache et al. [60] explore the use of several algorithms to solve the problem in Equation (2.19), such as orthogonal matching pursuit and basis pursuit. Among the advantages of sparse unmixing are that the abundance estimation neither depends on the availability of pure pixels in the image, nor in the capacity of an endmember extraction algorithm. However, most of the time the spectral libraries are not acquired under the same conditions as the spectral image and a correct sparse solution depends on the degree of coherence of the library and the sparseness of the fractional abundances.

Castrodad et al. [57] present a supervised unmixing algorithm based on dictionary learning. Unlike Iordache et al [60], they do not use spectral libraries. Given a set of training samples per class \mathbf{Y}_i , the algorithm seeks a dictionary \mathbf{D} that is used as the endmember matrix to solve the unmixing problem. The dictionaries \mathbf{D}_i for each training sample set \mathbf{Y}_i are learned solving the problem:

$$\min_{\mathbf{X}_i, \mathbf{D}_i} \|\mathbf{X}_i\|_1 \quad \text{subject to} \quad \|\mathbf{D}_i \mathbf{X}_i - \mathbf{Y}_i\|_2 < \varepsilon \quad (2.20)$$

where \mathbf{X}_i is the sparse representation, $\|\cdot\|_1$ and $\|\cdot\|_2$ are the norm ℓ_1 and ℓ_2 respectively, and ε is a error threshold. The mixing problem is solved for each pixel using the dictionary $\mathbf{D} = [\mathbf{D}_1, \mathbf{D}_2, \dots, \mathbf{D}_c]$ as the endmember matrix.

There are several algorithms to solve the sparse regression problem. For instance, SUnSAL (spectral unmixing by splitting and augmented Lagrangian) and C-SUnSAL

(constrained SUnSAL) are based on the alternating direction method of multipliers [62]. SUnSAL solves the problem:

$$\hat{\mathbf{a}} = \arg \min \frac{1}{2} \|\mathbf{S}\mathbf{a} - \mathbf{y}\|_2^2 + \lambda \|\mathbf{a}\|_1 \quad \text{subject to } \mathbf{1}^T \mathbf{a} = 1 \quad \text{and } \mathbf{a} \geq 0 \quad (2.21)$$

where $\lambda \geq 0$ is a control parameter. C-SUnSAL algorithm solves the objective function given by:

$$\hat{\mathbf{a}} = \arg \min \|\mathbf{a}\|_1 \quad \text{subject to } \|\mathbf{S}\mathbf{a} - \mathbf{y}\|_2 \leq \delta, \quad \mathbf{1}^T \mathbf{a} = 1 \quad \text{and } \mathbf{a} \geq 0 \quad (2.22)$$

2.5 ESTIMATION OF THE NUMBER OF ENDMEMBERS

Most unmixing algorithms reviewed in last sections do not estimate the number of endmembers. Several attempts to estimate the number of endmembers are described in the literature.

Estimators based on the signal subspace rank assume that the number of endmembers is equal to the rank of the covariance matrix. The sensed data \mathbf{y} is the result of the sum of the original signal \mathbf{x} and noise \mathbf{w} . Then, the covariance matrix of the sensed data \mathbf{K}_y is equal to the sum of the covariance matrix of the signal \mathbf{K}_x and the covariance of the noise \mathbf{K}_w . An estimator based on the signal subspace rank seeks to estimate the rank of the covariance matrix \mathbf{K}_x . Most estimators that use this approach assume that the noise is an independent and identically distributed random vector with $\mathbf{w} = \sigma \mathbf{I}$. Note that covariance matrix of the sensed signal has full rank. Rank estimators based on information criteria such as minimum descriptor length (MDL) or Akaike information theoretic criteria (AIC) are part of this category. These approaches have been used for the estimation of the number of endmembers [63], [53]. AIC and MDL were developed in [64] and [65] respectively, and extended for signals embedded in white noise by Wax and Kailath [66]. The main assumptions

of these model selection methods are that the observations \mathbf{y}_i and the noise \mathbf{w} are identical and statistically independent with Gaussian distributions and zero mean. Wu et al. [67] show that both AIC and MDL do not estimate correctly the number of endmembers since the noise of hyperspectral images is not statistically independent.

Other approaches assumes that the number of endmembers is equal to the rank of the image matrix \mathbf{Y} that can be estimated using the correlation matrix given by [68]:

$$\mathbf{R}_Y = \frac{1}{m} \mathbf{Y}^T \mathbf{Y} \quad (2.23)$$

where m is the number of pixels in the image. Note that $\text{rank}(\mathbf{Y}) = \text{rank}(\mathbf{R}_Y)$

A widely used procedure to compute the number of endmembers is the virtual dimensionality (VD) proposed by Chang and Du [63]. VD compares the eigenvalues from the covariance matrix and correlation matrix to estimate the number of endmembers. However, Bajorski [69] shows that VD is based on incorrect assumptions and therefore VD is not considered in this work.

The positive rank of the image matrix \mathbf{Y} can be also used in the estimator for the number of endmembers [50]. The positive rank is defined as the least integer p for which a positive matrix factorization exists [70], i.e.:

$$\mathbf{Y} = \mathbf{S} \mathbf{A} \quad (2.24)$$

where $\mathbf{S} \in \mathbb{R}_+^{n \times p}$ and $\mathbf{A} \in \mathbb{R}_+^{p \times m}$.

Bioucas-Dias and Nascimento propose in [55] the hyperspectral signal identification by minimum error (HySIME) algorithm for the estimation of the dimensionality of a hyperspectral image. First, HySIME estimates the signal and the noise correlation matrices using multiple regression theory. The signal subspace is determined by selecting a subset of eigenvector of the signal correlation matrix. This subset is determined by minimizing the mean square error between image and a noise projection.

Despite the efforts made to address the problem of determining the number of endmembers from hyperspectral imagery, new techniques that take full advantage of spatial and spectral information are necessary. Here we present a technique for the estimation of the number of endmembers using both spatial and spectral information. Full automated unmixing algorithms such as AMEE addresses the problem of the number of endmembers jointly with the spectral signatures (see Section 2.3.3). However, AMEE performance depends of spatial kernel size and the threshold given for the MEI image. As far as we know, only the AMEE method use the spatial information in the estimation of the number of endmembers.

2.6 SCALE SPACES AND MULTISCALE REPRESENTATIONS

Computer vision and image processing aim to extract meaningful information from an image. The objects of interest is determined by the specific task where the computer vision system is employed and it exists on limited range of scales [24]. For instance, see the images in the Figure 2.5 which was generated by sub-sampling the image several times. The image with the finest scale allows to see most details in the texture of the trunk and the leaves. However, these details are lost in the coarsest scale image where only the largest objects can be noted such as the path and the trees. Figure 2.5 illustrates how, as the scale changes, different objects can be observed.

A methodology for dealing with the notion of scale is the generation of multiscale representations. Multiscale representations build a family of images where fine details are systematically removed using smoothing operations and where the objects can be analyzed at different scales [24].



Figure 2.5: Scale concept. Figure from [24].

A multiscale representation for a image $\mathbf{Y}(i, j)$ can be obtained by applying several Gaussian filters $G_{0,\sigma}$ with different variances σ^2 [25]:

$$\mathbf{Y}(i, j, \sigma) = \mathbf{Y}(i, j) * G_{0,\sigma} \quad (2.25)$$

The variances allow to generate different levels of smoothing that defines a *scale space* for a image. An example of scale space using Gaussian filters is presented in Figure 2.6.

The scale spaces should satisfy architectural axioms, morphological requirements, and stability [71]. Architectural axioms group the causality, recursivity, regularity, and locality properties. Let a family of transforms T_t which generates a sequence of images $u(t, \mathbf{x})$ when the transformations are applied to the original image \mathbf{x} . The recursivity property establishes that smoothed image in any scale can be obtained from the previous one:

$$\begin{aligned} T_0 u &= u \\ T_t u &= T_l(T_m u) \quad t = l + m \end{aligned} \quad (2.26)$$

where T_0 is the identity. The causality property ensures that a scale is the result of transformation of previous scales and not of images on higher scales. The regularity axiom establishes the continuity of the transformation. Let $t = nh$, then, $T_t = T_{nh}$ can be built from the n -th iteration of T_h . The regularity property says that the multiscale representation is independent of the selection of h . Finally, the locality axiom establishes that $T_t u$ is determined by a small neighborhood around u .

Morphological requirements establish that the multiscale representation should be invariant to changes of illumination and position:

$$\begin{aligned} \text{Grey - Level - Shift Invariance} \quad & T_t(0) = 0 \\ & T_t(f + C) = T_t(f) + C \\ \text{Grey - scale Invariance} \quad & T_t(h(f)) = h(T_t(f)) \\ \text{Translation Invariance} \quad & T_t(\tau.f) = \tau.T_t(f) \end{aligned}$$

Finally, the stability condition establishes that new structures should not appear in the coarsest scale. Coarser structures should be simplification of corresponding structures at finer scales [71, 24].

Alvarez et al. [71] show that a necessary condition for a scale-space is that it should satisfy the partial differential diffusion equation given by:

$$\frac{\partial \mathbf{Y}(i, j, \sigma)}{\partial t} = \frac{\partial^2 \mathbf{Y}(i, j, \sigma)}{\partial t^2} + \frac{\partial^2 \mathbf{Y}(i, j, \sigma)}{\partial j^2} = \nabla \mathbf{Y}(i, j, \sigma) \quad (2.27)$$

Equation (2.27) is called *isotropic* diffusion. Isotropic diffusion diffuses the information equally in all directions allowing the reduction of noise, but eliminating edges. This effect is noted in Figure 2.6 where a gray-scale image was smoothed for different values of σ .

Perona and Malik [72] propose to use either *nonlinear* or *anisotropic* diffusion to smooth an image while keeping the boundaries between regions or edges. Non-

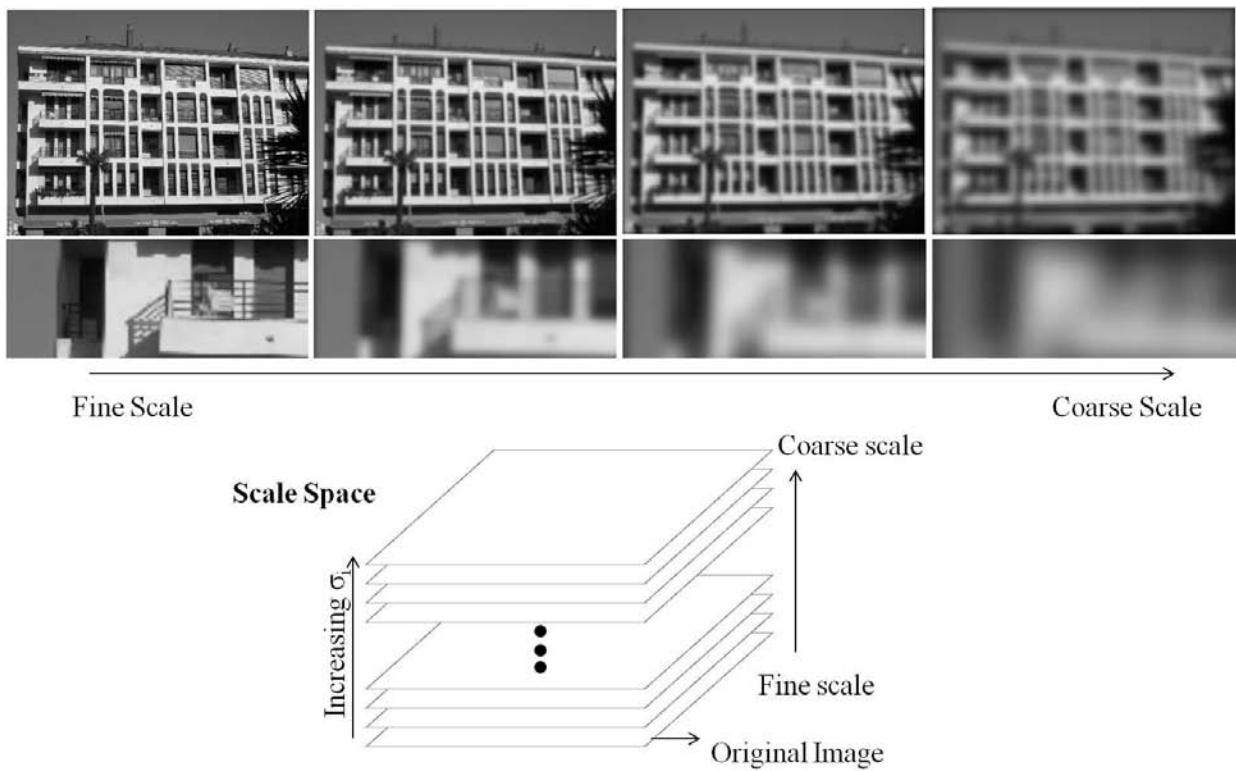


Figure 2.6: Isotropic diffusion and scale space. Figure from [24].

linear diffusion of hyperspectral imagery is used in this research. An algorithm proposed by Duarte et al. [26] that employs multigrid methods is used for the multiscale representation and the endmember extraction. The next chapter presents details about Duarte’s algorithm and how the endmembers are extracted using the multiscale representation.

2.7 SUMMARY

The state of the art in unmixing analysis evidences the need for most robust algorithms that use the spatial and spectral information contained in a hyperspectral image. Most of the spatial-spectral algorithms found in the literature use spatial kernels or windows into their procedures. Therefore, the obtained unmixing results depend on the size of these kernels. On the other hand, the RBSPP [17] algorithm employs

unsupervised clustering techniques to determine spectrally uniform regions where endmember are extracted avoiding to use spatial kernels. However, similar to most of existing spatial-spectral methods, RBSPP [17] does not use the spatial information for the estimation of the number of endmembers. In addition, RBSPP does not perform the endmember extraction. This is a pre-processing step that determines a set of spectra that are passed to a spectral-only technique for endmember extraction. As far as we know, only AMEE [9] uses the spatial information to estimate the number of endmembers, but as mentioned before its results depend on the size of the spatial kernels. Therefore, the development of new algorithms that use the spatial and spectral information of hyperspectral imagery for the joint estimation of the number of endmembers and their spectral signatures that do not use kernels is crucial.

SPECTRAL ENDMEMBER EXTRACTION BASED ON MULTISCALE REPRESENTATION

A spectral endmember extraction approach is presented in this chapter which is built upon the multiscale representation of hyperspectral imagery using multigrid methods proposed by Duarte et al. [26]. The developed endmember extraction method takes advantage of the sampling operation used to build the coarse grids in the multigrid method. To introduce this approach, a review of Duarte's method is presented where a detailed description of the procedure for building the multigrid is included. The proposed methodology requires the selection of an image from the multiscale representation. A study about how to determine a scale in the multiscale representation is performed. Several methods have been proposed for scale selection. Usually, these methods are used to determine when nonlinear filters remove the noise in an image, or when the solution of the nonlinear PDE achieves a stable state. In this research, these methods are used to determine a scale for endmember extraction. Experiments comparing different scale selection approaches are performed. Examples of scale effects and scale selection are presented using different hyperspectral images.

3.1 MULTISCALE REPRESENTATION OF HYPERSPECTRAL IMAGERY

Nonlinear diffusion for spectral image $\mathbf{Y} = [\mathbf{y}_1, \dots, \mathbf{y}_m]^T$ of n bands and m pixels is given by the nonlinear PDE [26]:

$$\frac{\partial \mathbf{y}_i}{\partial t} = \nabla [g(\theta(\nabla \mathbf{y}_{\sigma_g})) \nabla \mathbf{y}_i] \quad i = 1, \dots, m \quad (3.1)$$

where \mathbf{y}_{σ_g} is a smoothed version of \mathbf{y} with a Gaussian filter of zero mean and standard deviation σ_g , $\theta(\nabla \mathbf{y}_{\sigma_g})$ is a measure of the edge strength given by:

$$\theta(\nabla \mathbf{y}_{\sigma_g}) = \sqrt{\frac{1}{n} \sum_{j=1}^n |\nabla \mathbf{y}_{\sigma_g j}|^2} \quad (3.2)$$

and g is the diffusion coefficient. Duarte et al. [26] used the diffusion coefficient proposed by Weickert et al. [73]:

$$g(\theta) = \begin{cases} 1 & \theta = 0 \\ 1 - e^{-\frac{3.31488}{(\theta/\alpha)^8}} & \theta > 0 \end{cases} \quad (3.3)$$

where α is a threshold parameter to control the diffusion. In addition, Duarte et al. used a distance (e.g. Euclidian, spectral angle distance) as θ instead of Equation (3.2).

Examples of nonlinear diffusion applied to hyperspectral images are presented in Figure 3.1. Figure 3.1 shows RGB compositions for two images and their corresponding smoothed images. The first is an AVIRIS image from A.P. Hill and the second is the False Leaf image collected with the SOC 700. RGB compositions were built using bands 30 (654 nm), 20 (557 nm) and 9 (451 nm) for A.P. Hill and bands 57 (639 nm), 35 (548 nm) and 13 (460 nm) for False Leaf. The spatial effects of nonlinear smoothing in the leaves are presented in Figures 3.1(e) and 3.1(f). The smoothed

images in Figure 3.1 were obtained using Duarte's algorithm that is reviewed in the next section.

The semi-implicit discretization of the nonlinear diffusion PDE is expressed in matrix form as:

$$(\mathbf{I} - \mu \mathbf{G}_t) \mathbf{Y}_{t+1} = \mathbf{Y}_t \quad (3.4)$$

where μ is the scale step (i.e. $\mu \equiv \Delta t$), \mathbf{Y}_t is the hyperspectral image and $\mathbf{G} = [g_{ij}]$ is the diffusion coefficients matrix. Duarte et al. [74] showed that semi-implicit schemes can solve the nonlinear diffusion of hyperspectral images faster than using explicit discretization. An algorithm to solve the nonlinear PDE using semi-implicit methods for hyperspectral imagery using multigrid methods is presented in [26].

Multigrid methods are numerical techniques to solve linear systems of equations. Multigrid methods aim to build a hierarchical representation of the problem from a fine grid to a coarse grid, such that the linear system can be solved exactly in the coarsest grid. Then, the solution is propagated to the fine grid to solve the original linear system [27]. Algebraic multigrid methods have two main operations: sampling and interpolation. Sampling builds the multigrid structure and interpolation propagates the solution from the coarse to the fine grid. To build a multiscale representation, Equation (3.4) is solved several times using as initial condition the original image. A multigrid structure is built each time that the PDE is solved. An extended description of multigrid methods can be found in [27].

The developed endmember extraction method exploits the multigrid structure at the selected scale to determine the spectral endmembers. A review of the needed details about the multigrid structure is done below based on [26] and [75]. See [26] for more details about the solver and the interpolation operation.

The multigrid structure can be visualized as an inverted pyramid (see Figure 1.3) where each level, $s \in 0 \dots S$, is represented by a graph (V^s, E^s) in which V^s is the set

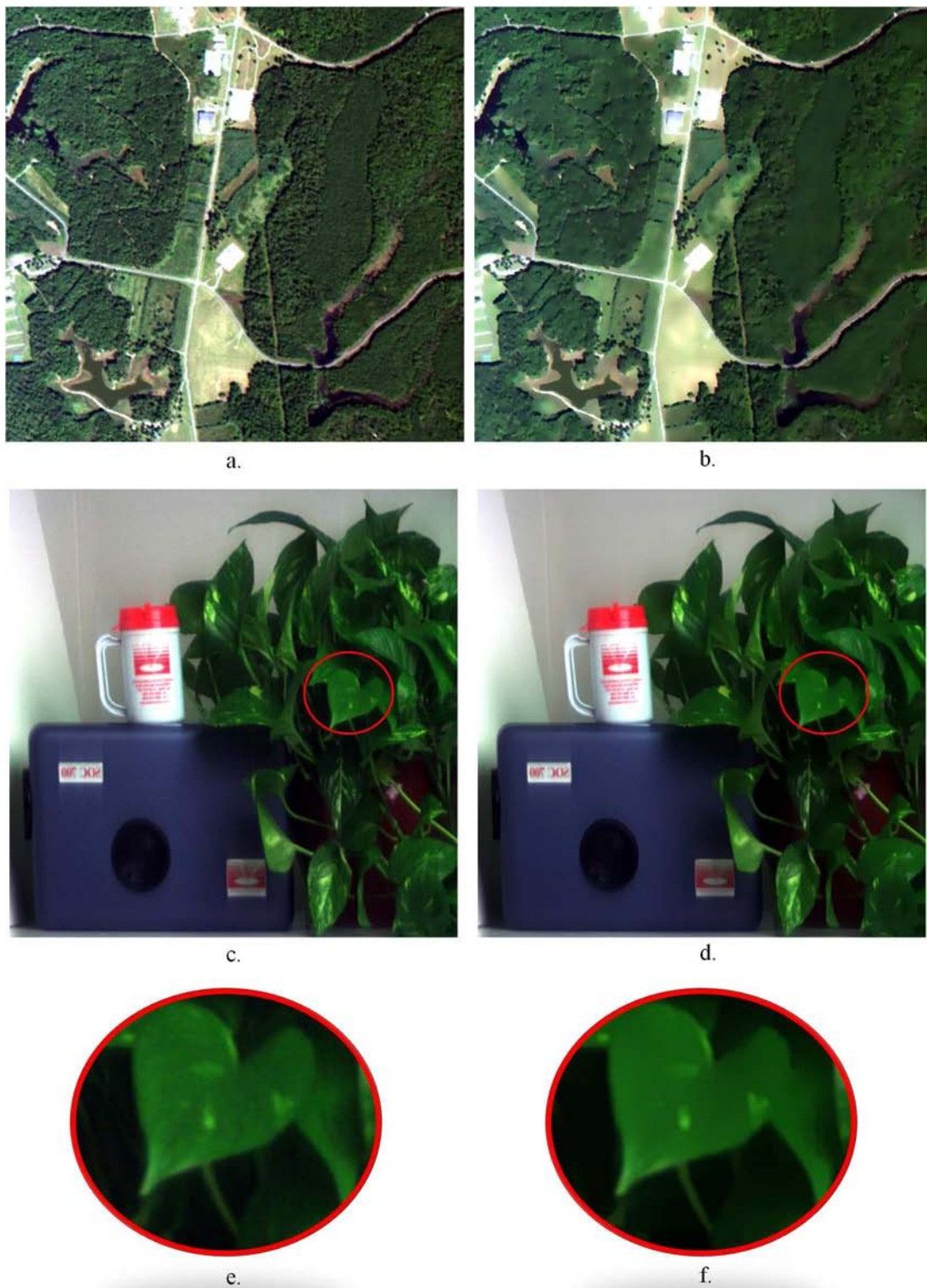


Figure 3.1: Example of nonlinear diffusion. A.P. Hill image: (a) Original. (b) Smoothed. RGB composition using bands 30 (650 nm), 20 (557 nm) and 9 (451 nm). False Leaf image: (c) Original. (d) Smoothed. (f) - (e) Smoothing effects in a leaf. RGB composition using bands 57 (639 nm), 35 (548 nm), 13 (460 nm).

of vertices in level s and E^s is the set of edges. Each edge (i, j) in E^s has a weight that represents the similarity between the vertices in \mathbf{u}_i^s and \mathbf{u}_j^s . The graph in level 0 is built by setting the pixels in the initial hyperspectral image as the vertices V^0 , i.e. $\mathbf{u}_i^0 = \mathbf{y}_i$, and the set of edges E^0 are formed by connecting each pixel with its four closest neighbors with weights g_{ij}^s given by Equation (3.3). To solve Equation (3.4), the initial hyperspectral image is a smoothed version of the original image \mathbf{y}_{σ_g} . The construction of the multigrid structure is achieved by consecutive sampling operations which consist of two main steps: the selection of next set of vertices (V^{s+1}) and the determination of the edges for the new set of nodes (E^{s+1}).

Let the mass of a vertex m_i^s be a measure of how many pixels in the finest grid can be assigned to the vertex in the coarse grid. The first vertex of V^{s+1} is selected as the vertex in V^s with the biggest mass. Remaining vertices in V^s are sorted in decreasing order of mass. Then, iterating on the vertices of V^s , a vertex is selected for the new grid if this satisfies the condition given by:

$$\frac{\sum_{j \in V^{s+1}} g_{ij}^s}{\sum_{(i,k) \in E^s} g_{ik}^s} \leq \tau \quad (3.5)$$

where i is a vertex in V^s and τ is a threshold parameter that controls the similarity of vertices in the new grid.

Once the vertices for the new grid are selected, it is necessary to compute the weights (w_{ij} in the Figure 1.3) between the vertices in V^{s+1} and the vertices in V^s not selected as representatives. These weights indicate the dependence between vertices of the current and the new grid, and are given by:

$$w_{ij}^s = \frac{g_{ij}^s}{\sum_{k \in V^{s+1}} g_{ik}^s} \quad (3.6)$$

where i is a vertex in V^s not selected as representative (i.e. $i \in V^s \setminus V^{s+1}$) and j is in V^{s+1} . The mass of new vertices is determined by:

$$m_j^{s+1} = m_j^s + \sum_{k \in V^s \setminus V^{s+1}} m_k^s w_{kj}^s \quad (3.7)$$

For $s = 0$, the masses are set equal to 1. Thus, the masses at any level $s + 1$ are obtained recursively from the masses at level s .

At each level, the vertices hold the mean of spectral signatures computed by the expression:

$$\mathbf{u}_j^{s+1} = \frac{\mathbf{u}_j^s + \sum_{k \in V^s \setminus V^{s+1}} w_{kj}^s \mathbf{u}_k^s}{1 + \sum_{k \in V^s \setminus V^{s+1}} w_{kj}^s} \quad (3.8)$$

Finally, the g_{ij}^{s+1} are computed to connect the vertices in the new grid. For that, Duarte et al. [26] derived the following expression:

$$g_{ij}^{s+1} = \begin{cases} g_{ij}^s & \text{if } (i, j) \in E^s \\ \frac{(w_{ki}^s g_{kj}^s + w_{kj}^s g_{ik}^s)}{1 + \sum_{k \in V^s \setminus V^{s+1}} w_{ki}^s} \exp(-\theta(\mathbf{u}_i^{s+1}, \mathbf{u}_j^{s+1})/\alpha) & \text{if } (i, k) \text{ and} \\ & (k, j) \in E^s \\ \frac{\left(\sum_{p, q \in V^s} w_{pi}^s g_{pq}^s w_{qj}^s \right)}{1 + \sum_{k \in V^s \setminus V^{s+1}} w_{ki}^s} \exp(-\theta(\mathbf{u}_i^{s+1}, \mathbf{u}_j^{s+1})/\alpha) & \text{if } (i, p), (p, q) \\ & \text{and } (q, j) \in E^s \end{cases} \quad (3.9)$$

The grid is coarsened until the dependence of a representative on its neighbors is small. This dependence is calculated by:

$$\Gamma_i = \frac{\sum_{j \in V_s} g_{ij}^s}{m_i^s} \leq \varepsilon \quad (3.10)$$

3.1.1 Input Parameters

The construction of the multigrid structure requires two threshold parameters τ (Equation 3.5) and ε (Equation 3.10). Parameter τ controls the similarity of vertices in the new grid and ε determines the similarity of the vertices in the coarse grid. Parameter α , in Equation (3.9), controls the amount the diffusion. Duarte et al. [26] suggests to set $\tau = 0.2$, $\varepsilon = 1e - 5$ and $0.005 \leq \alpha \leq 0.015$. In addition, the variance for the Gaussian filter used to generate \mathbf{y}_{σ_g} is required.

To find the multiscale representation, additional parameters μ , which corresponds with the scale step, and final scale T are needed. Duarte et al. [26] suggest $\mu \leq 5$ and two steps of nonlinear diffusion ($T = 2$).

In this work, the parameters determined by Duarte et al. are used for all images. Only the final scale, T , and the diffusion parameter, α , are varied. The diffusion parameter is set as the smallest value in $0.005 \leq \alpha \leq 0.015$ where the Duarte's algorithm find a solution for the PDE.

3.2 SPECTRAL ENDMEMBER EXTRACTION

Taking advantage of the multigrid structure, the proposed algorithm uses the vertices in the coarsest grid as the representative spectra in the hyperspectral image. The construction of the multigrid can be related to the problem of determining the distinct spectral signatures in the image. To see this relation, it is necessary to understand the selection of a new vertex as expressed in the Equation (3.5). Note that building a new grid begins with selecting the vertex with the largest mass, and then the most distinct vertices are added successively to the new grid using condition in Equation (3.5). Ordering the vertices base on their masses gives priority to those vertices that represent a large number of points in the previous grid. Rare pixels (i.e. spectra that

occupy small regions in the image) also are selected because their similarity with already selected vertices will tend to be small (see Equation (3.5)).

A modification in the mass initialization is done here for endmember extraction to give priority to pixels that are not in the edges (mixed pixels). Instead of initializing the masses to 1, the masses are initialized equal to the diffusion coefficients g_{ij} . Note that $g_{ij} = 1$ when the spectrum of a pixel (i, j) is equal to their neighbors (i.e. the pixel is inside of a very homogeneous region), and g_{ij} is close to zero when the pixel g_{ij} is near the edges. Thus, when the masses are sorted in descending order, then the first pixels will correspond with those inside spectrally uniform regions.

Vertices in the coarse grid have associated a value for \mathbf{u}_j^S , the spectral signature, and its position in the fine grid. The spectral endmembers correspond with the signatures of the pixels in the smoothed image \mathbf{Y}_t determined by the position of the vertices in the coarse grid. Note that the spectra from the smoothed image \mathbf{Y}_t are used as the spectral endmembers instead of the spectra in the original image \mathbf{Y} . The smoothed spectra can be seen as the average of spectrally similar and spatially close pixels which help to reduce the effect of noise and improve the representation of the different components in the image. Figure 3.2 shows a subset of the spectral endmembers extracted from the False Leaf image. Figure 3.2(a) shows the corresponding spectral signatures from the original image. Figure 3.2(b) shows the signatures from the smoothed image. It is clear how the smoothing helps to reduce the noise and preserve the signature shape. Figure 3.3 shows the methodology used for the spectral endmember extraction.

The abundance for the spectral endmembers can be computed using one of the methods reviewed in Section 2.4 depending of the number of spectral endmembers. If there are more spectral endmembers than bands, then, the inversion problem becomes an underconstrained system of equations and sparse regression algorithms should be used. On the other hand, if the number of spectral endmembers is less than or equal to the number of bands, then abundance can be obtained using con-

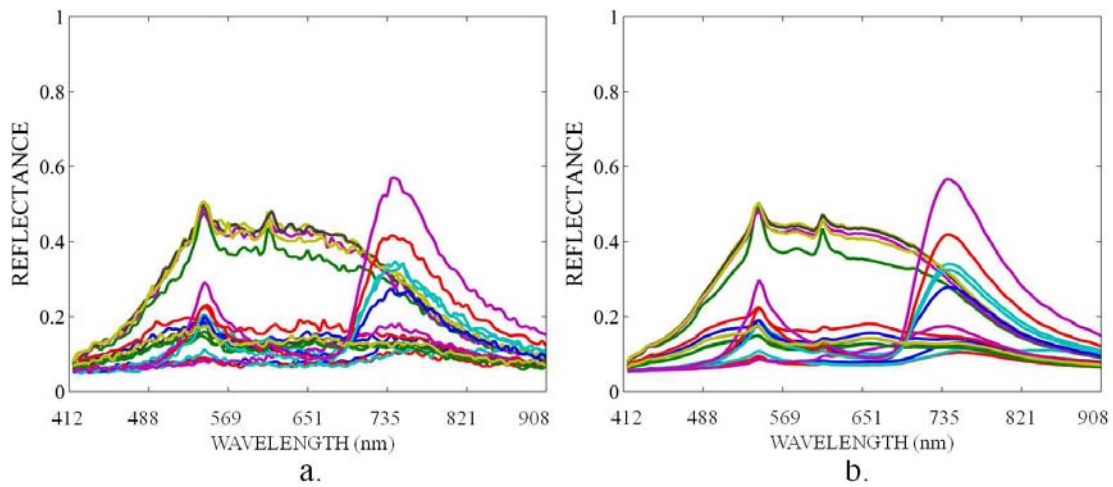


Figure 3.2: Example of representative spectra for False Leaf image. Spectra from (a) original and (b) smoothed image.

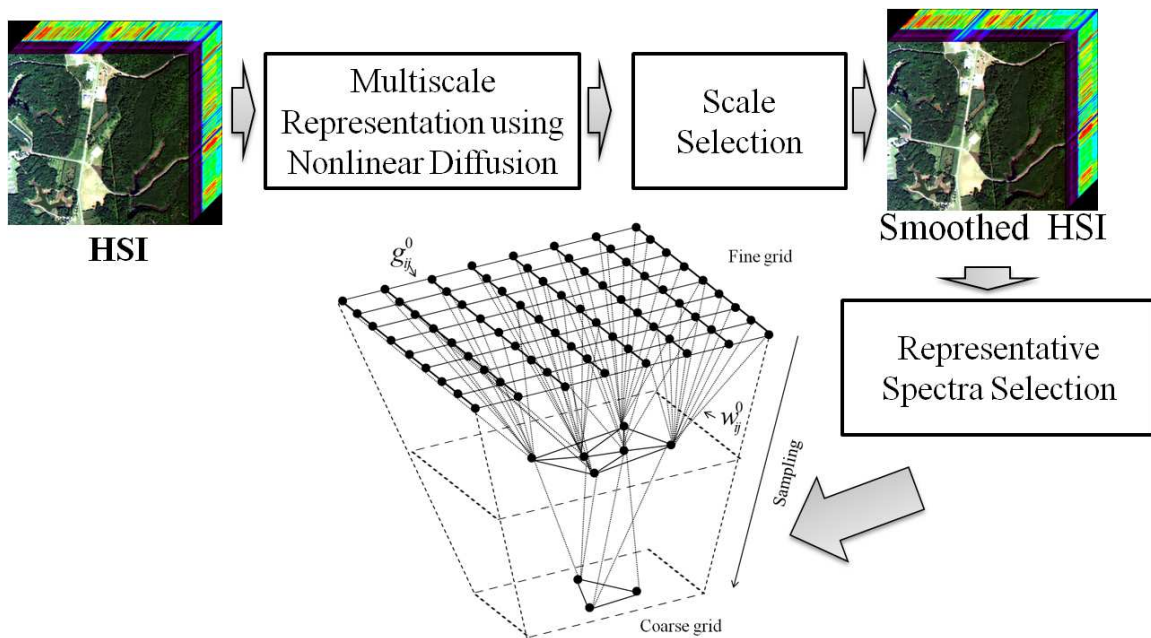


Figure 3.3: Spectral endmember extraction methodology.

strained least square methods. In particular, this work uses the NNSLO algorithm described by [37] for the least square case, and the SunSAL algorithm from [62] for the sparse regression.

Most of the existing spatial-spectral endmember extraction techniques require to define a spatial window. In contrast, the proposed approach takes advantage of the properties of PDE's and multigrid methods to select the spectral endmember without the need to define neighborhoods similar to RBSPP algorithm. However, the proposed approach performs the endmember extraction by itself instead of using spectral techniques as required by RBSPP.

The proposed method only uses one of the smoothed images from the multiscale representation for spectral endmember extraction. The next section presents different methods for scale selection. A comparison of the different methods is performed by evaluating the effects in the determination of spectral endmembers.

3.2.1 *Scale Selection*

The multiscale representation obtains a family of smoothed hyperspectral images $\{\mathbf{Y}_1, \dots, \mathbf{Y}_t, \dots, \mathbf{Y}_T\}$ making it necessary to select one the smoothed images for spectral endmember extraction. Several methods have been proposed to select the optimal scale T for nonlinear diffusion (see [76, 77, 78, 79, 80]). Most of these methods are used in filtering applications, and few others have been proposed for image reconstruction. This section presents a review of these methods and a comparative study is performed to determine their performance for endmember extraction. As presented below, most of the scale selection approaches seek the minimum or maximum of some criterion. However, most of the time, a unique solution is hardly found because the criterions do not achieve the global minimum or maximum or they do not provide discriminating information among scales. Most of the criterions form

a curve with a break point when plotted against scale. The end of the break point is selected as the optimal stopping scale \hat{T} . This methodology is adopted if a minimum or maximum cannot be determined. Additionally, a new stopping criterion is proposed using the entropy of the difference between the original image and the smoothed image at step t . This new criterion is compared with the existing methods described in Section 3.3. For notation, t represents the number of iterations which are required to solve the PDE in Equation (3.4).

3.2.1.1 SNR Criterion

The stopping time T should be selected before the diffusion process removes significant image details such as the edges [76]. Weickert [76] proposed to use the relative variance between the smoothed image \mathbf{Y}_t and the desired image \mathbf{X} (e.g. free-noise image) to determine the optimal final scale. Obviously, the desired image \mathbf{X} is unknown. However, Weickert [76] assumed that the signal-to-noise ratio (SNR) is known and then the relative variance can be compute by:

$$\frac{\sigma_{\mathbf{Y}_t}^2}{\sigma_{\mathbf{X}}^2} = \frac{1}{1 + \frac{1}{\text{SNR}}} \quad (3.11)$$

where $\sigma_{\mathbf{Y}_t}^2$ and $\sigma_{\mathbf{X}}^2$ are the variances of the smoothed and desired image respectively. Thus, the optimal time \hat{T} can be determined as the time where the condition:

$$\frac{\sigma_{\mathbf{Y}_t}^2}{\sigma_{\mathbf{Y}_0}^2} = \frac{1}{1 + \frac{1}{\text{SNR}}} \quad (3.12)$$

is met. Here $\sigma_{\mathbf{Y}_0}^2$ is the variance of the original image. Usually, this method requires the estimation of the SNR, therefore it is not used here.

3.2.1.2 Minimal Entropy Change

Sporring and Weickert [78] suggested to use the time where the minimal entropy change is achieved as the optimal stopping time because the minimal entropy change is an indicator of stable scales. The entropy for a gray-scale image is given by:

$$S = - \sum_{i=1}^K p_i \log p_i \quad (3.13)$$

where p_i is the histogram count for the intensities values from 1 to K. The optimal time \hat{T}_{MEC} is found by minimizing the entropy change ΔS :

$$\hat{T}_{MEC} = \arg \min_{t>0} \Delta S \quad (3.14)$$

To apply this criterion to vector-valued image, the average entropy across bands is used as S in Equation (3.14).

3.2.1.3 Decorrelation Criterion

Mrazek and Navarra [77] described a decorrelation method for the estimation of \hat{T} that consists in minimizing the correlation between the smoothed image in the time t and the image $\mathbf{Y}_t - \mathbf{Y}_0$:

$$\hat{T}_{corr} = \arg \min_{t>0} \rho(\mathbf{Y}_t - \mathbf{Y}_0, \mathbf{Y}_t) \quad (3.15)$$

where ρ is the coefficient of correlation:

$$\rho(\mathbf{Y}_t - \mathbf{Y}_0, \mathbf{Y}_t) = \frac{\text{cov}(\mathbf{Y}_t - \mathbf{Y}_0, \mathbf{Y}_t)}{\sqrt{\text{var}(\mathbf{Y}_t - \mathbf{Y}_0) \text{var}(\mathbf{Y}_t)}} \quad (3.16)$$

It is expected that the correlation between the smoothed image and $\mathbf{Y}_t - \mathbf{Y}_0$ after some time t decreases as more iterations are performed. If the smoothing operations

begin to remove significant details from the image, then the correlation begins to increase. Selecting the time where the correlation is minimum seeks to guarantee that important details of the image are not removed. In the original formulation of the decorrelation method [77], \mathbf{Y}_o is a gray-scale image. A generalization of this method for vector-value images is found in [79] where the correlation is computed for each band, and then these are averaged by a weighted sum:

$$\rho(\mathbf{Y}_t - \mathbf{Y}_o, \mathbf{Y}_t) = \sum_{i=1}^n w_i \rho(\mathbf{Y}_t(i) - \mathbf{Y}_o(i), \mathbf{Y}_t(i)) \quad (3.17)$$

where n is the number of bands, $\mathbf{Y}_t(i)$ is band i of the difference between the smoothed and original image, and w_i are selected such that $\sum w_i = 1$.

3.2.1.4 Diffusion Balance Criterion

Jiabin and Guizhong [80] proposed to use as stopping time the time when the multi-scale representation arrives to balance. Diffusion balance is achieved when:

$$|\Delta E_{\mathbf{Y}_t}| = |\Delta E_{\mathbf{D}_t}| \quad (3.18)$$

where $E_{\mathbf{Y}_t}$ and $E_{\mathbf{D}_t}$ are the energy of the smoothed image \mathbf{Y}_t and $\mathbf{D}_t = \mathbf{Y}_t - \mathbf{Y}_o$ at time t respectively. Using the criterion proposed in [80], the optimal time given by:

$$\hat{T}_{DE} = \arg \min_{t>0} ||\Delta E_{\mathbf{Y}_t}| - |\Delta E_{\mathbf{D}_t}|| \quad (3.19)$$

The generalization of the diffusion balance to vector-value images is performed by considering the Frobenious norm of the images as a measure of energy. The Frobenious norm of a matrix is given by:

$$\|\mathbf{A}\|_F = \sqrt{\text{trace}(\mathbf{A}^T \mathbf{A})} \quad (3.20)$$

3.2.1.5 Entropy Change

The methods presented before do not provide a solution in all the cases because they do not find global minimums and some times these criteria do not offer discriminating information among the scales. Thus, other stopping criterion is proposed in this work.

It is expected that the difference between the smoothed image and the original, $\mathbf{Y}_t - \mathbf{Y}_0$, has more details as more smoothing iterations are performed. Thus, the entropy of $\mathbf{Y}_t - \mathbf{Y}_0$ increases with the diffusion time. The entropy is seen here as a measure of information. Then, as more smoothing iterations are performed, more information is removed from the image. However, the entropy change of $\mathbf{Y}_t - \mathbf{Y}_0$ is significant in the first iterations. Experimentally, we found that the entropy change forms a smooth curve with a break point. The proposed approach selects the stopping time \hat{T}_{EC} as the point where the entropy changes are small, i.e. selecting the time at the end of break point. To generalize the procedure for any image, the perceptual difference between \mathbf{Y}_t and \mathbf{Y}_0 is used:

$$\mathbf{Y}_D(i, j, k) = \frac{|\mathbf{Y}_t(i, j, k) - \mathbf{Y}_0(i, j, k)|}{\mathbf{Y}_0(i, j, k)} \quad (3.21)$$

Note that \mathbf{Y}_D will have value between 0 and 1 for any image, and then a threshold can be set when the entropy change is small (e.g. 0.01).

3.3 EXPERIMENTS

Three images were used to compare the methods for scale selection described in the previous section. Figure 3.4 presents a RGB composition for each image. The first is the False Leaf image (Figure 3.4(a)) described in Section 1.4.2. The second image (Figure 3.4(b)) is a subset of 150x150 pixels of an AVIRIS image captured over Fort.

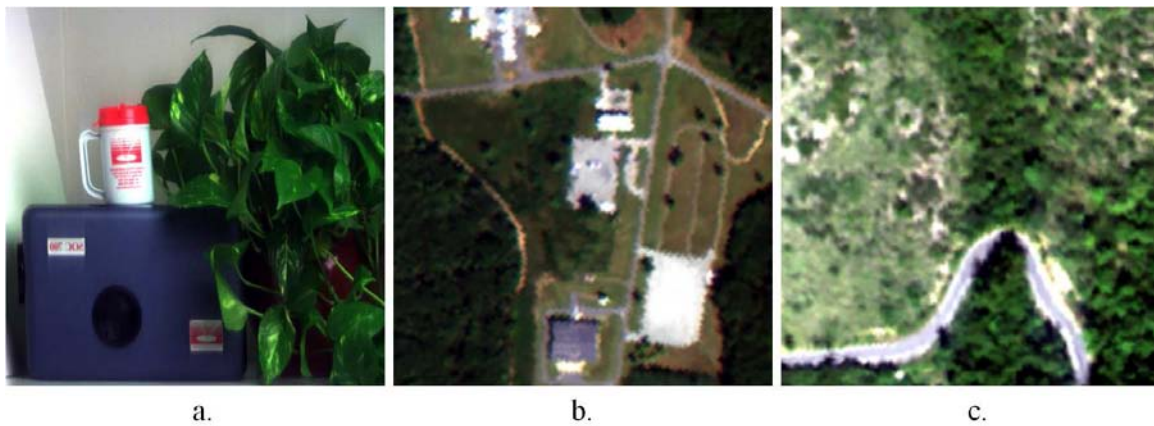


Figure 3.4: Test images for comparison of stopping criteria. RGB composition for (a) False Leaf image using bands 57 (639 nm), 35 (548 nm) and 13 (460 nm), (b) AP Hill subset using bands 30 (650 nm), 20 (557 nm) and 9 (451 nm). and (c) Guanica subset using bands 54 (639 nm), 35 (550 nm), and 15 (459 nm).

A. P. Hill, Virginia in September of 2001. The last image is a subset of 150×150 pixels from an image collected over Guanica Dry Forest in December of 2007. The Guanica image was collected using the AISA Eagle sensor at 1 meter of spatial resolution. The AVIRIS image has 224 bands from 380 nm to 2500 nm and the AISA image has 128 spectral bands from 397 nm to 995 nm. These three images represent different levels of complexity for the selection of an appropriate scale for endmember extraction. In the False Leaf image, many spectrally uniform regions can be easily identified. However, in the A.P. Hill and Guanica subsets, the identification of regions is more challenging because of the heterogeneity of the scenes and fine details.

The images were smoothed using nonlinear diffusion algorithm of Duarte et al. [26] with a scale step $\mu = 5$ in 20 smoothing iterations. Thus, 20 smoothed images were obtained for each test image. The diffusion parameter α (in Equation 3.3) was set experimentally for each image inside the range suggested by Duarte et al [26]. Diffusion parameter was fixed to 0.005, 0.011, and 0.011 for the False Leaf, A.P Hill subset, and Guanica subset images respectively. In the case of A.P Hill and Guanica subsets, Duarte et al. algorithm cannot solve the PDE when $\alpha < 0.011$. The remaining

parameters of the nonlinear diffusion algorithm were set following the approach described in Section 3.1.1.

Figure 3.5 shows the results obtained for the different methods. Figure 3.5(a-c) show the graphs for the entropy change in \mathbf{Y}_t for the three test images. The entropy changes obtained for the AP Hill subset and Guanica subset images do not provide some reasonable criterion to determine an optimal scale as can be noted in Figures 3.5(b) and 3.5(c). On the other hand, the entropy changes obtained for the False Leaf image has a minimum at iteration 13. However, there is no guarantee that this point corresponds to a global minimum. Figure 3.5(d-f) present the correlation coefficient between $\mathbf{Y}_t - \mathbf{Y}_0$ and \mathbf{Y}_t used in the decorrelation method proposed by Mrazek and Navarra [77]. Similar to the minimum entropy change criterion, the Mrazek decorrelation method does not provide discriminative information to determine the optimal scale for the AP Hill and Guanica subset images. However, the Mrazek decorrelation criterion allows to select iteration 3 as the optimal scale for the False Leaf image as presented in Figure 3.5(d). The diffusion balance allows to determine an optimal scale for the three images as seen in Figures 3.5(g-i). Figures 3.5(g-i) present the energy change $||\Delta E_{\mathbf{Y}_t}| - |\Delta E_{\mathbf{D}_t}||$ with respect to the smoothing iterations. The diffusion balance method selects the smoothed images obtained in iterations 11, 13 and 12 for the False Leaf, AP Hill subset and Guanica subset images respectively. Although there is no guarantee that these correspond to global minimum, it can be seen from Figures 3.5(g-i) as the nonlinear diffusion reaches a steady state (with respect to energy) for all three images. Finally, Figures 3.5(j-l) show the entropy change for the normalized image obtained for $\mathbf{Y}_t - \mathbf{Y}_0$ in the three images. Note that the entropy changes for $\mathbf{Y}_t - \mathbf{Y}_0$ does not present a global minimum. However, it is clear that more information is removed in the first smoothing iterations (before the break point) and then the smoothing effects significantly decrease. Although, both the minimal entropy change and the entropy change criterions use in some way the entropy to measure the smoothing effects along scale steps, only the entropy of $\mathbf{Y}_t - \mathbf{Y}_0$ allows

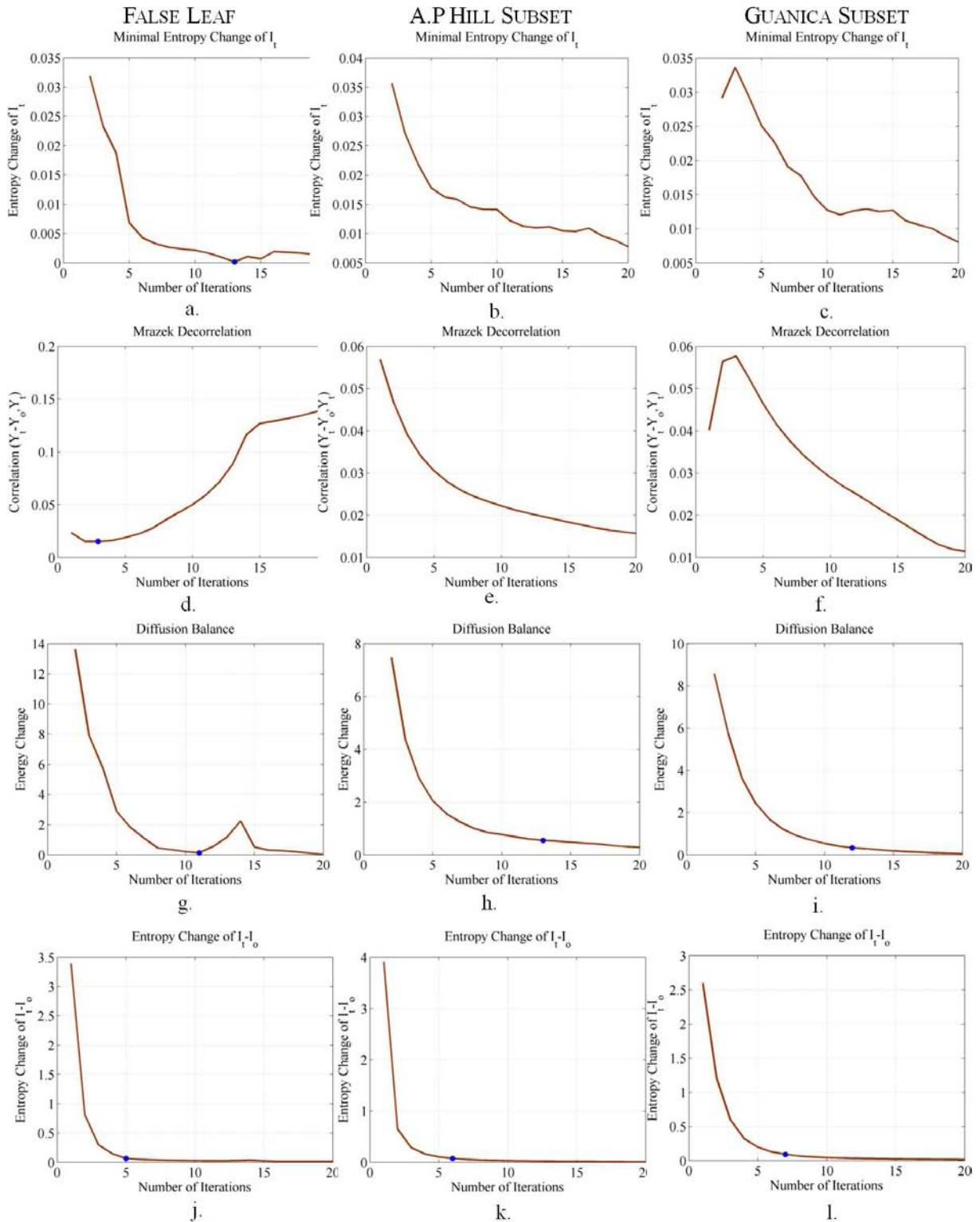


Figure 3.5: Comparison of scale selection criteria. Scale selection for False Leaf, AP Hill subset, and Guanica subset images for (a)-(c) minimal change entropy, (d)-(f) decorrelation methods, (g)-(i) diffusion balance, and (j)-(l) entropy change methods.

Table 3.1: Optimal stopping scale for False Leaf, AP Hill subset and Guanica Subset images.

	\hat{T}_{MEC}	\hat{T}_{corr}	\hat{T}_{DE}	\hat{T}_{EC}
False Leaf	13	3	11	5
AP Hill subset	—	—	13	6
Guanica subset	—	—	12	7

to determine optimal stopping scale for all the three images presenting the expected behavior. The entropy change criterion determines that iterations 5, 6, and 7 as the optimal scale for the False Leaf, AP Hill subset and Guanica subset respectively as illustrated in Figures 3.5(j-l). Table 3.1 summarizes the optimal scales determined by the four criteria for the three test images.

3.3.1 Scale Effects

Spatial and spectral scale effects are studied by comparing the smoothed image selected using the scale selection criteria. For the False Leaf image, four different scales (see Table 3.1) are obtained by the scale selection methods. But, for the AP Hill subset and Guanica subset images, only two scales are obtained. RGB compositions of the smoothed images are presented to visualize the spatial effects, and a comparison of the spectral endmember extracted by the proposed methodology using the selected scales is also performed.

Figures 3.6-3.8 show a comparison among the selected scales for a better understanding of scale effects. Figure 3.6 presents the RGB composition (using bands 57 (639 nm), 35 (548 nm) and 13 (460 nm)) of the smoothed images for the False Leaf obtained in iterations 3, 5, 11 and 13 which were selected by the Mrazek decorrelation, entropy change, diffusion balance, and minimum entropy change criteria respectively. An zoom on a leaf is included in the Figure 3.6 where the scale effects

can be better appreciated. For instance, see how the small details inside the leaf of Figure 3.6(i) and 3.6(j) are lost in iterations 11 and 13.

Similarly, Figure 3.7 shows the smoothed images for the AP Hill subset obtained in iterations 6 and 13, which are selected by the entropy change and diffusion balance criteria respectively. Figure 3.7 presents the RGB composition using bands 30, 20 and 9. An enlarged portion of the image is also included (Figures 3.7(d-f)). In the enlarged portion of the image, it can be seen how the path is lost in iteration 13. Additionally, Figure 3.8 presents the comparison between the smoothed images for the Guanica subset in iterations 7 and 12 selected by the entropy change and diffusion balance methods respectively. An enlarged portion of the forest is included in Figures 3.8(d-f). For this image, the scale effects can be noted mainly in the region with soil and sparse vegetation. Figure 3.8 shows how this highly heterogeneous region loses many spatial details with the smoothing iterations. Results present in Figures 3.6-3.8 for the False Leaf, AP Hill subset, and Guanica subset images suggest that a good stopping scale should be found in the few first iterations to avoid removing small features.

The spectral endmembers were extracted for the False Leaf, AP Hill subset, and Guanica subset using the proposed methodology to analyze the scale effects in the spectral signatures. Additionally, abundances were computed for the obtained spectral endmembers in each selected scale. Examples of spectral endmembers and their corresponding abundances are shown in the Figures 3.9-3.11 for the three test images.

Figure 3.9 shows two spectral endmembers (SE₁ and SE₂) obtained from the False Leaf image using scales 3, 5, and 11. For scale 13, these two spectral endmembers appear mixed (Figure 3.9(d)) which evidences how spectral features can be lost with too many smoothing iterations. In the Figures 3.9(k-r), an enlarged portion of the abundance images are presented. The two spectral endmembers can be better distinguished in these subsets. Figures 3.9(i-j) present the signatures for SE₁ and SE₂ respectively. Note that in each plot on Figures 3.9(i-j) the spectral endmembers ob-

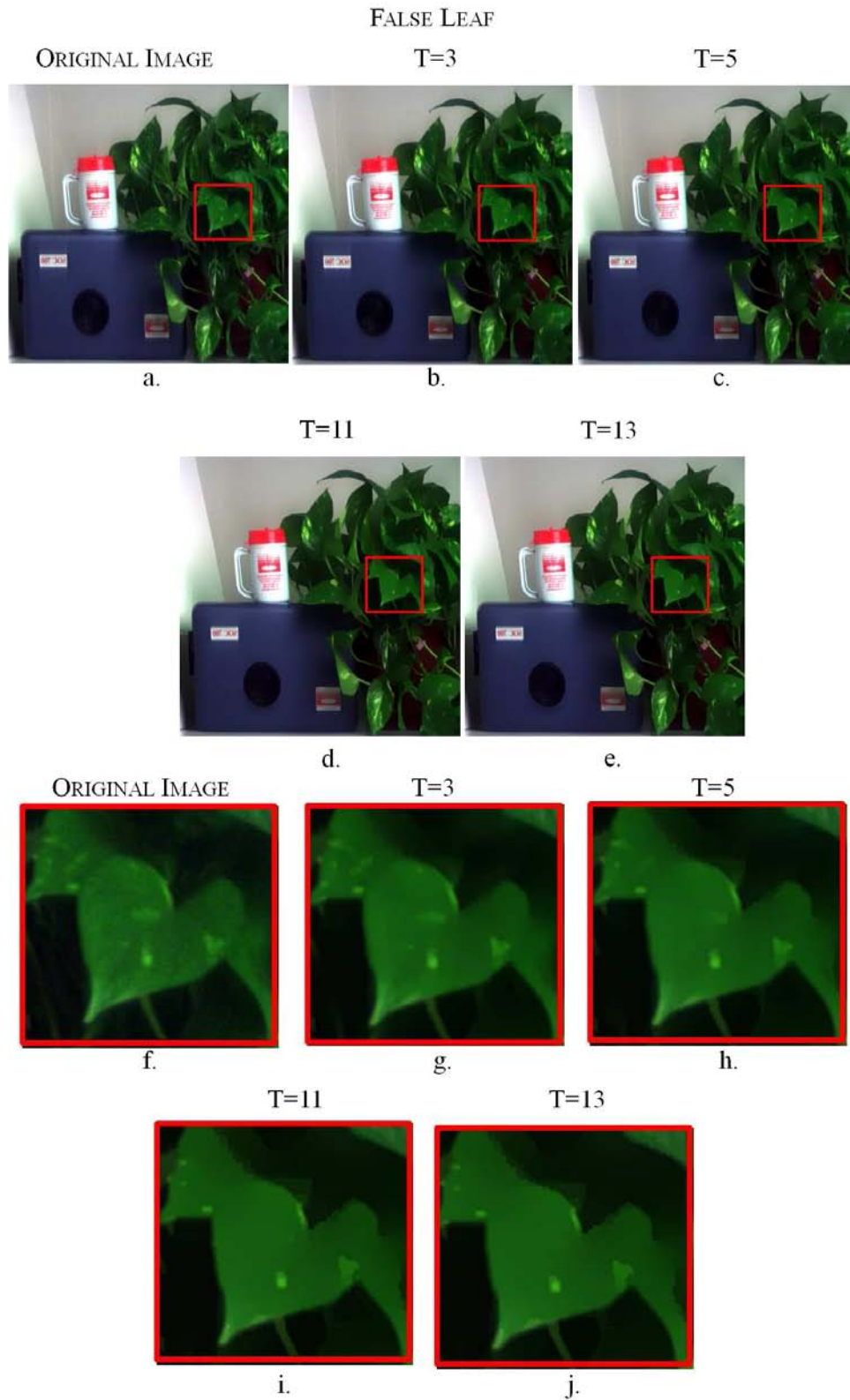


Figure 3.6: Comparison of selected scales for the False Leaf image. RGB images for (a) Original Image, and smoothed image in: (b) $\hat{T}_{corr} = 3$, (c) $\hat{T}_{EC} = 5$, (d) $\hat{T}_{DE} = 11$, and (e) $\hat{T}_{MEC} = 13$. (f)-(j) Comparison of original and smoothed images in a leaf.

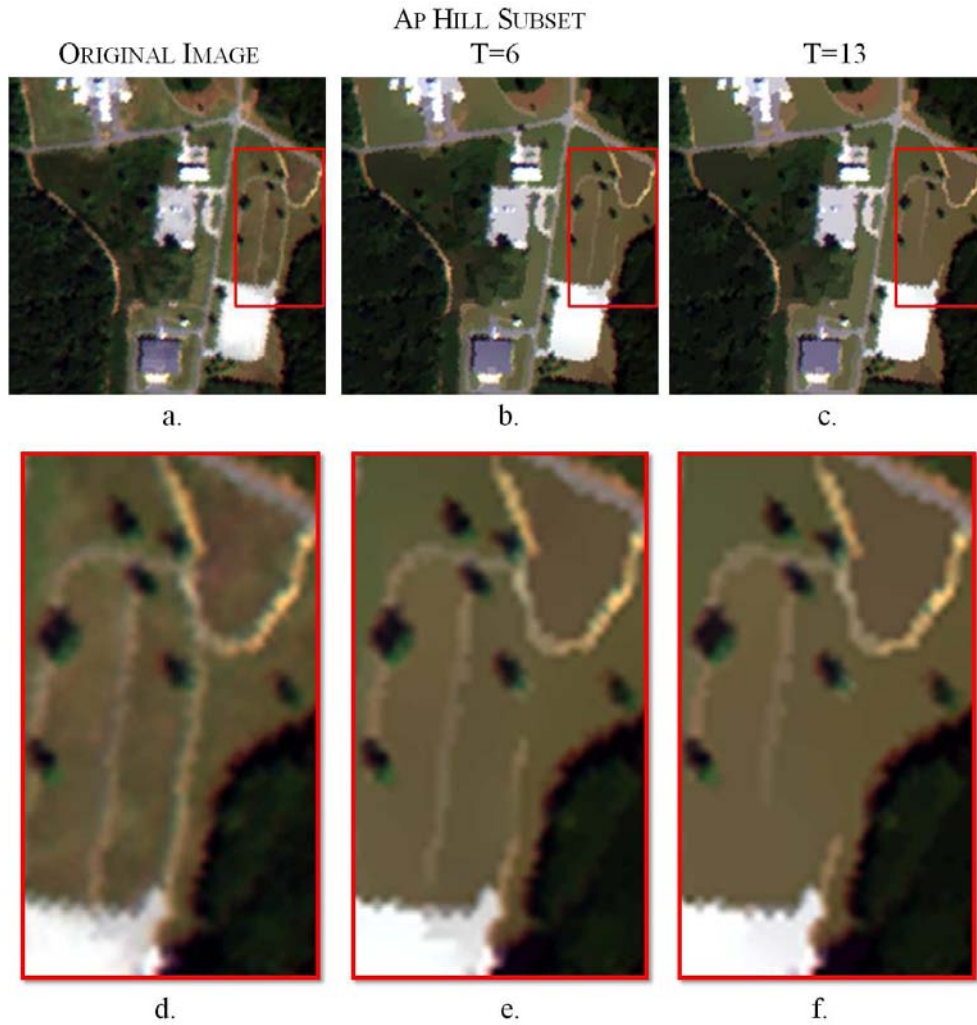


Figure 3.7: Comparison of selected scales for the AP Hill subset image. RGB images for (a) Original image, and smoothed image in: (b) $\hat{T}_{EC} = 6$ and (c) $\hat{T}_{DE} = 13$. (d)-(f) Comparison of original and smoothed images in an enlarged portion of AP Hill subset.

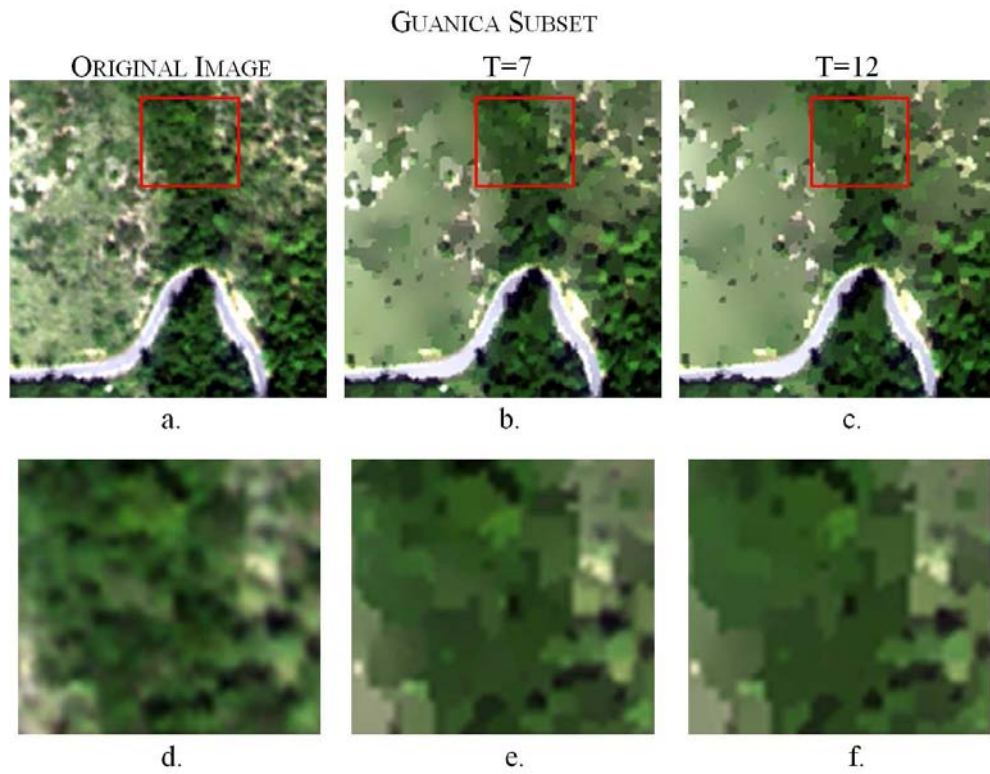


Figure 3.8: Comparison of selected scale for Guanica subset image. RGB images for (a) Original image, and smoothed image in: (b) $\hat{T}_{EC} = 7$ and (c) $\hat{T}_{DE} = 12$. (d)-(f). Comparison of original and smoothed images in an enlarged portion of Guanica subset.

Table 3.2: Number of spectral endmembers for False Leaf, AP Hill subset, and Guanica Subset images.

False Leaf	Scale 3: 264	Scale 5: 146	Scale 11: 138	Scale 13: 120
AP Hill subset	Scale 6: 113	Scale 13: 104	—	—
Guanica subset	Scale 7: 108	Scale 12: 99	—	—

tained in the scale 13 are included. This spectral endmember illustrates the mixed spectrum that can result from smoothing operations.

Figure 3.10 shows two spectral endmember (SE₁ and SE₂) for the AP Hill subset using scales 6 and 13. SE₁ appears invariant with the scale. On the other hand, SE₂ is identified in one single spectrum in scale 6, but in two spectra in scale 13. The comparison of spectra in Figures 3.10(c) and 3.10(g) shows the consistence in the signature shape. Although the change of SE₂ spectrum along the scales is not significant, abundance results present remarkable changes.

Finally, Figure 3.11 presents also two spectral endmembers for the Guanica subset image for scales 7 and 12. The first spectral endmember does not present changes along scale (Figure 3.11(c)), and the second one has a higher amplitude for scale 12.

Table 3.2 summarizes the number of spectral endmembers obtained for each image and the different selected scales. As shown in Table 3.2, the number of spectral endmembers decreases with the scale.

3.3.2 Analysis of Results

Scale selection methods found in the literature such as the decorrelation method and the minimum entropy change do not work very well for complex images such as AP Hill and Guanica subset where there is a greater heterogeneity in the surfaces. Only the diffusion balance and the proposed criterion based on the entropy change of $\mathbf{Y}_t - \mathbf{Y}_0$ allowed to determine an optimal scale for all images. The first one determines

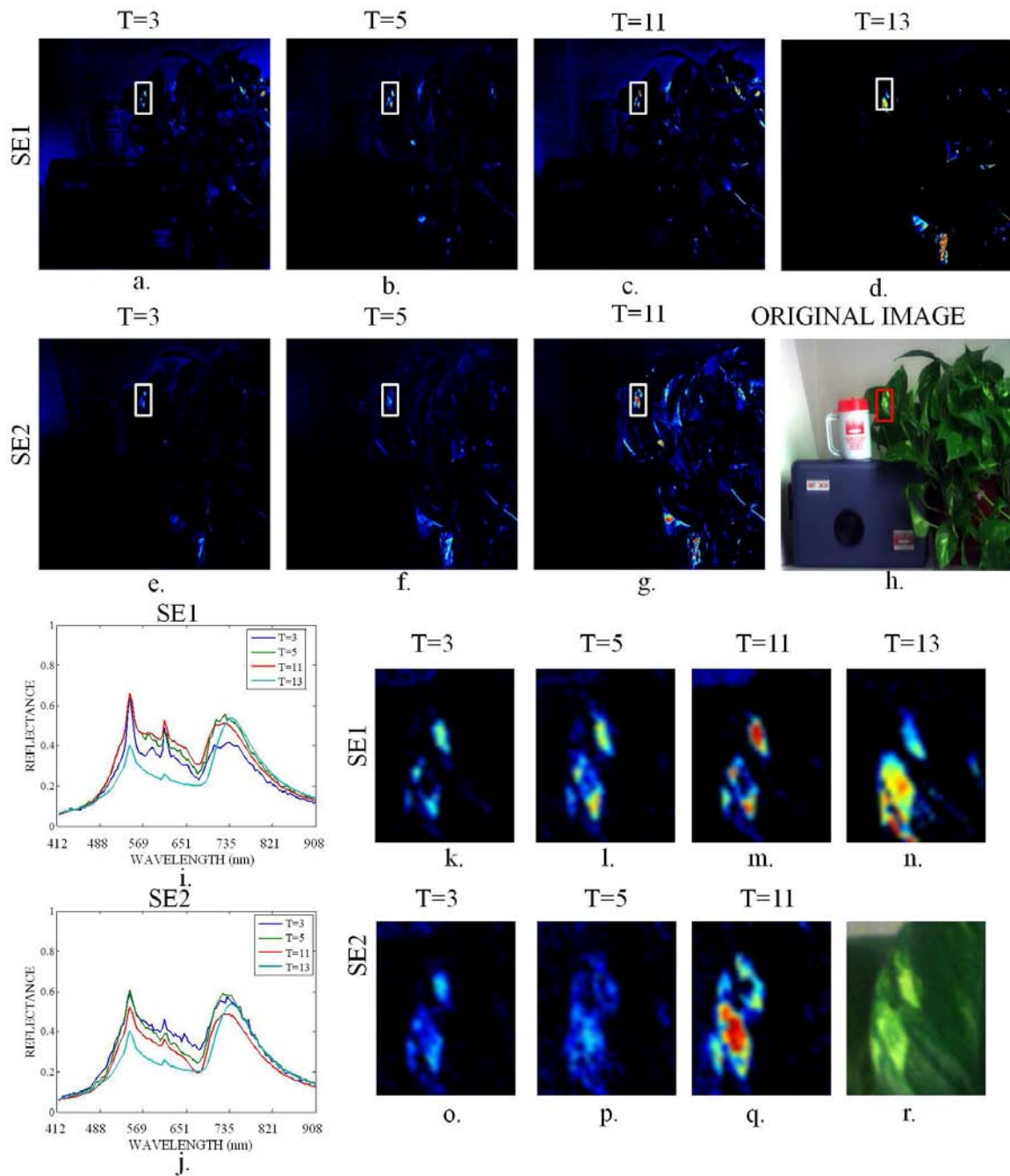


Figure 3.9: Example of spectral endmembers from False Leaf image. (a)-(c) Abundances for spectral endmember SE1 for scales 3, 5, and 11. (d) Abundance for mixed spectral endmember for scale 13. (e)-(g) Abundances for spectral endmember SE2 for scales 3, 5, and 11. (h) RGB composition original image highlights the portion of image presented in (k)-(r). (i) SE1 and (j) SE2 spectral endmembers.

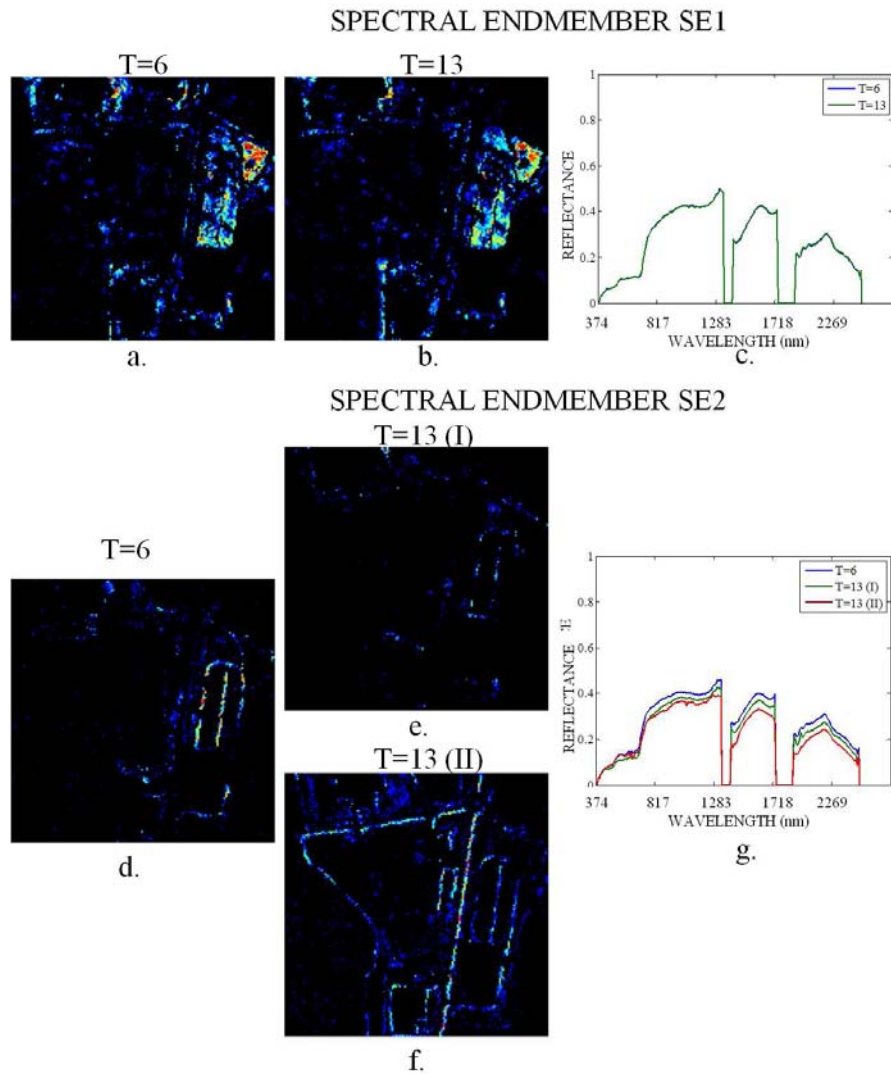


Figure 3.10: Example of spectral endmembers from AP Hill subset image. (a)-(b) Abundances and (c) signatures for spectral endmember SE1 for scales 6, and 13. (d)-(f) Abundances and (g) signatures for spectral endmember SE2 for scales 6 and 13.

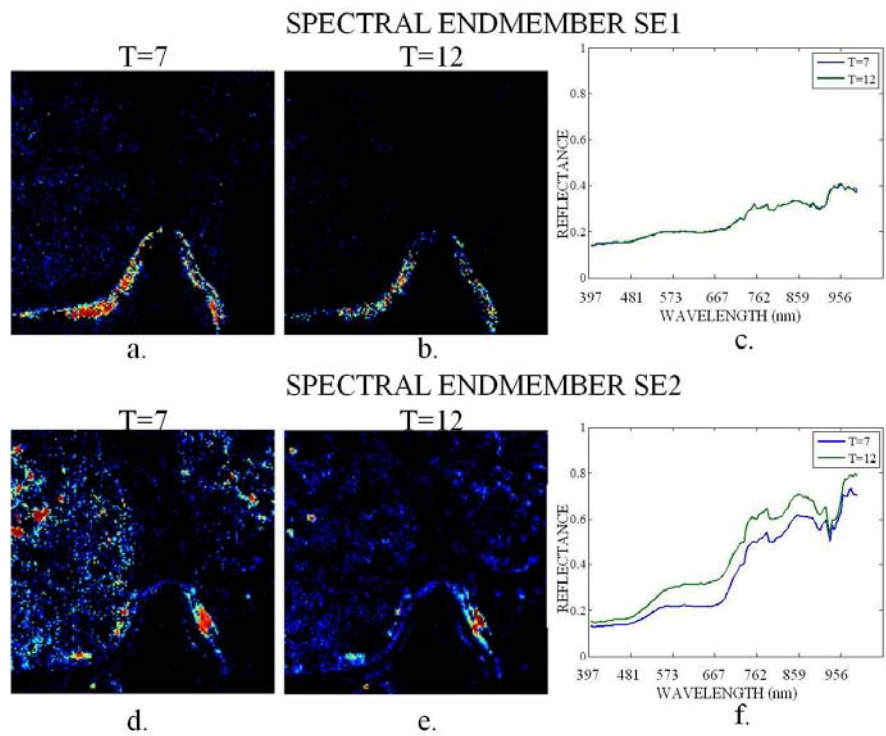


Figure 3.11: Example of spectral endmembers from Guanica subset image. (a)-(b) Abundances and (c) signatures for spectral endmember SE1 for scales 7, and 12. (d)-(e) Abundances and (f) signatures for spectral endmember SE2 for scales 7 and 12.

an optimal scale using an energy measure and the second one uses an information measure.

The scale effects in the spectral endmembers extraction can be several. Some spectral endmembers are not affected by the amount of smoothing iterations. However, other selected spectral endmembers are mixed. Thus, it is expected that better spectral endmembers extraction can be obtained by stopping at a low scale. This is supported also by the decreasing of number of spectral endmember with the scale such as presented in Table 3.2. Although diffusion balance and entropy change criterions allow to determine a optimal scale for all images, the entropy change criterion tends to select scales with fewer smoothing iteration than diffusion balance. Both methods are used in additional experiments in Chapter 6. However, the results indicate that the proposed method is a good criterion for automatic selection of scale for spectral endmember extraction.

3.4 SUMMARY

Assuming that spectral endmembers are representative signatures of uniform regions, a new spectral endmember extraction approach is proposed taking advantage of the capabilities of nonlinear diffusion and multigrid methods. Nonlinear diffusion decreases the local spectral variability allowing the identification of spectral uniform regions. Different levels of smoothing generate a multiscale representation. The proposed approach uses one of the images from the family of images of the multiscale representation for the spectral endmember extraction. A modified multigrid structure is used to extract the representative spectra from uniform regions in the selected image. The multigrid structure builds a hierarchical representation of the image. The more representative signatures of the image are found in the coarsest level. These signatures are used as spectral endmembers. The proposed approach

takes into account the spatial information without the need to define kernels such as others spatial-spectral methods.

As only one smoothed image is used for the identification of spectral endmembers, a method based on the entropy of $\mathbf{Y}_t - \mathbf{Y}_o$ is developed for the automatic scale selection. This method presents good results even in complex scenarios. Additionally, this method tends to select scales in the first few iterations of the nonlinear diffusion avoiding the mixing that occurs at higher iterations.

The developed spectral endmember extraction approach uses all spectra to compute abundances. As this can become tens or hundreds depending of the complexity of the image, different methods should be used for abundances estimation. If the number of spectral endmembers is less than the number of bands then constrained least square techniques are employed. On the other hand, if the number of spectral endmembers is larger than the number of bands then sparse regression is used.

The next chapter presents how these spectral endmembers can be grouped to form spectral endmember classes. The spectral endmember classes seek a better representation of the components of an image and their spectral variability.

SPECTRAL ENDMEMBER CLASS EXTRACTION USING CLUSTERING

A large number of spectral endmembers can be extracted with the multiscale representation approach presented in the previous chapter depending of the complexity of the scene. These spectral endmembers represent the distinct components in a scene as well as their spectral variability (see Section 1.2). Thus, it is necessary to group spectral endmembers into sets with similar spectral features, i.e. meaningful clusters that represent the distinct materials in the image. These meaningful sets of spectral endmembers are the spectral endmember classes.

The obvious way to build the spectral endmember classes is by using clustering techniques. Clustering is widely used in the fields of data mining, statistical analysis, machine learning, pattern recognition, and others. Clustering has been also used in hyperspectral imaging for applications in segmentation, classification, change detection, and unmixing (e.g. [16, 23, 81, 82, 83, 84]). Most of previous works have used clustering over the full image. In this work, cluster analysis is conducted in a small subset of spectra: the spectral endmembers. Thus, the computational cost is far less than in the other applications. Some unmixing methods have employed clustering to form sets of endmembers such as Canham et al. [16] and Somers et al. [23].

In this chapter, a comparative study of clustering techniques for building spectral endmember classes is performed. A brief review of clustering techniques is presented in Section 4.1. There are many references and books devoted to clustering. The reader can find more information in the book of Jain and Dubes [28], and the papers of Jain et al. [29] and Wu and Wunsch [30]. One of the most challenging

problems in clustering analysis is the determination of the number of clusters that in the proposed approach corresponds to the number of spectral endmember classes. Validity indexes are used for this task. Validity indexes are metrics to assess the clusters obtained from different methods or configuration of clustering methods (e.g. different number of clusters) [28, 31, 32]. Experiments using spectral endmembers from the False Leaf image are presented in the Section 4.3 to compare different clustering algorithms and several validity indexes in the estimation of the number of spectral endmember classes.

4.1 CLUSTER ANALYSIS

Clustering divides a collection of patterns into several subsets, the so called *clusters*, based on some criterion of similarity [28, 29, 30]. *Hard partition clustering* seeks a k -partition, $\mathbf{C} = \{\mathbf{C}_1, \mathbf{C}_2, \dots, \mathbf{C}_k\}$, of a dataset $\mathbf{S} = \{\mathbf{s}_1, \mathbf{s}_2, \dots, \mathbf{s}_m\}$, with $k \leq m$, such that each sample of \mathbf{S} belongs to one single partition \mathbf{C}_i [30]. On the other hand, *fuzzy clustering* allows samples to belong to several clusters with a degree of membership. The scope of this review is limited to hard partition techniques, referred as clustering techniques hereinafter.

Clustering algorithms can be *hierarchical*, *partitional*, or *graph-theory based* approaches. Most of these approaches perform clustering using a pair-wise distance matrix instead of the dataset. Thus, an adequate selection of the similarity metric is very important [28].

Clustering analysis is divided in four stages [29]. Initially, feature extraction or feature selection techniques can be used to improve the representation of the data. Second, calculate the similarity matrix. Using similarity measures, the clustering algorithm performs the separation of the samples into meaningful subsets. Finally, clustering results are assessed to determine how well the algorithms find the hidden

Table 4.1: Similarity metrics for hyperspectral data.

Metric	Equation
Euclidian Distance (ED)	$d_{ED} = \sqrt{(\mathbf{s}_A - \mathbf{s}_B)^T (\mathbf{s}_A - \mathbf{s}_B)}$
Spectral Angle [85] (SAM)	$d_{SAM} = 1 - \frac{\mathbf{s}_A^T \mathbf{s}_B}{\sqrt{(\mathbf{s}_A^T \mathbf{s}_A)(\mathbf{s}_B^T \mathbf{s}_B)}}$
Spectral Correlation [86] (SCM)	$d_{SCM} = 1 - \frac{(\mathbf{s}_A - \bar{\mathbf{s}}_A)^T (\mathbf{s}_B - \bar{\mathbf{s}}_B)}{\sqrt{(\mathbf{s}_A - \bar{\mathbf{s}}_A)^T (\mathbf{s}_A - \bar{\mathbf{s}}_A)} \sqrt{(\mathbf{s}_B - \bar{\mathbf{s}}_B)^T (\mathbf{s}_B - \bar{\mathbf{s}}_B)}}$ where $\bar{\mathbf{s}} = \frac{\sum s_i}{n}$
Spectral Information Divergence [87] (SID)	$d_{SID} = \sum_{i=1}^n p_i \log \left(\frac{p_i}{q_i} \right) + \sum_{i=1}^n q_i \log \left(\frac{q_i}{p_i} \right)$ where $p(i) = \frac{s_{Ai}}{\sum_{j=1}^n s_{Aj}}$ and $q(i) = \frac{s_{Bi}}{\sum_{j=1}^n s_{Bj}}$

data structure. This can be done using validity indexes. The next sections review different similarity metrics, clustering algorithm techniques, and validity indexes.

4.1.1 Similarity Metrics

In hyperspectral imaging, different metrics are used to compare two spectral signatures and determining how similar they are. Among of similarity metrics widely used for hyperspectral data are the Euclidian Distance (ED), the Spectral Angle (SAM) [85], the Spectral Correlation Measure (SCM [86]), and the Spectral Information Divergence (SID [87]). Table 4.1 summarized these four similarity measures for two spectral with n bands: $\mathbf{s}_A = (s_{A1}, \dots, s_{An})^T$ and $\mathbf{s}_B = (s_{B1}, \dots, s_{Bn})^T$.

4.1.2 Clustering Algorithms

Several clustering algorithms had been developed. These can be classified into *hierarchical*, *partitional*, and *graph-theory based* approaches. Implementations of hierarchical and partitional algorithms using graphs exist in the literature [28]. However, graph-theory based approaches, in this review, refer to algorithms that use the spectrum

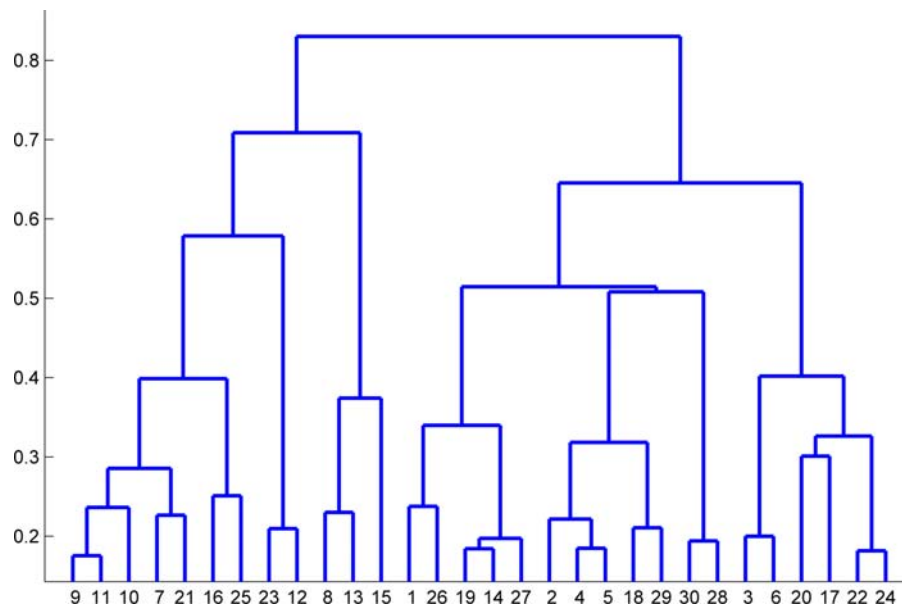


Figure 4.1: Dendrogram example for hierarchical clustering algorithms.

of the graph (Section 4.1.2.3) to perform the clustering. Next, the principles of these three types of clustering are briefly summarized.

4.1.2.1 Hierarchical Algorithms

Hierarchical clustering algorithms build a family of nested partitions which are usually represented by a dendrogram like the one shown in Figure 4.1. The greatest advantage of hierarchical approaches is that they do not require the number of clusters since the dendrogram can be broken at any level obtaining different partitions of the data [29, 30].

Hierarchical clustering algorithms can be agglomerative or divisive [30]. The first ones start with several clusters formed with one single sample, and then successive merge operations are performed using the similarity matrix until a single cluster with all samples is obtained. Divisive approaches start with a single cluster with all samples and perform division operations. Divisive hierarchical algorithms are rarely used since they are computationally expensive [30].

There are several criteria to conduct the merge operations among which stand single, complete, and average linkage. *Single linkage* defines the distance between two clusters as the minimum distance between all pairs of samples from the clusters. This tends to produce elongated clusters and it is very sensitive to outliers. On the other hand, *complete linkage* uses the maximum distance between all pair of samples from two clusters producing compact clusters. *Average linkage* employs the distance between centroids as the distance between clusters seeking a balance between both single and complete criteria [29]. The implementations of hierarchical algorithms found in MATLAB as part of the Statistic Toolbox¹ are used in this research. The computational complexity of hierarchical clustering (including single, complete and average linkage) is $O(N^2)$ [30], where N is the number of points or samples. These algorithms are very inefficient for large datasets. But for the current application, it is expected that the computational cost of hierarchical algorithms not to affect the overall performance of the technical approach since the obtained spectral endmembers is a relatively small dataset of few hundreds signatures.

4.1.2.2 Partitional Algorithms

Unlike hierarchical algorithms, partitional approaches obtain a single partition of the data which is of great advantage in large datasets [29]. Partitional clustering minimizes some criterion function to find the optimal partition of the data. The most common partitional algorithms are based on the squared error criterion [29, 30]. Let a set of m samples \mathbf{s}_j organized into k clusters. The squared error is given by [30]:

$$J(\mathbf{\Gamma}, \mathbf{M}) = \sum_{i=1}^k \sum_{j=1}^m \gamma_{ij} \|\mathbf{s}_j - \mathbf{m}_i\|^2 \quad (4.1)$$

¹ <http://www.mathworks.com/help/stats/clusterdata.html>

where $\Gamma = \{\gamma_{ij}\}$ is a partition matrix such that:

$$\gamma_{ij} = \begin{cases} 1 & \text{if } \mathbf{s}_j \in \text{cluster } i \\ 0 & \text{otherwise} \end{cases} \quad (4.2)$$

and \mathbf{M} is a matrix with the centroid of each cluster.

The most used partitional algorithm is *k-means*. *k-means* clustering starts with a random partition and iteratively reassigns the samples to the clusters according to the similarity between the sample and the cluster's centroid until convergence. It is very sensitive to outliers and noise [30]. The MATLAB function *kmeans* is used in this research, which is part of the Statistic toolbox². The computational time of *k-means* is $O(NKd)$ where d is the number of features of the dataset [30], N is the number of samples, and K the number of clusters. Usually, *k-means* is run several times with different initial partitions. The partition with the minimum square error J (Equation 4.1) is selected.

4.1.2.3 Graph Based Algorithms

Let the similarity graph $G = (V, E)$, where each vertex represents a sample and the edges are built by the connection of very similar vertices. The problem of clustering can be viewed as the task of partitioning the graph G such that the connection between subgraphs are weak (i.e. have low weights) and the connection within subgraphs are strong [88]. There are several criteria to build the edges in the similarity graph $G = (V, E)$. The most widespread similarity graphs are the ε -neighborhood graph, k -nearest neighbor graph, and fully connected graph [88]. The ε -neighborhood graph connects all points whose similarity are smaller than ε . The k -nearest neighbor graph connects each vertex with its k closest vertices. A symmetric similarity graph is necessary. Thus, k -nearest neighbor graph connects the vertices

² <http://www.mathworks.com/help/stats/kmeans.html>

v_i and v_j either v_i is one of the k -nearest neighbors of v_j or v_j is one of the k -nearest neighbors of v_i . Other type of similarity graph is the fully k -nearest neighbor graph where the vertices v_i and v_j are connected if v_i is one of the k -nearest neighbors of v_j and v_j is one of the k -nearest neighbors of v_i . The fully connected graph connects all points using a function that holds the local neighborhood relations. For instance, the Gaussian similarity function, $\exp\left(-\|x_i - x_j\|^2/2\sigma^2\right)$, is frequently used to build fully connected graphs.

The most promising graph-theory based methods are the spectral algorithms which use the eigenvalues and eigenvectors of the graph Laplacian for clustering [89, 90, 88]. Here the basics about spectral clustering are described. A complete presentation of spectral graph theory is found in [89], and in the review papers of Ng et al. [90] and Luxburg [88].

There are different algorithms to perform spectral clustering, which vary according to the Laplacian employed. G is assumed to be an undirected weighted graph with adjacency matrix \mathbf{W} and degree matrix \mathbf{D} given by:

$$\mathbf{D} = \begin{bmatrix} d_1 & & & \\ & d_2 & & \\ & & \ddots & \\ & & & d_n \end{bmatrix} \quad (4.3)$$

where d_i is the degree of the vertex v_i defined as:

$$d_i = \sum_{j=1}^n w_{ij} \quad (4.4)$$

Table 4.2: Spectral clustering algorithm. Algorithm based on [88].

<i>Inputs:</i> similarity matrix \mathbf{S} and number of clusters k .
- Construct the similarity graph \mathbf{W} .
- Compute the Laplacian \mathbf{L} .
- Compute the first k eigenvector of \mathbf{S} : $\mathbf{u}_1 \dots \mathbf{u}_k$.
- Let the matrix $\mathbf{U} \in \mathbb{R}^{n \times k}$ which columns are $\mathbf{u}_1 \dots \mathbf{u}_k$ and \mathbf{y}_i be the vector corresponding to the i -th row of \mathbf{U} .
- Cluster with k -means algorithm into $P_1 \dots P_k$ clusters.
<i>Output:</i> Clusters $C_1 \dots C_k$ where $C_i = \{j \mathbf{y}_j \in P_i\}$

The unnormalized Laplacian is defined as [88]:

$$\mathbf{L}_{UN} = \mathbf{D} - \mathbf{W} \quad (4.5)$$

and the normalized Laplacian [88] is given either by:

$$\mathbf{L}_{N1} = \mathbf{D}^{-1/2} \mathbf{L}_{UN} \mathbf{D}^{-1/2} = \mathbf{I} - \mathbf{D}^{-1/2} \mathbf{W} \mathbf{D}^{-1/2} \quad (4.6)$$

or by [88] :

$$\mathbf{L}_{N2} = \mathbf{D}^{-1} \mathbf{L}_{UN} = \mathbf{I} - \mathbf{D}^{-1} \mathbf{W} \quad (4.7)$$

The eigenvalues and eigenvector of \mathbf{L} are used to perform clustering of the dataset. The multiplicity of the eigenvalue 0 of \mathbf{L} is related to the number of connected components [88]. The algorithms are referred as un-normalized if they employ \mathbf{L}_{UN} , and normalized if they use \mathbf{L}_{N1} [91] or \mathbf{L}_{N2} [90]. Spectral clustering algorithm is summarized in Table 4.2. In this work, the similarity graph $G = (V, E)$ is built using k -nearest neighbor, and the three spectral clustering algorithms are compared to form spectral endmember classes.

4.1.3 *Validity Indexes*

One of the biggest problems in cluster analysis is how to determine the validity of clustering results. A way to quantify the performance of a clustering algorithm is by using validity indexes. Validity indexes are metrics that allow the assessment of clustering results obtained by different methods or by the same method with different input parameters [28, 31, 30, 32, 92].

Validity indexes can be *external*, *internal* or *relative* [30, 32, 92]. External indexes employ a priori information of the dataset, such as previous partitions, to assess the performance of clustering algorithms. For example, two external indexes are used in Section 4.3.2 to compare several clustering algorithms for the spectral endmember class extraction from synthetic data. The employed indexes quantify the cluster homogeneity and spectral endmember class preservation [93]. On the other hand, internal indexes do not depend on a priori information. These measure how well a clustering technique recovers the structure of the data. An example of an internal index is the *Cophenetic correlation coefficient* [28] that is used in hierarchical algorithms to compare the recovered structure within the dendrogram and the structure of the similarity matrix. Finally, relative indexes are metrics to compare different algorithms or configuration of algorithms in order to determine which one provides the best results.

Most of the relative indexes seek to measure two criteria: compactness and separability [32, 92]. Compactness is an indicator of how close are the elements within the clusters, and separability determines how different clusters are. Both criteria can be measured in several ways. Thus, different validity index can be formulated. Next, some validity indexes are reviewed. These are used to determine the number of spectral endmember classes in Section 4.3.3.

4.1.3.1 *Dunn's Index*

Dunn's index [94] uses the fact that well formed and separated clusters should present large distances between clusters and small diameters. Dunn's index employs the minimum distance between all pairs of samples within two clusters as the distance among clusters which is given by:

$$\delta(C_i, C_j) = \min\{dist(\mathbf{s}_k, \mathbf{s}_l)\} \quad \mathbf{s}_k \in C_i, \mathbf{s}_l \in C_j \quad (4.8)$$

where $dist$ is a distance metric. The diameter is defined as the maximum distance between all pairs of samples within a same clusters:

$$\Delta(C_i) = \max\{dist(\mathbf{s}_j, \mathbf{s}_k)\} \quad \mathbf{s}_j, \mathbf{s}_k \in C_i \quad (4.9)$$

Dunn's index is determined by the ratio:

$$v_D(k) = \min_{1 \leq i \leq k} \left\{ \min_{\substack{1 \leq j \leq k \\ j \neq i}} \left\{ \frac{\delta(C_i, C_j)}{\max_{1 \leq l \leq k} \Delta(C_l)} \right\} \right\} \quad (4.10)$$

where k is the number of clusters.

The optimal number of clusters is determined by maximizing v_D :

$$\hat{c} = \max v_D(k) \quad \text{for } k = 2 \dots c_{\max} \quad (4.11)$$

4.1.3.2 *Davies and Bouldin Index*

Davies and Bouldin [95] proposes a metric to select the number of clusters by using the average similarity of each cluster with its most similar cluster. The similarity

between clusters i and j , R_{ij} , is a function of a dispersion measure, d_i , and a distance measure, M_{ij} . R_{ij} can be defined in several ways. Usually, R_{ij} is defined as:

$$R_{ij} = \frac{d_i + d_j}{M_{ij}} \quad (4.12)$$

The dispersion measure d_i is given by:

$$d_i = \frac{1}{m_i} \sum_{j=1}^{m_i} \text{dist}(\mathbf{s}_j, \mu_i) \quad (4.13)$$

where μ_i is the centroid of the cluster i , m_i is the number of elements in cluster i , and dist is a similarity metric. M_{ij} is the distance between the centroids of cluster i and j .

The Davies and Bouldin DB index is defined as:

$$DB(k) = \frac{1}{k} \sum_{i=1}^k R_i \quad (4.14)$$

where k is the number of clusters and $R_i = \max_j R_{ij}$.

The number of clusters can be determine by minimizing DB :

$$\hat{c} = \min DB(k) \text{ for } k = 2 \dots c_{\max} \quad (4.15)$$

4.1.3.3 Kim's Index

Kim et al. [31] uses the mean intra-cluster distance V_u and the over-partition measure function V_o to determine the optimal number of clusters. The mean intra-cluster distance V_u is given by:

$$V_u(k) = \frac{1}{k} \sum_{i=1}^k \sum_{\mathbf{s} \in C_i} \frac{\text{dist}(\mathbf{s}, \mu_i)}{m_i} \quad (4.16)$$

where k is the number of clusters, m_i is the number of samples in cluster i , and μ_i is the centroid of cluster i . When the dataset is under-partitioned, i.e. less clusters

than the optimal number, then the intra-cluster distance V_u is large. As the number of partitions gets closer to the optimal value then V_u decreases.

The over-partition measure function V_o is given by:

$$V_o(k) = \frac{k}{d_{\min}} \quad (4.17)$$

where d_{\min} is the minimum distance between cluster centers. The behavior of the over-partition function is opposite to V_u . V_o is large when there are few clusters, and it decreases abruptly when the number of clusters is larger than the optimal.

Kim's index combines both the mean intra-cluster distance V_u and the over-partition measure function V_o . First, both metrics are normalized since V_u and V_o have different scales, then, Kim's index is computed as follow:

$$V_{sv}(k) = V_u(k) + V_o(k) \quad (4.18)$$

and the number of cluster is determined by:

$$\hat{c} = \min V_{sv}(k) \text{ for } k = 2 \dots c_{\max} \quad (4.19)$$

Kim and Ramakrishma [96] provides an alternate definition for the Kim index to consider the effects of clusters formed by unnecessary merging. The modified Kim index redefines the mean intra-cluster distance V_u as:

$$V_u(k) = \max_{i=1 \dots k} \sum_{\mathbf{s} \in C_i} \frac{\text{dist}(\mathbf{s}, \mu_i)}{m_i} \quad (4.20)$$

4.1.3.4 SD Index

Halkidi et al. [97] proposed the SD validity index in function of the average scattering for clusters, $Scat$, and the total separation between clusters, Dis . The average scatter-

ing for clusters uses the cluster variance instead of a distance metric to quantify the compactness of the clusters. The SD validity index is given by:

$$SD(k) = \alpha Scat(k) + Dis(k) \quad (4.21)$$

where the average scattering for clustering is defined as:

$$Scat(k) = \frac{1}{k} \sum_{i=1}^k \frac{\|\sigma^2(C_i)\|}{\|\sigma^2(\mathbf{S})\|} \quad (4.22)$$

with $\sigma^2(\mathbf{S})$ as the variance of all samples, $\sigma^2(C_i)$ as the variance of the cluster i , and k as the number of clusters. The total separation between clusters is defined as:

$$Dis(k) = \frac{D_{\max}}{D_{\min}} \sum_{i=1}^k \left(\sum_{j=1}^k dist(C_i, C_j) \right)^{-1} \quad (4.23)$$

where D_{\max} and D_{\min} are the maximum and minimum distance between cluster respectively, and $dist$ is a distance measure. The scale factor α in Equation (4.21) is selected equal to $Dis(c_{\max})$, where c_{\max} is the maximum number of clusters.

The number of clusters can be determined by minimizing the SD index:

$$\hat{c} = \min SD(k) \text{ for } k = 2 \dots c_{\max} \quad (4.24)$$

Kim and Ramakrishma [96] also presented a modified SD index where the scattering for clustering is defined as:

$$Scat(k) = \max_{i=1..k} \left\{ \frac{\|\sigma^2(C_i)\|}{\|\sigma^2(\mathbf{S})\|} \right\} \quad (4.25)$$

4.1.3.5 Calinski and Harabask Index

Calinski and Harabask (CH) index [98] measures the separation between clusters. CH is formulated in terms of the separation between clusters and the separation within clusters. CH can be written as [32]:

$$CH(k) = \frac{\sum_{l=1}^k m_l \|\mu_l - \mu\|}{k-1} \bigg/ \frac{\sum_{l=1}^k \sum_{j=1}^{m_l} \|\mathbf{s}_i - \mu_l\|}{m_i - k} \quad (4.26)$$

where m_i is the number of samples in cluster i , k is the number of clusters, μ_l is the centroid of cluster l , and μ is the centroid of the data set.

The number of clusters can be determined by maximizing the CH index:

$$\hat{c} = \max CH(k) \text{ for } k = 2 \dots c_{\max} \quad (4.27)$$

4.2 SPECTRAL ENDMEMBER CLASSES

Using the cluster analysis methodology described in [29], the spectral endmember classes can be built by the procedure described in Figure 4.2. The input data correspond with the spectral endmembers extracted by the multiscale representation approach, and the output is a set of labels that associate each spectral endmember to one spectral endmember class. The estimation of the number of spectral endmember classes is included as part of the cluster analysis process. The procedure requires the maximum number of clusters c_{\max} . Feature extraction or selection is an optional step. In the experiments shown here, feature extraction or selection is not performed. Future work can be conducted to study feature extraction and selection methods to improve the spectral endmember class extraction. Experiments in the next section aim to select the appropriate similarity metric, clustering technique, and validity index for the spectral endmember class extraction.

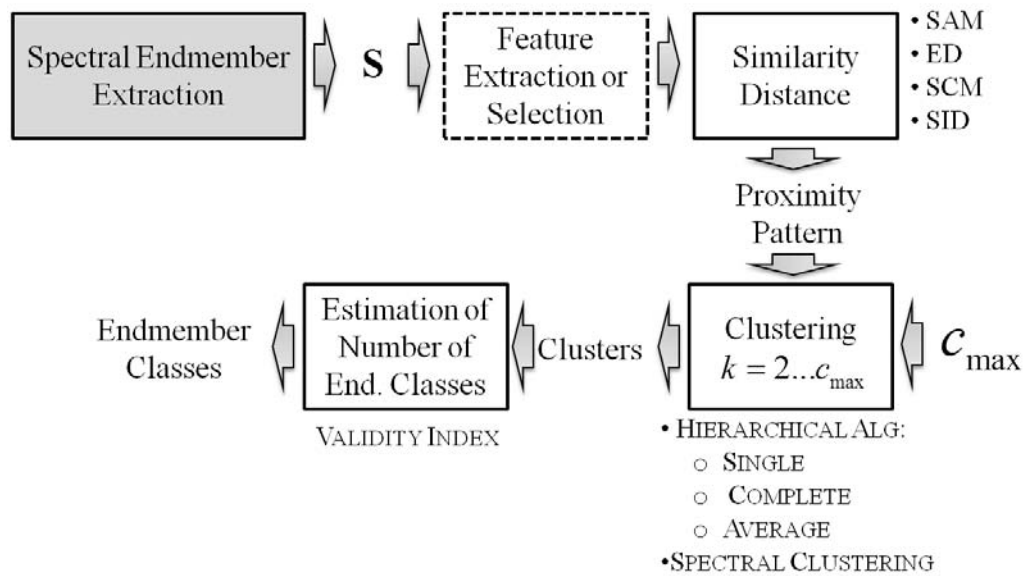


Figure 4.2: Spectral endmember class extraction using clustering.

4.3 EXPERIMENTS

This section presents experiments for comparing different clustering algorithms, and studying validity indexes for the estimation of the number of spectral endmember classes. Spectral endmembers from the False Leaf image are used to build a Test Data Set which is used to evaluate different clustering configurations.

4.3.1 Test Data Set

A test data set with 7 spectral endmember classes is built from the spectral endmembers extracted from the False Leaf image using the scale selected by the entropy change approach (5 smoothing iteration, Section 3.3.1). 61 spectra from the 146 spectral endmembers are used to build the test data. These spectra are manually grouped into 7 spectral endmember classes which represent uniform spectral regions on the image. The manual grouping was based on the position of the endmembers in the image and signature shape. The spectral endmember classes used are: *Wall and Mug*



Figure 4.3: Localization of spectra for each spectral endmember classes of Test Data.

Table 4.3: Number of spectra per spectral endmember class of Test Data.

Label	Name	Number of Spectra
c1	<i>Wall and Mug</i>	32
c2	<i>Camera</i>	8
c3	<i>Cover Camera</i>	2
c4	<i>False Leaf</i>	2
c5	<i>Vase</i>	1
c6	<i>Top Mug</i>	1
c7	<i>Leaf</i>	15

(c1), *Camera* (c2), *Cover Camera* (c3), *False Leaf* (c4), *Vase* (c5), *Top Mug* (c6), and *Leaf* (c7) and these are indicated in Figure 4.3. The spectral signatures for each spectral endmember class are presented in Figure 4.4. Note that *Wall and Mug* are a single spectral endmember class since the spectral responses of these regions (red points in the Figure 4.3) are very similar. Table 4.3 shows the number of samples per spectral endmember classes. Some spectral endmember classes have one single spectral endmember such as *Vase* and *Top Mug*. These cases correspond to highly spectrally uniform regions or small regions in the image. Clustering methods can see these spectral signatures as outliers affecting the performance of the algorithms. In these experiments, it is expected to find some algorithms that allow the determination of spectral endmember classes with these features.

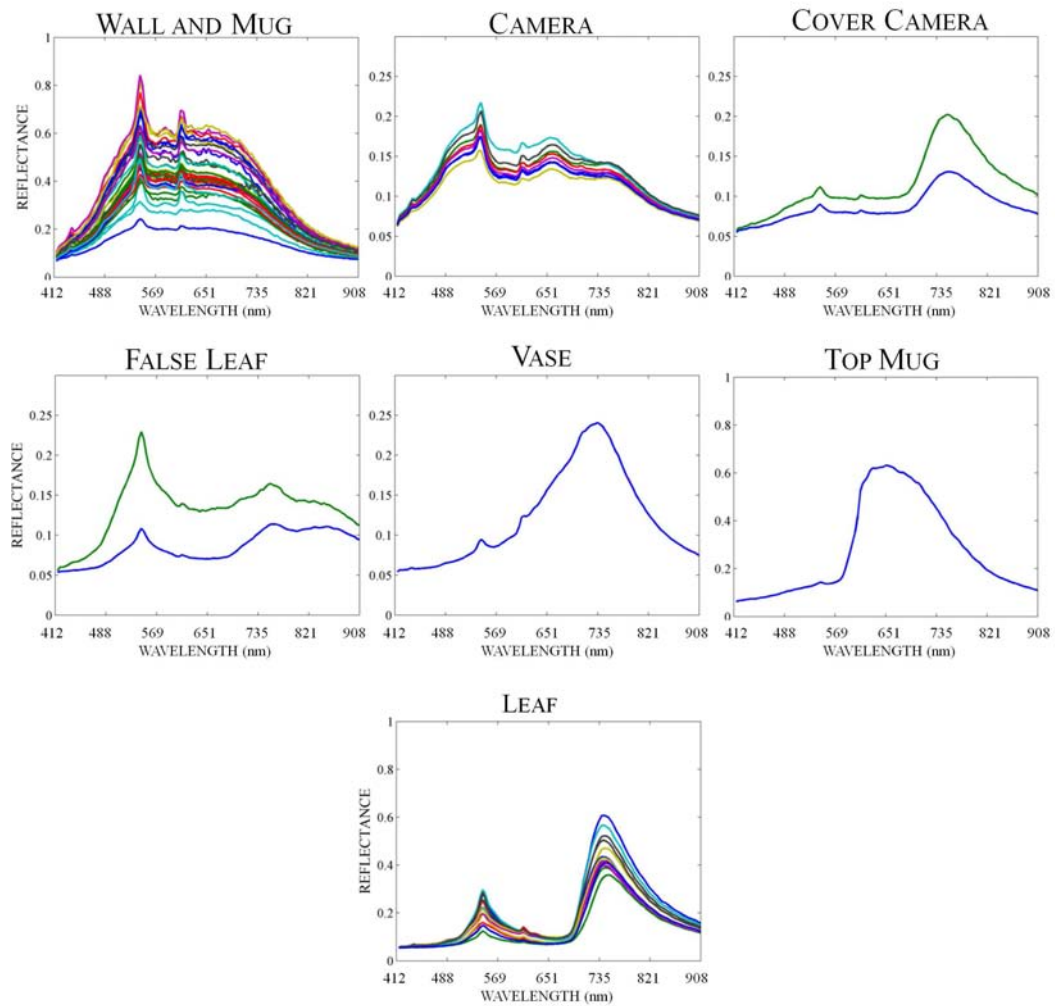


Figure 4.4: Test Data set.

4.3.2 Comparison of Clustering Algorithms

Complete and average linkage are used with the four similarity metrics reviewed in Section 4.1.1 (ED, SAM, CORR, SID) to form eight configurations for hierarchical clustering. *K-means* clustering results also are included for comparison purposes. Additionally, twelve spectral clustering configurations are also compared. The *k*-nearest neighbor affinity matrices formed with 15 neighbors are built from the similarity matrix obtained from the ED, SAM, CORR, and SID metrics. Unnormalized and normalized spectral clustering algorithms [91, 90, 88] are employed. *k-means* is repeated 500 times in the last step of spectral clustering (Section 4.1.2.3) and the result is selected as the trial with the minimum square error (Equation 4.1).

The comparison of clustering algorithms is done by analyzing the homogeneity of the clusters and the preservation of the spectral endmember classes [93]. It is expected that samples from the same spectral endmember class are assigned to the same cluster. Thus, if a cluster has less than 95% of the samples from the same spectral endmember class then it is considered a mixed cluster. If the clustering results are highly homogeneous, few mixed clusters should be obtained [93]. Each cluster is assigned to the spectral endmember class to which most of its samples belong. The preservation of the spectral endmember classes is measured by counting the detected spectral endmember classes [93].

First, six spectral endmember classes were randomly selected from the test data set. Samples in the selected spectral endmember classes were randomly swapped, and then, the different clustering configurations were used to determine the clusters. This process was repeated five times. For all algorithms, the number of clusters was set to six because the objective of this experiment was to select the algorithms capable to determine the known clusters. Section 4.3.3 studies methods for the estimation of the number of clusters. Table 4.4 shows the results obtained with the different clustering

algorithms over the test data in the different trials. In addition, Table 4.4 shows the number of detected spectral endmember classes (*class* column in Table 4.4) and the obtained number of mixed clusters (*mixed* column in Table 4.4). The algorithms that obtained the six classes and less than 1 mixed cluster are highlighted in the table.

Spectral clustering techniques and *k-means* present poor results in comparison with hierarchical techniques. Most of the spectral clustering configurations obtained 2 or more mixed clusters, and only detected 4 or fewer spectral endmember classes. On the other hand, the best results were obtained with the hierarchical configurations using SAM with both average and complete linkage. These identified all six spectral endmember classes for the five trials and only generated a single or any mixed cluster. Single linkage using SAM, and complete linkages using SID detected the six spectral endmember classes for the trials 1, 3, and 4. And, single and average linkage using SID detected the six spectral endmember classes for the trials 1, 3, 4, and 5.

In other experiment, the seven endmember spectral classes were used to compare the clustering algorithms. The number of clusters was set to seven in all algorithms. This experiment was performed once. Table 4.5 shows the results obtained with the different clustering algorithms over the test data. The extracted clusters are labeled with the letters A-G and the spectral endmember classes are labeled from c1-c7. Table 4.5 includes the percentages of samples from the same spectral endmember class in each cluster (columns 2 to 7). The last two columns present the number of detected spectral endmember classes and mixed clusters respectively. The algorithms with the best results are highlighted in the table.

Similar to the result obtained for six spectral endmember classes, spectral clustering techniques present poor results in comparison with hierarchical techniques using the full test data. Most of the spectral clustering configurations obtained 3 or more mixed clusters, and only detected 4 or fewer spectral endmember classes. Classes c1 and c7 were split in several clusters or mixed with other classes by the spectral clustering approaches. The spectral endmember classes c4 and c3 were mixed in the

Table 4.4: Clustering results for six spectral endmember classes from Test Data Set. Columns 1-5 show the number of detected spectral endmember classes (*class* columns) and the number of mixed clusters (*mixed* columns) for the five trials.

	TRIAL 1		TRIAL 2		TRIAL 3		TRIAL 4		TRIAL 5	
	CLASS	MIXED								
SINGLE + ED	5	1	5	2	5	2	5	1	5	2
SINGLE + SAM	6	0	5	1	6	1	6	1	5	1
SINGLE + SCM	6	0	5	1	5	1	5	1	5	1
SINGLE + SID	6	0	5	1	6	1	6	1	6	1
COMPLETE + ED	4	1	4	1	4	3	5	1	3	1
COMPLETE + SAM	6	0	6	1	6	1	6	1	6	1
COMPLETE + SCM	5	1	5	1	5	1	5	1	5	1
COMPLETE + SID	6	1	6	2	6	1	6	1	6	2
AVERAGE + ED	4	1	4	1	5	2	5	1	4	1
AVERAGE + SAM	6	0	6	1	6	1	6	1	6	1
AVERAGE + SCM	6	0	5	1	5	1	5	1	5	1
AVERAGE + SID	6	1	6	2	6	1	6	1	6	1
KMEANS	4	1	4	1	4	3	5	3	4	2
SPECTRAL + ED + UN	3	3	3	2	4	1	4	1	3	2
SPECTRAL + ED + N1	3	2	3	3	3	3	3	4	3	2
SPECTRAL + ED + N2	3	3	3	3	3	4	4	4	2	3
SPECTRAL + SAM + UN	4	3	4	3	5	2	4	2	4	3
SPECTRAL + SAM + N1	3	3	4	3	4	3	4	3	3	3
SPECTRAL + SAM + N2	3	2	4	3	4	2	4	3	3	3
SPECTRAL + SCM + UN	3	3	3	4	4	3	4	3	4	2
SPECTRAL + SCM + N1	3	3	4	3	4	3	3	2	3	4
SPECTRAL + SCM + N2	3	3	4	3	4	3	4	3	3	3
SPECTRAL + SID + UN	5	2	4	3	4	2	5	2	4	3
SPECTRAL + SID + N1	3	2	3	3	5	2	3	3	3	2
SPECTRAL + SID + N2	3	2	3	2	4	3	4	2	3	3

Table 4.5: Clustering results for the seven spectral endmember classes from the Test Data set. Columns A-G show the percentages (%) of samples belong to each spectral endmember class (c1-c7). Last two columns present the number of detected spectral endmember classes and mixed clusters.

METHOD	CLUSTERS							CLASSES	MIXED CLUSTERS
	A	B	C	D	E	F	G		
SINGLE + ED	C3-100	C3-50 C4-50	C2-80 C4-10 C1-10	C5-100	C1-100	C7-100	C6-100	6	2
SINGLE + SAM	C4-100	C3-100	C4-100	C1-80 C2-20	C7-100	C5-100	C6-100	6	1
SINGLE + SCM	C1-100	C2-100	C4-100	C7-88.2 C3-11.8	C5-100	C6-100	C4-100	6	1
SINGLE + SID	C4-100	C3-100	C4-100	C1-80 C2-20	C7-100	C5-100	C6-100	6	1
COMPLETE + ED	C1-100	C1-100	C1-100	C2-61.5 C3-15.4 C4-15.4 C5-7.7	C6-100	C1-100	C7-100	4	1
COMPLETE + SAM	C4-100	C2-100	C1-100	C5-100	C6-100	C7-100	C3-66.7 C4-33.3	7	1
COMPLETE + SCM	C2-100	C1-100	C5-100	C6-100	C4-100	C7-88.2 C3-11.8	C4-100	6	1
COMPLETE + SID	C4-100	C3-66.7 C4-33.3	C1-100	C2-88.9 C1-11.1	C5-100	C6-100	C7-100	7	2
AVERAGE + ED	C1-100	C1-100	C1-100	C2-57.1 C3-14.3 C4-14.3 C5-7.1 C1-7.1	C7-100	C1-100	C6-100	4	1
AVERAGE + SAM	C4-100	C2-100	C1-100	C5-100	C3-66.7 C4-33.3	C7-100	C6-100	7	1
AVERAGE + SCM	C1-100	C2-100	C4-100	C7-88.2 C3-11.8	C5-100	C6-100	C4-100	6	1
AVERAGE + SID	C4-100	C3-66.7 C4-33.3	C1-100	C2-88.9 C1-11.1	C5-100	C7-100	C6-100	7	2
KMEANS	C1-100	C1-100	C6-100	C2-57.1 C3-14.3 C4-14.3 C5-7.1 C1-7.1	C7-100	C1-100	C7-100	4	1
SPECTRAL + ED + UN	C1-100	C1-50 C2-50	C7-100	C1-100	C7-100	C2-54.5 C3-18.2 C4-18.2 C5-9.1	C1-90.9 C6-9.1	3	3
SPECTRAL + ED + N1	C1-100	C1-90.9 C6-9.1	C7-100	C2-50 C1-50	C2-54.5 C3-18.2 C4-18.2 C5-9.1	C7-100	C1-100	3	3
SPECTRAL + ED + N2	C1-100	C1-100	C1-90.9 C6-9.1	C2-54.5 C3-18.2 C4-18.2 C5-9.1	C2-50 C1-50	C7-100	C7-100	3	3
SPECTRAL + SAM + UN	C1-92.9 C6-7.1	C7-75 C5-12.5 C3-12.5	C1-100	C1-100	C4-66.7 C3-33.3	C7-100	C2-80 C1-20	4	4
SPECTRAL + SAM + N1	C1-100	C1-100	C1-83.3 C6-16.7	C2-72.7 C4-18.2 C3-9.1	C7-75 C3-12.5 C5-12.5	C7-100	C1-100	3	3
SPECTRAL + SAM + N2	C1-100	C7-75 C3-12.5 C5-12.5	C1-83.3 C6-16.7	C7-100	C1-100	C2-72.7 C4-18.2 C3-9.1	C1-100	3	3
SPECTRAL + SCM + UN	C1-88.9 C6-11.1	C1-90 C4-10	C2-88.9 C1-11.1	C1-100	C7-90.9 C5-9.1	C1-100	C7-62.5 C3-25 C4-12.5	3	5
SPECTRAL + SCM + N1	C1-90 C6-10	C7-90.9 C5-9.1	C2-100	C1-100	C1-100	C7-62.5 C3-25 C4-12.5	C1-90 C4-10	3	4
SPECTRAL + SCM + N2	C1-83.3 C6-16.7	C1-100	C7-62.5 C3-25 C4-12.5	C1-90 C4-10	C1-100	C2-100	C7-90.9 C5-9.1	3	4
SPECTRAL + SID + UN	C1-100	C7-100	C3-50 C4-50	C2-80 C1-20	C7-90.0 C5-9.1	C1-91.7 C6-8.3	C1-100	3	4
SPECTRAL + SID + N1	C1-100	C1-100	C1-100	C2-72.7 C4-18.2 C3-9.1	C1-85.7 C6-14.3	C7-100	C7-75 C3-12.5 C5-12.5	3	3
SPECTRAL + SID + N2	C7-75 C3-12.5 C5-12.5	C2-72.7 C4-18.2 C3-9.1	C1-100	C1-100	C1-87.5 C6-12.5	C1-100	C7-100	3	3

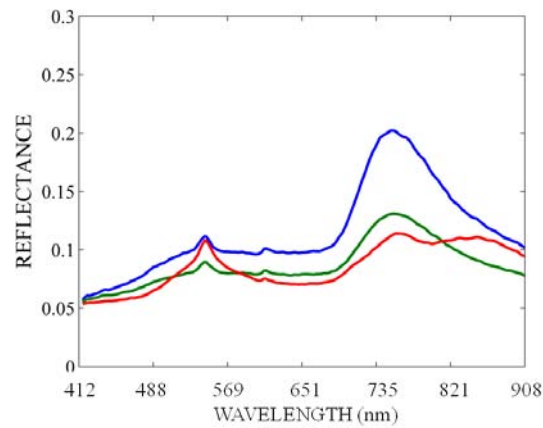


Figure 4.5: Mixed cluster from hierarchical clustering and SAM.

same cluster by most of the spectral configurations. Similarly, *k-means* obtained poor results detecting 4 classes and a single mixed cluster. Spectral endmember classes c_1 and c_7 were divided into several clusters, and mixed cluster were formed with samples from spectral endmember classes c_1 , c_2 , c_3 , c_4 and c_5 .

The best results were obtained with the hierarchical configurations using SAM with both average and complete linkage. Both complete and average linkages obtained the same clusters. These identified all seven classes and only generated a single mixed cluster with samples from c_3 (*Cover Camera*) and c_4 (*False Leaf*). Spectra in the mixed clusters are shown in Figure 4.5. Hierarchical clustering with ED and complete and average linkage only detected 4 spectral endmember classes generating several clusters for the spectral endmember classes c_1 and highly mixed clusters with samples from the spectral endmember classes c_2 , c_3 , c_4 and c_5 . All single linkage configurations obtained six classes similar to complete and average linkage with SCM. On other hand, average and complete linkage using the SID similarity metric obtained 7 spectral endmember classes but two mixed clusters. Both average and complete linkage with SID mixed c_3 and c_4 in a single cluster as well as samples from spectral endmember classes c_2 and c_1 .

As the seven spectral endmember classes are formed by average and complete linkages and SAM, and the data is labeled, clustering results for these configurations can

Table 4.6: Confusion matrix for clustering results of average and complete linkages using SAM in Test Data set. Both algorithms get exactly the same results.

		ACTUAL CLUSTER						TOTAL	USER ACCURACY
		C4	C2	C1	C5	C6	C7		
CLUSTERED AS:	A	1						1	100%
	B		8					1	100%
	C			32				3	100%
	D				1			7	100%
	E					1		26	100%
	F						15	1	100%
	G	1						2	66.7%
TOTAL		2	8	32	1	1	15	2	
PRODUCER ACC.		50%	100%	100%	100%	100%	100%	100%	
OVERALL ACCURACY				98.36%		KAPPA:			97.45%

be seen as a supervised classification where each cluster corresponds with the class with the highest number of samples within the cluster. Table 4.6 presents a "confusion matrix" for the clustering results obtained for both configurations: average and complete linkages. The obtained overall accuracy for hierarchical clustering using complete and average linkage with SAM was as high as 98.36%, and the obtained kappa statistic was 97.45%. Both experiments, using six and seven classes from the test data, show that the hierarchical clustering using average and complete linkages with SAM are a good methodology for the extraction of spectral endmember classes. Both configurations allow to detect spectral endmember classes with single or few spectra such as the *Vase* and *Top Mug* for the test data set. Note that these classes with single spectrum can be found in real data into very homogeneous and small regions. For the previous experiments, the number of clusters was set manually. The next section compares several validity indexes for the estimation of the number of clusters.

4.3.3 Estimation of the Number of Spectral Endmember Classes

The use of validity indexes described in Section 4.1.3 to determine the number of spectral endmember classes is evaluated using the Test Data set and the full set of

Table 4.7: Estimated number of clusters for Test Data set.

	Compl+SAM		Aver+SAM	
	\hat{c}	<i>Index</i>	\hat{c}	<i>Index</i>
Dunn	8	0.3194	8	0.3194
DB	9	1.7e-16	10	1.53e-16
Kim	8	0.0517	8	0.0636
Mod. Kim	8	0.089	11	0.1412
SD	7	515.4	7	417.3
Mod. SD	6	2.01e3	6	1.5e3
CH	6	46.1	6	46.1

spectral endmembers extracted from the False Leaf image. These experiments are used to select one of these validity indexes to estimate the number of spectral end-member classes within the proposed unsupervised unmixing methodology. In these experiments, only hierarchical clustering algorithms using the complete and average linkages jointly with SAM are used since these were the methods that showed the best performance for spectral endmember class estimation. Most of the validity indexes employ a similarity metric to compute the compactness or separability of the clusters. Then, the same metric used for the clustering is used to calculate the index. Extracted spectral endmember classes and their estimated abundances are used to establish what validity index has the best performance.

4.3.3.1 Results using Test Data

Number of clusters is varied from 2 to 20 for clustering analysis of the Test Data. The seven validity indexes are presented in Figure 4.6. Each plot presents the validity indexes for average and complete linkage with SAM. Table 4.7 summarizes the optimal number of clusters selected for each criterion.

Figure 4.6(a) plots the Dunn's index as a function of the number of clusters. The optimal number of clusters \hat{c} is selected equal to 8 for average and complete linkage

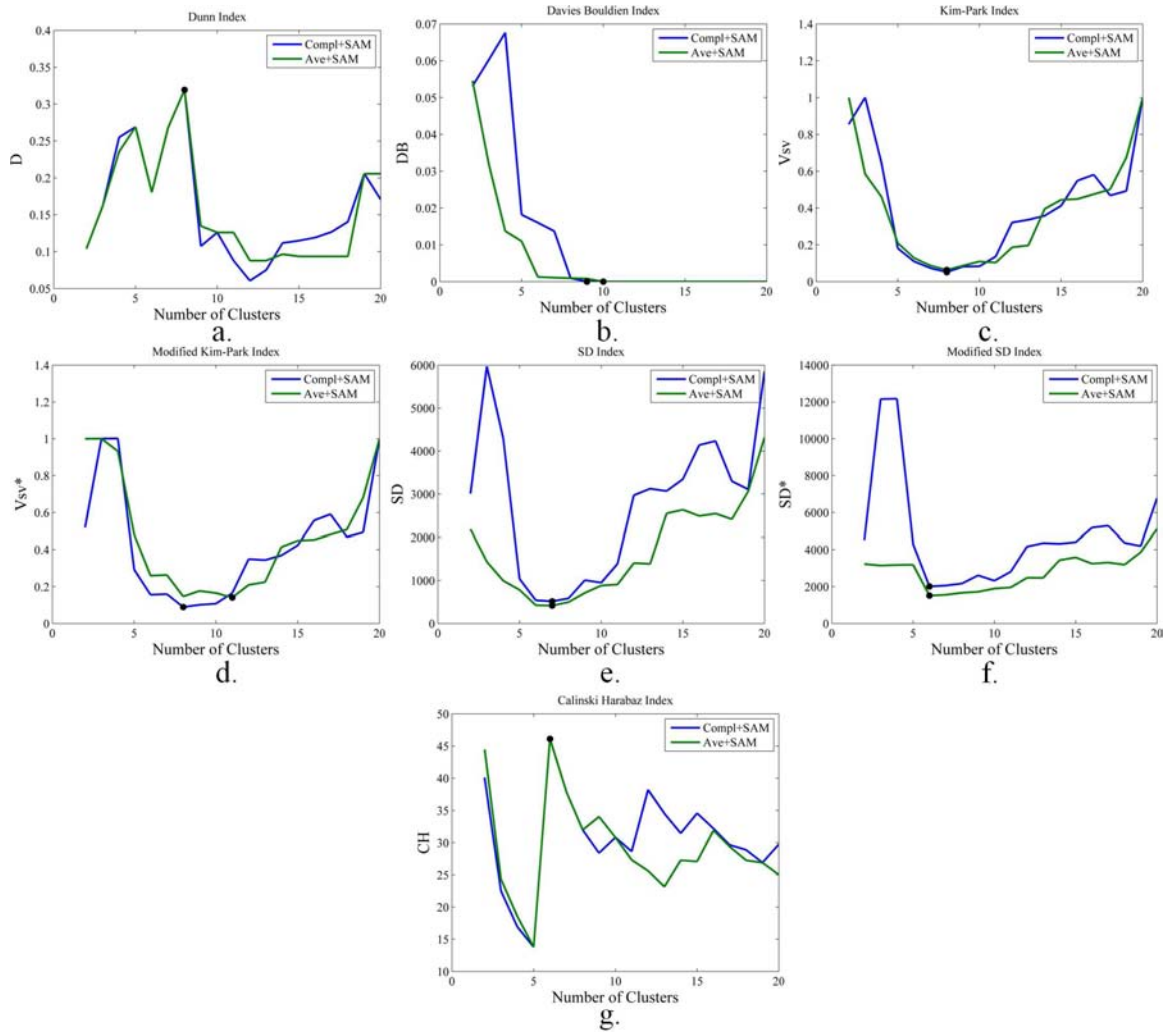


Figure 4.6: Validity indexes for Test Data set. (a) Dunn's, (b) Davies and Bouldin, (c) Kim, (d) modified Kim, (e) modified SD, (f) SD, and (g) CH indexes. Plots show the validity indexes for both clustering configurations: complete and average linkage using SAM.

using SAM. Clusters obtained by average and complete linkages are the same when the number of clusters is between 5 and 8.

Figure 4.6(b) shows the Davies and Bouldin index as a function of the number of clusters. This criterion decreases as the number of clusters increase. As the number of clusters increase unnecessary partitions are created, and the similarity of each cluster with its most similar clusters becomes smaller. Davies and Bouldin index does not present a global minimum. DB forms a L shape curve with respect to the number of clusters. The optimal number of clusters is selected as the end of the break point of the curve. This point is automatically selected as the point where the change of DB is small. A threshold of 0.01 is set for these experiments. The optimal number of clusters estimated by Davies and Bouldien index is 9 and 10 using SAM with and complete and average linkage respectively.

Figures 4.6(c) and 4.6(d) present the plots for the mean-intra cluster distance V_u computed from the Kim and modified Kim indexes respectively. Both graphs are approximately a parabola as described by [31]. \hat{c} from Kim index is 8 for both average and complete linkages. The estimated number of clusters is 8 or 11 according to modified Kim index for complete and average linkages respectively.

Figure 4.6(e) and 4.6(f) show the SD and modified SD indexes. These indexes decrease quickly as the optimum number of clusters is approached and then begin to grow slowly, allowing the identification of a global minimum. This behavior is the results of the compensation between the scattering and total separation terms in the SD index. The scattering, $Scat$, decreases as the number of clusters increases since each cluster becomes more compact. On the other hand, the total separation, Dis increases with the number of clusters because the inverse of the distance between the centroids is used to compute the total separation. The selected optimal number of clusters is 7 for both average and complete linkages for the original SD index. For the modified SD index, the number of clusters is 6.

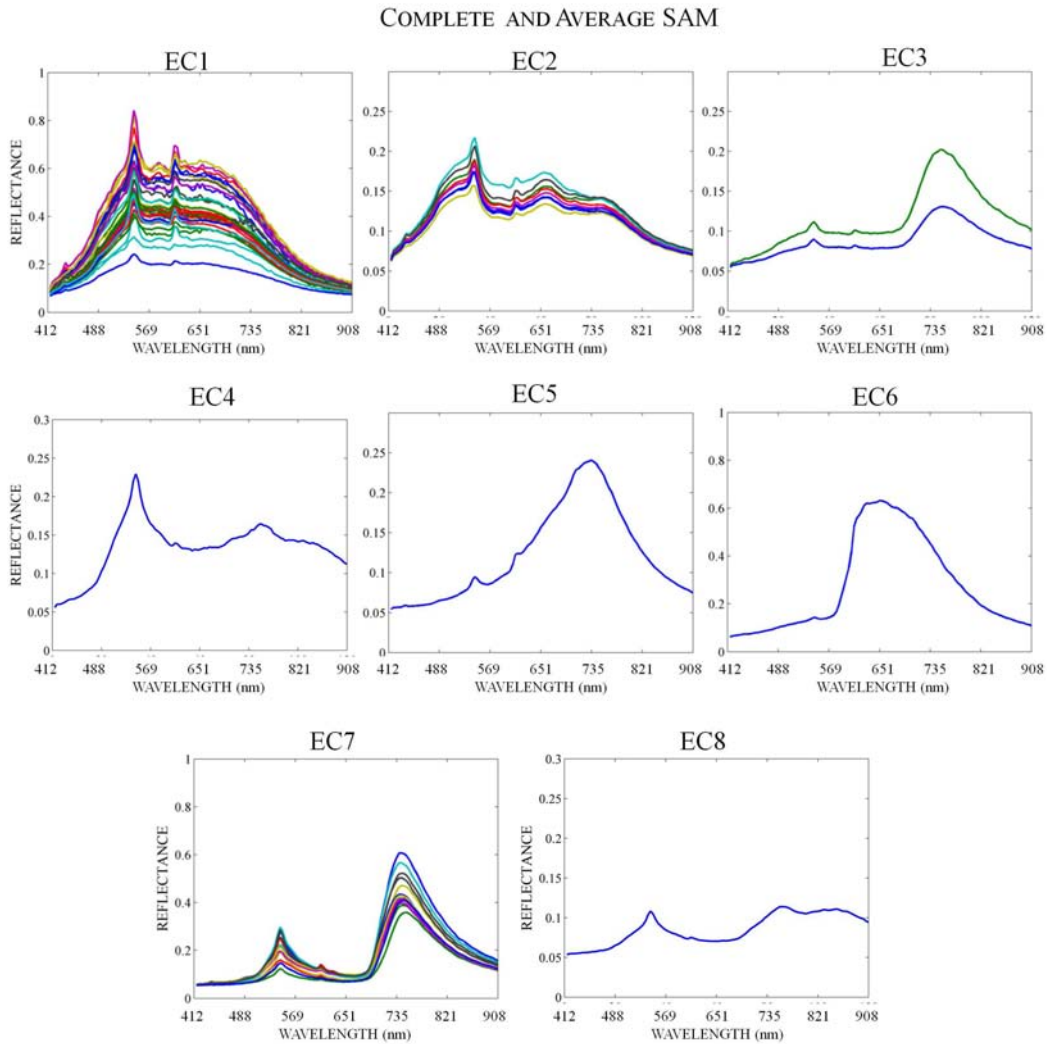


Figure 4.7: Spectral endmember classes for Test Data with $\hat{c} = 8$.

Figure 4.6(g) shows the CH index which presents several local maximums. CH is a measure of the separation among clusters. This index estimates 6 as the optimal number of cluster for both complete and average linkage using SAM.

Only the SD index estimated $\hat{c} = 7$ for the Test Data for both complete and average linkage. Both clustering obtained the same results with one mixed cluster that is presented in the Figure 4.5. Figure 4.7 shows the spectral endmember classes for $\hat{c} = 8$. Similar to the clustering results for $\hat{c} = 7$, average and complete linkage obtained the same results. The mixed cluster obtained with $\hat{c} = 7$ is splitted in two

Table 4.8: Estimated number of clusters for False Leaf image.

	Compl+SAM		Aver+SAM	
	\hat{c}	<i>Index</i>	\hat{c}	<i>Index</i>
Dunn	30	0.076	7	0.053
DB	14	9.12e-4	9	0.0037
Kim	8	0.26	14	0.1795
Mod. Kim	13	0.4631	14	0.2604
SD	4	490	7	424
Mod. SD	8	961	6	904
CH	5	77.36	6	83.28

class (EC₃ and EC₈) for $\hat{c} = 8$. Kim, modified Kim, and Dunn's indexes estimated $\hat{c} = 8$ for the Test Data.

4.3.3.2 Results using False Leaf image

The 146 spectral endmembers selected by the endmember extraction approach based on multiscale representation are used in this next experiment. The number of clusters is varied from 2 to 30. Figure 4.8 presents plots of the different criteria, and Table 4.8 summarizes the selected optimal number of clusters for both average and complete linkage.

It is expected that a higher number of spectral endmember classes is estimated for the full set of spectral endmembers than for the Test Data. Additional spectral endmember classes should include representations for parts of leaves that are not in the Test Data (e.g. small lighted regions) as well as the labels for the camera, the mug, shadows, and others. However, note that in Table 4.8 the number of clusters estimated by SD, modified SD, and CH indexes are less than or equal to 8. Even more, some of those indexes estimated fewer clusters for the False Leaf than for the Test Data such as SD and CH indexes with complete linkage. The significant poor performance of SD, modified SD and CH indexes illustrates the problem of clustering with poorly separated groups. As the False Leaf image has more samples per clusters

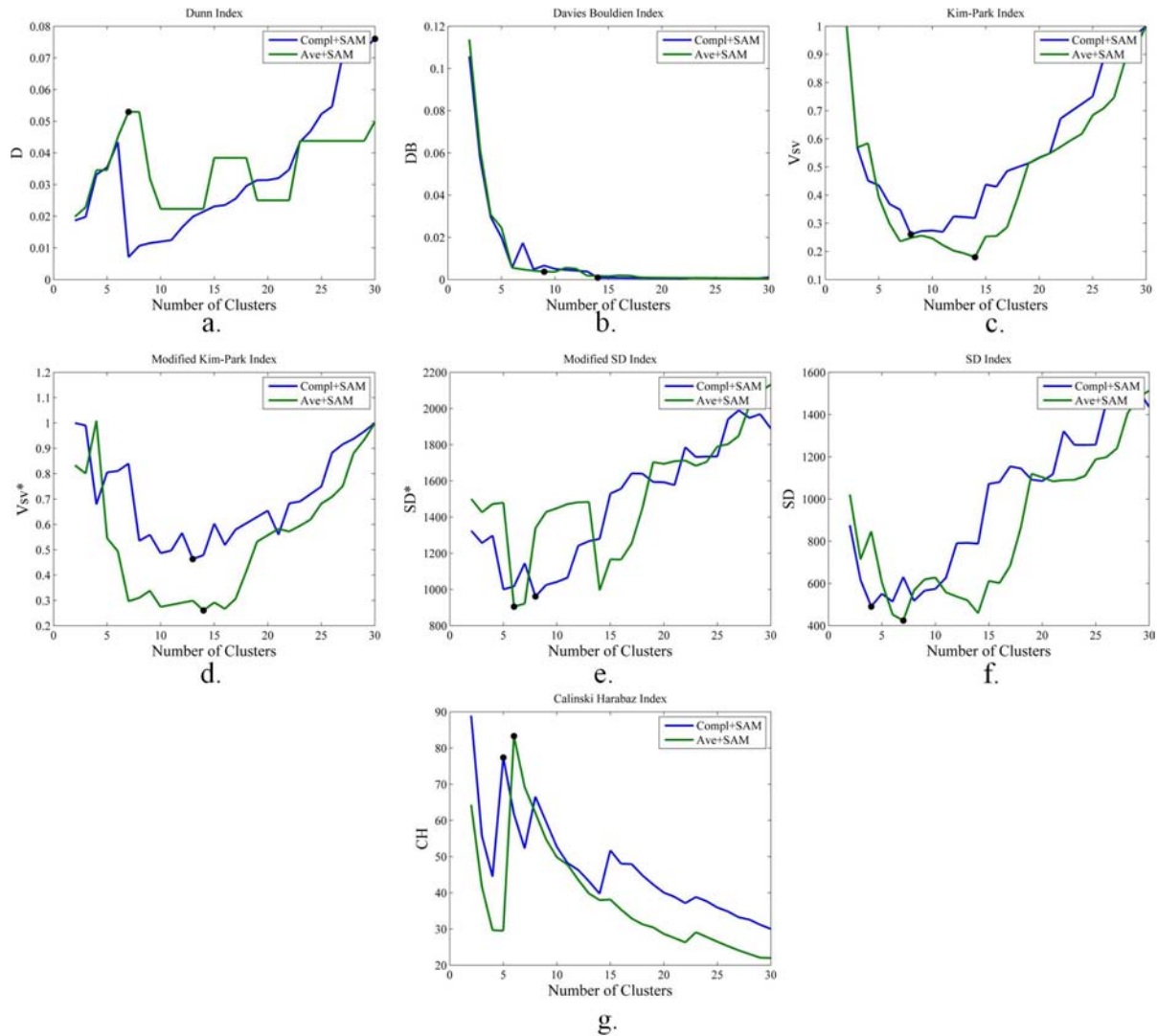


Figure 4.8: Validity indexes for the all spectral endmembers for the False Leaf Image: (a) Dunn's, (b) Davies and Bouldin, (c) Kim, (d) modified Kim, (e) modified SD, (f) SD, and (g) CH indexes. Plots show the validity indexes for both clustering configurations: complete and average linkage using SAM.

than the Test Data, it is expected that the variability of each cluster increases at the same time as the distance among clusters decreases. The modified Kim index (Figure 4.8(d)) estimated 13 and 14 clusters for the False Leaf data using complete and average linkage respectively. On the other hand, Dunn's index estimated 30 and 7 as the optimal number of clusters. But, there are no guarantees that v_D achieves a global maximum in 30 since this is the maximum number of clusters considered in these experiments, and similar to SD and CH indexes, Dunn's index estimated fewer spectral endmember classes for the False Leaf data than for the Test Data when average linkage is used. Finally, the Davies and Bouldin index selects 14 and 9 as the optimal number of clusters using the end of the break point as with the Test Data. The plot of DB shows the behavior expected for this index: decreasing until reaching zero.

Figures 4.9 - 4.12 show the spectral endmember classes obtained by the clustering algorithms with $\hat{c} = 14$, which is the value estimated by Davies and Bouldin for clustering using complete linkage, and by Kim and modified Kim for clustering using average linkage.

Figure 4.9 presents the 14 spectral endmember classes from the clustering results obtained with complete linkage and SAM similarity metric. It is evident that there are some mixed clusters. For example: EC₃, EC₄, EC₈ and EC₉ have spectral signatures that do not correspond to the same spectral endmember classes (see the different shape of spectra in these classes). Also mixed clusters are obtained for the average linkage and SAM as shown in Figure 4.11. EC₃, EC₈ and EC₉ are examples of these mixed clusters. Figures 4.10 and 4.12 present the abundances corresponding to each of the classes. The abundances are computed by adding the individual abundances of the spectral endmembers belonging to the same cluster. In Figures 4.10 and 4.12, it is clear how the spectral endmember class EC₄ from complete linkage mixes part of the false leaf with a part of a real leaf. EC₈ mixes the label of the camera with a shadow in the real leaves. EC₉ mixes other part of the false leaf with the cover

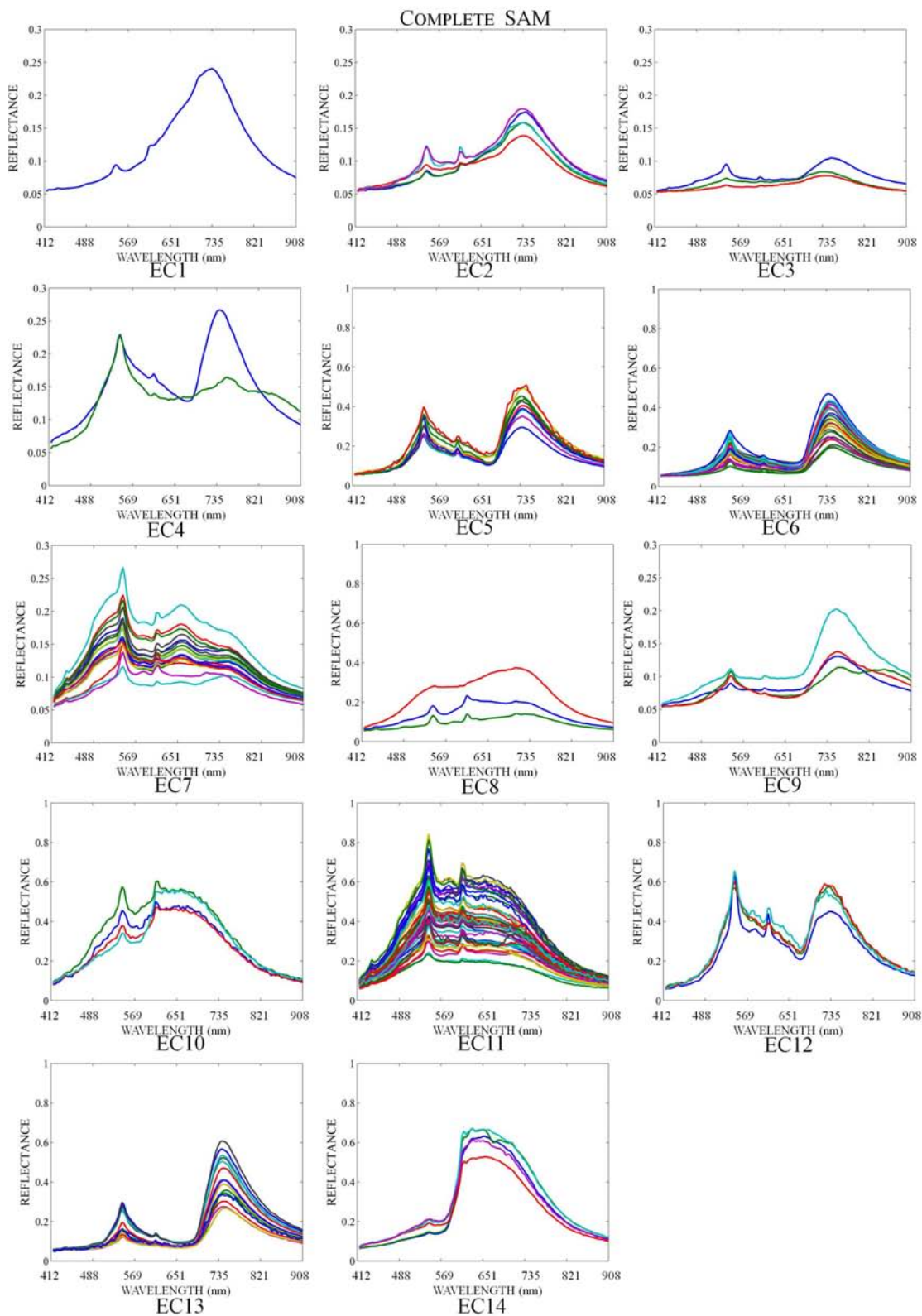


Figure 4.9: Spectral endmember classes for False Leaf image with $\hat{c} = 14$ using complete linkage and SAM.

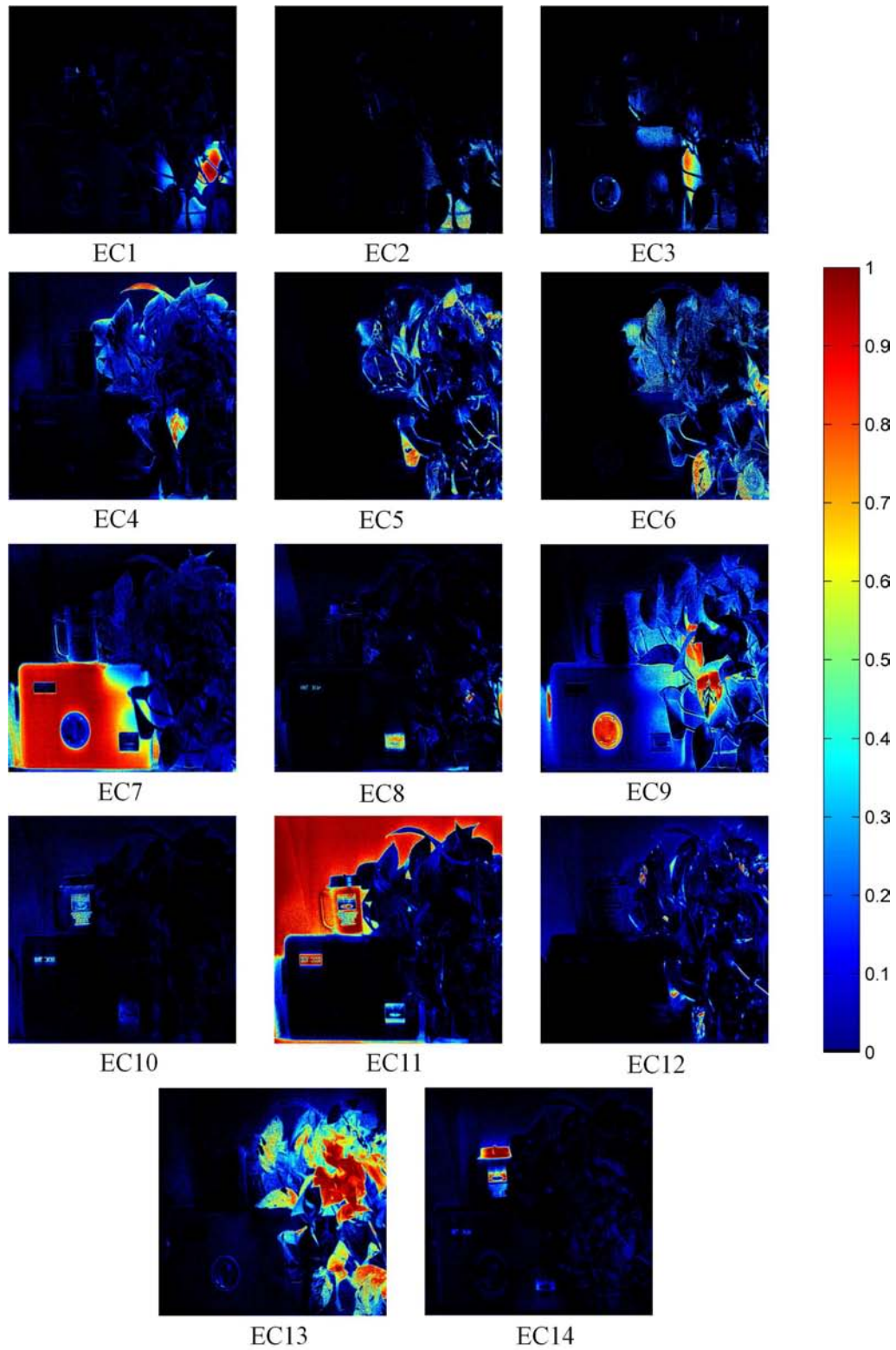


Figure 4.10: Spectral endmember class abundances for False Leaf image with $\hat{c} = 14$ using complete linkage and SAM.

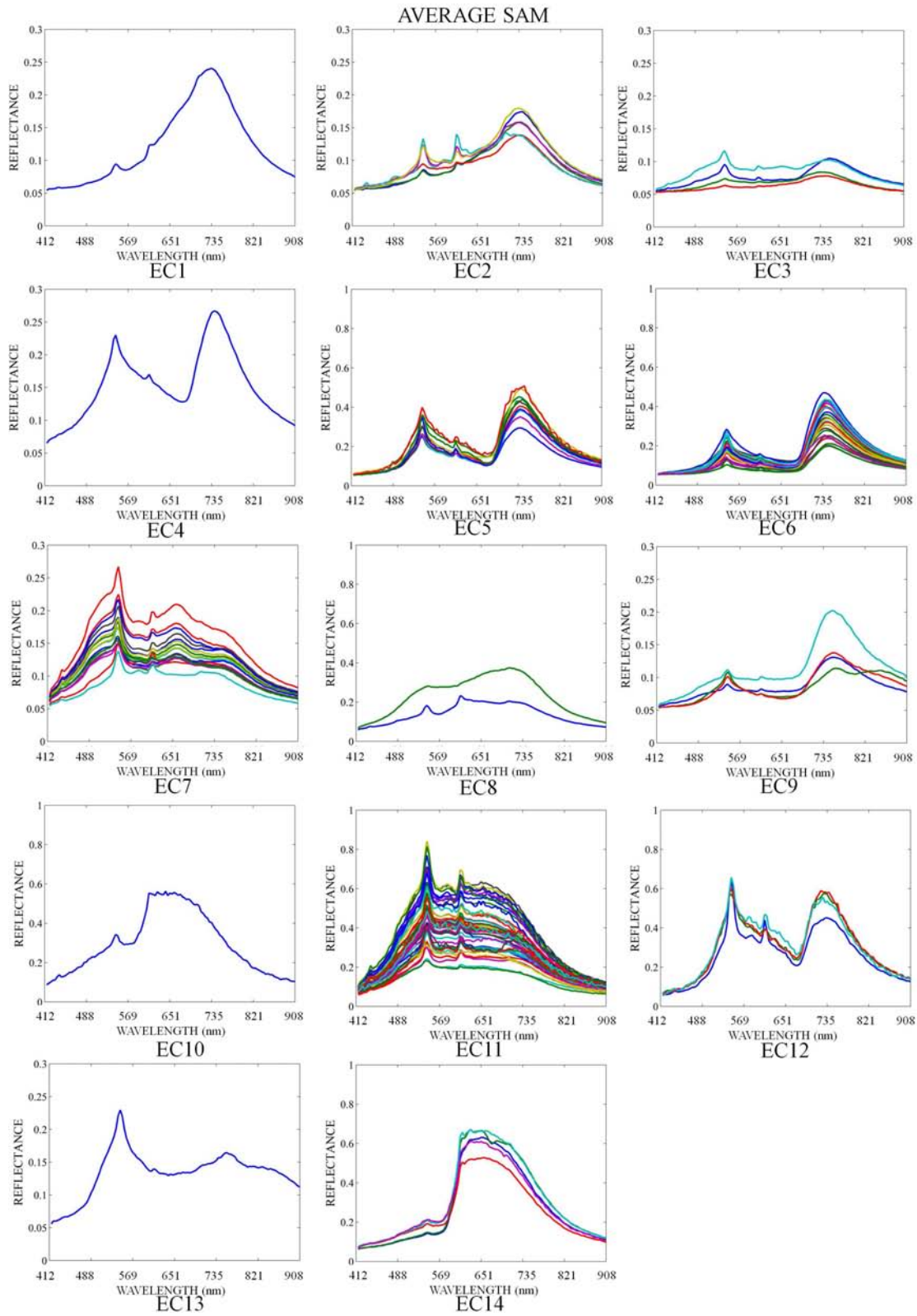


Figure 4.11: Spectral endmember classes for False Leaf image with $\hat{c} = 14$ using average linkage and SAM.

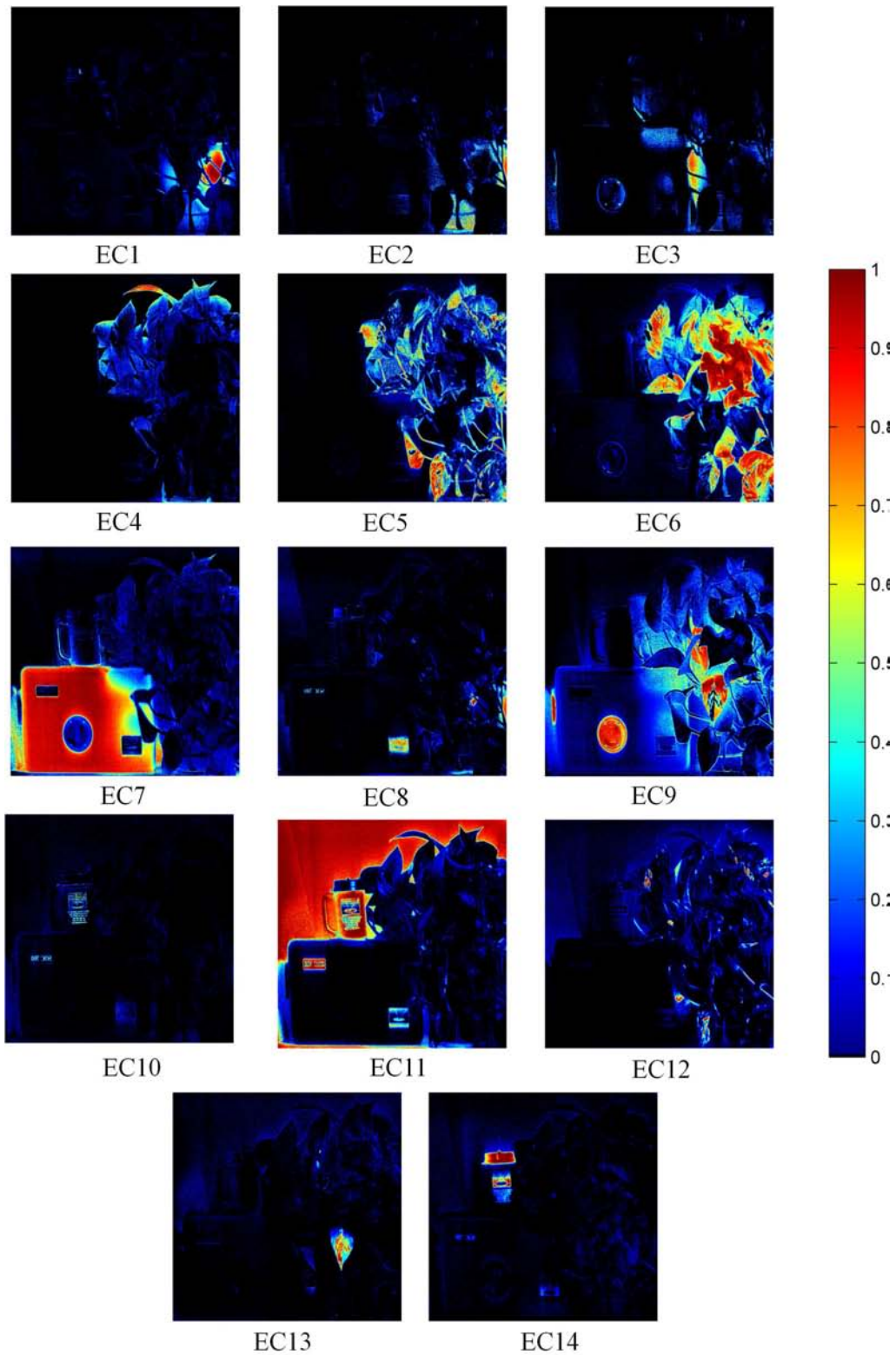


Figure 4.12: Spectral endmember classes abundances for False Leaf image with $\hat{c} = 14$ using average linkage and SAM.

of the camera. However, most of the uniform regions within the False Leaf image have good representation in the spectral endmember classes obtained using $\hat{c} = 14$. For instance, spectral endmember classes EC₁ and EC₂ from both complete and average linkage represent the vase in the False Leaf image. There are several spectral endmember classes related with the real leaves: EC₅, EC₆, and EC₁₂. Even EC₁₂ is the representation of the small and brightest part of leaves. EC₁₀ in both clustering results mixed the labels in the camera and the mug. Complete linkage obtained an additional spectral endmember class for the leaves (EC₁₃) but this clustering mixed the false leaf with some part of the real leaves in EC₄.

4.3.4 Discussion of Results

The comparison between clustering techniques showed that hierarchical techniques perform better than spectral and partitional clustering algorithms. Complete and average linkages were able to extract the seven spectral endmember classes for the Test Data. The results obtained with the full set of spectral endmembers from the False Leaf showed that the hierarchical clustering with average and complete linkage and spectral angle metric are suitable for the extraction of spectral endmember classes.

Validity indexes were compared for the estimation of the number of spectral endmember classes. Dunn, SD, modified SD and CH indexes presented poor results with the False Leaf image. Even some of these indexes estimated fewer spectral endmember classes for the False Leaf image than for the Test Data. Thus, Dunn, SD, modified SD, and CH indexes are not considered furthermore for the estimation of the number of spectral endmember classes. On other hand, Davies and Bouldin, Kim and modified Kim indexes obtained good results for both Test Data and False Leaf.

Test Data is well separated for complete and average linkage using SAM with $\hat{c} = 8$, which is the estimate obtained by Kim and Modified Kim indexes. In the case

of False Leaf, the best clustering result is obtained with $\hat{c} = 14$, which is estimated by Davies and Bouldin using complete linkage and also by Kim and modified Kim indexes for average linkage. For the False Leaf data, complete and average linkage with $\hat{c} = 14$ obtained different spectral endmember classes both with few mixed clusters.

It is interesting to note how the spectral angle measure and the different linkage approaches generated mixed cluster EC8 for the False Leaf image. Despite the noticeable difference of the shape of the spectra, SAM does not allow their discrimination. The cosine distances between the spectral signatures within EC8 of the Figures 4.11 is just 0.0064 being 0 and 1 the minimum and maximum value for SAM. SAM is the distance most used for hyperspectral data since it compares spectral shapes. In the comparison among different clustering configuration, those that used SAM and hierarchical clustering presented the best performance. However, this metric is not always able to differentiate the spectra although they are so different such as in the spectral endmember class EC8.

The spectral endmember classes obtained using clustering represent the different components in the image. Note that these classes are extracted automatically based on the spectral similarity. However, the assignation of labels that related the spectral endmember classes with known materials requires the interpretation and analysis of experts. The developed unsupervised unmixing approach is a tool that automatically extracts information from the hyperspectral image, and these results require of analysts to bring the information to a higher level of abstraction.

4.4 SUMMARY

Spectral endmembers extracted by the proposed approach are grouped into spectral endmember classes allowing a better representation of the distinct components of

the hyperspectral image. Clustering algorithms were compared in this chapter to select the appropriate methods for spectral endmember class extraction.

Hierarchical, partitional, and spectral clustering were compared using a test data set generated from the spectral endmembers extracted from the False Leaf image. Hierarchical clustering with complete and average linkage outperforms partitional and spectral clustering results. Different distances were employed obtaining the best results with the spectral angle measure.

Complete and average linkage were used in the comparison of validity indexes for estimation of the number of spectral endmember classes. Validity indexes are metrics that allow the comparison of different configuration of clustering. Davies and Bouldin, Kim and the modified Kim indexes presented the best results for the estimation of the number of spectral endmember classes in the data used.

Additional experiments are conducted in Chapter 6 with hyperspectral imagery from more complex scenarios where Davies and Bouldin, Kim and modified Kim indexes are compared as well as average and complete linkage. Davies and Bouldin index shows consistent results for those images used in Chapter 6, especially for clustering obtained by complete linkage.

The simulation of the different conditions present in real hyperspectral images is a very difficult task. Spectral variability, topographic and atmospheric effects, noise, and spatial complexity are some of the phenomena that affect real hyperspectral images. Most of the synthetic data used in published work consist of data point clouds generated randomly (e.g. [34, 48, 49, 42]). In this synthetic data, parameters such as abundances, noise level, and number of endmembers are controlled. But, these dataset do not include spatial complexity. Since the proposed approach takes advantage of spatial information, it is necessary to generate synthetic data with spatial distribution. Some spatial-spectral approaches had used synthetic data generated with simple spatial distributions with rectangular regions (e.g. [9, 16, 15]). Other works used complex synthetic data generated using fractals (e.g. [17, 99]). In this work, two sets of synthetic data are generated for the quantitative assessment of the unmixing approach based on multiscale representation. The first set is an image with a simple spatial distribution that consists of a grid arrangement of different materials with a very small spatial complexity. However, this dataset allows the control of noise and spectral variability. The second set simulates the spatial complexity in a scene based on abundances extracted from real data. The following section presents the details about the generation of the synthetic data and the metrics used in the assessment. Then, the unmixing results for the two sets of images are presented. A comparison with SMACC, VCA, and RBSPP unmixing techniques is also included.

5.1 SYNTHETIC DATA SETS

The first data set (Synthetic Data *I*) was built using a grid arrangement of four materials using signatures from the USGS spectral library¹. These spectra and the grid arrangement are shown in Figure 5.1. Square regions of 47 × 47 pixels for each material are generated. A scale parameter γ multiplies the spectral signature of each pixel to generate spectral variability. The scale parameters γ are randomly generated with a Beta distribution with parameters [10, 1]. The generated image had 188 × 188 pixels with 224 spectral bands. An average mask was passed through the image without overlapping to generate mixed pixels. The final image had 46 × 46 pixels. Gaussian distributed uncorrelated noise was added to the final image producing signal to noise ratios (SNR) of 50 db, 40db, and 30 db. The SNR was calculated by the expression [34]:

$$SNR \equiv 10 \log_{10} \frac{E[\mathbf{Y}^T \mathbf{Y}]}{E[\mathbf{n}^T \mathbf{n}]} \quad (5.1)$$

where \mathbf{Y} is the noise-free image and \mathbf{n} is the noise. RGB compositions for the original and final images are shown in Figure 5.1. Bands 185 (2120 nm), 195 (2220 nm), and 205 (2319 nm) were used in those RGB compositions.

The second data set seeks to simulate the spatial complexity of real hyperspectral images. For that, abundance maps extracted from real hyperspectral images are used to generate the synthetic data. Abundance maps preserve the spatial distribution of the materials. Generating data from these maps preserve the spatial features and at the same time that endmembers and abundances are known. Abundances extracted from the A.P. Hill AVIRIS image (see Chapter 6) are used to build three images. Two images are generated using spectra from the USGS spectral library using 125 spectral bands from the 1280 nm to 2500 nm with 7 (Synthetic Data *II*, Figure 5.2)

¹ <http://speclab.cr.usgs.gov/spectral-lib.html>

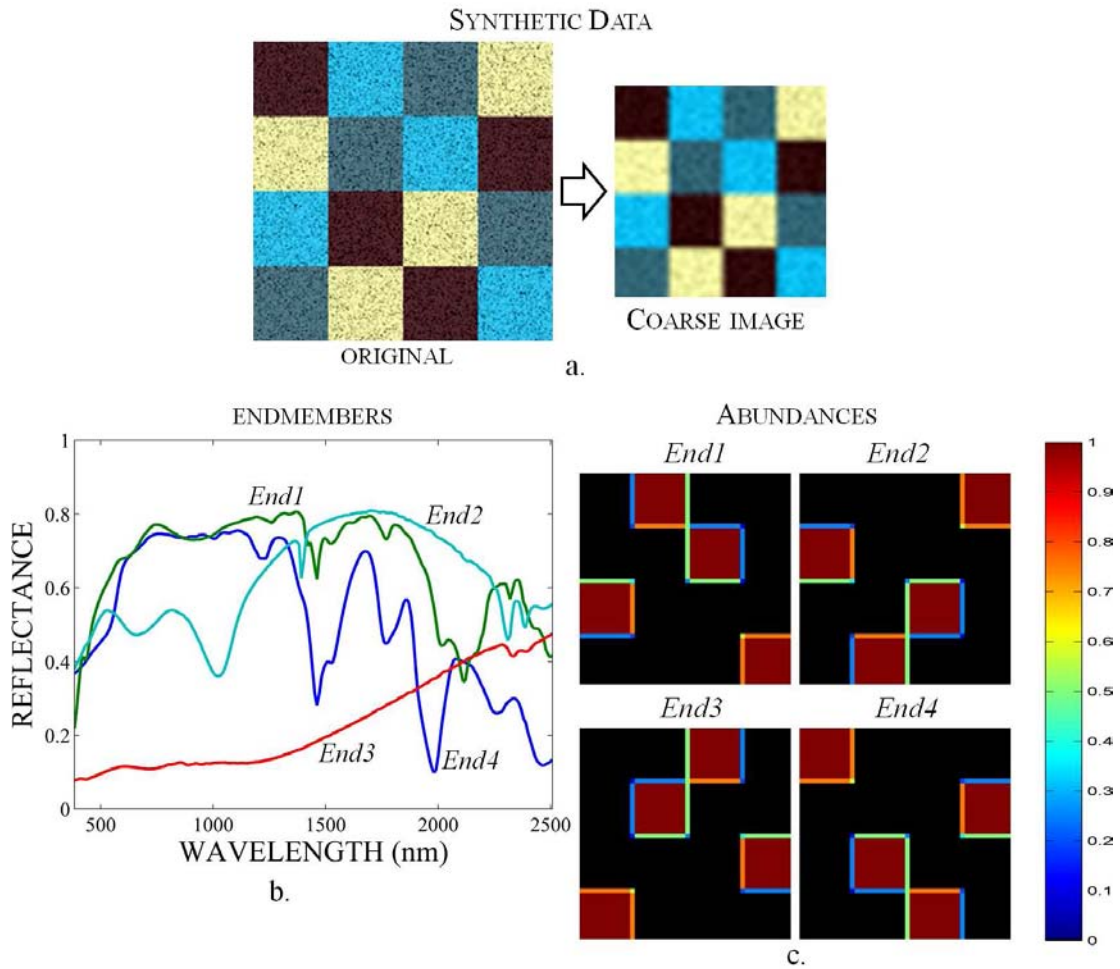


Figure 5.1: Synthetic Data I with a grid arrangement of four materials. (a) RGB composition using 185 (2120 nm), 195 (2220 nm) and 205 (2319 nm) bands. (b) Spectral signatures for the selected endmembers. (c) Abundances for each endmember.

and 8 (Synthetic Data *III*, Figure 5.3) endmembers, respectively. Both images, *II* and *III*, have 201×201 pixels and correspond to different regions of the A.P. Hill image (see Chapter 6). The linear mixing model in Equation 2.2 was used to generate the synthetic data. RGB compositions for both images are shown in Figures 5.2 and 5.3. Figure 5.4 presents the sum of abundances for each image. Notice that the abundances used to generate the synthetic data satisfy a less than or equal to one constraint. The minimum abundances are 0.4326, and 0.3450 for Synthetic Data *II* and *III*, respectively. This is a way to include topographic effects in synthetic data.

5.2 ASSESSMENT METRICS

Experiments presented in this chapter try to assess the accuracy of the abundances estimated by the proposed approach as well as to compare the extracted spectral endmembers with the spectra used to generate the data. The accuracy in the abundance estimation is measured using the mean square error (*mse*):

$$mse(\hat{\mathbf{A}}) = \frac{\sum (a_i - \hat{a}_i)^2}{m} \quad (5.2)$$

where m is the number of pixels, a_i is the known abundances, and \hat{a}_i is the estimated abundance in the i th pixel. The standard deviation of the error, $\sigma_{se}(\hat{\mathbf{A}})$, is also computed.

The accuracy in the abundance estimation is also measured by the relative error norm given by:

$$e(\hat{\mathbf{A}}) = \frac{\|\mathbf{A} - \hat{\mathbf{A}}\|}{\|\mathbf{A}\|} \times 100\% \quad (5.3)$$

where $\| \cdot \|$ is the Frobenious norm.

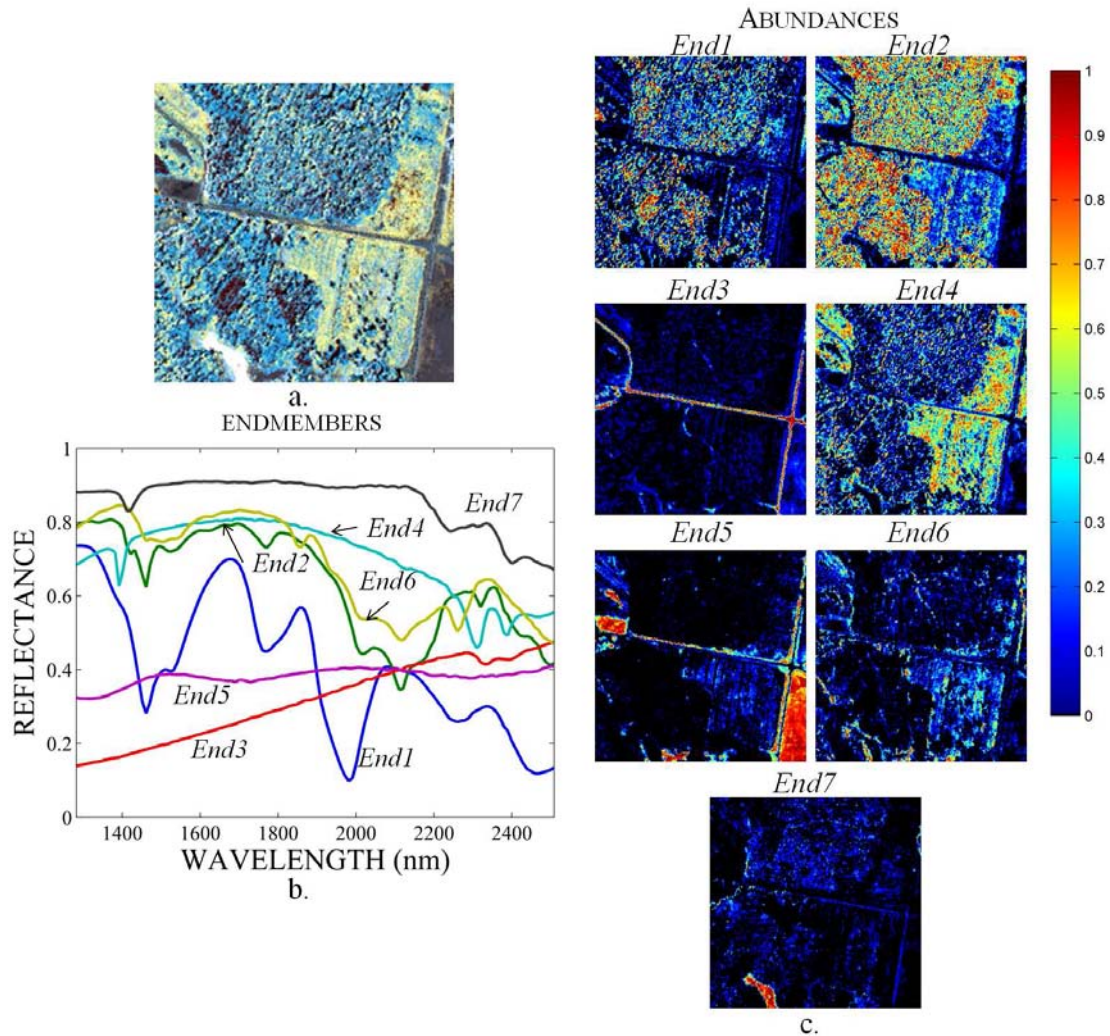


Figure 5.2: Synthetic Data II with 7 endmembers and abundances from real data. a. RGB composition using 185 (2120 nm), 195 (2220 nm) and 205 (2319 nm) bands. b. Spectral signatures for the selected endmembers. c. Abundances for each end-member.

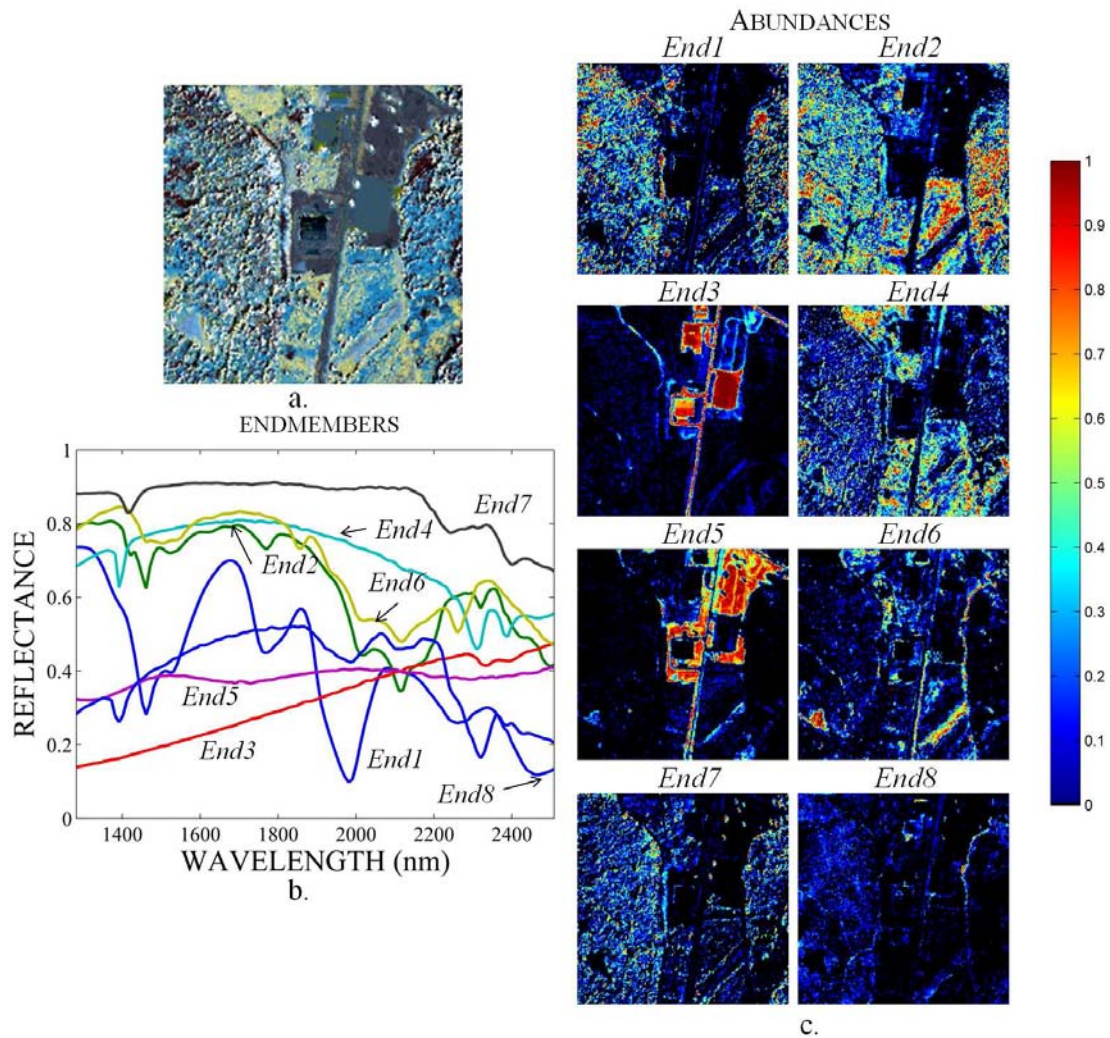


Figure 5.3: Synthetic Data III with 8 endmembers and abundances from real data. a. RGB composition using 185 (2120 nm), 195 (2220 nm) and 205 (2319 nm) bands. b. Spectral signatures for the selected endmembers. c. Abundances for each end-member.

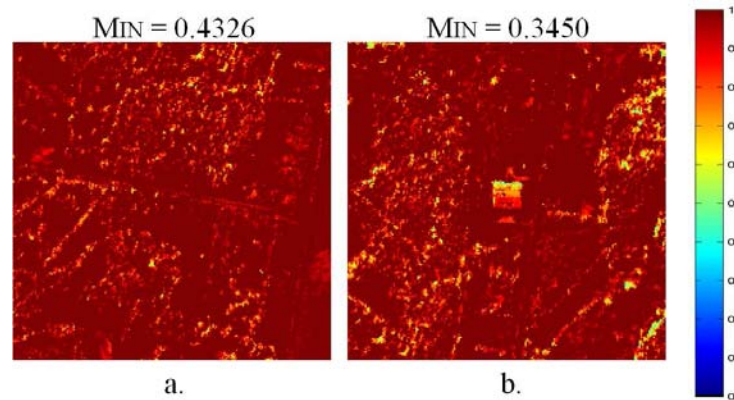


Figure 5.4: Sum of abundances used for Synthetic Data: (a) II, and (b) III.

The extracted spectral endmembers are compared with the original spectral using the spectral angle distance (see Table 4.1). The mean and standard deviation for SAM distance are computed for the different spectra that belong to the same spectral endmember class.

5.3 UNMIXING ANALYSIS OF SYNTHETIC DATA

The experiment with the synthetic data is divided in two parts. The first part studies the effects of noise in the abundance estimation and endmember extraction using the synthetic data with the grid configuration. In the second part of these experiments, the synthetic data generated from abundances of real imagery are employed to assess the proposed approach. A comparison of unmixing results obtained by the proposed approach and the results from SMACC, VCA, and RBSPP are included in both simulation studies.

5.3.1 *Experiments with Grid Synthetic Data*

The first experiment with Synthetic Data *I* consists of the comparison of unmixing results for different noise levels. Gaussian noise was added to Synthetic Data *I* such that SNR = 50 dB, 40 dB, and 30 dB are obtained. The proposed approach was used to perform the unmixing analysis of Synthetic Data *I* fixing the diffusion parameter $\alpha = 0.01$ and the maximum number of spectral endmember classes to 20. Table 5.1 presents the mean square errors ($mse(\hat{\mathbf{A}})$) and the standard deviation ($\sigma_{se}(\hat{\mathbf{A}})$) calculated for the estimated abundance from the unmixing of Synthetic Data *I* with different noise levels after 10 repetitions of the experiment. The mean square errors obtained for the image with noise are larger than the obtained with the noise-free image as expected. Similar errors for the estimated abundances were obtained at

Table 5.1: Mean square errors (standard deviations) for the estimate abundance from Synthetic Data I.

	<i>end1</i>	<i>end2</i>	<i>end3</i>	<i>end4</i>	average
noise-free	0.0007 (0.0036)	0.0003 (0.0015)	0.0005 (0.0035)	0.0002 (0.0009)	0.0004
50 db	0.0031 (0.0301)	0.0019 (0.0181)	0.0019 (0.0182)	0.0009 (0.0083)	0.0020
40 db	0.0020 (0.0215)	0.0013 (0.0142)	0.0017 (0.0215)	0.0010 (0.0119)	0.0015
30 db	0.0021 (0.0278)	0.0010 (0.0132)	0.0015 (0.0178)	0.0009 (0.0114)	0.0014

different noise levels. For instance, the mean square error for the abundance of *end1* is 0.0007 for the noise-free image and between 0.0020 and 0.0031 for the three noise levels. The mean square error is of 0.0002 for the abundance of *end4* for the noise-free image and this error is up to 0.0010 for the noise image. Table 5.1 also includes the average of the mean square error obtained from the different abundances. In this average, it can also be noted that the relative error was similar for all noise levels. For the noise-free image, the average *mse* was 0.0004. In the case of noise images, the average *mse* were 0.0020, 0.0015, and 0.0014 for the 50 db, 40 db, and 30 db cases respectively. The difference between of *mse* from the noise-free and noise images are small. However, it can be noted in Table 5.1 that the standard deviation of this error increased in the case of noisy images.

Table 5.2 presents a comparison of the relative error calculated using Equation 5.3. For the noise-free image, an average error of 4.42% was obtained for all abundances. The average errors for the estimated abundances from the noisy images were of 7.94% in the case of 50 db and 7.27% in both 40 db and 30 db. Figure 5.5 shows an example of the estimated abundances for each endmember and noise level. In this figure, it can be noted the effect of the noise as a small estimated abundance (up to 10%) in regions with zero abundances. These small abundance (blue pixels) increased with the noise level.

The spectra angle distance between the estimated and original endmembers are presented in the Table 5.3. These distances correspond to the average of the distances

Table 5.2: Relative error (%) for the estimate abundance from Synthetic Data I.

	<i>end1</i>	<i>end2</i>	<i>end3</i>	<i>end4</i>	average
noise-free	5.62	3.98	4.75	3.32	4.42
50 db	11.22	6.76	8.65	5.12	7.94
40 db	7.66	7.94	7.94	6.33	7.27
30 db	9.11	6.36	7.64	5.97	7.27

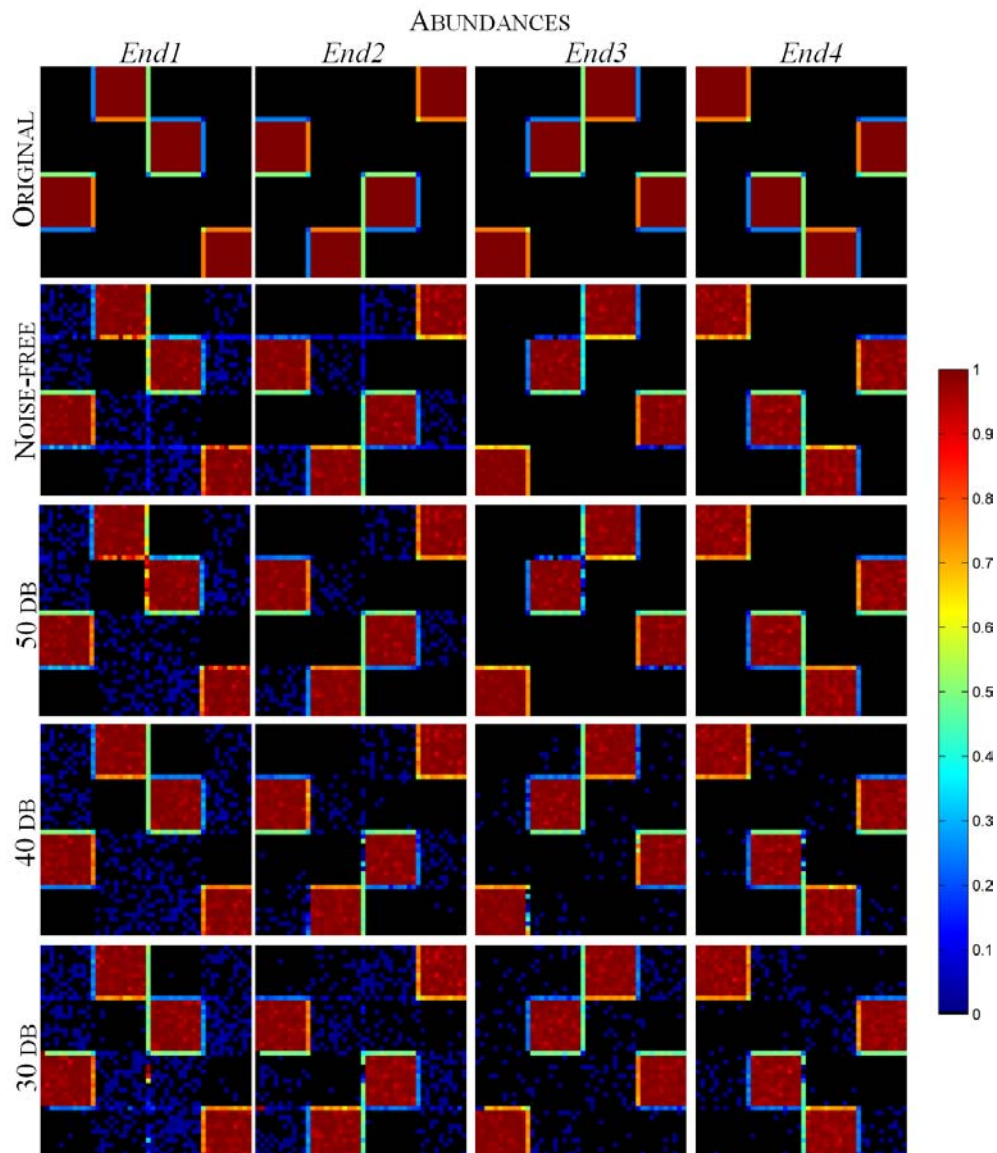


Figure 5.5: Abundances estimated from Synthetic Data I at different noise levels.

Table 5.3: SAM (σ) for the extracted spectral endmembers and original endmembers for Synthetic Data I.

	end_1	end_2	end_3	end_4	average
noise-free	0.0016 (0.0030)	0.0031 (0.0067)	0.0016 (0.0030)	0.0000 (0.0000)	0.0016
50 dB	0.0012 (0.0024)	0.0012 (0.0029)	0.0011 (0.0024)	0.0012 (0.0029)	0.0012
40 dB	0.0013 (0.0024)	0.0013 (0.0023)	0.0013 (0.0024)	0.0012 (0.0021)	0.0013
30 dB	0.0020 (0.0030)	0.0020 (0.0035)	0.0019 (0.0028)	0.0019 (0.0034)	0.0020

to each spectral endmembers belonging to the same spectral endmember class and the original endmembers. The variances are also included in the Table 5.3, and it can be seen as a measure of the spectral variability obtained for each spectral endmember class. Note that the spectral angle distance, as defined in Table 4.1, has a maximum value of 1 (i.e. very distinct spectra) and a minimum value of 0 (i.e. very similar spectra). All obtained distances are less than or equal to 0.0020. The obtained standard deviation are in the same order as the mean with values up to 0.0067. Examples of spectral signatures are shown in Figure 5.6. Note that the obtained spectra are not noisy even for the image with a SNR of 30 dB. This is a result of the smoothing operations used for building the multiscale representation. Most of the noise is removed by the nonlinear diffusion filtering, and the effects of noise in the unmixing analysis are then reduced. In Figure 5.6, it can be noted that an additional spectrum is extracted from the image (a mixed signature) in the case of 30 dB.

The second experiment with Synthetic Data I consists of the comparison of unmixing results obtained by the proposed approach and SMACC, VCA, and RBSPP algorithms. Synthetic Data I with a SNR = 30 dB was used in this experiment. Similarly to the first experiment, the unmixing analysis was repeated 10 times, and each time Gaussian noise was added to Synthetic Data I.

Tables 5.4 and 5.5 summarize the mean square errors and the relative errors computed from the estimated abundances and original abundances. The smallest abun-

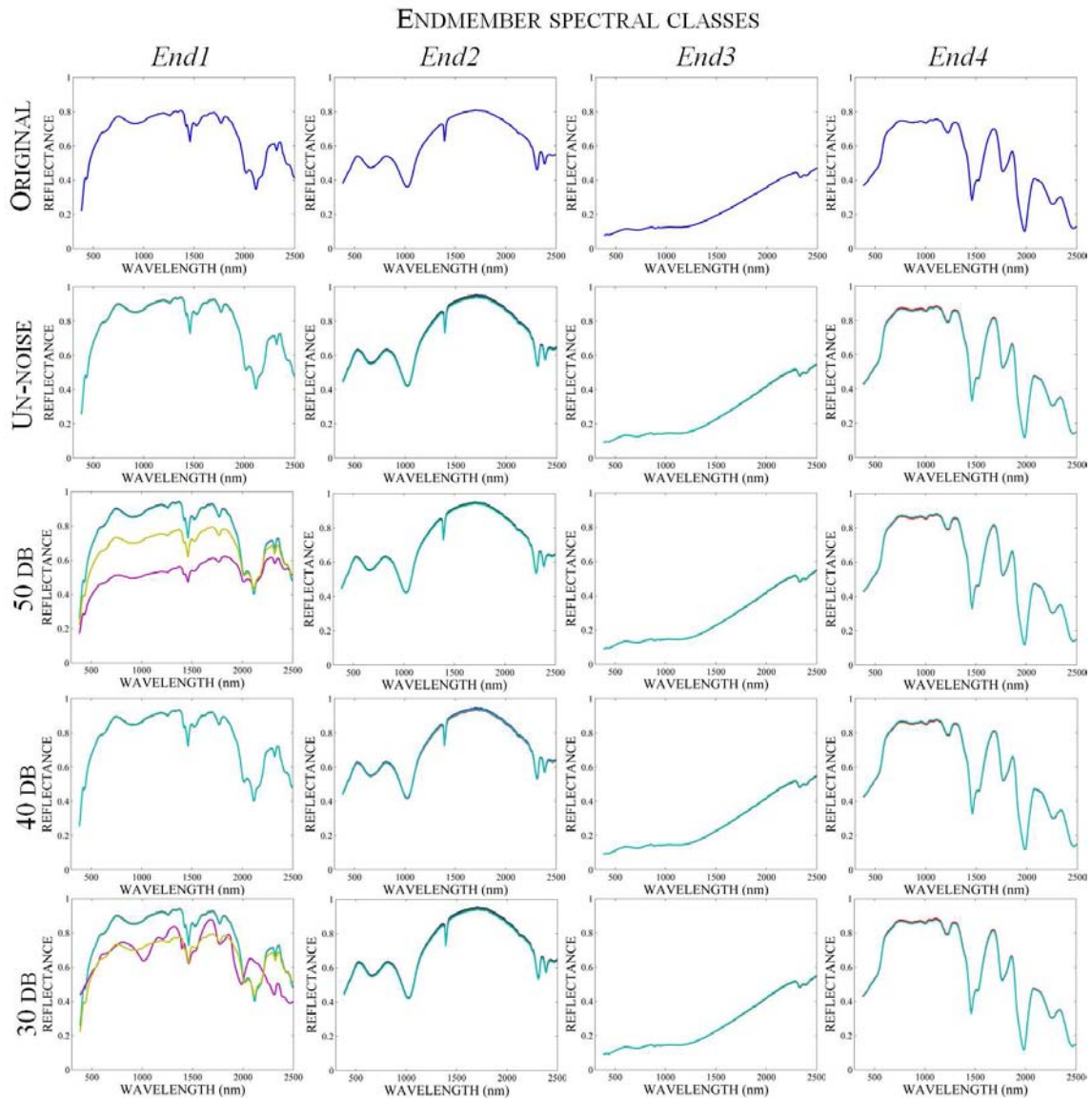


Figure 5.6: Spectral endmember classes extracted from Synthetic Data *I* at different noise levels.

Table 5.4: Mean square errors (standard deviations) for the estimate abundance from Synthetic Data *I* using the proposed approach, SMACC, VCA, and RBSPP.

	<i>end1</i>	<i>end2</i>	<i>end3</i>	<i>end4</i>	average
Proposed App.	0.0021 (0.0278)	0.0010 (0.0132)	0.0015 (0.0178)	0.0009 (0.0114)	0.0014
SMACC	0.0023 (0.0045)	0.0013 (0.0026)	0.0017 (0.0035)	0.0013 (0.0025)	0.0033
VCA	0.0015 (0.0030)	0.0007 (0.0014)	0.0004 (0.0009)	0.0009 (0.0019)	0.0008
RBSPP	0.0009 (0.0022)	0.0006 (0.0014)	0.0003 (0.0007)	0.0006 (0.0014)	0.0006

Table 5.5: Relative error (%) for the estimate abundance from Synthetic Data *I* using the proposed approach, SMACC, VCA, and RBSPP.

	<i>end1</i>	<i>end2</i>	<i>end3</i>	<i>end4</i>	average
Proposed App.	9.11	6.36	7.64	5.97	7.27
SMACC	9.80	7.39	8.57	7.38	8.28
VCA	7.39	5.42	4.05	5.72	5.64
RBSPP	5.95	4.98	3.52	4.93	4.85

dance errors were obtained by the RBSPP algorithm combined with VCA. The mean square error for the estimated abundances by this algorithm was 0.0006, and the relative error was 4.85%. The proposed approach obtained a mean square error of 0.0014 and a relative error of 7.27%. SMACC and VCA obtained relative errors of 8.28% and 5.64%, respectively. Although the mean square errors obtained for the proposed approach are comparable with the errors obtained by the other techniques, it can be noted in the Table 5.4 that the proposed approach obtained the highest standard deviations for the square errors indicating that larger errors are obtained in some pixels by the proposed approach.

Table 5.6 shows the spectral angle distances between the extracted endmembers and the original endmembers. The smallest distances were obtained by the proposed approach. The average for the spectral angle distances was 0.0020 for the proposed approach in comparison with the 0.2631, 0.2318, and 0.2648 obtained for SMACC, VCA, and RBSPP, respectively. The smaller spectral angle distances obtained for the proposed approach can be due to the reduction of the noise by the smoothing oper-

Table 5.6: SAM for the extracted spectral endmembers and original endmembers for Synthetic Data I.

	<i>end1</i>	<i>end2</i>	<i>end3</i>	<i>end4</i>	average
Proposed App.	0.0020	0.0020	0.0019	0.0019	0.0020
SMACC	0.3154	0.2274	0.2193	0.2903	0.2631
VCA	0.2272	0.2087	0.2388	0.2524	0.2318
RBSPP	0.2325	0.2170	0.2556	0.2803	0.2464

ation, and the integration of the spectral variability. SMACC does not perform any processing over the spectra obtaining noisy signatures. VCA performs a projection where noise is also filtered.

5.3.2 Experiments with Synthetic Data Including Spatial Complexity

This experiment aims at identifying the advantages and limitations of the proposed approach. For that, Synthetic Data II and III include spatially uniform regions as well as small regions with significant topographic effects. Although Synthetic Data II and III include more complex spatial distribution than the previous experiments, this image did not include spectral variability on the endmembers. Results included in this section use the synthetic data without noise. For each image, unmixing also was done using SMACC, VCA, and RBSPP. The diffusion parameter was fixed in 0.007 and the maximum number of spectral endmember classes is set to 20 for the proposed approach.

Table 5.7 presents the estimated number of spectral endmember classes by the proposed approach for both Synthetic Data II and III. Table 5.7 also includes the estimated number of endmembers by HySIME [55], and the estimated ranks for the covariance and correlation matrices (see Section 2.5). HySIME estimated 7 endmembers for Synthetic Data II and 8 endmembers for Synthetic Data III. The ranks of covariance (K) and correlation (R) matrices were 3 for Synthetic Data II. For

Table 5.7: Comparison of estimated number of endmembers for Synthetic Data *II* and *III*.

	HySIME	Rank(K)	Rank(R)	End. Classes
Synthetic Data II	7	3	3	13
Synthetic Data III	8	6	4	13

Synthetic Data *III*, the rank of the covariance (K) was 6 and for the correlation (R) was 4. The proposed approach estimated 13 spectral endmember classes for both synthetic data sets.

Figure 5.7 presents the abundances estimated from Synthetic Data *II* by the proposed approach, SMACC, VCA, and RBSPP algorithms. The corresponding endmembers are shown in Figure 5.8. Figure 5.9 shows the six additional spectral endmember classes extracted by the multiscale approach. It can be seen in Figure 5.9 that *End8*, *End9*, *End10*, and *End12* appear to be additional partitions of endmember *End1* (see Figure 5.8). In addition, *End11* and *End13* are related with the endmembers *End3* and *End5*, respectively. These additional partitions are the results of the clustering algorithm (i.e. hierarchical algorithm with complete linkage) employed in the proposed approach. Despite the additional spectral endmember classes, it can be seen in Figure 5.7 that the proposed approach resolved the spatial distribution of most materials in the image. Endmembers *End1*, *End4*, *End5*, and *End7* are the best estimated by the proposed approach.

Table 5.8 summarize the mean square errors for the estimated abundances and Table 5.9 shows the spectral angle distances for the extracted endmembers. The proposed approach extracted *End6* with an average spectral angle distance of 0.0014. But, the estimated abundance for this endmember had a mean square error as high as 0.0618. The abundances for endmembers *End1*, *End4*, *End5*, and *End7* had errors of 0.0097, 0.0058, 0.0262, and 0.0102, respectively. Their corresponding spectral angle distances were 0.0011, 0.0018, 0.0012, and 0.0011. Table 5.9 also includes the standard deviations for each spectral endmember class. The spectral endmember classes

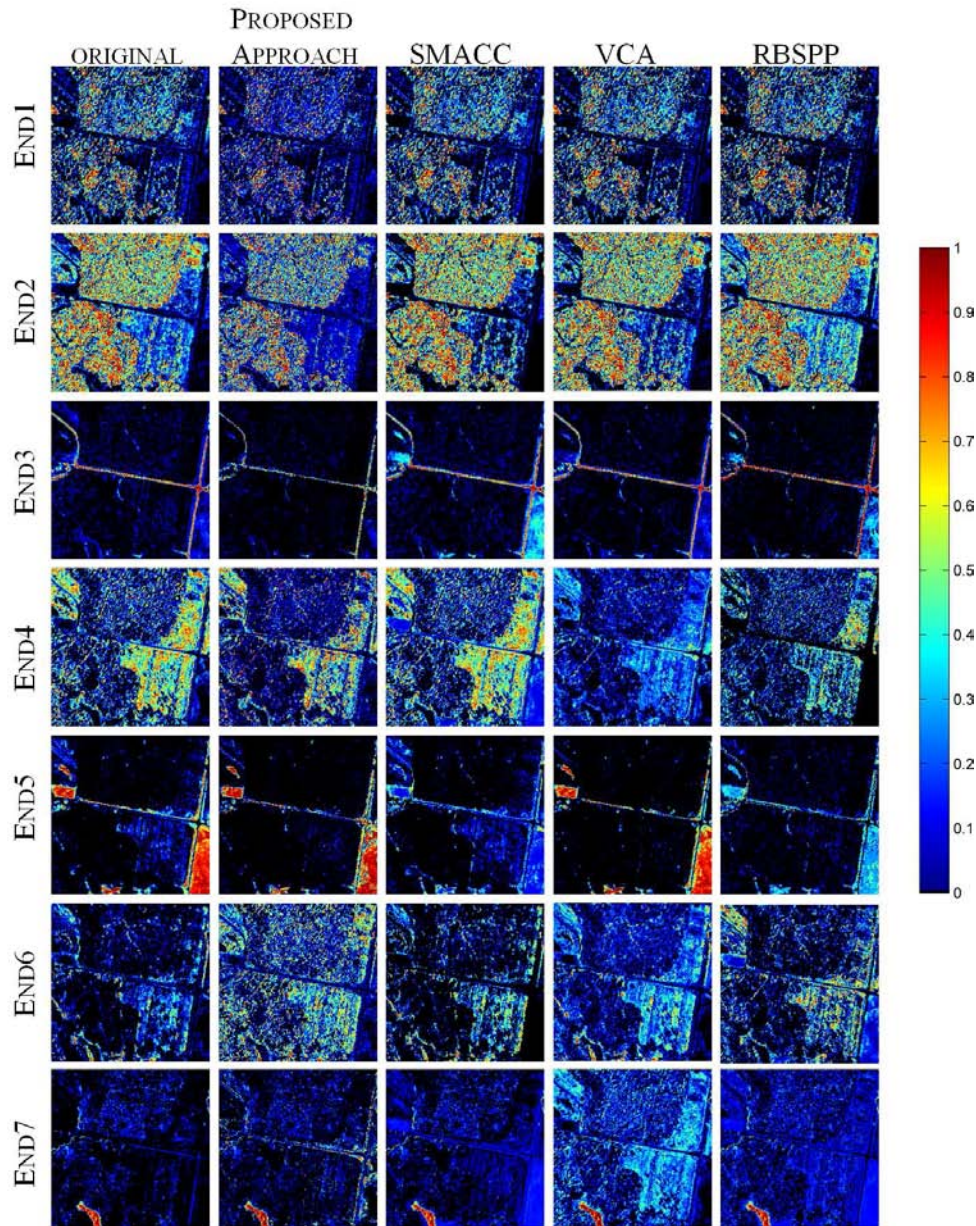


Figure 5.7: Estimated abundances for Synthetic Data II.

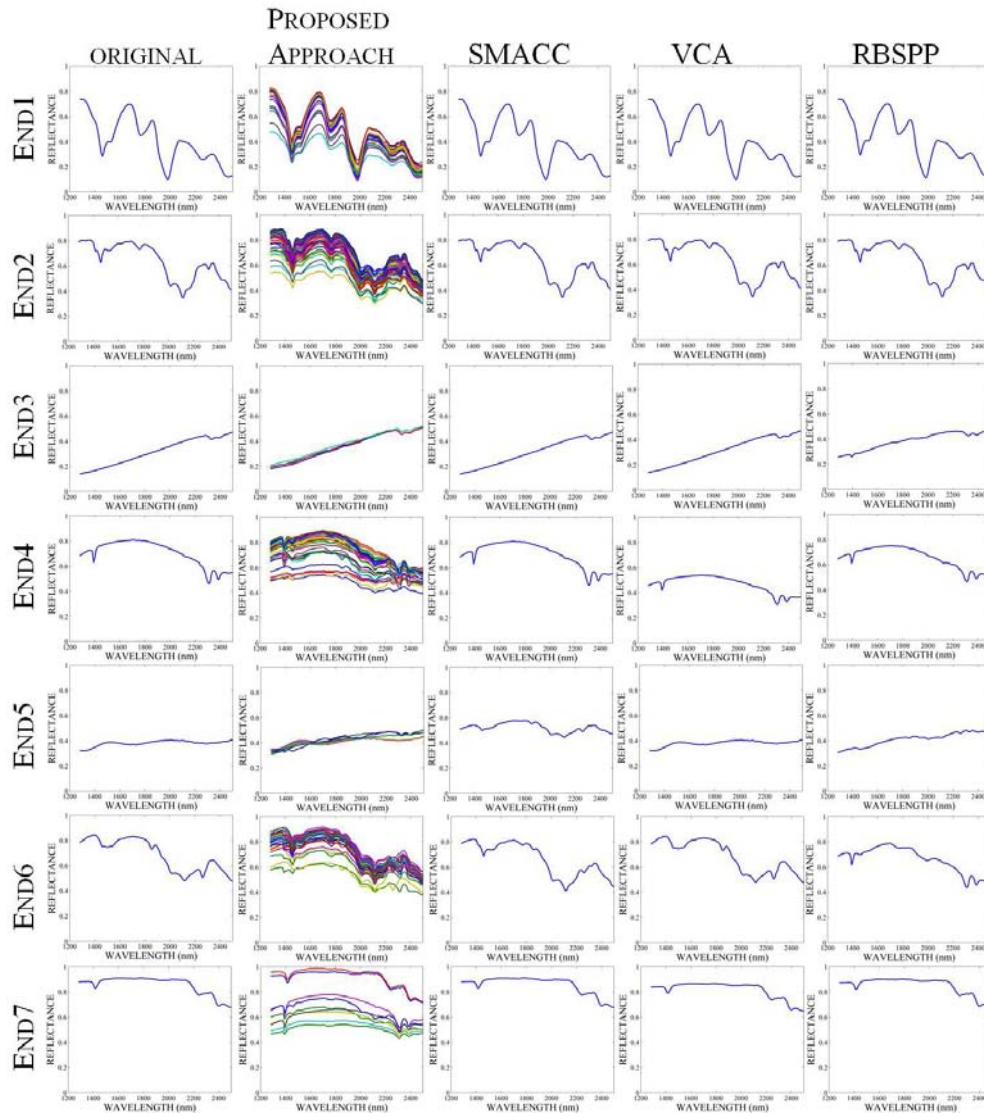


Figure 5.8: Extracted endmembers for Synthetic Data II.

OTHER ENDMEMBER SPECTRAL CLASS EXTRACTED
BY THE PROPOSED APPROACH

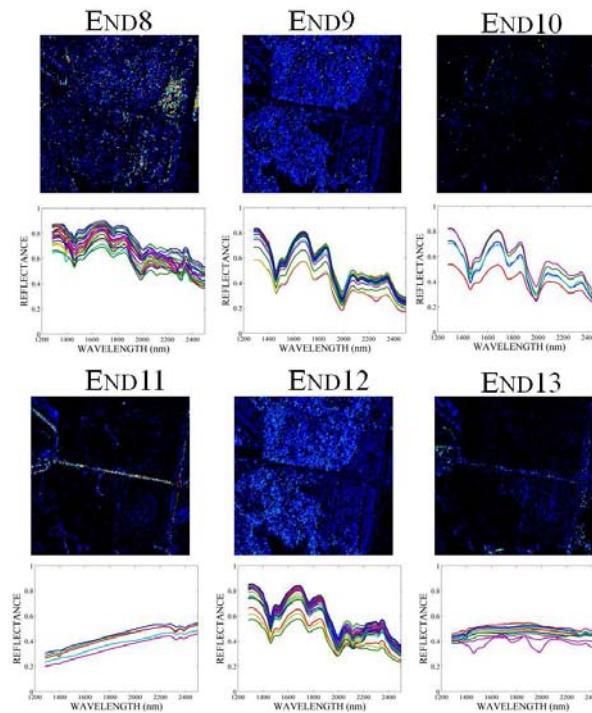


Figure 5.9: Additional spectral endmember classes for Synthetic Data II.

with most spectral variability corresponds to endmembers End_1 and End_4 . SMACC algorithm obtained the best results for Synthetic Data II. The average of the mse for the estimated abundance with this algorithm was 0.0073. The average mse for the estimated abundance by VCA, RBSPP and the proposed approach were of 0.019, 0.0215, and 0.0217.

Histograms for the errors of the estimated abundances by the proposed approach and SMACC are presented in Figure 5.10. It can be noted in the histograms that the proposed approach obtained comparable errors to SMACC. The estimated abundances for endmembers End_2 and End_6 have the largest errors in the proposed approach.

A similar analysis was performed for the unmixing results for Synthetic Data III. This second experiment is included to show the behavior of the algorithms with different spatial distributions. Figure 5.11 presents the abundances estimated from

Table 5.8: Mean square error and standard deviation for the estimate abundances from Synthetic Data II.

		<i>End1</i>	<i>End2</i>	<i>End3</i>	<i>End4</i>	<i>End5</i>	<i>End6</i>	<i>End7</i>	<i>average</i>
Proposed Approach	<i>mse</i>	0.0097	0.0274	0.0058	0.0262	0.0111	0.0618	0.0102	0.0217
	σ_{se}	0.0211	0.0423	0.0476	0.0627	0.0702	0.1290	0.0628	
SMACC	<i>mse</i>	0.0000	0.0052	0.0043	0.0004	0.0331	0.0060	0.0014	0.0073
	σ_{se}	0.0002	0.0163	0.0161	0.0023	0.1212	0.0179	0.0044	
VCA	<i>mse</i>	0.0001	0.0028	0.0002	0.0414	0.0032	0.0104	0.0319	0.0129
	σ_{se}	0.0004	0.0053	0.0013	0.0781	0.0128	0.0188	0.0529	
RBSPP	<i>mse</i>	0.0007	0.0114	0.0039	0.0515	0.0242	0.0548	0.044	0.0215
	σ_{se}	0.0020	0.0427	0.0185	0.0989	0.0803	0.1172	0.0082	

Table 5.9: SAM (σ) for the extracted spectral endmembers and original endmembers for Synthetic Data II.

		<i>end1</i>	<i>end2</i>	<i>end3</i>	<i>end4</i>	<i>end5</i>	<i>end6</i>	<i>end7</i>	<i>average</i>
Proposed Approach	SAM	0.0011	0.0010	0.0015	0.0018	0.0012	0.0014	0.0011	0.0013
	σ	0.0015	0.0010	0.0007	0.0016	0.0016	0.0006	0.007	
SMACC	SAM	0.0000	0.0000	0.0000	0.0000	0.0055	0.000	0.000	0.0007
VCA	SAM	0.0000	0.0000	0.0000	0.0000	0.0000	0.0000	0.0000	0.0000
RBSPP	SAM	0.0000	0.0000	0.0119	0.0000	0.0046	0.0074	0.000	0.0034

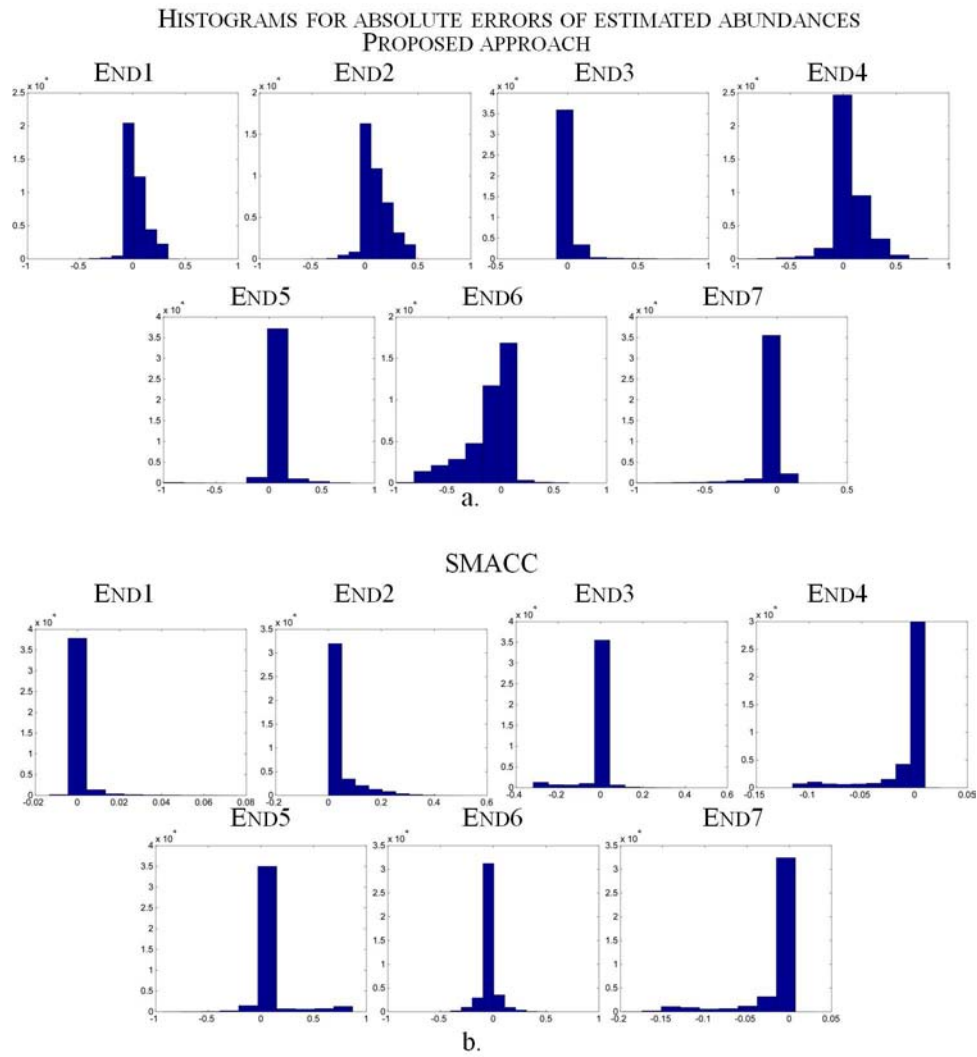


Figure 5.10: Histograms for the absolute errors of the estimated abundance from Synthetic Data II using the proposed approach and SMACC.

Synthetic Data *III* by the four algorithms: the proposed approach, SMACC, VCA, and RBSPP. Figure 5.12 shows the corresponding endmembers. In addition, Figure 5.13 shows the five additional spectral endmember classes extracted by the proposed approach. Endmembers End_{11} , End_{12} , and End_{13} appear to be additional partitions of endmember End_1 (see Figure 5.12) since these have similar spectral features (see Figure 5.12). In addition, End_{10} is related with endmember End_5 . These additional partitions are the results of the clustering algorithm. The endmembers End_1 , End_3 , End_5 , End_7 , and End_8 are the better estimated by the proposed approach.

Table 5.10 summarizes the mean square error for the estimated abundances and Table 5.11 shows the spectral angle distances for the extracted endmembers. For this image, the proposed approach also obtained a high error for endmember End_6 . The average spectral angle distance was of 0.0020 and the mean square error for the estimated abundance was 0.0734 for End_6 . The abundances for endmembers End_1 , End_3 , End_5 , End_7 , and End_8 have errors of 0.0166, 0.0030, 0.0225, 0.0298, and 0.0018 respectively. Their corresponding spectral angle distances were 0.0001, 0.0010, 0.0006, 0.0014, and 0.00053. Table 5.11 also includes the standard deviation for each spectral endmember class. The spectral endmember classes with most spectral variability correspond to endmembers End_2 , End_4 , and End_7 . The RBSPP algorithm obtained the best results for Synthetic Data *III*. The average *mse* for the estimated abundance with this algorithm was 0.0026. The average *mse* for the estimated abundance by SMACC, the proposed approach, and VCA were equal to 0.0241, 0.0262, and 0.0521 respectively.

For this second example, histograms for the errors in the estimated abundances are also included (see Figure 5.14). The histograms show the distribution of the errors for the estimated abundances by the proposed approach and RBSPP. Using the histogram, a better comparison of the errors can be done. The histogram shows clearly the small errors obtained by the RBSPP algorithm. In addition, it can be seen

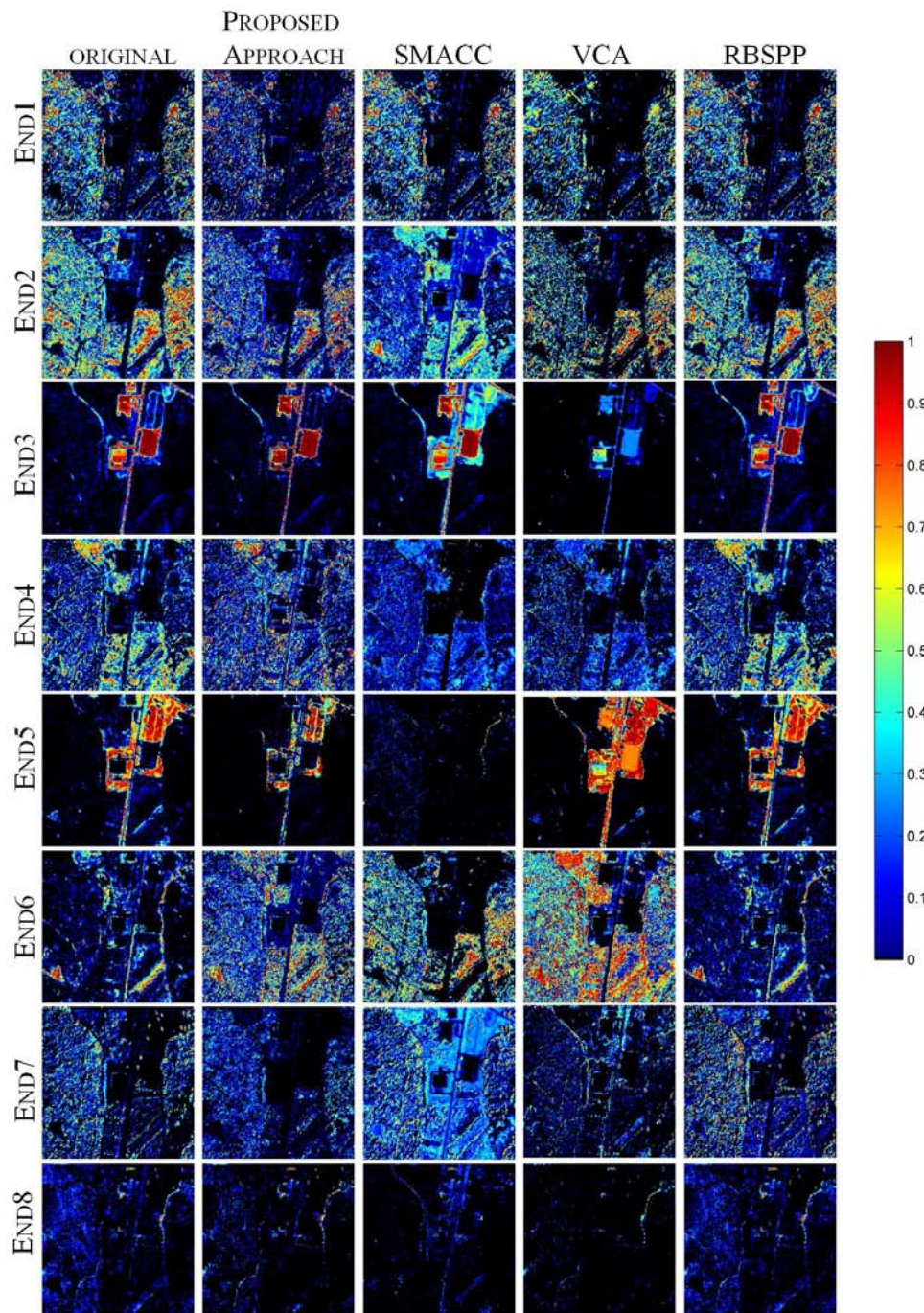


Figure 5.11: Estimated abundances for Synthetic Data III.

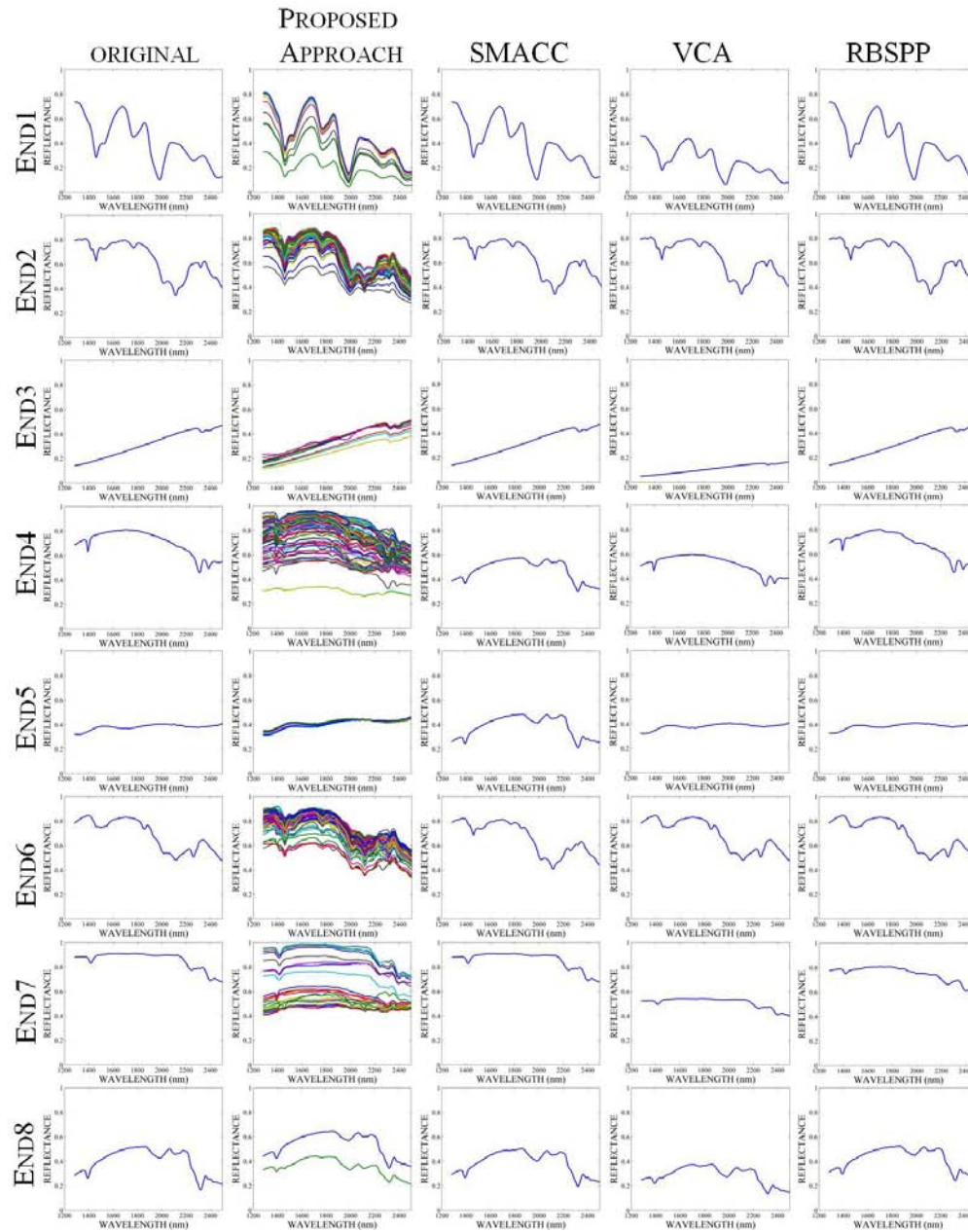


Figure 5.12: Extracted endmembers for Synthetic Data III.

OTHER ENDMEMBER SPECTRAL CLASS EXTRACTED
BY THE PROPOSED APPROACH

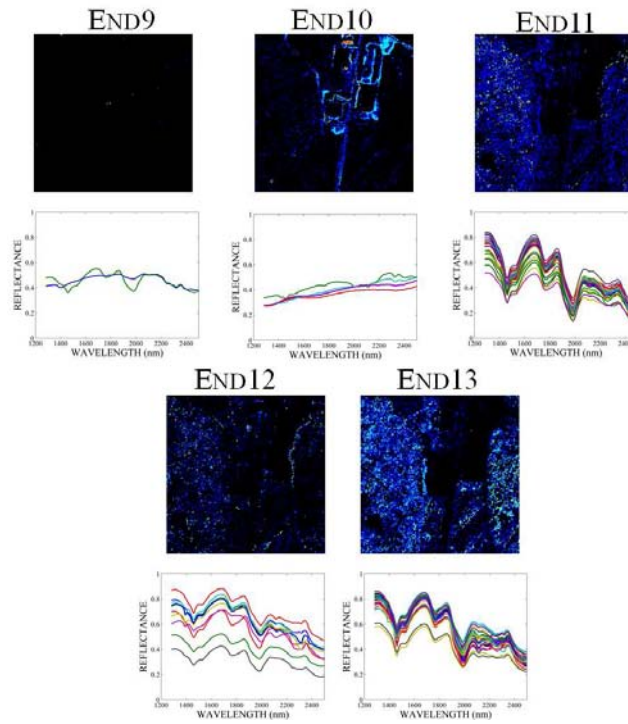


Figure 5.13: Additional spectral endmember classes for Synthetic Data III.

Table 5.10: Mean square errors and standard deviations for the estimate abundance from Synthetic Data II.

		End_1	End_2	End_3	End_4	End_5	End_6	End_7	End_8	average
Proposed Approach	mse	0.0166	0.0221	0.0030	0.0405	0.0225	0.0734	0.0298	0.0018	0.0262
	σ_{se}	0.0394	0.0422	0.0180	0.0981	0.0921	0.1578	0.1000	0.0085	
SMACC	mse	0.0001	0.0150	0.0074	0.0332	0.0750	0.0321	0.0246	0.0051	0.00241
	σ_{se}	0.0004	0.0309	0.0215	0.0684	0.2032	0.0579	0.0384	0.0226	
VCA	mse	0.0124	0.0316	0.0337	0.0380	0.0448	0.2224	0.0310	0.0033	0.0521
	σ_{se}	0.0257	0.0624	0.1151	0.0908	0.1440	0.2929	0.0928	0.0132	
RBSPP	mse	0.0004	0.0043	0.0001	0.0041	0.0004	0.0016	0.0095	0.0003	0.0026
	σ_{se}	0.0018	0.0160	0.0008	0.0185	0.0023	0.0058	0.0305	0.0016	

Table 5.11: SAM (σ) for the extracted spectral endmembers and original endmember for Synthetic Data III.

		end_1	end_2	end_3	end_4	end_5	end_6	end_7	end_8	average
Proposed Approach	SAM	0.0001	0.0017	0.0010	0.0019	0.0006	0.0020	0.0014	0.0053	0.0017
	σ	0.0002	0.0016	0.0015	0.0017	0.0005	0.0011	0.0014	0.0024	
SMACC	SAM	0.000	0.0000	0.0000	0.0055	0.0251	0.0000	0.0000	0.0019	0.0041
VCA	SAM	0.0001	0.0000	0.0000	0.0000	0.0000	0.0000	0.0000	0.0015	0.0002
RBSPP	SAM	0.0000	0.0000	0.0001	0.0000	0.0000	0.0000	0.0002	0.0019	0.0002

the good results obtained with the proposed approach with endmember End_1 , End_3 , End_5 , End_7 , and End_8 .

5.3.3 Analysis of Results

Unmixing results from Synthetic Data I and the proposed approach show that similar abundance errors are obtained for different noise levels. The proposed approach reduces the noise effects because nonlinear diffusion is used in the first stage of the unmixing. In addition, the extracted spectral endmembers correspond with signatures from the smoothed image (see Section 3.2), and thus different levels of noise are filtered before abundance estimation. This fact explains the small differences obtained among the errors for the estimated abundance from the synthetic data with SNR of 50 dB, 40 dB, and 30 dB. In the case of 30 dB, a mixed spectrum was selected by the multigrid procedure as a spectral endmember for End_1 (see Figure 5.6).

RBSPP obtained the best unmixing results for Synthetic Data I according the mean square error and the relative error, and the multiscale approach obtained the smallest spectral angle distance between the extracted spectral endmembers and original signatures. Although the errors of the proposed algorithm are larger than errors of VCA and RBSPP these are not far away. In addition, the spectral endmember extracted with the proposed approach are more similar according the spectral an-

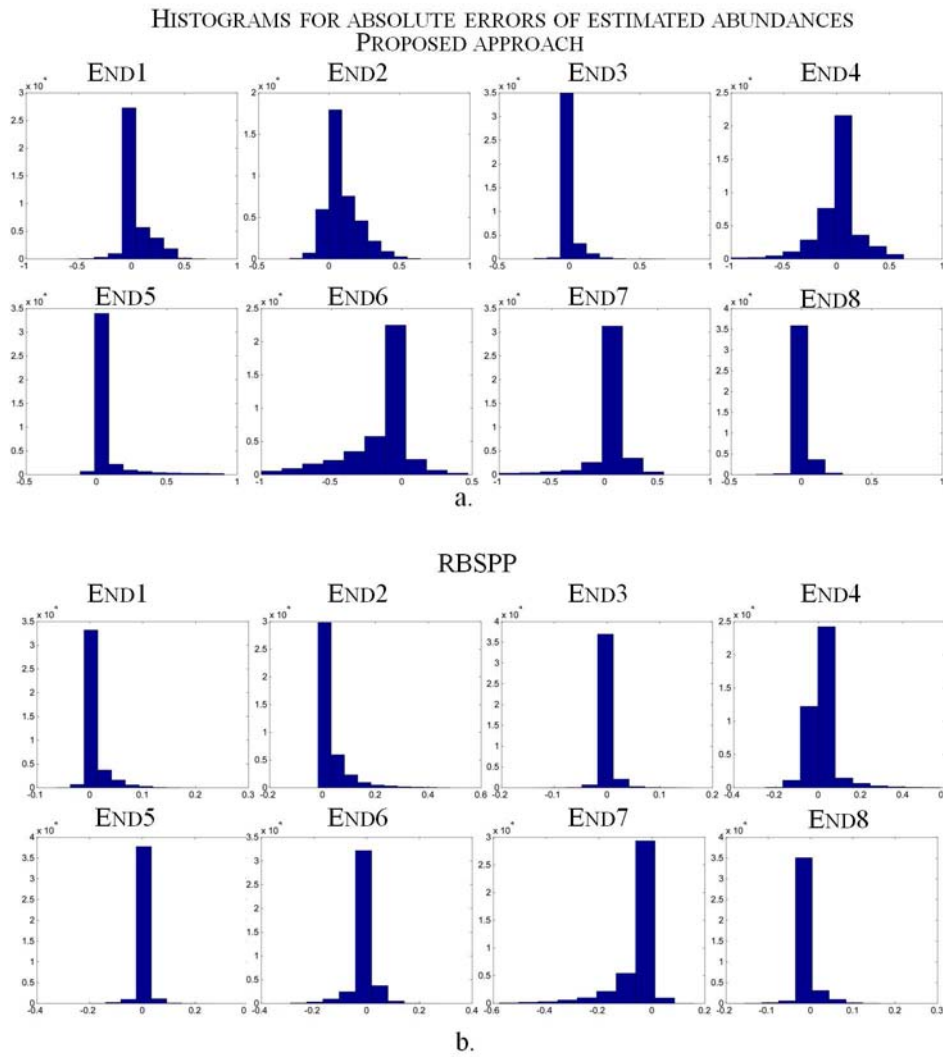


Figure 5.14: Histograms for the absolute errors of the estimated abundance from Synthetic Data II using the proposed approach and RBSPP.

gle distance to the original signatures since the proposed approach filters the image when performs the smoothing reducing noise levels.

The proposed approach extracted several spectral endmembers for each original endmember from Synthetic Data *II* and *III* (see Figure 5.8 and 5.12). Given that these synthetic data were generated using a single spectra, but the proposed approach preserve spectral variability along the unmixing analysis, some errors in the estimated abundance can be expected because of the difference of amplitude in the extracted endmembers. However, the extracted spectral endmembers should preserve the spectral features of the materials used to generate the data, and their abundances should show relation with the original distributions. It can be noted that the better estimated endmembers using the proposed approach corresponds with endmembers that show high abundances in the original abundance maps, i.e. belong to spectrally uniform regions. For instance, see endmembers *End3*, *End5* and *End7* for both Synthetic Data *II* and *III*. This also can be noted in endmember *End8* of Synthetic Data *III*. Although this endmember does not occupy a large image region, it is highly concentrated in a small region.

SMACC and RBSPP algorithms showed better results for Synthetic data *II* and *III* than the proposed approach. Since SMACC and RBSPP assumed a single representation for each material, then the way as the synthetic data was generated favors these algorithms. These comparisons allow to see some of the limitations of the proposed approach with low abundance materials. For instance, endmember *End6* in Synthetic Data *II* is the worst estimated by the proposed approach (see Figure 5.7). However, the difference between of errors obtained with SMACC, RBSPP, VCA, and the proposed approach are comparable. Although the proposed unmixing approach performs the analysis in an unsupervised fashion, the obtained errors are comparable to those obtained by SMACC, RBSPP, and VCA where important parameters such as the number of endmembers are needed a priori.

The additional spectral endmember classes extracted using the proposed approach are overpartitions due to the clustering algorithms. These additional spectral endmember classes helped to increase the errors.

5.4 SUMMARY

This chapter presented a quantitative assessment of the proposed approach using synthetic data. It is very difficult to generate data that include the several conditions found in real images such as the topographic effects, noise, and spectral variability. Thus, two separate experiments were performed to assess the proposed approach. The first experiment sought to determine the effects of noise in the unmixing results. These experiments allowed to see that the proposed approach is not significantly affected by noise since the nonlinear diffusion used in the first step removed most of the noise in the image. The proposed approach extracted the spectral endmember more similar to the original signatures in comparison with RBSPP, SMACC and VCA. Since the multiscale unmixing smoothes the image then reduces the noise effects. The second experiment sought to simulate the spatial complexity found in real hyperspectral data. For that, two synthetic data were generated using abundances previously extracted from real data. These abundances maps allow to preserve the spatial complexity in the image. However, single endmembers were used to generate the data. SMACC and RBSPP obtained the best results for these images. The proposed approach is capable of detecting all materials. Some of the abundance achieved higher errors due to the mixed cluster produced by the clustering. Also the abundance estimation errors are affected because the spectral endmember classes had several spectra to represent the spectral variability that is not considered in the generation of the images. However, the results obtained by the proposed approach are comparable with the results of SMACC, and RBSPP. Next chapter presents a

quantitative assessment of the proposed approach using real hyperspectral data. A new assessment methodology is developed to enable the comparison of unmixing results with classification maps.

This chapter presents experiments to evaluate the performance of unsupervised unmixing analysis based on multiscale representation using real hyperspectral images. Additional examples presented in Chapters 3 and 4 were included to demonstrate the capabilities of the proposed approach and the techniques for scale selection and estimation of the number of spectral endmember classes. Four images are used in this chapter: A.P. Hill, Cuprite, and two images from the Guanica Dry Forest. A detailed description of these images is presented in Section 6.1. A.P. Hill and Cuprite are used in Section 6.3 to study the performance of the proposed approach. For this purpose, a comparison of the spectral endmembers with available spectral libraries is performed as well as a quantitative comparison of the distribution of materials and classification maps is conducted. Finally, this chapter presents a study of the effects of spatial resolution in the spectral endmember extraction and abundance estimation using two AISA images from the Guanica Dry Forest at two different spatial resolutions.

6.1 DATA SETS

Four hyperspectral images were selected for the experiments. A.P. Hill and Cuprite were selected because of the availability of published spectral libraries and classification maps that allow assessment of unmixing results. Two images from the Guanica Dry Forest are also used in this chapter. These images were selected because they

were collected at two different resolutions, 1 and 4 meters, allowing the study of spatial resolution effects over the proposed approach.

6.1.1 A.P. Hill

An image captured over Fort. A.P. Hill, Virginia in September of 2001 using the AVIRIS sensor is used to evaluate the proposed unmixing approach. The image consists of 224 bands from 380 to 2500 nm with a spatial resolution of 3.5 meters. Only 197 bands are used for the unmixing analysis. Water absorption bands (bands 107 to 114 (1353 nm to 1422 nm), and 153 to 167 (1811 nm to 1939 nm)) were removed. Figure 6.1(a) presents the RGB composition using bands 30 (654 nm), 20 (557 nm) and 9 (451 nm). A classification map for the A.P. Hill image from [100] is used in here as a reference. The classification map (Figure 6.1(b)) shows 14 different classes: three types of soil (*soil ag field #1*, *soil ag field #2*, *soil ag field #2*), eight types of vegetation (*summer deciduous forest*, *loblolly pine*, *autumn deciduous #1*, *autumn deciduous #2*, *autumn deciduous #3*, *green ag field #1*, *shaded vegetation*, and *grass field*), two made man classes (*generic road* and *gravel*), and *river water*. In addition, there is a spectral library documented in [101] (Figure 6.2). Only the plots for the spectral library are available, then a quantitative assessment of the spectral signatures cannot be performed. However, the plots are visually compared with the spectral endmember classes obtained with the proposed approach. The spectral library of [101] contains image-derived endmembers.

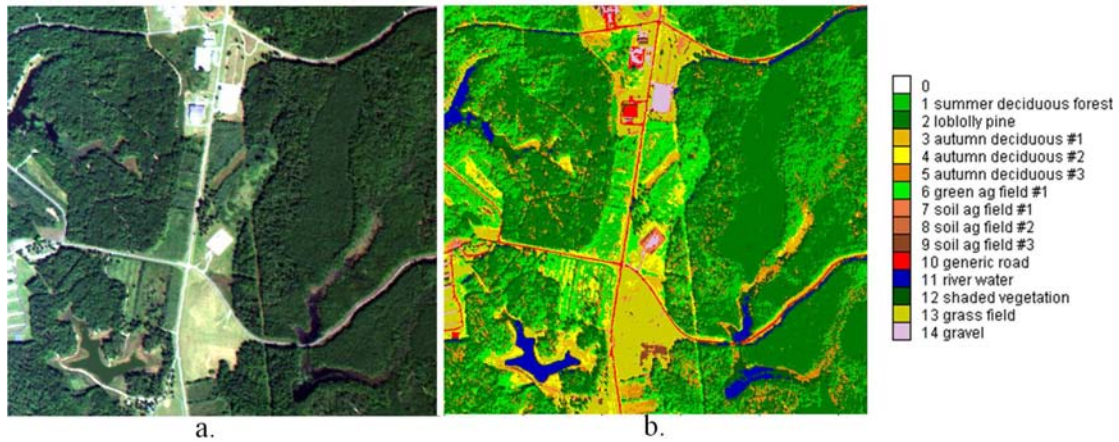


Figure 6.1: A.P. Hill hyperspectral image. (a) RGB composition using bands 30 (654 nm), 20 (557 nm) and 9 (451nm), and (b) classification map from [100].

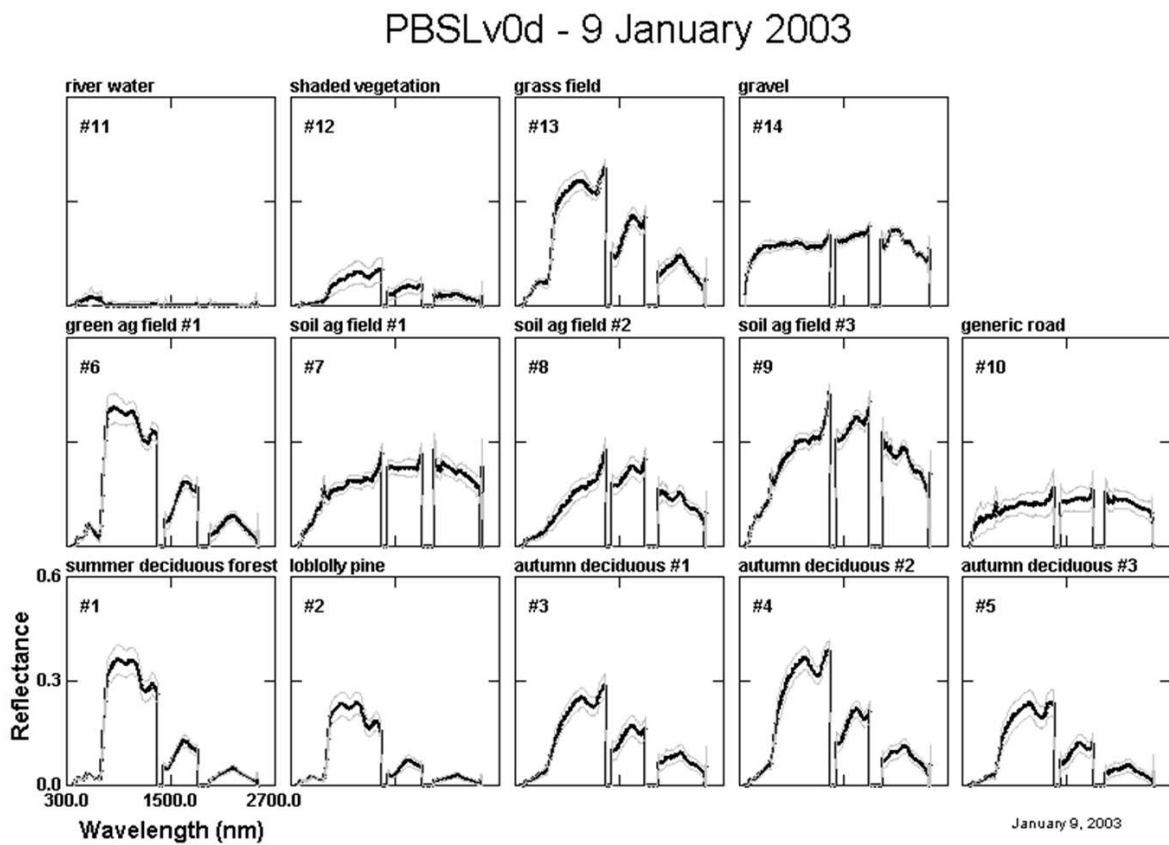


Figure 6.2: Spectral library for A.P. Hill. Figure from [101].

6.1.2 *Cuprite*

Cuprite is an AVIRIS image captured over a mining district in Cuprite, NV. The data is available online¹ and it corresponds with a flight conducted in 1995. This image has 224 bands and a spatial resolution of 20 meters. Figure 6.3 presents a RGB composite (bands 181 (2080 nm), 191 (2180 nm) and 201 (2280 nm)) of the image used to evaluate the proposed approach. Only 51 spectral bands and a subset of 400 × 400 pixels are employed here. Spectral bands between 2009 nm to 2507 nm (bands 174 to 224) are used since these are the wavelengths employed in mineral identification². A classification map from the USGS is used as references here. Figure 6.4 shows the map which was derived from the AVIRIS image collected in 1995 using the spectral region from 2000 to 2500 nm. The map in Figure 6.4(a) includes 25 classes. Figure 6.4(b) shows the region corresponding to the image used in the experiment. More information about this classification map can be found in the webpage of the USGS Speclab³. Spectroscopy of the different minerals in the mining district can be found in the USGS spectral library⁴. This image is selected to evaluate the proposed approach since it is a complex scenerario with small spectral uniform regions and several materials. Several materials within Cuprite do not meet the main assumption of the proposed algorithm of local uniformity (see Section 1.2). Then, this image allows to understand the limitations of the proposed algorithm.

6.1.3 *Guanica Dry Forest*

The Guánica Dry Forest is located in southwestern Puerto Rico. It is a tropical dry forest designated as a UNESCO man and Biosphere Reserve in 1981, and the core

¹ <ftp://ftpext.cr.usgs.gov/pub/cr/co/denver/speclab/pub/cuprite/>

² <http://speclab.cr.usgs.gov/map.intro.html>

³ <http://speclab.cr.usgs.gov/PAPERS.imspec.evol/aviris.evolution.html>

⁴ <http://speclab.cr.usgs.gov/spectral-lib.html>

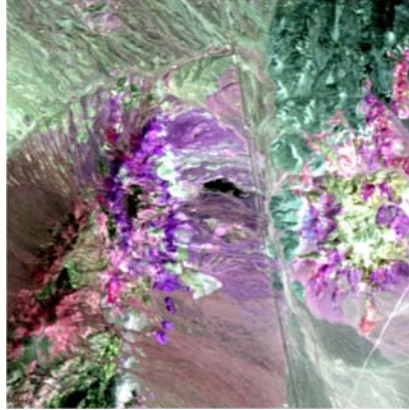


Figure 6.3: Cuprite hyperspectral image. RGB composition using bands 181 (2079 nm), 191 (2179 nm) and 201 (2279 nm) from original data cube.

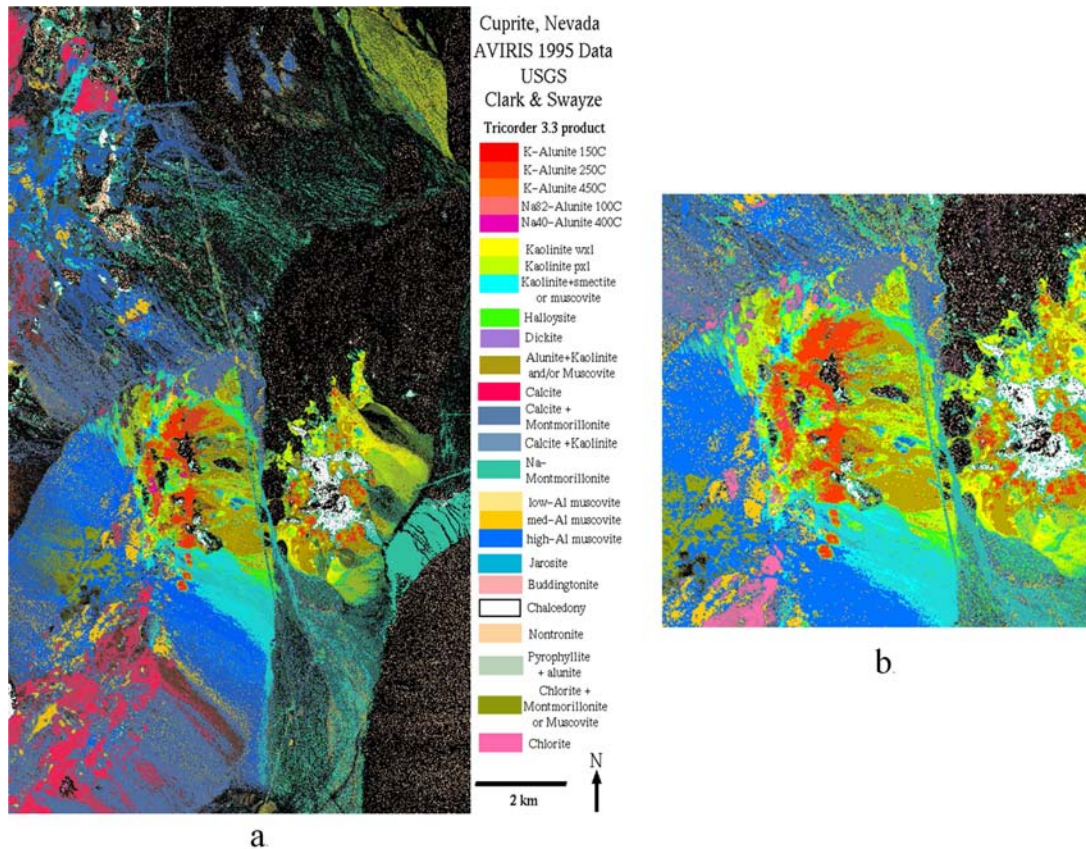


Figure 6.4: Classification map for Cuprite. (a) Map from USGS derived from AVIRIS image of 1995 using the spectral region from 2000 to 2500 nm. Map from <http://speclab.cr.usgs.gov/PAPERS.imspec.evol/aviris.evolution.html>. (b) Map subset of the area covered by the hyperspectral image.



Figure 6.5: Guanica Forest hyperspectral image. RGB composition using bands 54 (639 nm), 35 (550 nm), and 15 (459 nm) for (a) 1 meter and (b) 4 meters of spatial resolution.

site of the Atlantic Neotropical Domain of the US National Ecological Observatory Network (NEON). AISA images collected over the forest in December of 2007 are used in this work. These image consists of 128 spectral bands from 397 nm to 995 nm. These images are part of the hyperspectral remote sensing mission conducted over Southwestern Puerto Rico [102]. The data was collected at two different spatial resolutions: 1 and 4 meters. The available AISA data cover the complete forest. Only a spatial subset shown in Figure 6.5 is used in this work to study spatial resolution effects. The image with 1 meter spatial resolution has 396 x 600 pixels, and the image with 4 meters has 99 x 150 pixels. This subset was selected because a detailed description of this region is found in [68]. RGB composites were built using bands 54 (639 nm), 35 (550 nm), and 15 (459 nm). There are not classification maps for the forest. However, the Guanica Forest has been widely studied by faculty and students at the University of Puerto Rico. Santos [68] presents a description of the region used in this study based on field work conducted in the area in 2009 (Figure 6.6). The Guanica image is composed of tall and low vegetation, with a region covered by grass. Two types of roads are in the scene: paved road, and dirt road. A building is located near the center of the scene (see Figure 6.6).



Figure 6.6: Composition of Guanica Forest scene. Figure from [68].

6.2 ASSESSMENT METHODOLOGY

Most of the times, hyperspectral datasets have documented classification maps and spectral libraries such as A.P. Hill and Cuprite images. But, there is no ground truth about abundance maps. The lack of this information becomes a great limitation for any effort to determine the reliability and accuracy of unmixing results. Commonly, unmixing results are evaluated by computing the spectral angle between the extracted endmembers and spectral references, and using the reconstruction error that compares the image reconstructed from the estimated abundances and endmembers ($\tilde{Y} = SA$) and the original image [103]. But, the comparison between extracted endmembers and spectral references is limited to the fact that the extracted endmembers are image-derived signatures and the spectral references correspond usually to laboratory spectra. In addition, the reconstruction error only assess the fitting error but not the accuracy of the estimated abundances or endmembers.

In this work, a new quantitative assessment methodology is proposed that uses the information within classification maps. It is expected that a single or a combi-

nation of spectral endmember classes can be related to information classes within classification maps. Using these relations, a quantitative assessment methodology can be performed to determine how well the unmixing algorithm detects the distinct components of an image. The methodology follows two ways to assess the unmixing results. The first one is inspired in detection theory and seeks to establish if the materials that are part of an information class are detected or are not. The second is based on classification accuracy analysis. A classification map is obtained using the estimated abundances and majority vote criterion. Then, an agreement analysis between the generated classification map and the reference map is performed. Before performing the quantitative assessment, it is necessary to identify the relation between spectral endmember classes and information classes. For that, a qualitative comparison between abundances and classification maps is performed. Next sections describe each step of the assessment methodology.

6.2.1 *Qualitative Evaluation*

The qualitative evaluation relates the spectral endmember classes with the information classes. For that, two analyses are conducted. First, a comparison of the spectral endmember classes with available spectral libraries from the distinct images is performed. The comparison is done using the shape of the spectral signatures, and validated using the spectral angle (see 4.1) when the reference spectra is available (e.g. Cuprite spectral library). Second, abundance maps are compared to classification maps. The classification maps allow to know the different components of an image, and these provide some information about the spatial distribution of the materials. Then, it can be expected that similar distribution are obtained in the estimated abundance. This step of the assessment methodology requires the intervention of an image analyst.

Table 6.1: Contingent Matrix.

		True Class	
		C_1	C_2
\hat{C}_1		True Positives	False Positives
\hat{C}_2		False Negatives	True Negatives

Note that one or more spectral endmember classes can be related to one or more information classes. For the next step in the assessment methodology, spectral endmember classes related to the same information classes are combined, as well as, if an extracted spectral endmember class is related to several information classes, then the information classes are combined into a single class. Recall that the proposed approach is a machine-based approach so it may confront difficulties in separating spectrally similar classes.

6.2.2 Quantitative Assessment of Detected Classes

In the assessment of detection systems, we seek to quantify the ability to discriminate between information patterns (called *targets*) and random patterns (called *noise*) [104]. The problem can be set as a two-class problem, where the first class (C_1) represents when the target is present and the second class (C_2) when the target is not present. Thus, the response of detection systems can be categorized into four types [104]: choose C_1 , given that the target is present (C_1 is correct), is called a *Hit* or a *True Positive*; choose C_2 , given that the target is not present (C_2 is correct), is called a *Correct Rejection* or a *True Negative*; choose C_2 , given that C_1 is correct, is a *Miss* or a *False Negative*; and choose C_1 , given that C_2 is correct, is a *False Alarm* or a *False Positive*. These outputs can be organized in a *contingent matrix* or confusion matrix such as that presented in Table 6.1 [104].

The assessment methodology for the unmixing algorithm use the matrix in Table 6.1 to quantify how well the algorithm detects the materials that are part of an information class. Once the spectral endmember classes are related to the information classes, each class is used to set a detection problem. Let C_l be class l in the map, and let \mathbf{A}_l be the abundance maps related to the endmember class l . The *True Positives* corresponds with the number of pixels that have the label l in the reference map and have abundances different from zero. The *False Positives* are the number of pixels with labels different than l in the reference map and have abundances \mathbf{A}_l different from zero. The *False Negatives* are the number of pixels that have label l in the reference map and have abundances in \mathbf{A}_l equal to zero. The *True Negatives* are the number of pixels that have labels different than l in the reference map, and have abundances \mathbf{A}_l equal to zero. True positive rate (P), false positive rate (FP) and false negative rate (FN) are computed for the quantitative assessment of the unmixing algorithm using the following expressions:

$$P(\%) = \frac{\text{True Positive}}{\text{Number of Pixels in Class } l} \times 100 \quad (6.1)$$

$$FP(\%) = \frac{\text{False Positive}}{\text{Number of Pixels in Other Classes}} \times 100 \quad (6.2)$$

$$FN(\%) = \frac{\text{False Negative}}{\text{Number of Pixels in Class } l} \times 100 \quad (6.3)$$

It is very important to note that *False Positives* cannot be considered errors as in detection theory. Since the classification maps do not provide full information about the different materials presents in a single pixels, it is expected that pixels belonging to different classes have abundances different to zero for all classes present. But, it

is expected that smaller abundances will be estimated in these pixels than the one for the class assumed. Histograms for the abundances of the *True Positives* and *False Positives* are computed to compare their distributions.

6.2.3 Agreement Assessment of Classification Maps

A second way to assess the unmixing results is generating a classification map that can be compared with the reference map using an agreement matrix. A majority vote criterion is used to generate a classification map from the estimated abundance. The agreement matrix is built similarly to the confusion matrix used to evaluate a supervised classifier. Three statistics are computed from the agreement matrix: the *between-class agreement* that indicates the percentage of pixels labeled as l in the reference map assigned to the class l in the new classification map (equivalent to the producer's accuracy in the confusion matrix), the *assignment-class agreement* that indicated the percentage of pixels assigned to the class l in the new classification map that correspond with pixels labeled as l in the reference map (equivalent to the user's accuracy in the confusion matrix), and the *overall agreement* that is indicated the percentage of pixels with the same label in both the reference map and the new classification map.

6.3 UNMIXING ANALYSIS OF A.P. HILL AND CUPRITE

A.P. Hill and Cuprite are analyzed using the approach presented in Figure 1.4. First, the multiscale representation and scale selection are described in Section 6.3.1. Then, spectral endmembers are extracted using the multigrid approach and spectral end-member classes are built using clustering algorithms. Section 6.3.2 presents the ob-

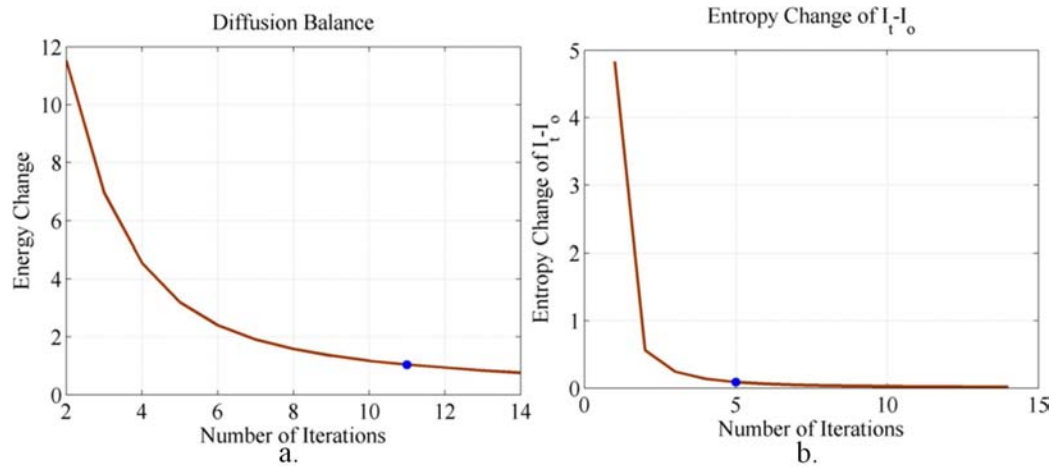


Figure 6.7: Scale selection for A.P. Hill. (a) Diffusion balance and (b) entropy change criteria. Blue points indicate the selected smoothing iterations.

tained spectral endmember classes. Finally, the unmixing results are evaluated in Section 6.3.3 using the proposed methodology.

6.3.1 Multiscale Representation and Scale Selection

AVIRIS images from A.P Hill and Cuprite were smoothed using the nonlinear diffusion algorithm reviewed in Section 3.1. The scale step μ was set to 5 for both A.P. Hill and Cuprite images. The final scale was set to 70 and the diffusion parameter α to 0.005 for the A.P. Hill image. Only 14 smoothed images were obtained for the multiscale representation for A.P. Hill due to memory limitations. The final scale was fixed to 100 and the diffusion parameter α to 0.005 for the Cuprite image. In this case, 20 smoothed images were obtained for the multiscale representation. Remaining parameters of the PDE solver were set to the values suggested by Duarte et al. (see Section 3.1.1, [26]).

Diffusion balance and entropy change methods were used for the scale selection. Figure 6.7 presents the criterion curves for A.P. Hill. The blue dots indicate the selected smoothed images. Diffusion balance selected the image in the eleventh iteration and the entropy change in the fifth iteration. For the Cuprite image, entropy

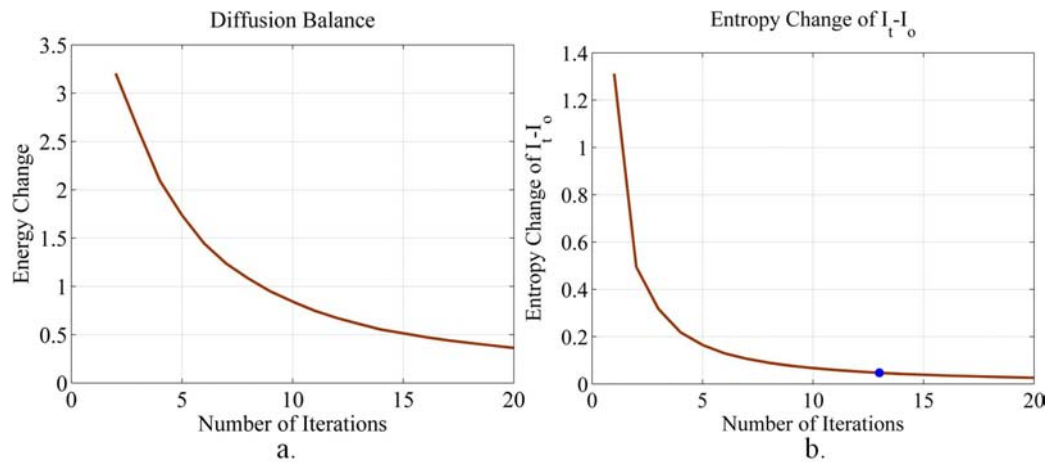


Figure 6.8: Scale selection for Cuprite. (a) Diffusion balance and (b) entropy change criteria. Blue points indicate the selected smoothing iterations.

change selected the thirteenth iteration and the diffusion balance did not produce a scale. Diffusion balance and entropy change criteria for Cuprite are plotted in Figure 6.8.

Similar to the results presented in Section 3.3, entropy change approach selected the smoothed image with fewer iterations than diffusion balance. The behavior of this criterion is very consistent for different types of hyperspectral images. Smoothed images selected using entropy change are employed in the unmixing analysis. Figure 6.9 presents RGB composites of smoothed images in the fifth iteration for A.P. Hill and the thirteenth iteration for Cuprite.

6.3.2 Spectral Endmember and Spectral Endmember Class Extraction

The spectral endmembers for A.P. Hill and Cuprite are extracted using the methodology described in Section 3.2 based on the multigrid structure and the selected smoothed images. Using the proposed approach, 176 spectral endmembers were extracted from A.P. Hill and 287 from Cuprite. Spectral endmembers were clustered into the spectral endmember classes using average and complete linkage. Spectral angle was employed as the similarity metric. The number of clusters was varied

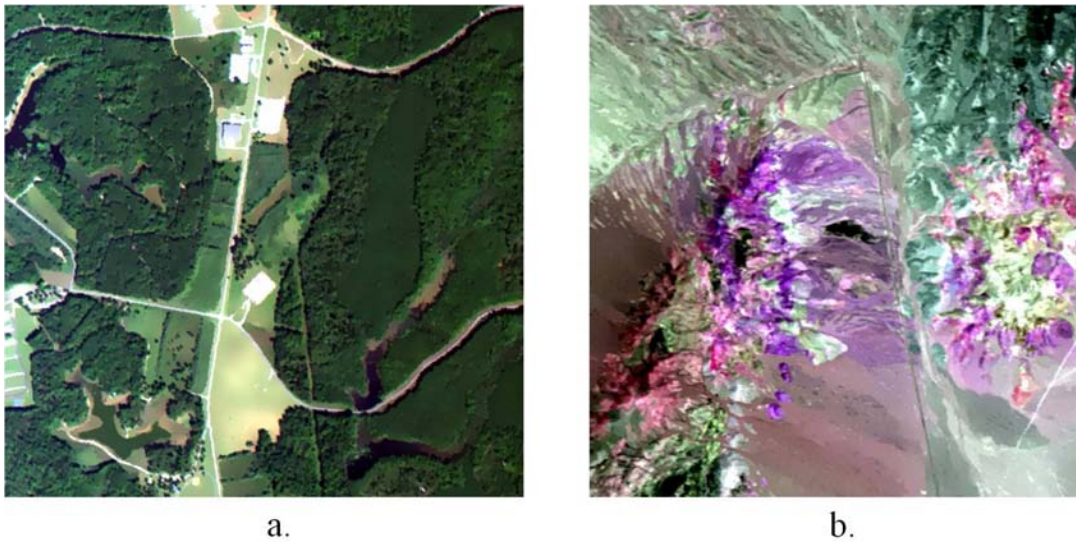


Figure 6.9: Smoothed A.P. Hill and Cuprite images. (a) Smoothed A.P. Hill image with fifth iterations and (b) Smoothed Cuprite image with thirteenth iterations.

between 2 and 30 for both A.P. Hill and Cuprite. Davies and Bouldin, Kim, and modified Kim indexes were calculated for determining the number of spectral endmember classes.

Figures 6.10 and 6.11 show the validity indexes computed for A.P. Hill and Cuprite, respectively. Table 6.2 summarizes the estimated number of clusters. Kim and modified Kim indexes estimated values less than or equal to 10 spectral endmember classes for A.P. Hill. It is expected that at least 14 materials are present in this image according to the available classification map (Figure 6.1(b)). Davies and Bouldin index estimated 14 spectral endmember classes using the complete linkage with SAM. This index estimated only 9 clusters using average linkage.

Cuprite is a very difficult image to analyze, and extracting all materials presents in the image is a hard task due to the large number of materials and their distribution. Many of the materials present in Cuprite are within small regions or are mixed with other materials. There are 25 materials identified by the classification map (Figure 6.4). However, Davies and Bouldin index estimated 17 spectral endmember classes using complete linkage with SAM. The estimated number of spectral endmember

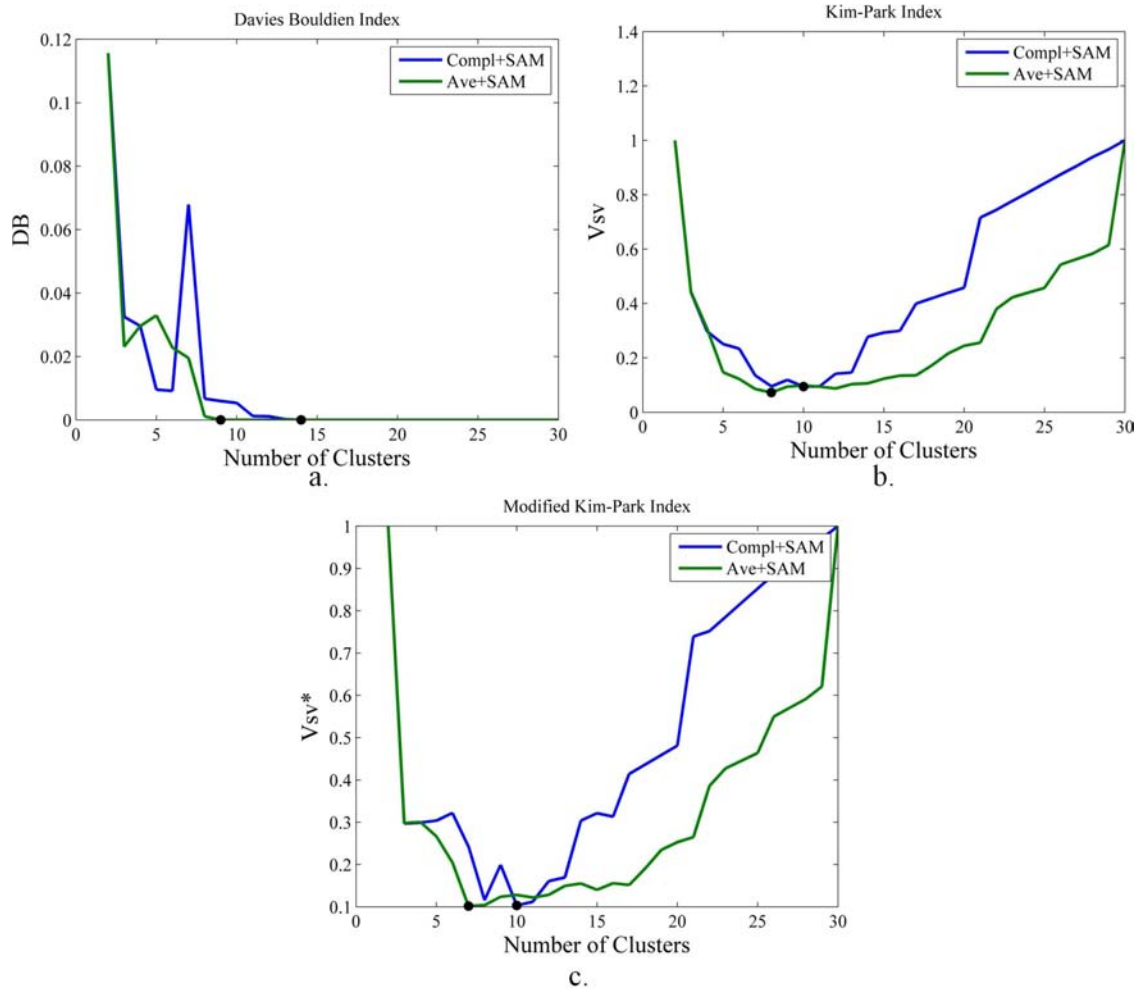


Figure 6.10: Validity indexes for the estimation of the number of spectral endmember classes for the A.P. Hill data. (a) Davies and Bouldin, (b) Kim and (c) modified Kim indexes using complete and average linkages with spectral angle measure.

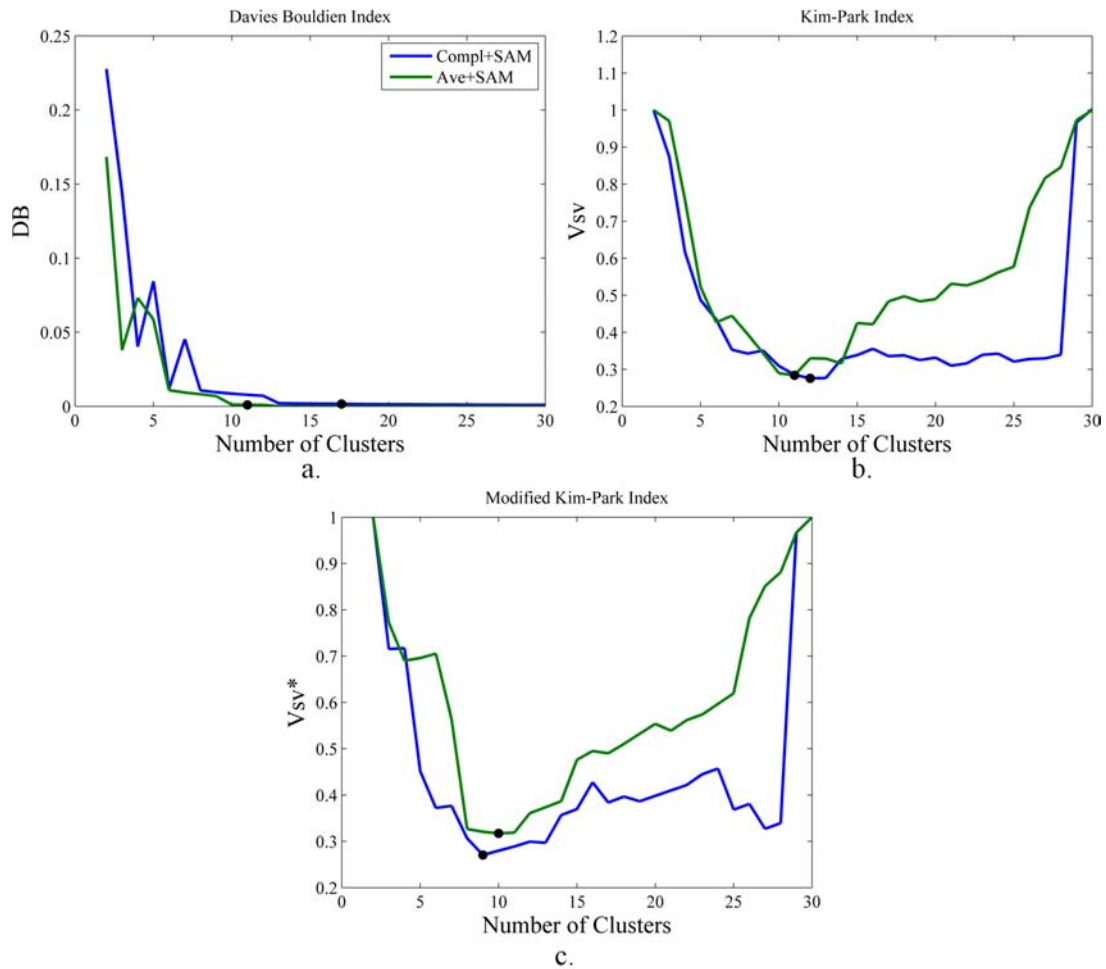


Figure 6.11: Validity indexes for the estimation of the number of spectral endmember classes for the Cuprite data. (a) Davies and Bouldin, (b) Kim, and (c) modified Kim indexes using complete and average linkages with spectral angle measure.

classes was equal to 12 and 11 according to Kim and modified Kim indexes respectively.

Note that Davies and Bouldin with complete linkage and SAM estimated the largest number of spectral endmember classes for both A.P. Hill and Cuprite image (see Table 6.2) as well as for the False Leaf image analyzed in Section 4.3.3.2. The spectral endmember classes obtained by complete linkage and the number of spectral endmember classes estimated by Davies and Bouldin index are used in Chapter 7 to compare the proposed unmixing approach with other existing algorithms. But first, an evaluation of these results is presented in Section 6.3.3.

Table 6.2: Estimated number of spectral endmember classes using validity indexes for A.P. Hill and Cuprite.

	Compl+SAM		Aver+SAM	
	\hat{c}	<i>index</i>	\hat{c}	<i>index</i>
A.P. Hill				
DB	14	2.12e-15	9	3.30e-15
Kim	10	0.0943	8	0.0727
Mod. Kim	10	0.1037	7	0.1028
Cuprite				
DB	17	0.0016	11	0.0010
Kim	12	0.2760	11	0.2842
Mod. Kim	9	0.2705	10	0.3172

Table 6.3: Comparison of estimated number of endmembers for A.P. Hill and Cuprite images.

	HySIME	Rank(K)	Rank(R)	End. Classes
A.P. Hill	21	5	5	14
Cuprite	6	5	6	17

Figures 6.12 and 6.13 show the spectral endmember classes and abundances for A.P. Hill using $\hat{c} = 14$. Figure 6.14 illustrates the spectral endmember classes for Cuprite using $\hat{c} = 17$ and Figure 6.15 presents their corresponding abundances.

Table 6.3 presents the estimated number of endmembers using HySIME [55], and the estimated ranks for the covariance, and correlation matrices (see Section 2.5). HySIME estimated 21 endmembers for A.P. Hill and only 6 for Cuprite. Instead, the ranks of covariance (K) and correlation (R) matrices are estimated only up to 6 endmembers for both images.

6.3.3 Assessment of Unmixing Results

Evaluation of unmixing results is performed using the assessment methodology presented in Section 6.2. First, the evaluation of unmixing results is performed by comparing extracted spectral endmember classes and estimated abundances with pub-

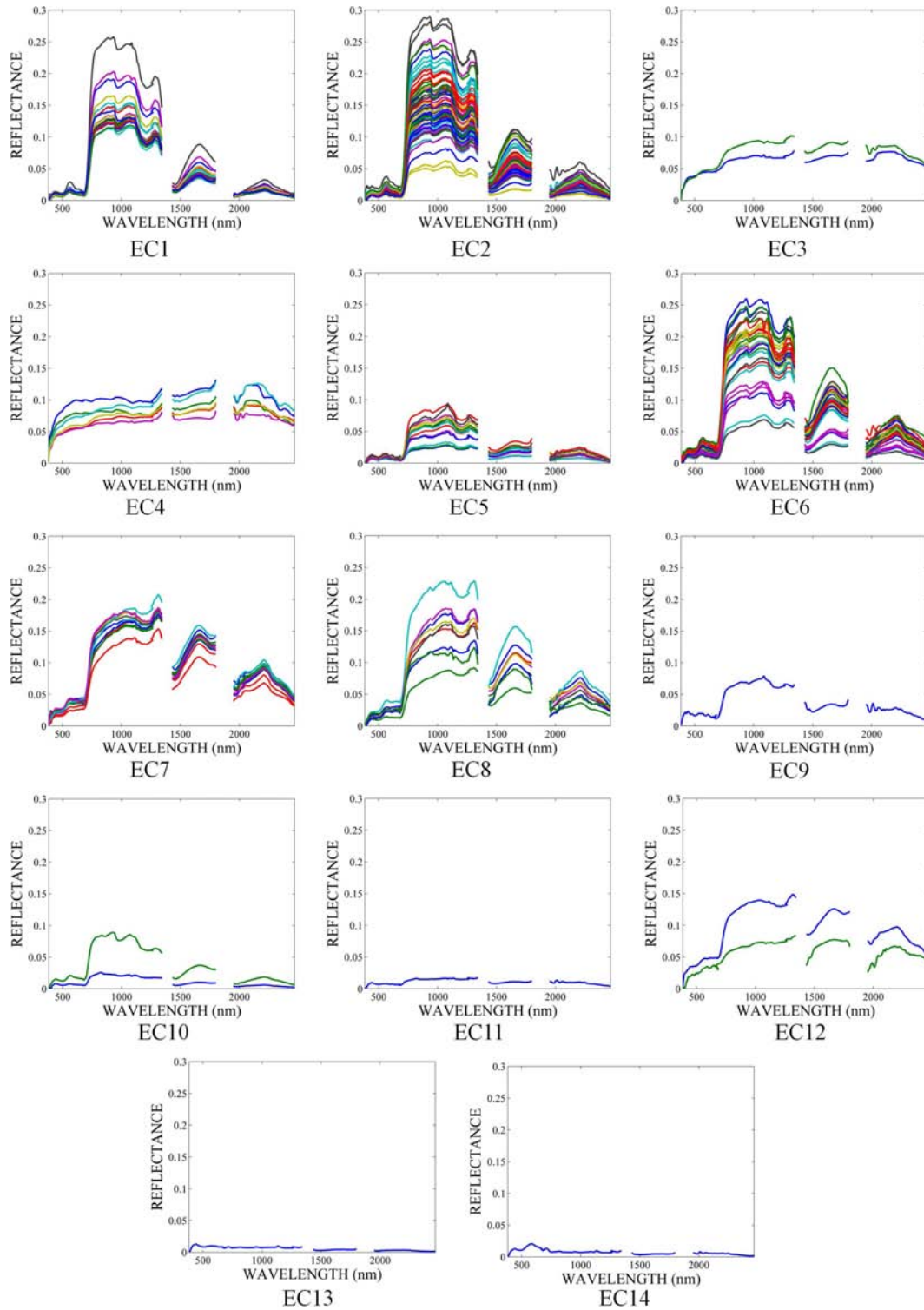


Figure 6.12: Spectral endmember classes for A.P. Hill using proposed approach with complete linkage and $\hat{c} = 14$.

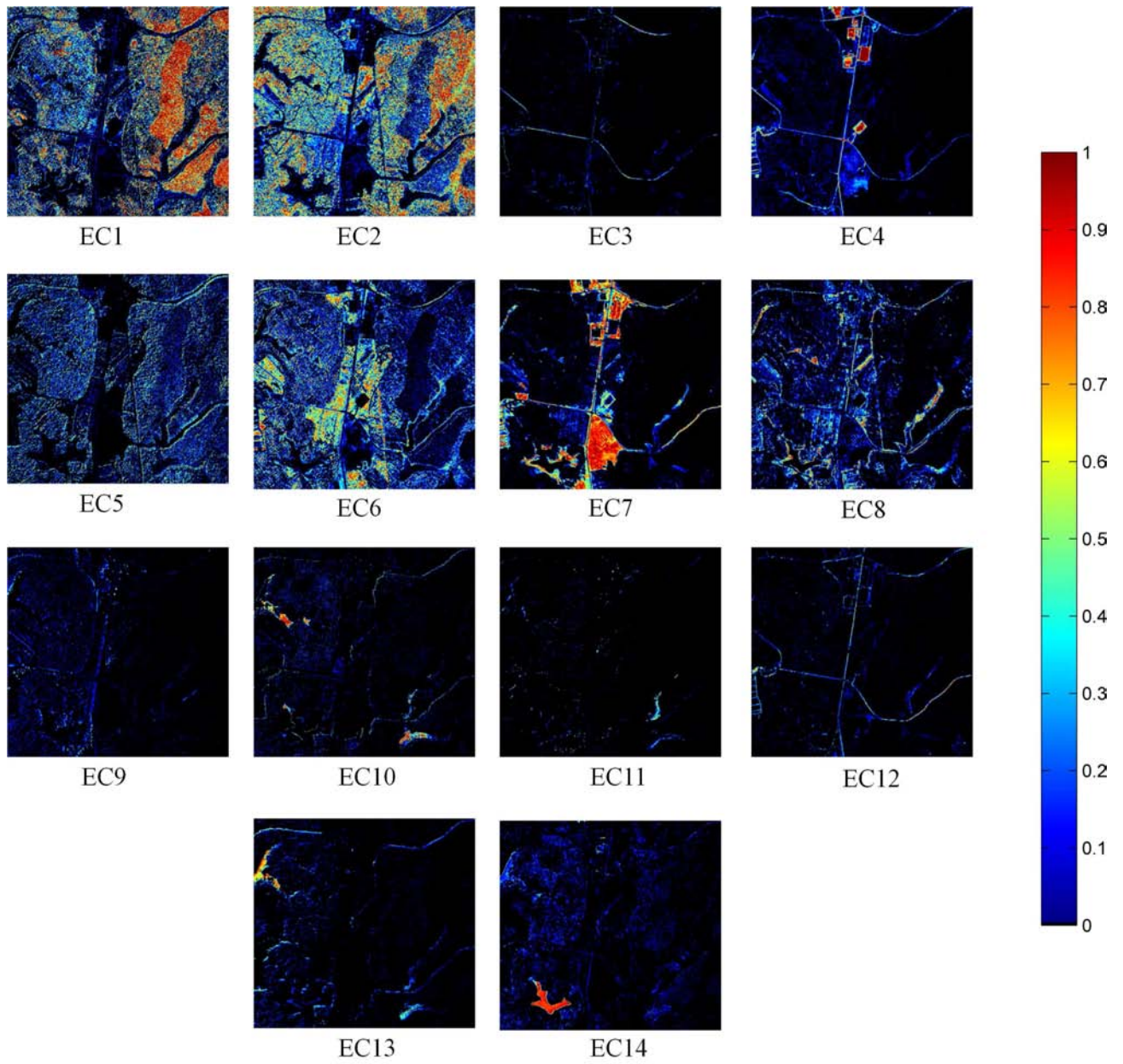


Figure 6.13: Abundances of spectral endmember classes for A.P. Hill using proposed approach with complete linkage and $\hat{c} = 14$.

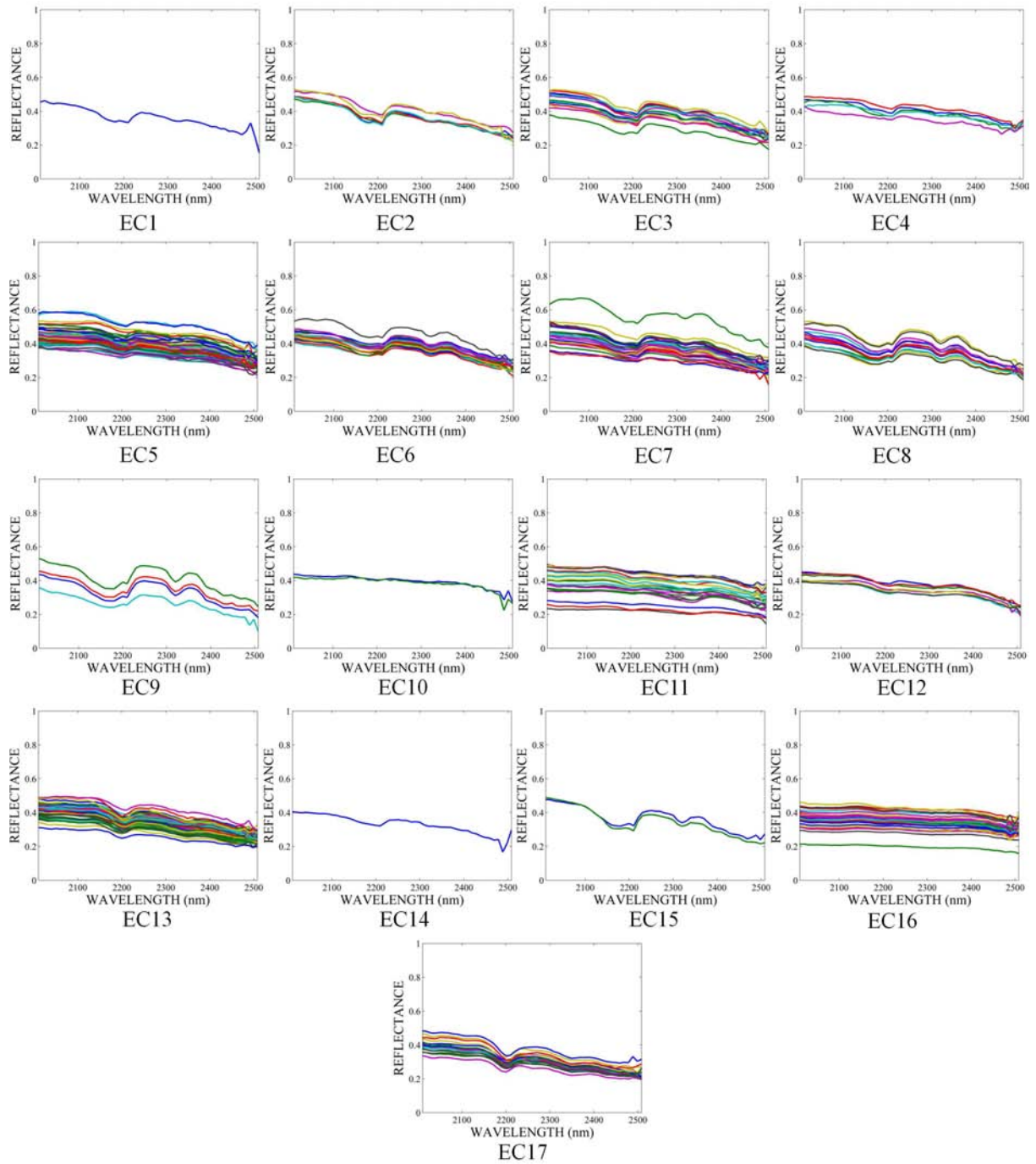


Figure 6.14: Spectral endmember classes for Cuprite using proposed approach with complete linkage and $\hat{c} = 17$.

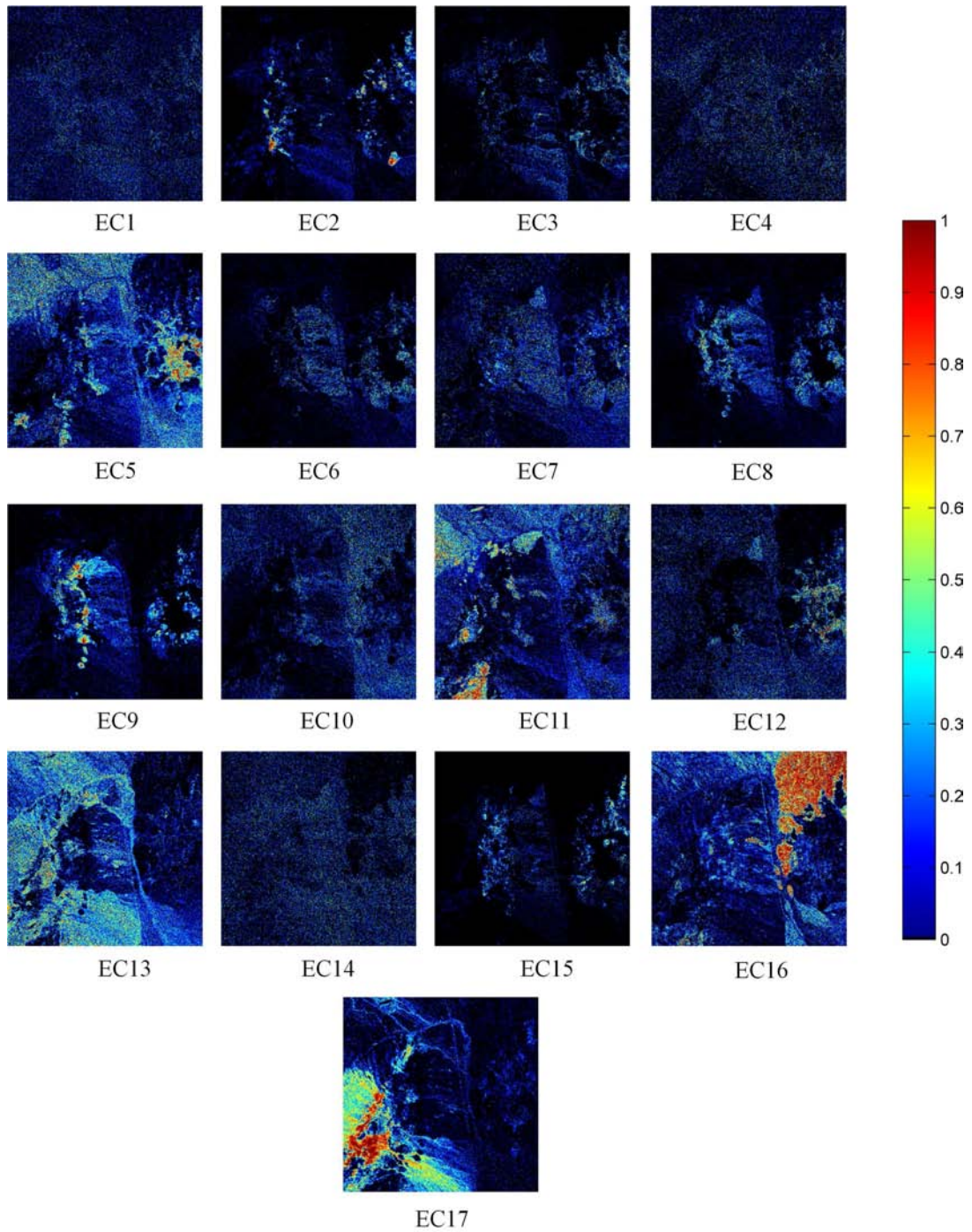


Figure 6.15: Abundances of spectral endmember classes for Cuprite using proposed approach with complete linkage and $\hat{c} = 17$.

lished spectral libraries and classification maps in Section 6.3.3.1. Then, the quantitative assessment is performed using the true positive rate, false positive rate, and false negative rate in Section 6.3.3.2. Finally, classification maps are generated from the estimated abundance, and these are compared with the reference maps in Section 6.3.3.3.

6.3.3.1 Qualitative Evaluation of A.P. Hill and Cuprite Unmixing Results

Figure 6.16 presents a comparison between some spectral endmember classes extracted from A.P. Hill using the proposed approach and the reference classification. Figure 6.16(a) shows spectral endmember class EC₁ which is related to the *loblolly pine* class. Note the consistence in the distribution of this constituent as well as the similarity between the spectra in the spectral endmember class and the spectral library. Similarly, Figure 6.16(b) presents the comparison of spectral endmember class EC₂ with the *summer deciduous forest* class. The distribution of this material in the image is consistent with the classification map as well as the retrieved endmember spectra have similar shapes to the reference spectrum.

Spectral endmember classes EC₆ and EC₇ are compared with the classification map and spectral library in the Figures 6.16(c) and 6.16(d). EC₆ is clearly related to *green ag field 1* and EC₇ represents *grass field*. Similar comparisons can be conducted for EC₅, and EC₈ which correspond to *shaded vegetation* and *autumn deciduous* classes respectively. Spectral endmember class EC₅ has spectra with lower amplitude than other vegetation types and its abundance map shows that this material is scattered across the scene. A single *autumn deciduous* spectral endmember class (EC₈) was obtained by the proposed approach instead of the three *autumn deciduous* classes shown in the classification map (Figure 6.1(b)). However, the spectra obtained for this class are consistent with the signatures in the spectral library as well as the distribution of this material along the scene. This single spectral endmember class can be a result of the similarity between the signatures.

Table 6.4: Relation between spectral endmember classes and information classes for A.P. Hill.

Spectral Endmember Class	Information Class	Group Name
EC1	<i>loblolly pine</i>	<i>loblolly pine</i>
EC2	<i>summer deciduous</i>	<i>summer deciduous</i>
EC3, EC4, EC12	<i>soil ag field, generic road, gravel</i>	<i>soil</i>
EC5, EC9, EC10	<i>shaded vegetation</i>	<i>shaded vegetation</i>
EC6	<i>green ag field</i>	<i>green field</i>
EC7	<i>grass field</i>	<i>grass field</i>
EC8	<i>autumn deciduous</i>	<i>autumn deciduous</i>
EC11, EC13, EC14	<i>river water</i>	<i>water</i>

The *river water* is divided into EC11, EC13, and EC14 spectral endmember classes. The *generic road* is detected in spectral endmember class EC3 and it is also mixed with *gravel* in class EC4. Comparing the spectra of EC3 and EC4 in Figure 6.12 and *generic road* and *gravel* in the spectral library presented in Figure 6.2, the similarity among the signature shapes can be noted. Spectral endmember class EC9 has a single spectra that appears to be the result of mixing different components. It is very similar to *shaded vegetation* (EC5) except in the first few bands. The spectral endmember class EC10 is related to the *shaded vegetation* close to the river. The *soil ag field* is detected only in spectral endmember class EC12. But this spectral endmember class is formed by two very distinct spectral signatures. Most of the pixels that are labeled as some type of *soil ag field* in the classification map (Figure 6.1(b)) are mixed with vegetation. Then, the proposed approach cannot was not capable of extracting these spectra.

Using the comparison presented above, the spectral endmember classes are related to the class such as summarized in Table 6.4. The classes *soil ag field*, *generic road*, and *gravel* are grouped into a single one since their spectral signatures are similar and the extracted spectral endmember classes EC3, EC4, and EC12 mix these signatures.

A similar comparison between abundance maps, spectral endmembers, and the reference classification maps and reference spectra library was performed for Cuprite.

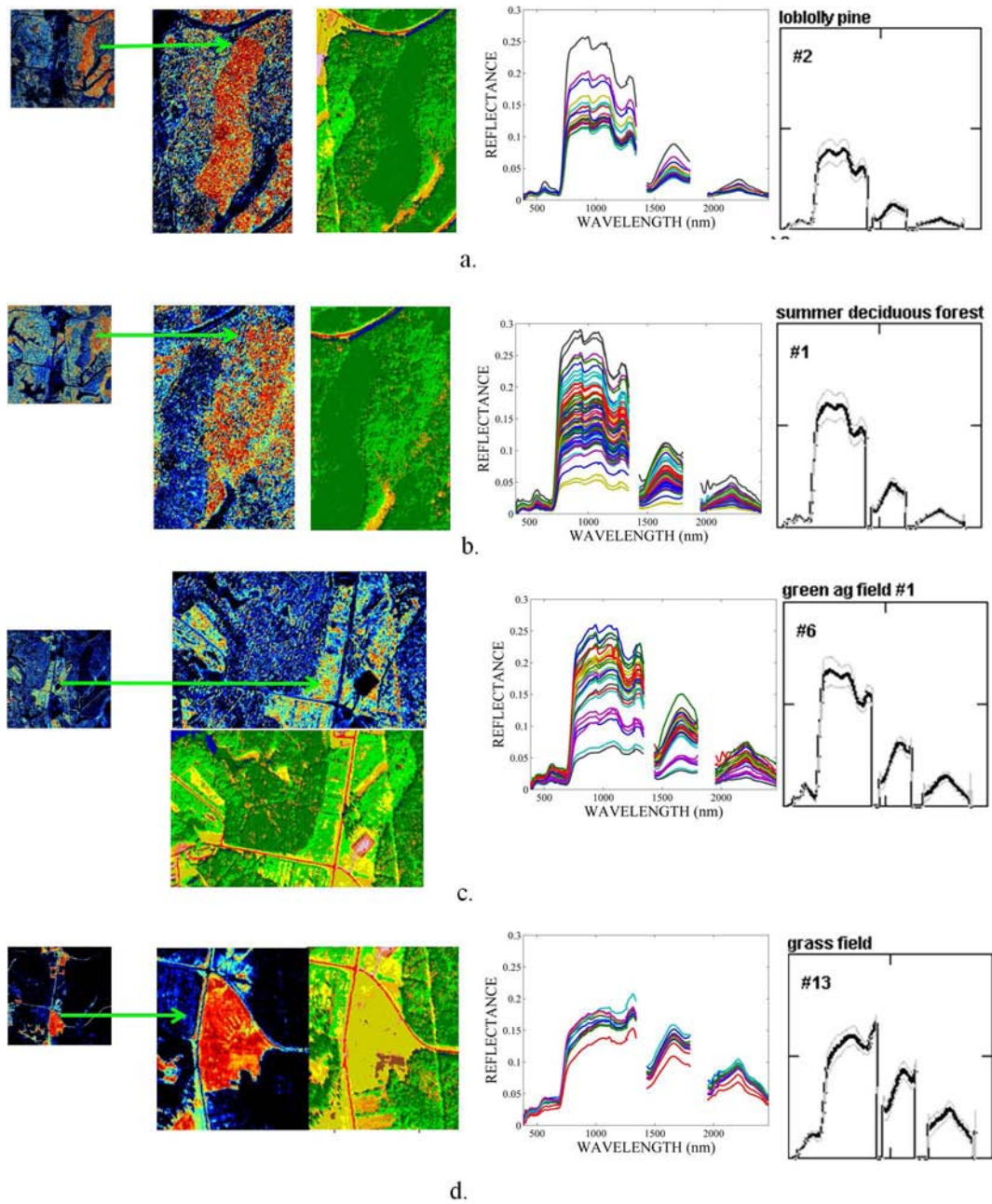


Figure 6.16: Evaluation of unmixing results from A.P. Hill for endmember classes (a) EC1 (*loblolly pine*), (b) EC2 (*summer deciduous forest*), (c) EC6 (*green ag field 1*), and (d) EC7 (*grass field*).

For instance, Figures 6.17 – 6.19 present the validation for 9 of the 17 extracted spectral endmember classes.

Figure 6.17(a) shows endmember classes EC₂ and EC₁₅ which are related to *kaolinite wxl* and *kaolinite pxl* in the classification map (Figure 6.4(a)). The arrows indicate points where the material is present in both the abundance and the classification maps. In addition, comparisons among the spectral endmembers belonging to these spectral endmember classes and the two spectra of *kaolinite* (black spectra in Figure 6.17(a)) are included. The extracted spectral endmembers keep the spectral features of these materials. A difference can be noticed between the amplitudes of the extracted spectral endmembers and signatures from the spectral library since both are measured under different conditions.

Figure 6.17(b) shows the comparison between spectral endmember classes EC₅ and EC₁₂ with the *chalcedony* class in the classification map (Figure 6.4(a)). The comparison between the spectral endmembers within EC₅ and the reference spectra in the spectral library of the USGS shows that EC₂ mixes the spectra of *chalcedony* with another material. However, the comparison of the abundance of EC₂ and the classification map shows the unmixing algorithm detected *chalcedony* with abundances close to 100% in the region where this material is indicated by the reference map. This grouping of different materials within the same spectral endmember class is due to the clustering algorithm.

Figure 6.18 shows a similar analysis using spectral endmember classes EC₁₁ and EC₁₇ with *calcite* and *muscovite* classes respectively. Both spectra (black spectra in Figure 6.18(a) and 6.18(b)) are in the spectral library of the USGS. In the case of EC₁₇, the spectral endmembers are very similar to *muscovite* reference spectrum. But, the spectral endmember of EC₁₁ presents a significant difference with the *calcite* spectrum. But, the distribution of abundances of EC₁₁ shows the relationship of this spectral endmember class with *calcite*.

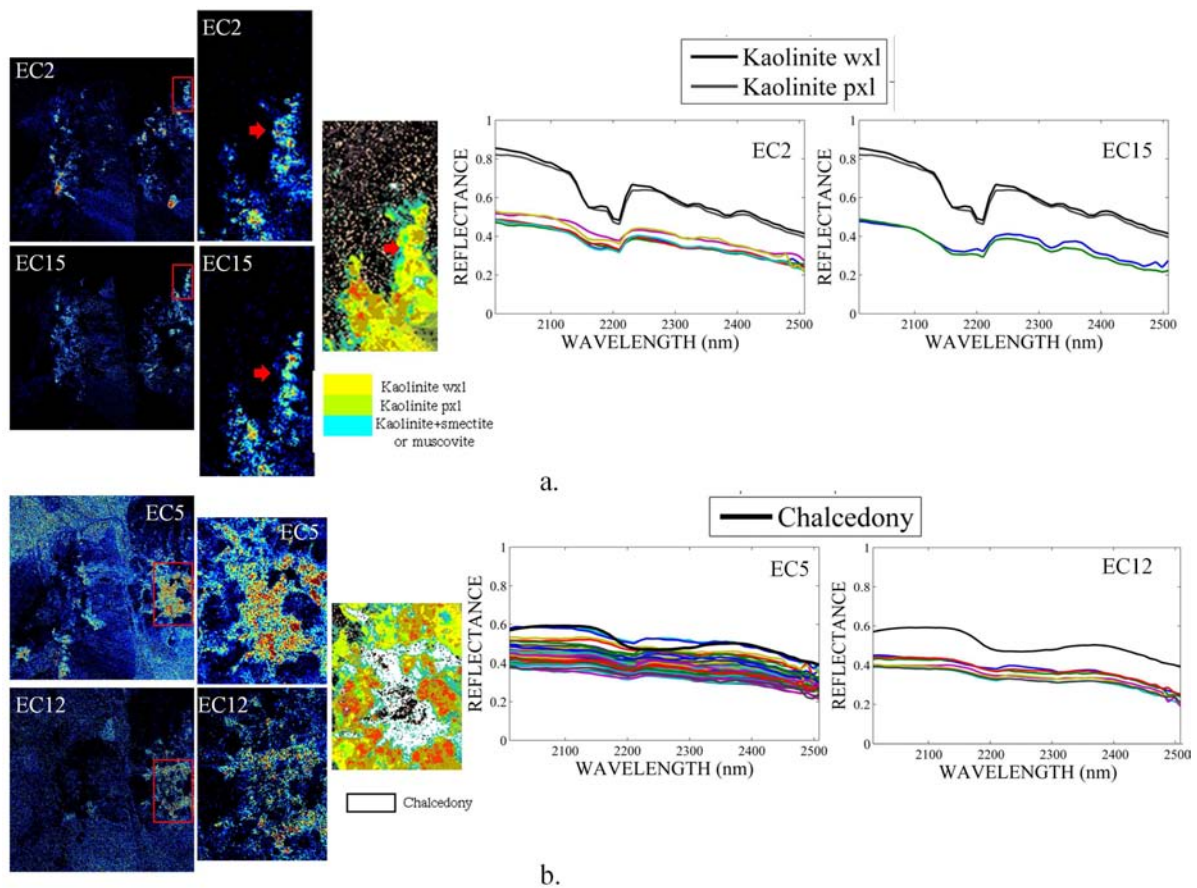


Figure 6.17: Evaluation of unmixing results for Cuprite: *kaolinite* and *chalcedony*. Comparison of abundance maps and spectral endmembers for spectral endmember classes (a) EC2 and EC15 with *kaolinite*, and (b) EC5 and EC12 with *chalcedony*.

Figure 6.19 presents spectral endmember classes EC13, EC9, and EC8 related to *kaolinite+smectite* and *alunite*. EC13 corresponds to *kaolinite+smectite* (Figure 6.19(a)), and EC9 and EC8 to *alunite* (6.19(b)). Note that the spectral endmember class EC13 is related to the different types of *alunite* of the classification map.

The comparison between the abundances and the classification map allows the identification of six classes: *kaolinite* (Figure 6.17(a)), *chalcedony* (Figure 6.17(b)), *calcite* (Figure 6.18(a)), *muscovite* (Figure 6.18(b)), *kaolinite+smectite* (Figure 6.19(a)), and *alunite* (Figure 6.19(b)). *Kaolinite* class includes both *kaolinite wxl* and *kaolinite pxl* classes of the classification map. *Muscovite* includes the classes label as *chlorite + montmorillonite* or *muscovite*, *low-Al muscovite*, *med-Al muscovite*, and *high-Al muscovite* in the classification map. Similarly, *alunite* class groups the *K-alunite 150c*, *K-alunite*

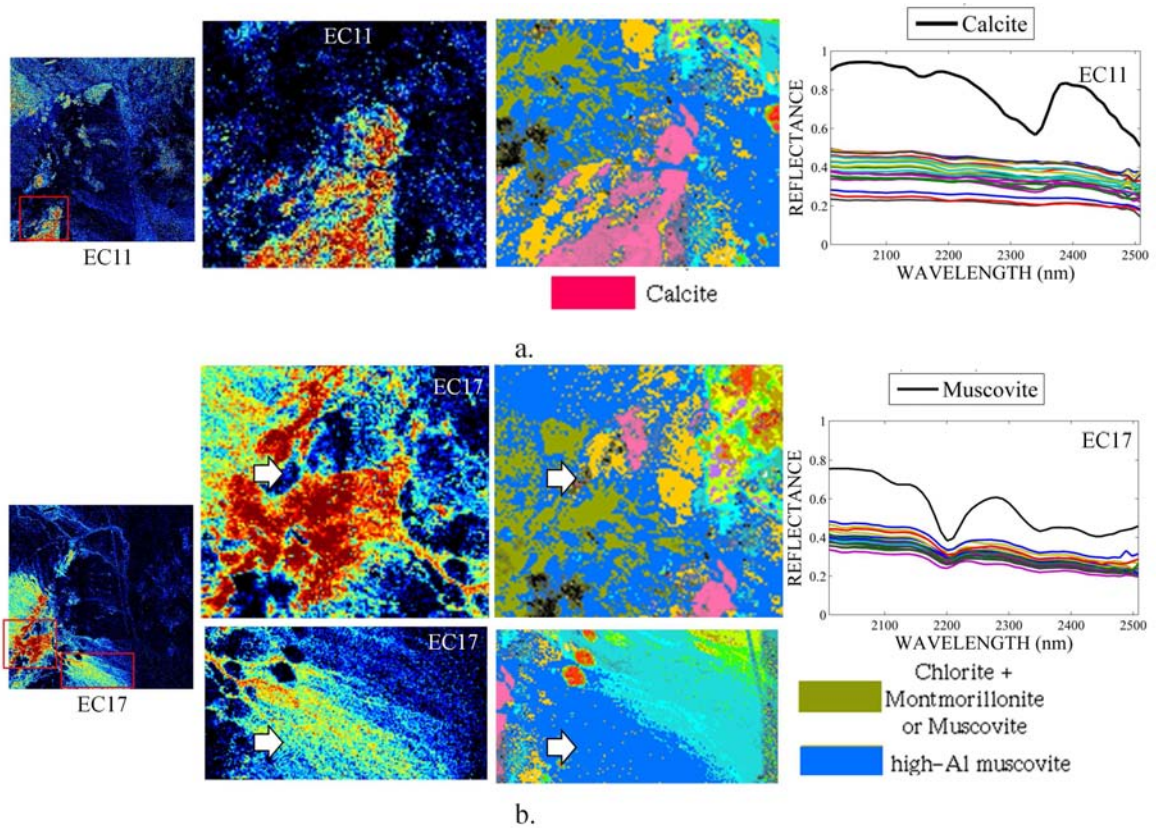


Figure 6.18: Evaluation of unmixing results for Cuprite: *calcite* and *muscovite*. Comparison of abundance maps and spectral endmembers for spectral endmember classes (a) EC11 with *calcite*, and (b) EC17 with *muscovite*.

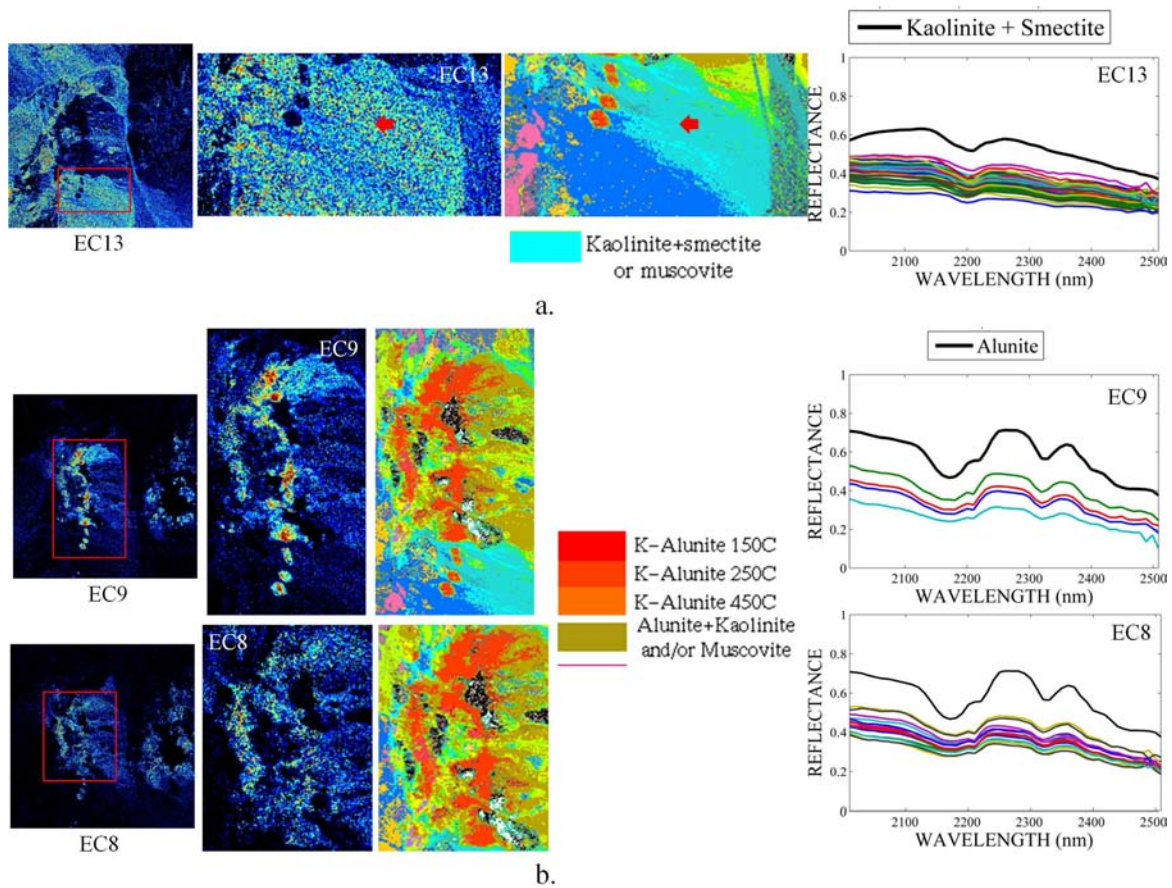


Figure 6.19: Evaluation of unmixing results for Cuprite: *kaolinite-smectite* and *alunite*. Comparison of abundance maps and spectral endmembers for spectral endmember classes (a) EC13 with *kaolinite-smectite* and (b) EC8 and EC9 with *alunite*.

Table 6.5: Relation between spectral endmember classes and information classes for Cuprite.

Spectral Endmember Class	Information Class	Group Name
EC ₂ , EC ₁₅	<i>kaolinite wxl, kaolinite pxl</i>	<i>kaolinite</i>
EC ₅ , EC ₁₂	<i>chalcedony</i>	<i>chalcedony</i>
EC ₁₁	<i>calcite</i>	<i>calcite</i>
EC ₁₇	<i>chlorite + montmorillonite or muscovite, low-Al muscovite, med-Al muscovite, high-Al muscovite</i>	<i>muscovite</i>
EC ₁₃	<i>kaolinite+smectite</i>	<i>kaolinite+smectite</i>
EC ₈ , EC ₉	<i>K-alunite 150c, K-alunite 250c, K-alunite 450c, alunite+kaolinite</i>	<i>alunite</i>

250c, K-alunite 450c, and alunite+kaolinite. The spectral endmember classes are related to the class such as summarized in Table 6.5.

Table 6.6 presents the spectral angle between the spectral endmembers classes in Table 6.5 and the reference spectra for *kaolinite*, *chalcedony*, *calcite*, *muscovite*, *kaolinite+smectite*, and *alunite* that are part of the USGS spectral library. The blue color highlights the average of the spectra angles between the spectral endmember and reference spectra of the classes related by the comparison of the abundances and the classification map (see Table 6.5). Note that EC₅ and EC₁₂ have smaller spectral angle with *kaolinite+smectite* than with *chalcedony* in Table 6.6. However, the abundance distribution of EC₅ and EC₁₂ related these spectral endmember classes to *chalcedony* class. Similarly, EC₁₇ has a smaller angle with *kaolinite+smectite* than with *muscovite* reference spectrum, and EC₁₁ has a smaller angle with *chalcedony* than with *calcite*. These can due to several reasons. The grouping the spectra from different materials into the same spectral endmember class for the clustering algorithm can result in that the spectral endmember classes are related to two or more information classes. In addition, the different conditions in the acquisition of spectral endmembers, which are image-derived spectra, and laboratory reference spectra, can result in errors in

Table 6.6: Spectral angle between spectral endmembers and reference spectra.

	<i>kaolinite</i>	<i>chalcedony</i>	<i>calcite</i>	<i>muscovite</i>	<i>kaol.+smectite</i>	<i>alunite</i>
EC2	0.0014	0.0049	0.0079	0.0051	0.0029	0.0058
EC15	0.0020	0.0092	0.0133	0.0067	0.0061	0.0039
EC5	0.0075	0.0014	0.0045	0.0106	0.0011	0.0075
EC12	0.0062	0.0013	0.0045	0.0097	0.0012	0.0077
EC11	0.0101	0.0016	0.0044	0.0133	0.0021	0.0092
EC17	0.0031	0.0038	0.0065	0.0036	0.0023	0.0099
EC13	0.0047	0.0021	0.0049	0.0065	0.0009	0.0075
EC8	0.0046	0.0065	0.0105	0.0101	0.0034	0.0019
EC9	0.0052	0.0111	0.0153	0.0127	0.0085	0.0014

material identification (e.g. see Figure 6.18(a)). Finally, the similarity between the different spectra can also result in errors in material identification. The identified relations summarize in Table 6.5 are used for the next steps in the assessment.

6.3.3.2 Quantitative Assessment of Detected Classes in A.P. Hill and Cuprite Results

In the previous section, the spectral endmember classes extracted from A.P. Hill and Cuprite images were related with the information classes documented in the classification maps. The next step in the assessment methodology described in Section 6.2 performs a quantitative evaluation of the detected classes. For that, three statistics are computed: true positive rate, false alarm rate, and false positive rate.

Figures 6.20 and 6.21 show a comparison among abundances (first column), masks generated for each information class from the classification map (second column), and masks that identified the true positive, false positive, and false negative pixels for A.P. Hill classes (third to fifth column). Table 6.7 summarizes the true positive rate, false positive rate, and false negative rate for each class. In addition, Table 6.7 includes the average and standard deviation, σ , of the abundances in the pixels identified as true positives and false positives. Figure 6.22 shows the histogram for the abundances of true positive and false positive pixels.

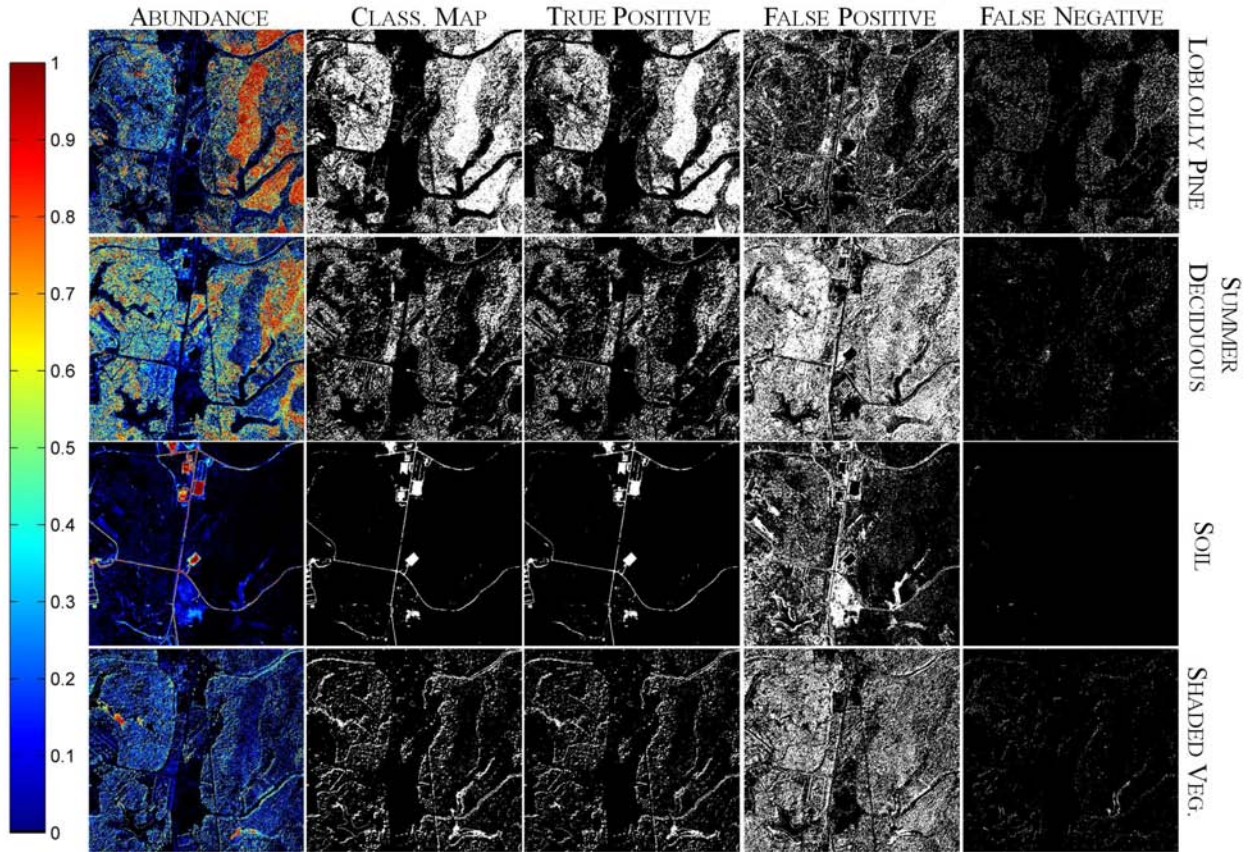


Figure 6.20: Comparison among abundances, classification map, and true positives, false positives, and false negatives of *loblolly pine*, *summer deciduous*, *soil*, *shaded vegetation* classes from A.P. Hill.

Table 6.7: True positive, false positive, and false negative rates for A.P. Hill classes.

ID	Class	True Positive			False Positive			False Negative
		%	Abundance		%	Abundance		
			Mean	σ		Mean	σ	
A	<i>loblolly pine</i>	89.9	0.53	0.31	37.7	0.31	0.29	17.1
B	<i>sum. deciduous</i>	91.8	0.54	0.28	67.3	0.36	0.26	8.2
C	<i>soil</i>	98.9	0.68	0.26	22.3	0.06	0.10	1.1
D	<i>shaded veg.</i>	86.4	0.40	0.23	39.7	0.18	0.16	13.6
E	<i>green field</i>	68.3	0.39	0.25	52.9	0.24	0.22	31.7
F	<i>grass field</i>	97.6	0.70	0.23	14.1	0.21	0.23	2.4
G	<i>autumn deciduous</i>	74.8	0.31	0.24	20.8	0.12	0.13	25.3
H	<i>water</i>	97.3	0.58	0.30	19.1	0.09	0.11	2.7

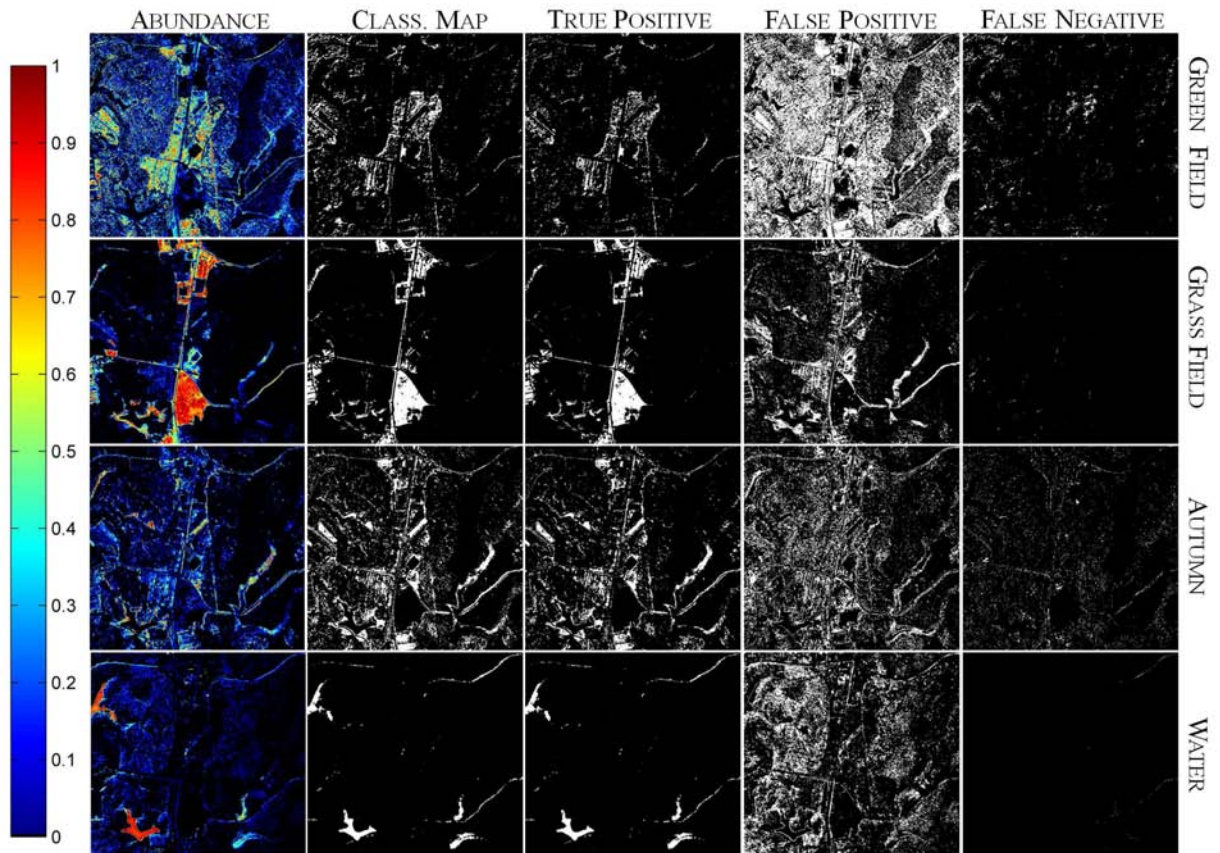


Figure 6.21: Comparison among abundances, classification map, and true positives, false positives, and false negatives of *green field*, *grass field*, *autumn deciduous*, and *water* classes from A.P. Hill.

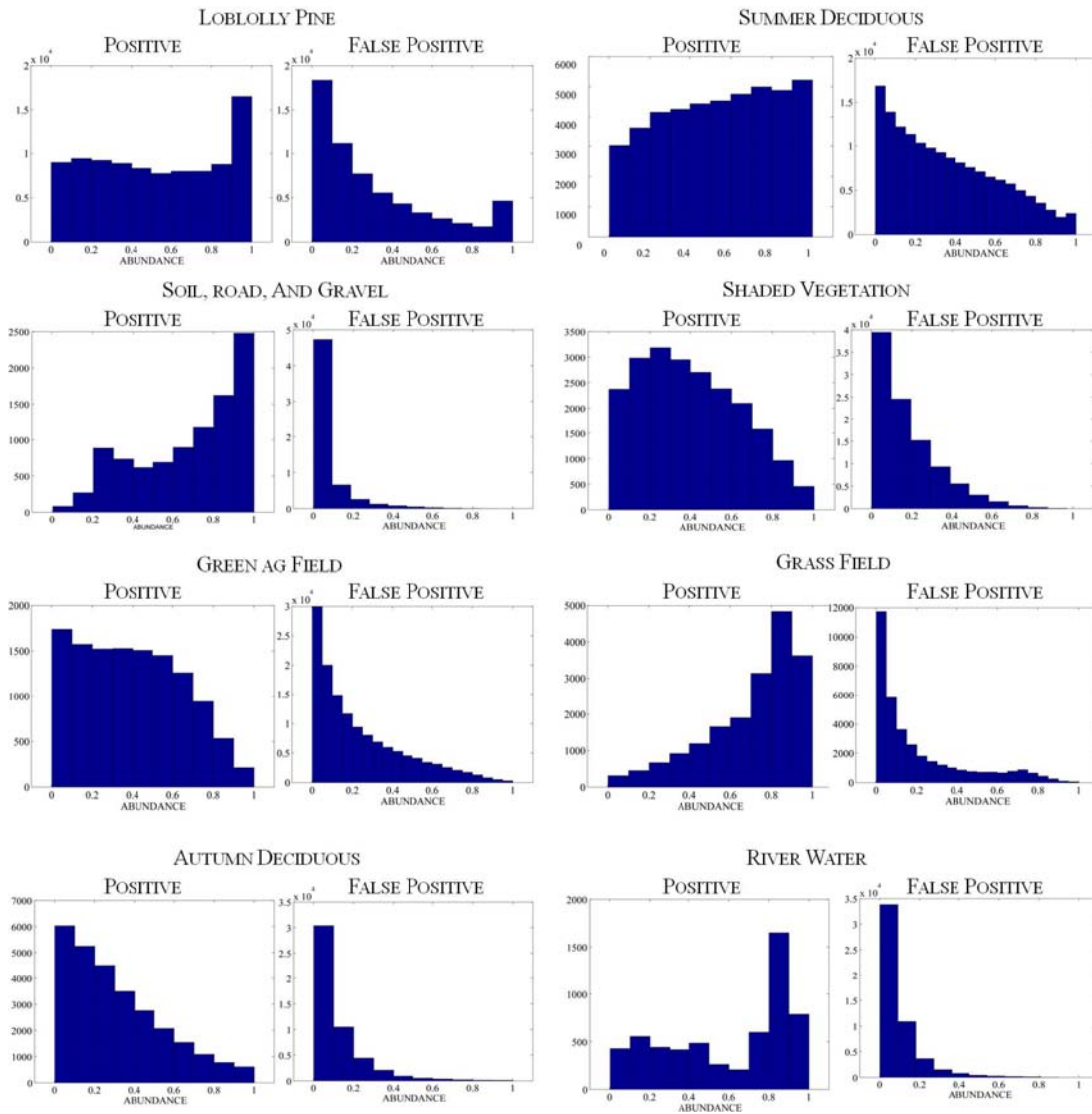


Figure 6.22: Histogram for the abundances of true positive and false positive pixels of A.P. Hill classes.

Soil, grass field, and water obtained true positive rates higher than 97%. The true positive rate for *loblolly pine, summer deciduous, and shaded vegetation* classes are larger than 80%. *Green field* and *autumn deciduous* classes have true positive rates equal to 68.3% and 74.8% respectively. The average estimated abundances from true positive pixels within *loblolly pine, summer deciduous, soil, grass field, and water* classes are higher than 0.5 with standard deviation between 0.2 and 0.3. Smaller averages of estimated abundances for true positive pixels are obtained for *shaded vegetation, green field, and autumn deciduous* classes which are between 0.3 and 0.4 with standard deviation of 0.2.

The highest false positive rate is obtained for *summer deciduous* class (67.2%). Comparing the mask of the false positives of *summer deciduous* and the abundance map (Figure 6.20) can be note that several false positive pixels correspond to pixels with low abundances. This can be also noted in the histogram (Figure 6.22) where the concentration of pixels with abundances less than 0.4 is bigger than pixels with higher abundances. The abundance mean for the false positive pixels of *summer deciduous* was of 0.36 with a standard deviation of 0.26. *Green field* also obtained a higher false positive rate (52.9%) with an abundance mean of 0.24 and standard deviation of 0.22. Comparing the mask of false positives of *green field* (Figure 6.21) with the abundance map, it can be noted that most of the false positive pixels have also low abundances. The histogram in Figure 6.22 shows that most of these pixels have abundances less than 0.2. *Loblolly pine* and *shaded vegetation* classes have false positive rates equal to 37.7% and 39.7% respectively. Abundance mean for the false positive pixels of *loblolly pine* is 0.31 and for the *shaded vegetation* class is 0.18. *Soil, grass field, autumn deciduous, and water* classes have false positive rates smaller than 22%. False positive pixels within *soil* and *water* classes have abundance mean lower than 0.09 that evidence that several of the false positive pixels of these classes have small abundances (see histogram in Figure 6.22).

Table 6.8: True positive, false positive, and false negative rates for Cuprite classes.

ID	Class	True Positive			False Positive			False Negative
		%	Abundance		%	Abundance		
			Mean	σ		Mean	σ	
A	<i>kaolinite</i>	62.42	0.22	0.24	29.99	0.09	0.13	47.88
B	<i>chalcedony</i>	87.45	0.66	0.28	68.39	0.23	0.21	12.55
C	<i>calcite</i>	75.94	0.41	0.29	55.64	0.16	0.17	24.06
D	<i>muscovite</i>	76.09	0.39	0.28	43.22	0.09	0.12	23.91
E	<i>kaolinite+smectite</i>	88.70	0.28	0.19	65.21	0.22	0.20	11.30
F	<i>alunite</i>	91.83	0.36	0.23	36.87	0.06	0.09	8.17

In general, the endmember classes obtained from the A.P. Hill image present a good correspondence with the information provides by the reference map which can be noted by comparing the true positive masks with the mask generated from the classification map (Figures 6.20 and 6.21). In addition, the pixels that the algorithm does not detect in each class are few as can be seen in the false negative masks. The different classes preserve the spatial distribution of the information classes. In addition, the comparison of the false positive pixels and the abundance maps shows that most of these pixels have small abundances. These can be also seen in the histograms shown in Figure 6.22 where it is clear that the true positive pixels have larger abundances than the false positives pixels.

A similar analysis was performed for Cuprite classes. Figure 6.23 shows a comparison between abundances (first column), masks generated for each information class from the classification map (second column) and masks that identified the true positive, false positive, and false negative pixels for Cuprite (third to fifth column). Table 6.8 presents the true positive rate, false alarm rate, and false positive rate for each class of Cuprite results. Figure 6.24 shows the histogram for the abundances of true positive and false positive pixels.

Alunite class obtained a true positive rate equal to 91.83%. The true positive pixels have an abundance mean of 0.36 with a standard deviation of 0.23. *Chalcedony*

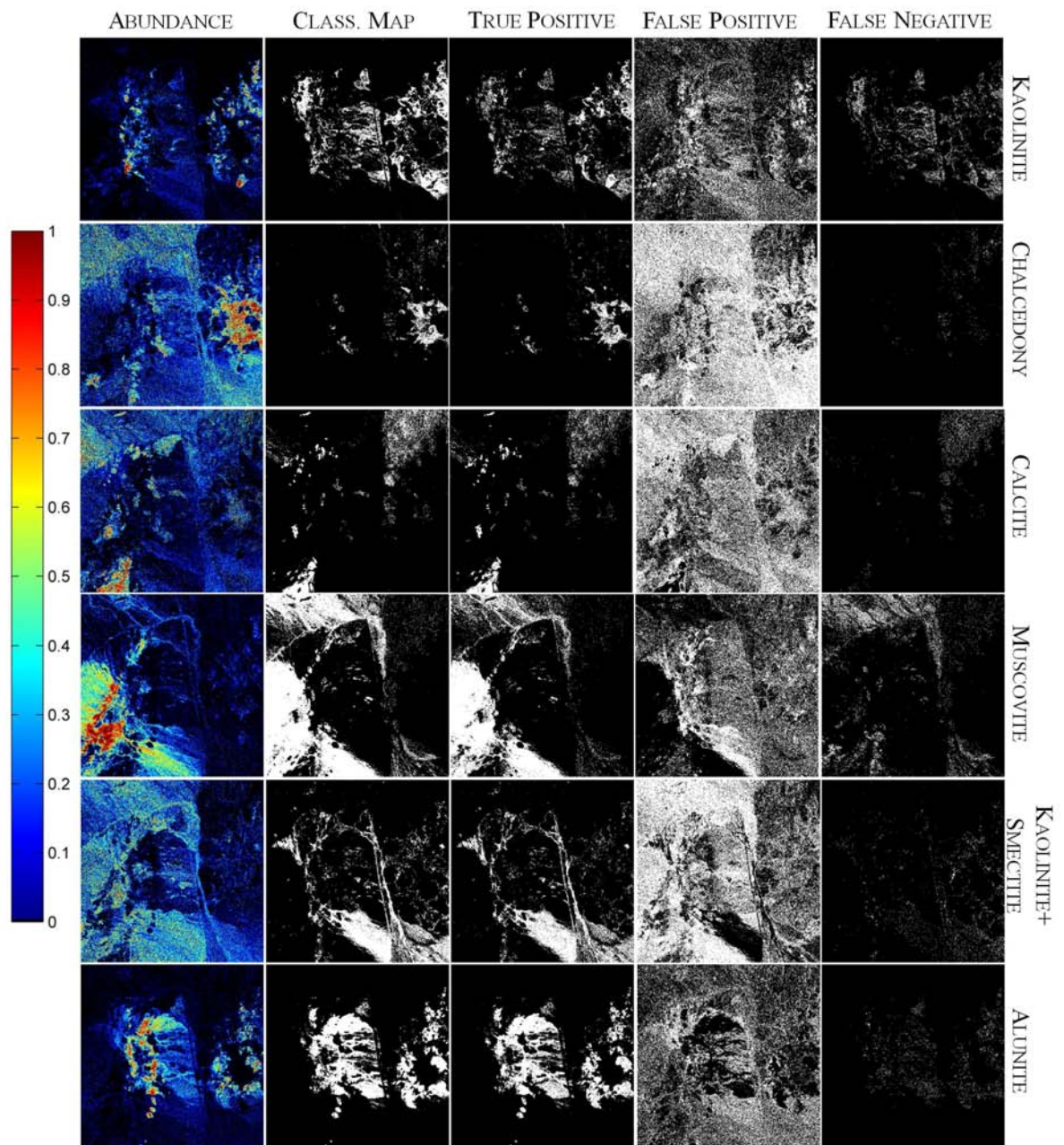


Figure 6.23: Comparison among abundances, classification map, and true positives, false positives, and false negatives of Cuprite classes.

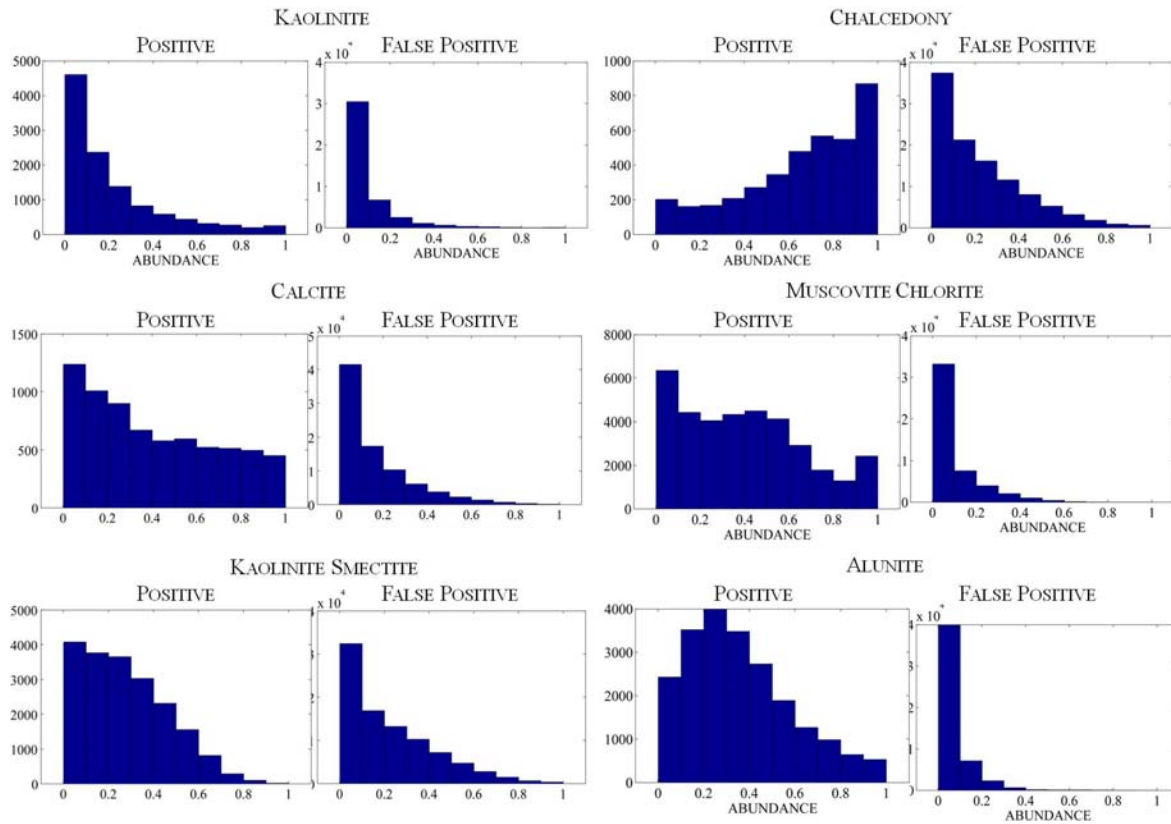


Figure 6.24: Histogram for the abundances of true positive and false positive pixels of Cuprite classes.

and *kaolinite+smectite* classes obtained true positive rates equal to 87% and 88% respectively. True positive pixels within the *chalcedony* class have an abundance mean of 0.66, and true positive pixels within the *kaolinite+smectite* class obtained an abundance mean equal to 0.28. The true positive rate of *calcite*, *muscovite*, and *kaolinite* classes were 75%, 76% and 63%, respectively. True positive pixels within *calcite* have an abundance mean of 0.41. And the true positives of *muscovite* and *kaolinite* have abundance means of 0.39 and 0.22 respectively. Note that most of the abundance mean of true positive pixels are smaller than 0.4 (Table 6.8). *Chalcedony* is the only class that obtained an abundance mean higher than 0.5. However, *chalcedony* is the class with the higher number of false positive pixels obtaining a false positive rate of 68.39%. The comparison between *chalcedony* estimated abundance and the mask of false positive pixels (Figure 6.23) shows that most of the false positive pixels have abundances smaller than the true positive pixels. It can also be seen in the histograms of abundance (Figure 6.24). *Kaolinite+smectite* class also obtained a false positive rate as high as 65% with an abundance mean of 0.22. The comparison of the abundance map and the mask for the false positives of *kaolinite+smectite* (Figure 6.23) shows that these pixels have similar abundance that the true positives pixels which can be also noted in the histogram (Figure 6.24). The spectra of *kaolinite+smectite* class are similar to spectra of *chalcedony* and *muscovite* classes (see spectral angle in Table 6.6), and then, the inversion process estimates abundances of those materials in pixels that are not part of the *kaolinite+smectite* class in the reference map. The false positive rate for *calcite*, *muscovite*, *alunite*, and *kaolinite* were 55%, 43%, 36% and 36% respectively (Table 6.8). The comparison of *calcite*, *muscovite*, and *alunite* histograms (Figure 6.24) shows that false positive pixels have smaller abundances than the true positive pixels. For *kaolinite* class, the true positive pixels have smaller abundances with a mean of 0.22, and the false positive pixels have an abundance mean of 0.09.

Similar to the results obtained for A.P.Hill classes, the Cuprite results shows good true positive rates. Although, the false positive rates can be as high as 68% , most of

the classes show that the false positive pixels have smaller abundances than the true positive pixels. Note that the false positives can be the result the different factors (see Section 6.2.2) such as the similarity among the spectra, the lack of information about mixing materials in the reference map, and the grouping the spectra from different materials into a same spectral endmember class.

6.3.3.3 Agreement Assessment of Classification Maps

The next step in the assessment methodology generates classification maps using the estimated abundances and the relation of spectral endmember classes and information classes (Tables 6.4 and 6.5). The resulting classification maps and the reference maps are compared using agreement matrices, which are built similar to the confusion matrix. Confusion matrices are employed to evaluate supervised classifiers. Three statistics are computed from agreement matrices: between-class agreement, assignment-class agreement, and the overall agreement (see Section 6.2.3).

Figure 6.25 shows the classification maps for A.P Hill. Figure 6.25(a) shows the classification map obtained from the reference map (Figure 6.1(b)) by merging some classes as indicated in Table 6.4. Figure 6.25(b) shows the classification map generated from the abundance maps estimated by the proposed algorithm. Table 6.9 presents the agreement matrix.

The classification map obtained from the unmixing results of A.P. Hill has an overall agreement of 50.5% with the reference map. *Soil*, *grass field*, and *water* classes have between-class agreements higher than 73%. This high agreement can be also noted in the Figure 6.25. *Loblolly pine* and *summer deciduous* classes obtained between-class agreements equal to 51.22% and 57.02% respectively. Many pixels that belong to *loblolly pine* in the reference map are assigned to *summer deciduous* (43673 pixels). Also, it can be seen in the agreement matrix that most of the false positive pixels of *summer deciduous* identified in Figure 6.20 belong to the *loblolly pine* class (see column B in Table 6.9). In addition, many pixels that belong to *summer deciduous* class in the

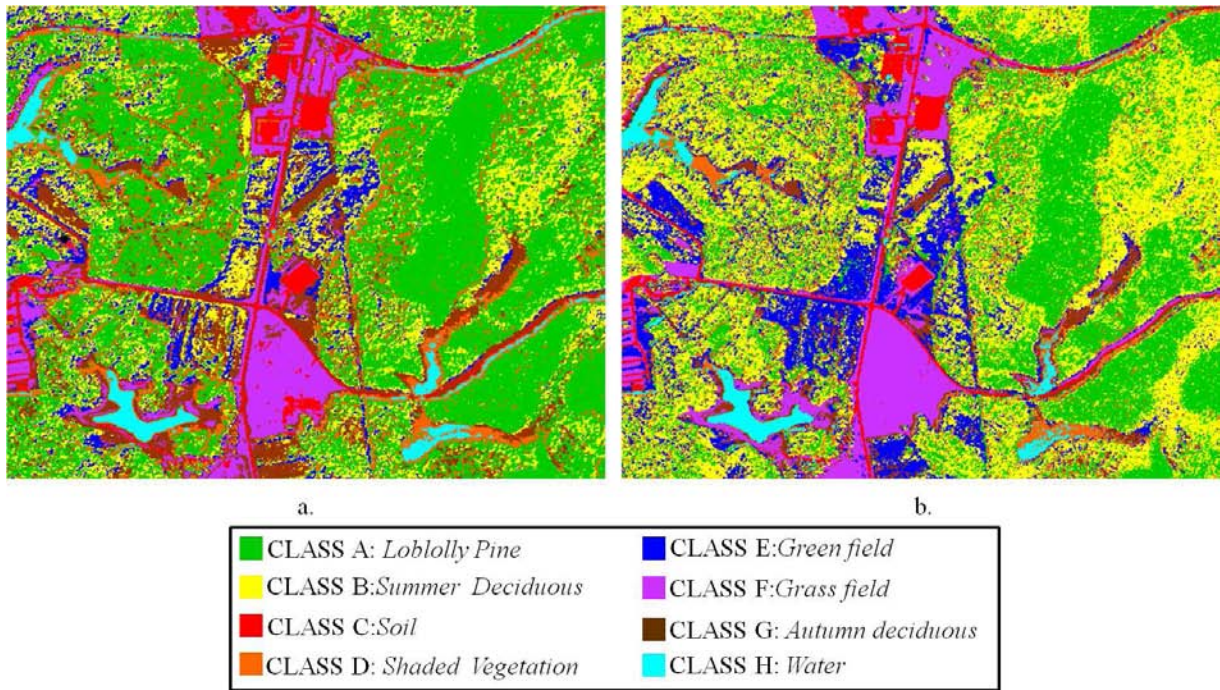


Figure 6.25: Classification map from unmixing results of A.P. Hill. (a) Reference map, (b) Classification map using the abundances and the majority vote criterion.

Table 6.9: Agreement matrix between reference map and generated classification map from unmixing results of A.P. Hill.

	A	B	C	D	E	F	G	H	TOTAL	BETWEEN CLASS AGREEMENT (%)
<i>Loblolly Pine</i>	58027	43673	0	8547	2857	0	76	93	113273	51.22
<i>Summer Deciduous</i>	12798	27260	3	138	7345	2	255	0	47801	57.02
<i>Soil</i>	1	0	7149	31	11	2195	137	21	9545	74.89
<i>Shaded Vegetation</i>	2192	4393	306	11458	3831	60	1044	1817	25101	45.54
<i>Green field</i>	2537	9728	0	0	5606	9	101	0	17981	31.17
<i>Grass field</i>	1	142	162	0	1397	16223	1253	0	19178	84.59
<i>Autumn deciduous</i>	271	4029	1331	1914	15707	4862	9399	97	37610	24.99
<i>Water</i>	4	125	9	1309	27	0	4	4513	5991	73.33
TOTAL	75831	89350	8960	23397	36781	23351	12269	6541		
ASSIGNMENT CLASS AGREEMENT (%)	76.52	30.50	79.79	48.97	15.24	69.47	76.61	68.99	OVERALL CLASS AGREEMENT (%)	50.50

reference map are assigned to *loblolly pine* (12798 pixels). This confusion between *loblolly pine* and *summer deciduous* is the result of the similarity among their spectral signatures (see Figure 6.12). *Shaded vegetation*, *green field*, and *autumn* obtained between-class agreements smaller than 45%. Many pixels that belong to *shaded vegetation* in the reference map are assigned to *summer deciduous* (4393 pixels), *green field* (3831 pixels), and *loblolly pine* (2192 pixels). Most of the pixels labeled as *green field* in the reference map are assigned to *summer deciduous* (9728 pixels), and most of the pixels labeled as *autumn deciduous* in the reference map are assigned to *green field* (15707 pixels). Many pixels labeled as *autumn deciduous* are also assigned to *grass field* (4862 pixels), and *summer deciduous* (4029 pixels). *Autumn deciduous* is the class that presents most confusion in the new classification map. The highest assignment-class agreement were obtained for the Class A (*loblolly pine*), Class C (*soil*), and Class G (*autumn deciduous*) which are higher than 76%. Class F (*grass field*) and Class H (*water*) obtained 69% and 68% of assignment-class agreements respectively. The other classes (*Class B*, *Class D*, and *Class E*) have assignment-class agreements between 15% and 48%.

Figure 6.26 shows the classification maps for Cuprite. Figure 6.26(a) shows the classification map obtaining from the reference map (Figure 6.4), and Figure 6.26(b) shows the classification map generated from the estimated abundance. Table 6.10 presents the agreement matrix.

The overall agreement between the classification map generated from the unmixing results and the reference map of Cuprite was of 46.12%. *Chalcedony* was the class with the best between-class agreement (78.88%). *Calcite* and *alunite* obtained 69% and 66% of between-class agreement respectively, and *kaolinite*, *muscovite*, and *kaolinite+smectite* obtained between-class agreement smaller than 43%. Many pixels that belong to *calcite* in the reference map were assigned to *chalcedony* (1036 pixels), *kaolinite+smectite* (781 pixels), and *muscovite* (534 pixels). Many pixels labeled as *alunite* in the reference map were assigned to *kaolinite* (3302 pixels), *chalcedony* (2653 pixels),

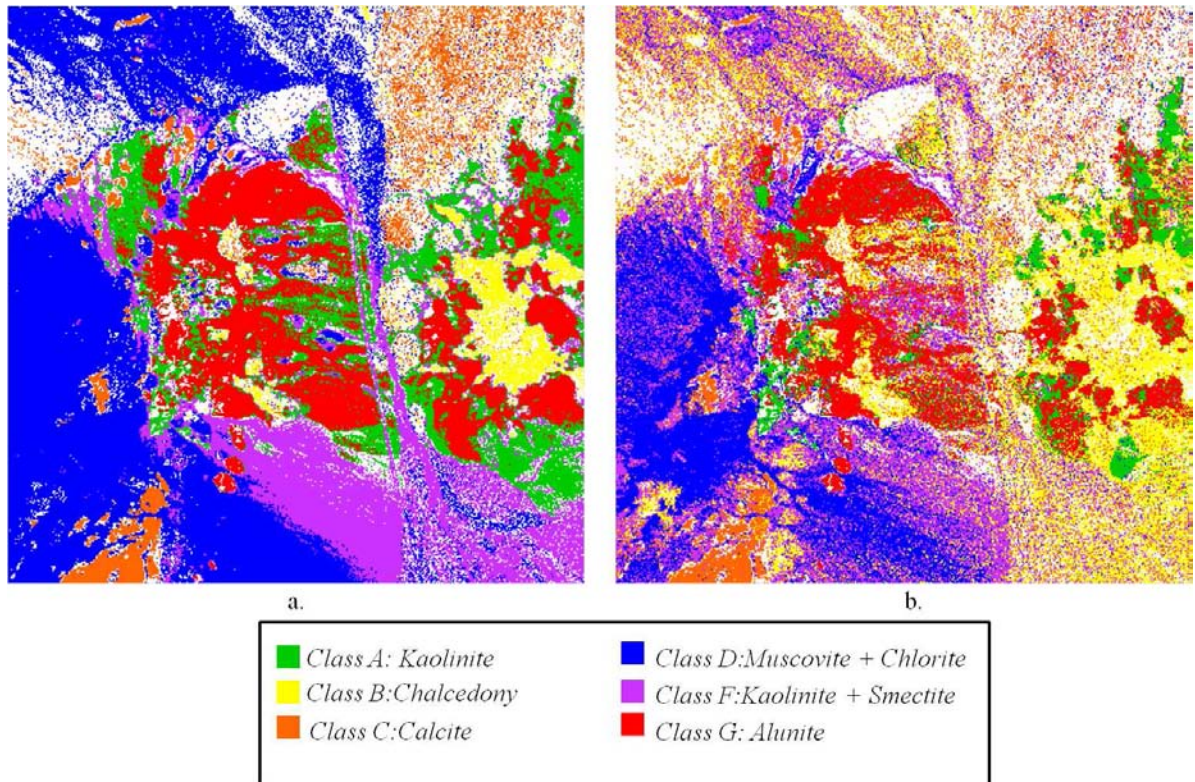


Figure 6.26: Classification map from unmixing results of Cuprite. (a) Reference map, (b) Classification map using the abundances and the majority vote criterion.

Table 6.10: Agreement matrix between reference map and generated classification map from unmixing results of Cuprite.

	A	B	C	D	E	F	TOTAL	BETWEEN CLASS AGREEMENT (%)
<i>Kaolinite</i>	4062	7026	1407	764	3201	1559	18020	22.54
<i>Chalcedony</i>	4	3331	649	125	76	38	4223	78.88
<i>Calcite</i>	10	1036	5828	534	781	178	8367	69.65
<i>Muscovite</i>	2	8323	4561	18653	15787	59	47385	39.36
<i>Kaolite+Smectite</i>	103	7552	1408	3358	9611	35	22067	43.55
<i>Alumite</i>	3302	2653	530	124	1317	15438	23364	66.08
TOTAL	7483	29921	14384	23558	30773	17307	OVERALL CLASS AGREEMENT (%)	46.12
ASSIGNMENT CLASS AGREEMENT (%)	54.28	11.13	40.52	79.18	31.23	89.20		

and *kaolinite+smectite* (1317 pixels). *Kaolinite* was the class with the lowest between-class agreement. Most of the pixels belonging to *kaolinite* were assigned to *chalcedony* (7026 pixels), and *kaolinite* pixels also were assigned to *kaolinite+smectite* (3201 pixels), *alunite* (1559 pixels) and *calcite* (1407 pixels). Many *muscovite* pixels were assigned to *kaolinite+smectite* (15787 pixels), *chalcedony* (8323 pixels) and *calcite* (4561 pixels). *Kaolinite+smectite* pixels are assigned to *chalcedony* (7552 pixels) and *muscovite* (3358 pixels). The high number of pixels assigned to *chalcedony* class that are not part of this class in the reference map are the result of the grouping of different spectra inside of the spectral endmember class EC5 (see Figure 6.17(b)) that is part of *chalcedony* class (see Table 6.5). It is expected that pixels labeled as *kaolinite+smectite* in the reference map are found into *muscovite* class since the reference map indicates that this material is in some of these pixels according the classification map (Figure 6.4). In general, the mixing of materials present in Cuprite make it difficult the identification of information classes without overlapping of information. The similarity among spectra (e.g. *kaolinite+smectite*, *muscovite*, and *chalcedony*), and the clustering of different spectral endmembers into the same spectral endmember class (e.g. EC5 belong to *chalcedony* class) difficult obtaining a better overall agreement.

6.3.4 Analysis of Results

The entropy change method proposed for the selection of an optimal scale in Section 3.2.1.5 presents a consistent performance for A.P. Hill and Cuprite. The proposed method selected a smoothed image in the firsts few iterations (fifth iteration) for A.P. Hill image. In the case of Cuprite, the proposed method selected the thirteenth iteration. However, the diffusion balance did not allow to select a scale for Cuprite. The entropy change criterion shows a behavior similar to that obtained with the images in Section 3.3 regardless the complexity of A.P. Hill and Cuprite scenes.

Davies and Bouldin validity index obtained an adequate number of spectral end-member classes for both images. This index estimated 14 spectral endmember classes for A.P. Hill and 17 for Cuprite using complete linkage. Note that 14 and 25 classes are identified in the reference maps. In addition, Davies and Bouldin index also estimated the best number of spectral endmember classes for the False Leaf image in Section 4.3.3.2 using complete linkage. Thus, this validity index is selected for the estimation of the number of spectral endmember classes within the proposed approach.

Comparing the estimated number of spectral endmember classes by the validity index with other methods for estimation of the number of endmembers such as HySIME and the rank of the covariance and correlation matrices (Table 6.3), the advantage of using spatial information is clear. The rank of the covariance and correlation matrices only estimated up to 6 endmembers for both images. On the other hand, HySIME estimated 21 endmembers for A.P. Hill, but only 6 for Cuprite image.

Unmixing results obtained for the proposed approach from A.P. Hill and Cuprite were evaluated using the proposed methodology in Section 6.2. First, spectral end-member classes and their abundances were analytically compared to published classification maps and spectral libraries. 9 of the 14 classes of A.P. Hill were detected using the unsupervised unmixing analysis. The class *autumn deciduous* was grouped into one single spectral endmember class and the *water river* was split into several spectral endmember classes. However, the spatial distribution of the abundances in A.P. Hill were consistent with the classification map as well as the shape of extracted spectral endmembers were very similar to the spectra in the library. For Cuprite, 6 distinct materials were clearly identified and related to 14 of the classes of Cuprite.

Once the relations between the spectral endmembers classes and the information classes in the classification map were established, the quantitative assessment based on detection theory (Section 6.3.3.2) allows to compute three statistics to characterize

the unmixing results: true positive rate, false positive rate, and false negative rate. Most of the classes in both images have true positive rates higher than 70%, and false positive rates between 15% and 65%. In the comparison between abundance and mask from the false positive pixels (Figures 6.20, 6.21, and 6.23) was clear that most of the false positive pixels have smaller estimated abundances than true positive pixels. This can also be noted in the histograms of estimated abundances (Figure 6.22 and Figure 6.24).

Finally, new classification maps were generated using the estimated abundance by the proposed approach and a majority vote criterion for both A.P. Hill and Cuprite. The overall agreements between the new classification maps and the published reference maps were of 50% and 46% for A.P. Hill and Cuprite respectively. The differences found between the new classification and the published maps are due to several reasons. For instance, the grouping of different materials into a same end-member class by the clustering algorithm because spectral similarity produces lower assignment-class agreement such as the obtained for the *chalcedony* class of Cuprite and the *summer deciduous* class of A.P. Hill. In addition, the accuracy of published classification maps is not available allowing us only to do relative analysis. Despite the low percentages of agreement between the classification maps, the agreement analysis is very important for the comparison of the proposed algorithm with other unmixing techniques as will see in the next chapter.

6.4 SPATIAL RESOLUTION EFFECTS

Unmixing results for two images from the Guanica Forest (see Section 6.1.3) collected at 1 (I1) meter and 4 (I4) meters are used to evaluate the performance with respect to spatial resolution. Multiscale representation using the nonlinear diffusion algorithm of Duarte et al. [26] was done for both images. The scale step μ was set in 5 and

the final scale to 100 obtaining 20 smoothed images for both I₁ and I₄. The diffusion parameter α was set to 0.005 for I₄ and 0.01 for the image I₁. Values of diffusion parameter were selected experimentally as described by Duarte et al. [26]. Entropy change was used to select the adequate scale for the unmixing analysis. The sixth iteration was selected for I₁ and the fifth iteration for I₄ (see Figure 6.27(a) and 6.27(b)). RGB composites for the selected smoothed images are presented in Figures 6.27(c) and 6.27(d) using bands 54 (639 nm), 35 (550 nm), and 15 (459 nm). Using the proposed spectral endmember extraction process, 447 spectral endmembers were extracted from I₁ and 148 from I₄. Complete linkage and SAM were used to build the spectral endmember classes. The number of spectral endmember classes was estimated using the Davies and Buildin index obtaining 11 and 9 spectral endmember classes for I₁ and I₄ respectively. Figure 6.28 presents the validity index graphs.

The spectral endmember classes were organized in four groups to compare the results. Figure 6.29 presents the abundances estimated from the spectral endmember classes for both Guanica images. The first group shows the spectral endmember classes related with vegetation: EC₁ to EC₃ from I₁, and EC₁ to EC₄ from I₄. The second group presents the spectral endmember classes for soil. This group includes the dirty road and is formed by the spectral endmember classes EC₄ to EC₆ from I₁, and EC₅ to EC₆ from I₄. The next group includes the spectral endmember classes related with manmade materials such as buildings and paved road. This group is formed by the spectral endmember classes EC₇ to EC₉ for I₁ and EC₇ to EC₉ for I₄. Other two spectral endmember classes were obtained for I₁: EC₁₀ and EC₁₁. Figure 6.30 presents the spectral endmembers corresponding to each spectral endmember class.

EC₁ spectral endmember class from I₁ identified the grass or low vegetation and EC₂ is related with the forest vegetation (tall vegetation). The spectra of vegetation spectral endmember classes have a high variability for image I₁. Spectral endmember classes EC₄ to EC₆ detected the dirt road and regions with open soil. The three

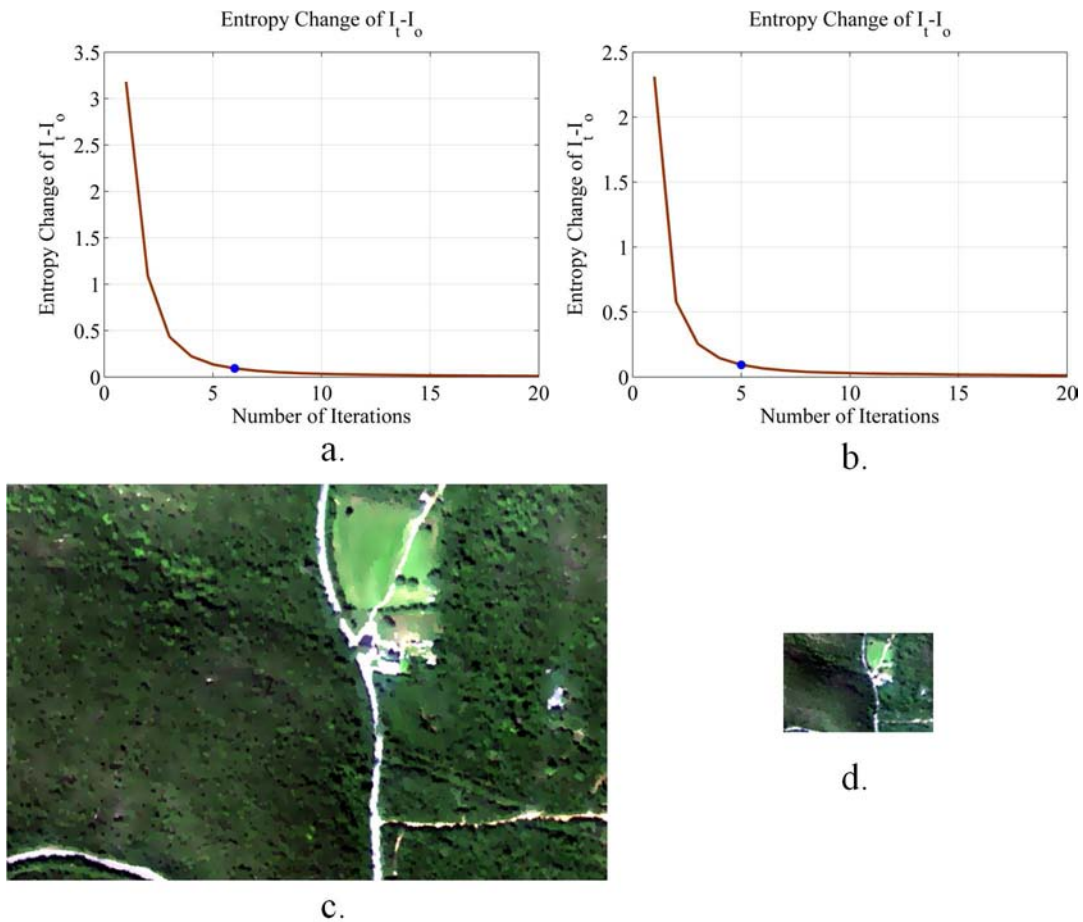


Figure 6.27: Scale selection for Guanica images. Entropy change criteria for Guanica images to (a) 1 meter and (b) 4 meters. RGB composition of selected scale using bands 54, 35, and 15 for images to (c) 1 meter and (d) 4 meters.

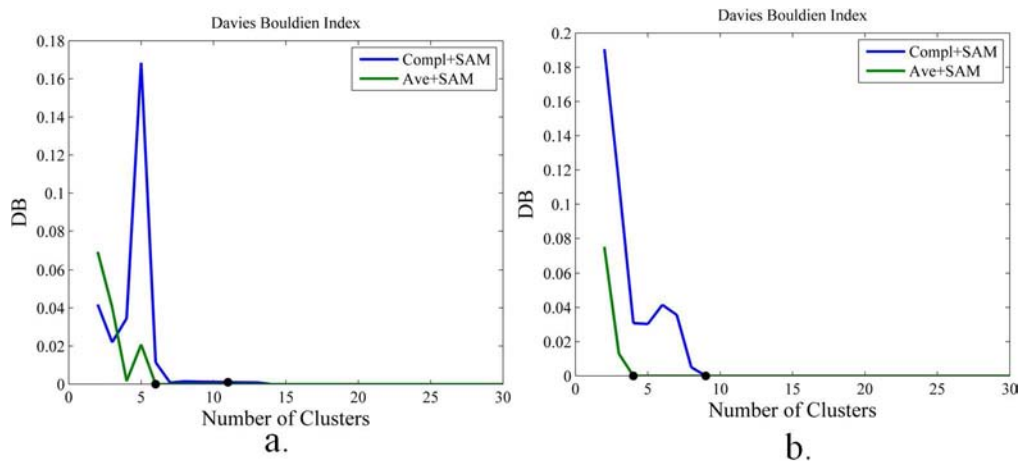


Figure 6.28: Estimation of the number of spectral endmember classes for Guanica images. Davies and Bouldin validity index for Guanica images to (a) 1 meter and (b) 4 meters.

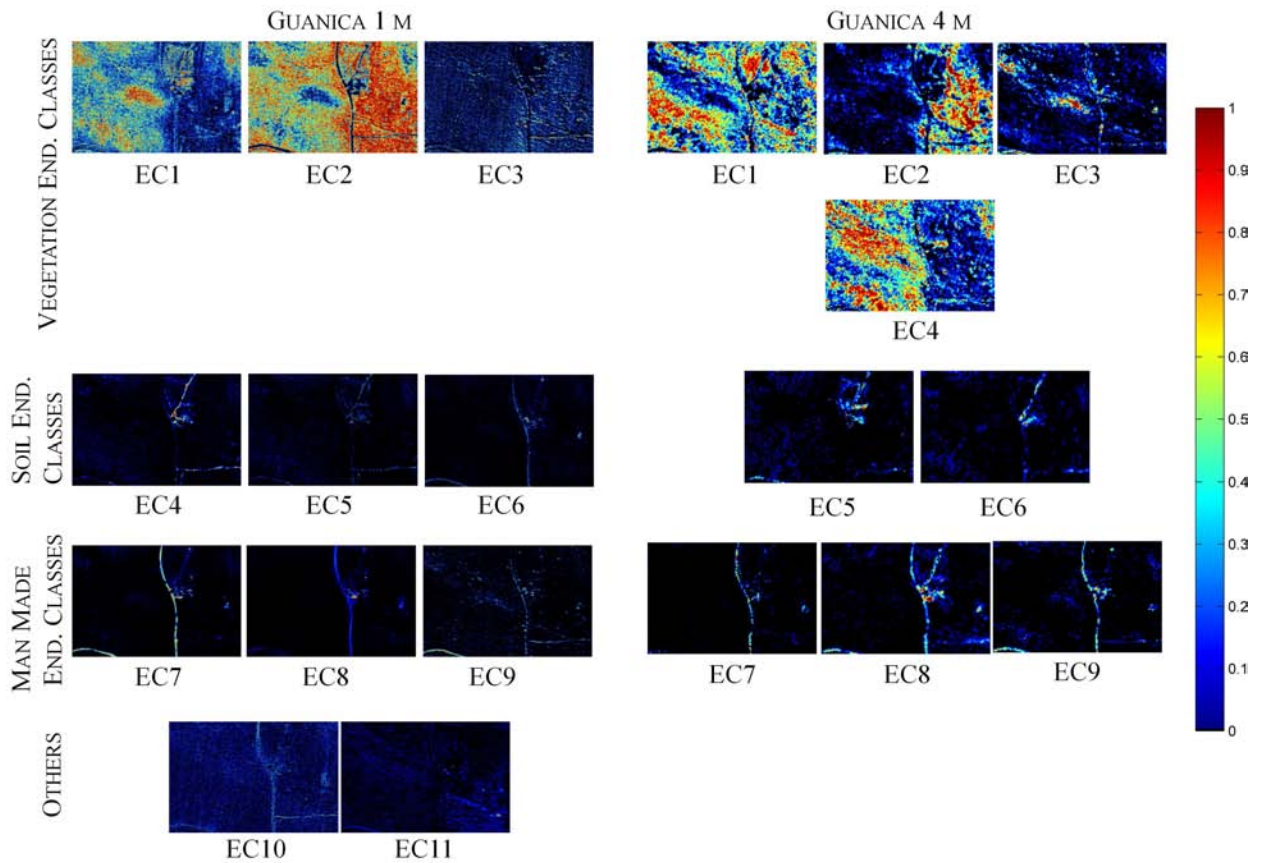


Figure 6.29: Abundances for extracted spectral endmember classes of Guanica images. Left: abundance from 1 meter Guanica image. Right: abundance from 4 meters Guanica image.

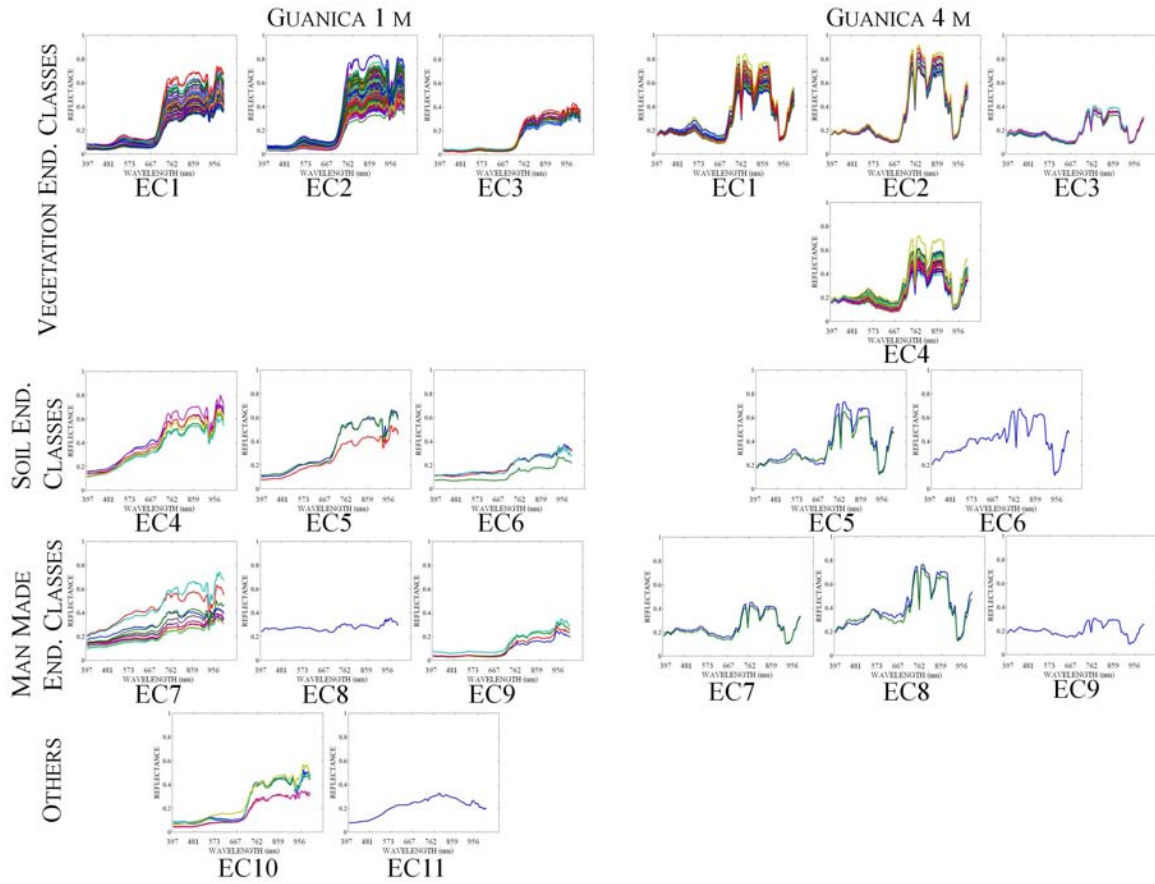


Figure 6.30: Extracted spectral endmember classes for Guanica images. Left: abundance from 1 meter Guanica image. Right: abundance from 4 meters Guanica image.

groups of spectra are consistent and similar. Spectral endmember class EC8 detected the building in the center of the image (see Figure 6.6) and spectral endmember classes EC7 and EC9 detected the paved road.

Unlike the three vegetation spectral endmember classes identified from I₁, spectral endmember classes from I₄ detected three spectral endmember classes associated with the forest vegetation and one with the grass. This over-partition of the forest can be due to topographic effects. This can be noted in the RGB composite of the scenes (see Figure 6.5) that there are shadows over the forest vegetation. Two spectral endmember classes associated with soil were detected in I₄. The building is identified in EC8 and the road in EC7 and EC9. Less variability of spectra within the spectral endmember classes is obtained from I₄ than for I₁.

The spatial resolution affects significantly the extraction of spectral endmember classes related with vegetation. For instance, Figure 6.31 presents a comparison between the spectral endmember class EC2 for image I₁ with the spectral endmember classes EC1 and EC2 for image I₄. The topography effects can be noted in the Figure 6.31 for the spectral endmember classes from the lower spatial resolution image. Figure 6.32 presents the sum of abundance from spectral endmember classes related with vegetation in both image I₁ and I₄. Note the consistence between the distributions of vegetation in both images. Although, the spectral endmember classes related to vegetation individually presents differences such as the shown in Figure 6.31, the complete vegetation in both images is correctly extracted by the proposed unmixing approach..

6.4.1 *Analysis of Results*

Vegetation spectral endmember classes are affected significantly by shadows and topographic effect in the 4 meters image. Forest vegetation is divided in several

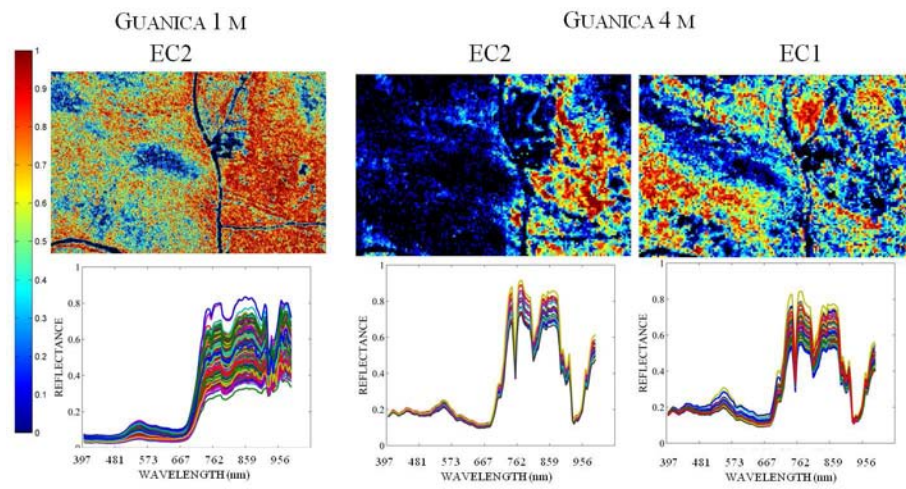


Figure 6.31: Comparison of vegetation spectral endmember classes from Guanica images.

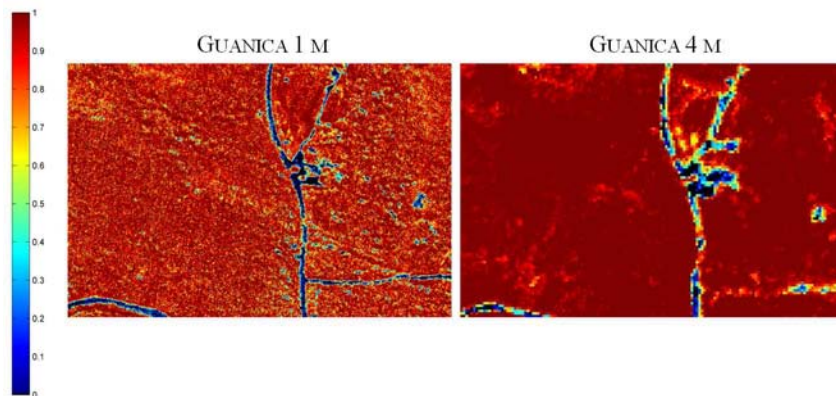


Figure 6.32: Estimated vegetation from Guanica images.

spectral endmember classes with abundances related to the shadows observed in the RGB composite of the image. Vegetation results from 1 meter Guanica were more consistent with the description of this scene found in [68]. Two types of vegetation were identified by the proposed approach over 1 meter Guanica: forest vegetation and grass. Other components of the image such as the roads and soil are represented very consistently at both spatial resolutions. A high variability within the vegetation spectral endmember classes were observed for the unmixing results of 1 meter Guanica as expected due to the higher spatial resolution.

6.5 SUMMARY

Hyperspectral images from different scenarios were used to study the performance of the proposed unsupervised unmixing approach based on multiscale representation. A.P. Hill and Cuprite images allowed the assessment of the proposed scale selection method using entropy change. Smoothed images with fewer iteration were selected by the entropy change criterion in comparison with diffusion balance. In the estimation of the number of spectral endmember classes, the best results were obtained using the Davies and Bouldin index with complete linkage and spectral angle measure. Thus, the entropy change and Davies and Bouldin index are selected for the implementation of the computational system. Unmixing results for A.P. Hill and Cuprite extracted several materials identified in the classification maps. It is important to highlight that the proposed unmixing approach is an unsupervised method that only uses the information within the hyperspectral image. The consistency among spectral endmember classes and the classification maps showed the capabilities of the proposed approach for application where little information about the basic components is available.

Unmixing analysis of Guanica images showed that vegetation spectral endmember classes are affected by topographic effects. Other spectral endmember classes such as manmade and soils appear not affected by the spatial resolution. Results obtained from the image at 1 meter were consistent with the description of the image found in [68].

The proposed approach presented good results for the different scenarios regardless of the complexity of the scene. In addition, entropy change criterion and Davies and Bouldin index appear adequate methods for the scale selection and the estimation of number of spectral endmember classes respectively. These procedures help to automate the proposed approach as illustrated in Figure 1.4. The implementation of a computational system based on the proposed approach for the automatic unmixing analysis of hyperspectral imagery is described in the Chapter 8. In the next chapter, the assessment methodology is used to compare the proposed approach with other unmixing techniques.

This chapter presents a comparison among the proposed unmixing approach, SMACC [33], VCA [34] and RBSPP [17] algorithm using A.P. Hill and Cuprite. These algorithms were selected for several reasons. First, SMACC and VCA are widely used geometric approaches which require only the number of endmembers, and RBSPP is a spatial-spectral approach that does not depend of spatial kernels similar to the proposed approach. In addition, these algorithms assume that endmembers are pixels in the image similar to the developed unmixing approach.

RBSPP is compared with different geometrical and spatial-spectral approaches in [17]. N-FINDR [40, 41], OSP [105], and VCA [34] are used by Martin and Plaza to assess the capabilities of RBSPP. In addition, results from SPP [15], SSEE [14] and AMEE [9] are used by Martin and Plaza to compare RBSPP results. Spectral similarity among extracted endmember and the spectral library of Cuprite are used to compare these algorithms. Endmembers extracted by RBSPP are comparable with results from the other unmixing techniques [17]. The experiments with Cuprite [17] showed that RBSPP helps to reduce the reconstruction errors for OPS and VCA regardless the clustering algorithm employed for segmenting the image. Further, AMEE and SSEE results presented larger reconstruction errors in several pixels than RBSPP combined with VCA, N-FINDR, or OSP [17].

SMACC is included in the ENVI software and a MATLAB implementation of VCA is found on the web page of J. Bioucas-Dias¹. SMACC extracts the endmembers as well as performs abundance estimation. However, the abundances used in the

¹ <http://www.lx.it.pt/bioucas/publications.html>

comparison are estimated by the function NNSLO available in MATLAB (see Section 2.4.1) from the extracted endmembers with ENVI. This function is employed for the three algorithms to ensure equal conditions for all algorithms. RBSPP was implemented following the description presented in [17]. RBSPP requires a clustering algorithm and a segmentation procedure to find the spectrally uniform regions. ISODATA and segmentation functions of ENVI were used. The minimum number of clusters was set to p (the number of endmembers) and the maximum to $2 * p$ as suggested in [17]. The segmentation results were used in MATLAB where the orthogonal projection was implemented for the selection of the more distinct regions. VCA was used to extract endmembers using as input the pixels within selected regions. For all algorithms, the number of endmembers p was set equal to the number of spectral endmember classes estimated using the proposed approach: 14 for A.P. Hill and 17 for Cuprite.

7.1 UNMIXING ANALYSIS OF A.P. HILL

Unmixing results of A.P. Hill using SMACC, VCA and RBSPP combined with VCA are presented in Section 7.1.1. Then, the assessment methodology presented in Section 6.2 is used to evaluate SMACC, VCA, and RBSPP results (Section 7.1.2). The quantitative analysis based on detection theory and classification agreement provides different statistics allowing to compare the performance of the proposed approach with SMACC, VCA, and RBSPP.

7.1.1 *Unmixing using SMACC, VCA, and RBSPP for A.P. Hill*

SMACC, VCA, and RBSPP were used to extract the endmembers for A.P Hill setting the number of endmembers to 14. NNSLO was used to estimate the abundances.

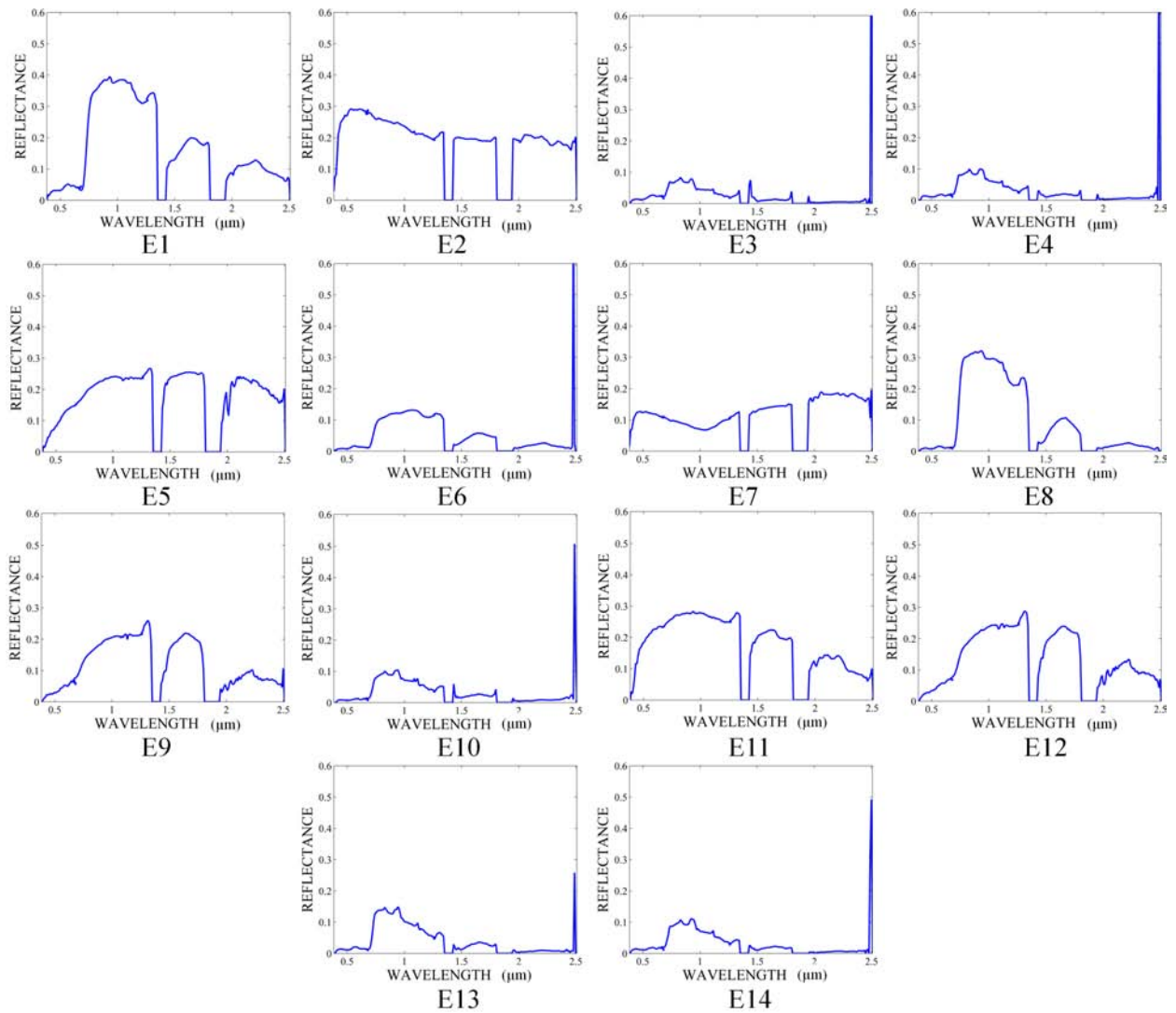


Figure 7.1: Extracted endmembers from A.P. Hill using SMACC.

Figures 7.1 to 7.6 present the unmixing results obtained for SMACC, VCA, and RB-SPP combined with VCA for A.P. Hill. Figures 7.1, 7.3, and 7.5 present the spectra for the extracted endmembers, and Figures 7.2, 7.4, and 7.6 present the estimated abundance using NNSLO.

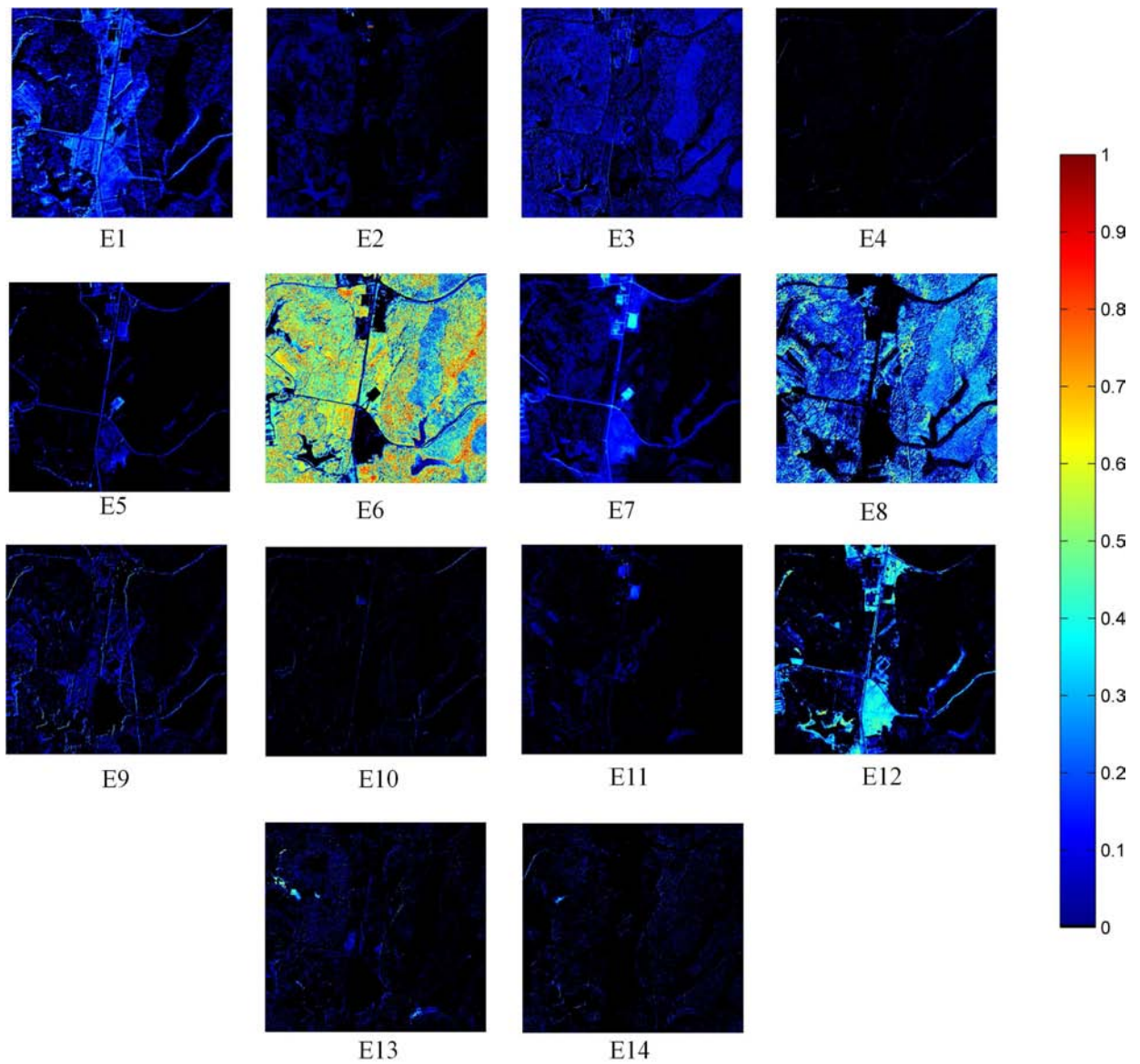


Figure 7.2: Abundances for extracted endmembers from A.P. Hill using SMACC.

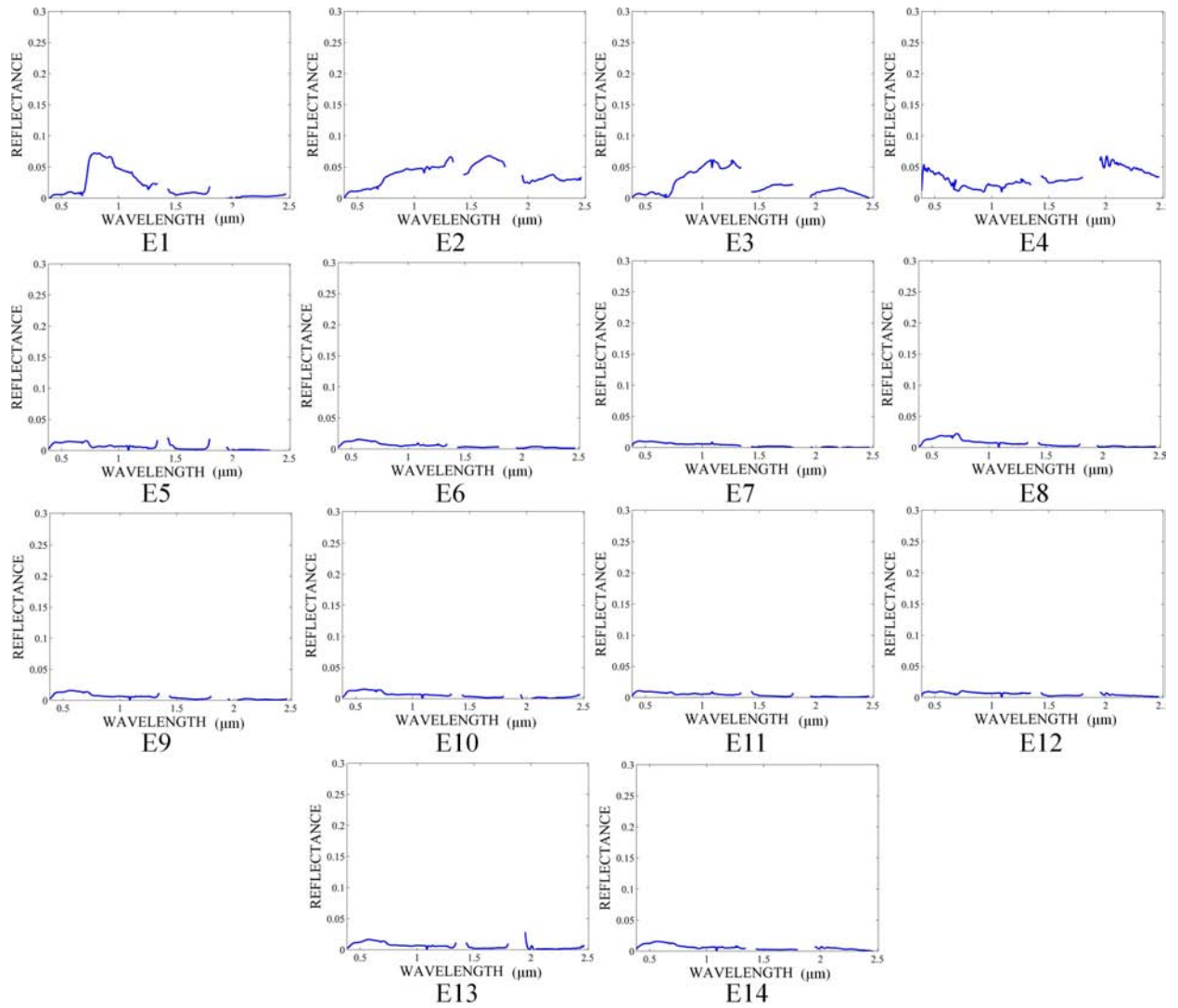


Figure 7.3: Extracted endmembers from A.P. Hill using VCA.

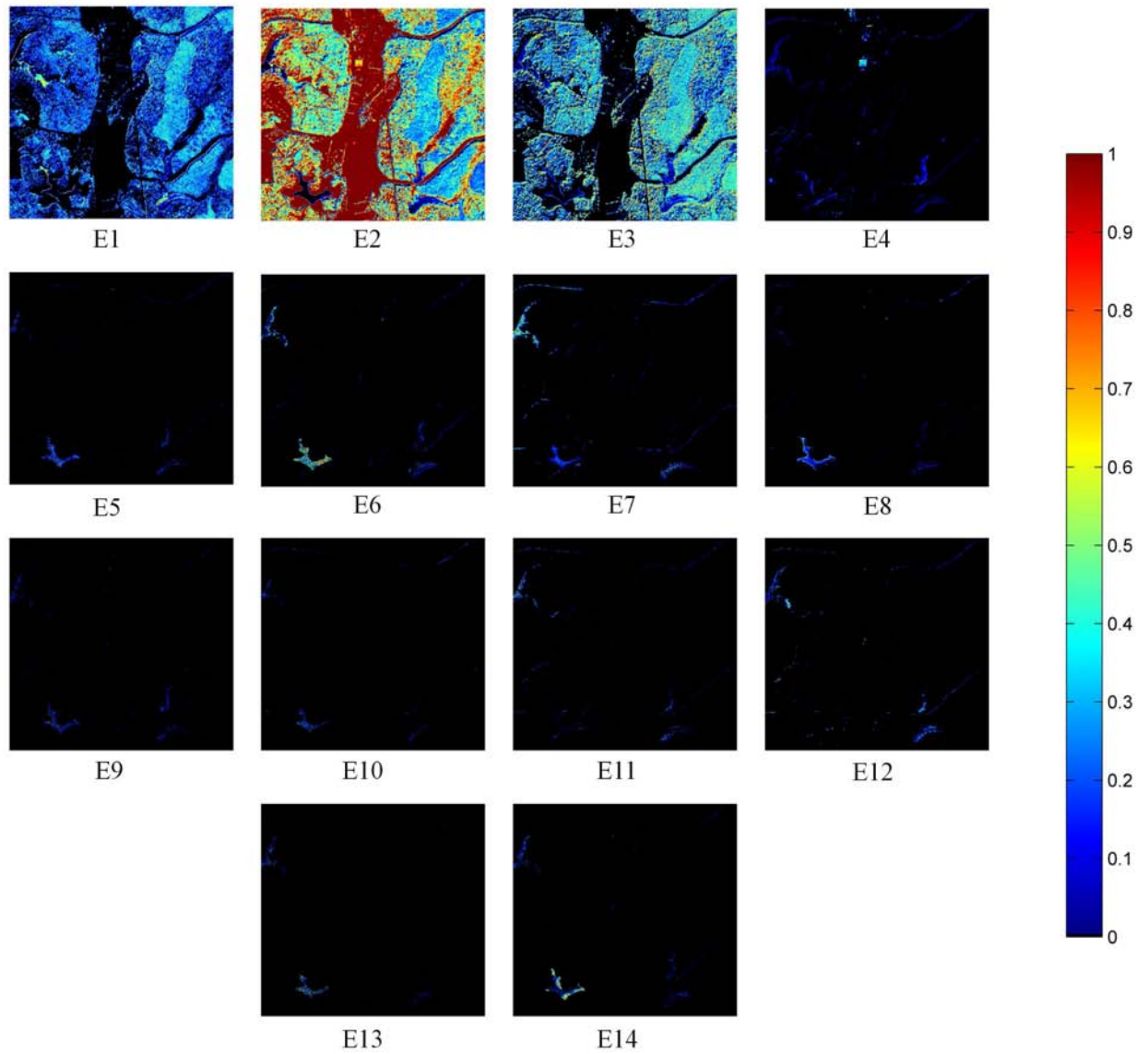


Figure 7.4: Abundances for extracted endmembers from A.P. Hill using VCA.

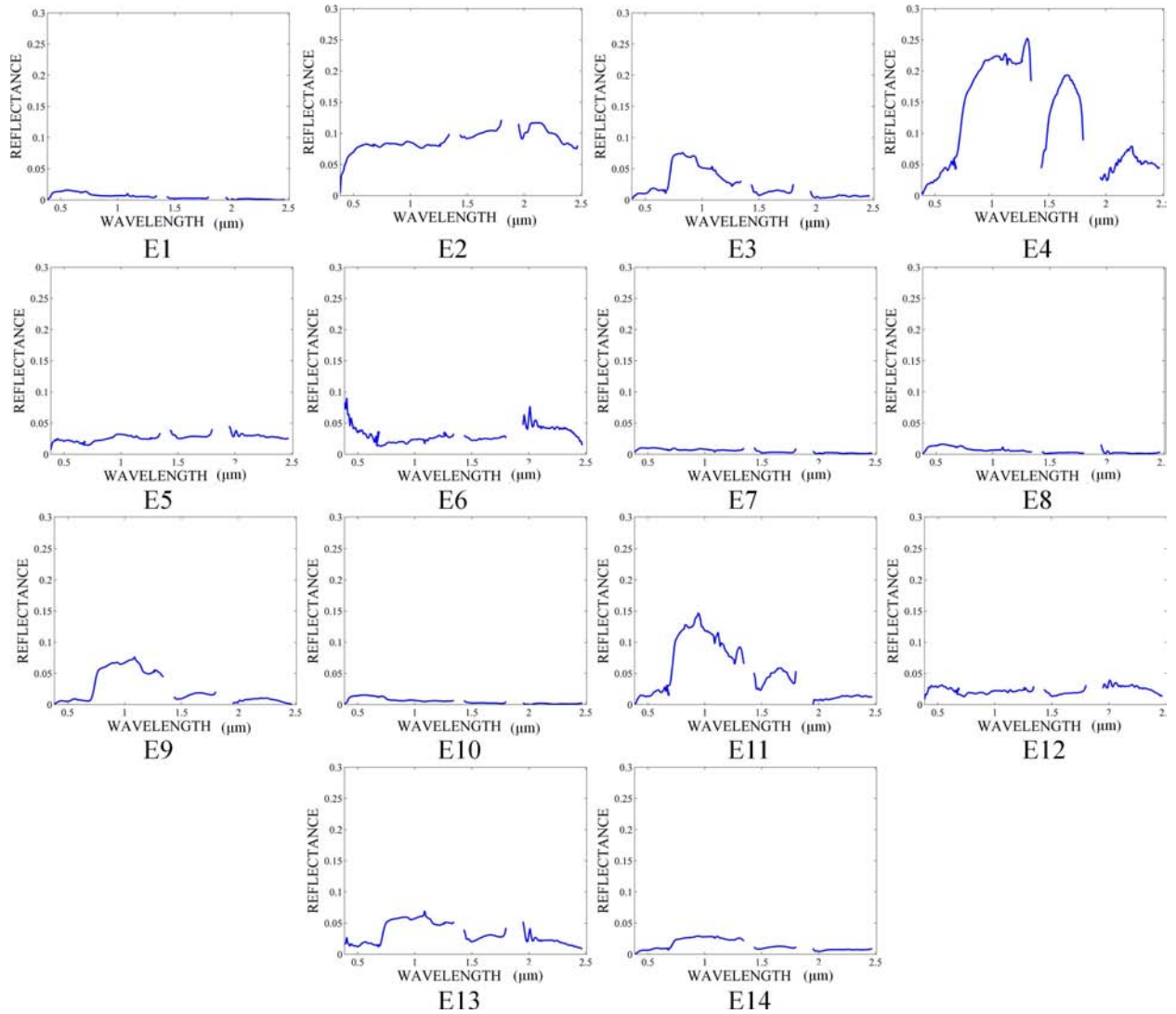


Figure 7.5: Extracted endmembers from A.P. Hill using RBSPP combined with VCA.

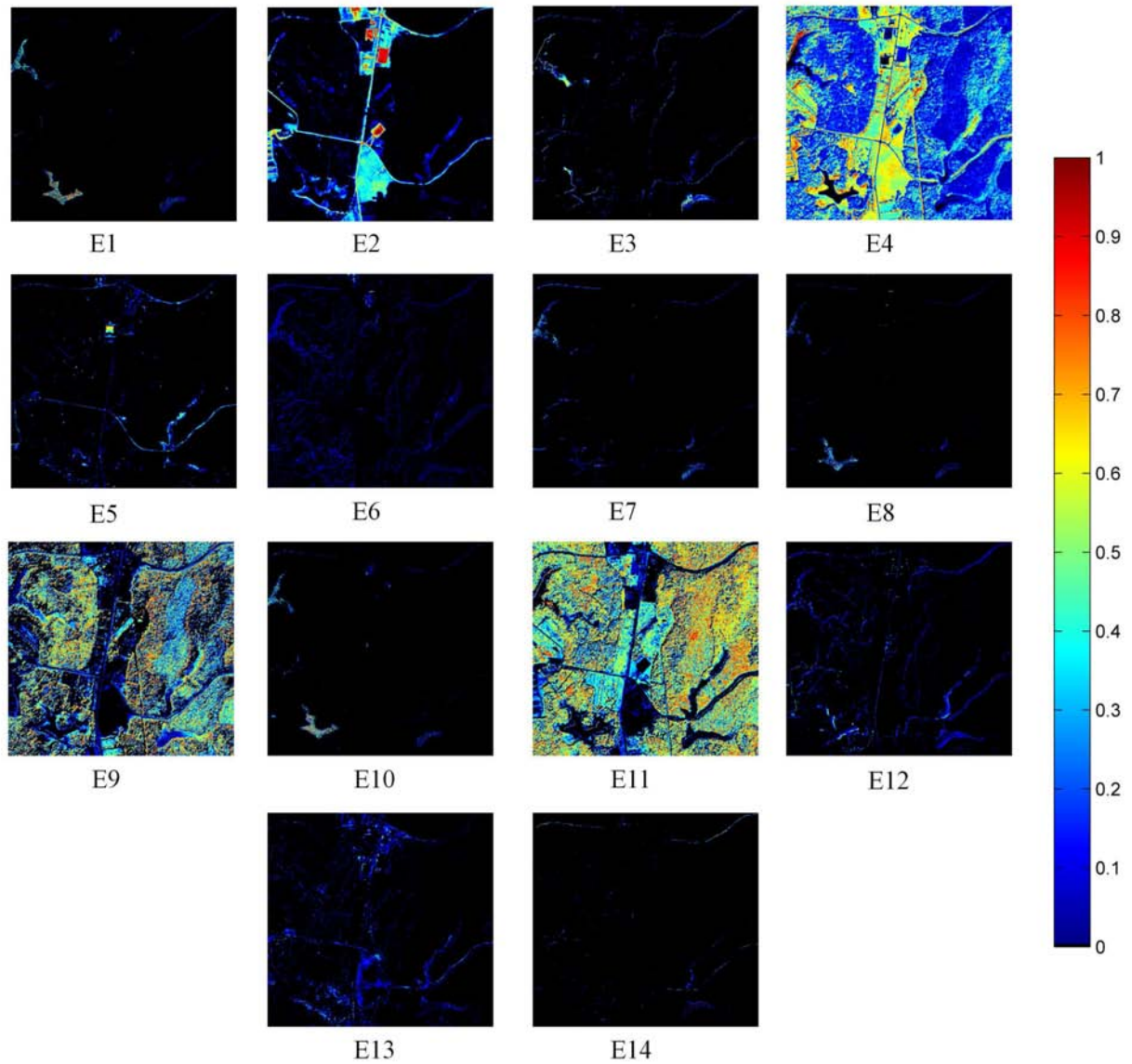


Figure 7.6: Abundances for extracted endmembers from A.P. Hill using RBSPP combined with VCA.

7.1.2 *Assessment of Unmixing Results*

Unmixing assessments of SMACC, VCA, and RBSPP results for A.P. Hill are performed using the methodology presented in Section 6.2. First, a comparison among the extracted endmembers and estimated abundances with published spectral libraries and classification maps is performed (Section 7.1.2.1). Then, the quantitative assessment is performed using true positive rate, false positive rate, and false negative rate described in Section 7.1.2.2. These statistics are used to compare the performance of the proposed approach with the other unmixing techniques. Finally, classification maps are generated from the estimated abundance, and these are compared with the reference maps in Section 7.1.2.3.

7.1.2.1 *Qualitative Evaluation*

Unmixing of A.P.Hill using SMACC extracted endmembers (Figure 7.1) related to the classes of *green field* (endmember E1), *summer deciduous forest* (endmember E6), *loblolly pine* (endmember E8), and *grass field* (endmembers E9 and E12). Endmember E9 is very similar to E12 but its abundances is less than 20% along the whole image. Endmember E5 is related with *gravel* class and has a signature very similar to the spectrum in the spectral library (Figure 6.2). However, the abundance for E5 is less than 20% for pixels identified as *gravel* for the classification map. Endmembers E11 and E7 are related to *generic road* class but their abundances also are less than 20%. Endmember E3 includes *river water* and *shaded vegetation*. The remaining endmembers are very difficult to relate with the classes in the classification map and the spectral library of A.P. Hill since the shapes or abundance do not correspond with any of the classes.

VCA presents poor results for A.P. Hill image. Endmembers E5 to E14 (Figure 7.3) have signatures very similar to *river water*. Any endmembers extracted with VCA

Table 7.1: Relation between endmembers extracted by SMACC and RBSPP, and information classes for A.P. Hill.

Information Class	Group Name	SMACC Endmembers	RBSPP Endmembers
<i>loblolly pine</i>	<i>loblolly pine</i>	E8	E9
<i>summer deciduous</i>	<i>summer deciduous</i>	E6	E11
<i>soil ag field, generic road, gravel</i>	<i>soil</i>	E2, E5, E7, E11	E2, E5
<i>shaded vegetation</i>	<i>shaded vegetation</i>	E4, E13, E14	E3
<i>green ag field</i>	<i>green field</i>	E1	NOT DETECTED
<i>grass field</i>	<i>grass field</i>	E9, E12	E4
<i>autumn deciduous</i>	<i>autumn deciduous</i>	NOT DETECTED	NOT DETECTED
<i>river water</i>	<i>water</i>	E3	E1, E7, E8, E10

have the shape of a vegetation signature. VCA results are not taken into account for the quantitative comparison of A.P. Hill unmixing results. RBSPP preprocessing algorithm helps to improve a little bit the results obtained by VCA. RBSPP combined with VCA identified endmembers (see Figure 7.5) related with *grass field* (endmember E4), *summer deciduous forest* (endmember E11), *loblolly pine* (endmember E9), *gravel* (endmember E2), and *shaded vegetation* (endmember E3). Endmember E5 is related with *generic road*, and endmembers E1, E7, E8, and E10 are related with *river water*. Any other endmember cannot be related with the information in the classification map and the spectral library.

Table 7.1 presents a summary of the relation among the endmembers extracted by SMACC and RBSPP, and the information classes. VCA is not taken into account for this analysis since the obtained unmixing results are poor, and these cannot be related with the classes in the classification map. *Autumn deciduous* class is not extracted by neither SMACC or RBSPP. In addition, *green field* is not extracted by RBSPP.

Figure 7.7 presents a comparison of two classes detected by all unmixing algorithms including the proposed approach. Figures 7.7(a-d) present the estimated abundances corresponding with the *loblolly pine* class. The endmembers are shown

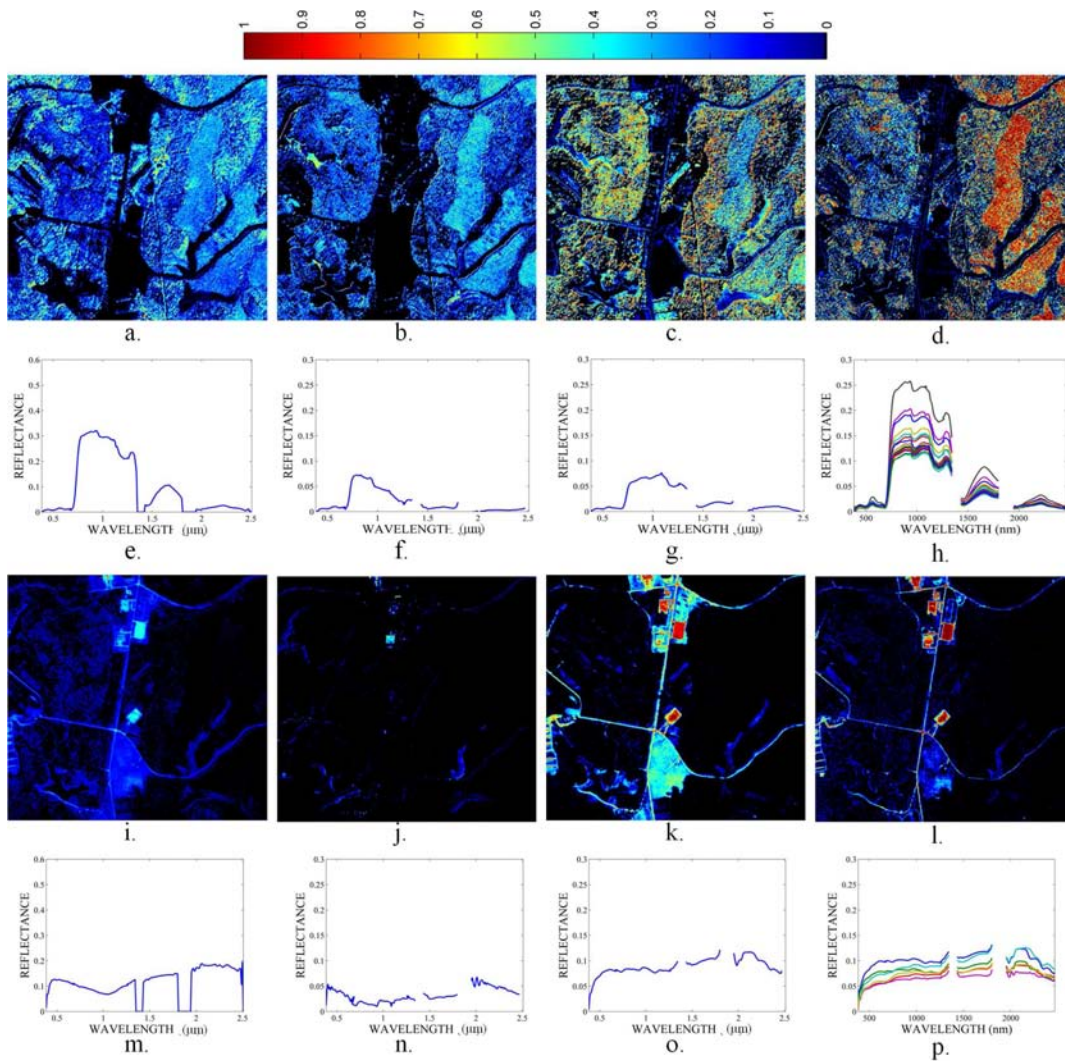


Figure 7.7: Comparison of *loblolly pine* and *gravel* endmembers. Abundances and endmembers for *loblolly pine* (a)-(h) and *gravel* (i)-(p) extracted using SMACC, VCA, RB-SPP, and the proposed approach.

in Figures 7.7(e-h). Only SMACC and the proposed approach based on multiscale segmentation obtained spectra consistent with the signatures in the spectral library for *loblolly pine*. In addition, Figures 7.7(i)-(l) present the estimated abundances for the endmembers closest to *gravel* class and Figure 7.7(m)-(p) present their respective spectral signatures. Endmember E2 of RBSPP (Figure 7.7(o)) and the spectral endmember class E4 (Figure 7.7(p)) extracted by the proposed approach are clearly related to *gravel*. However, extracted spectra by SMACC and VCA are not consistent with *gravel* signature in the spectral library (Figure 6.2).

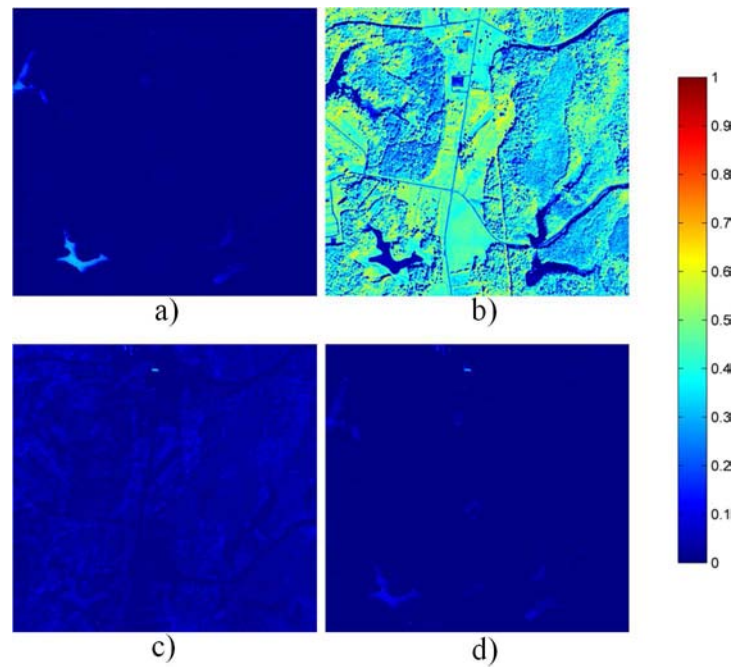


Figure 7.8: Reconstruction error from unmixing results of A.P. Hill. (a) SMACC, (b) VCA, (c) RBSPP combined with VCA, and (d) proposed approach based on multiscale representation.

The reconstruction error from the unmixing results of SMACC, VCA, RBSPP and the proposed approach were calculated. These are presented in Figure 7.8. The largest errors were obtained for VCA as expected since this algorithm did not extract any endmember related with classes in the classification map; most of the extracted endmembers correspond to water signatures. SMACC obtained errors around 30% for some pixels of water. Both spatial-spectral algorithms, RBSPP and the proposed approach, obtained the lowest reconstruction errors.

7.1.2.2 Quantitative Assessment of Detected Classes

Figures 7.9, 7.10, and 7.12 show the comparison among the estimated abundances (first column), the masks generated from the information classes within the classification map (second column), and the masks that identified the true positive, false positive, and false negative pixels (third to fifth column) for A.P. Hill using SMACC (Figures 7.9 and 7.10), and RBSPP (Figure 7.12). Tables 7.2 and 7.3 summarize the

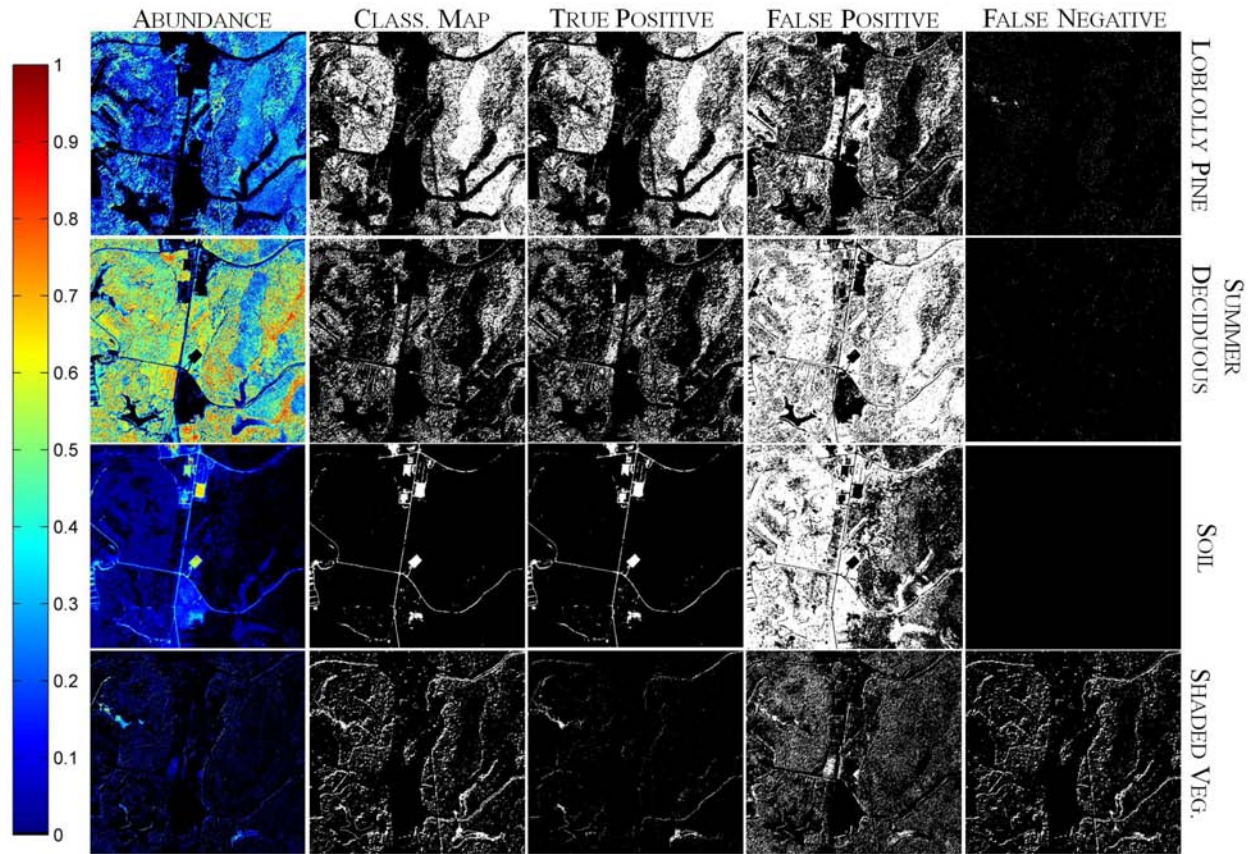


Figure 7.9: Comparison among abundances, classification map, and true positives, false positives, and false negatives of *loblolly pine*, *summer deciduous*, *soil*, *shaded vegetation* classes extracted using SMACC.

true positive rate, false positive rate, and false negative rate for each information class. In addition, Tables 7.2 and 7.3 include the average and standard deviation of estimated abundances for true positive and false positive pixels. Figures 7.11 and 7.13 show the histogram for the estimated abundances corresponding to true positive and false positive pixels obtained from SMACC and RBSPP results respectively.

SMACC extracted *loblolly pine*, *summer deciduous*, *soil*, *green field*, and *grass field* classes with true positive rates larger than 96%. But, the estimated abundances for *loblolly pine*, *green field*, and *grass field* are small with averages of 0.21, 0.19, and 0.34 respectively. On the other hand, *shaded vegetation* and *water* classes extracted using SMACC obtained 13% and 57% of true positive rates. A high false positive rate is

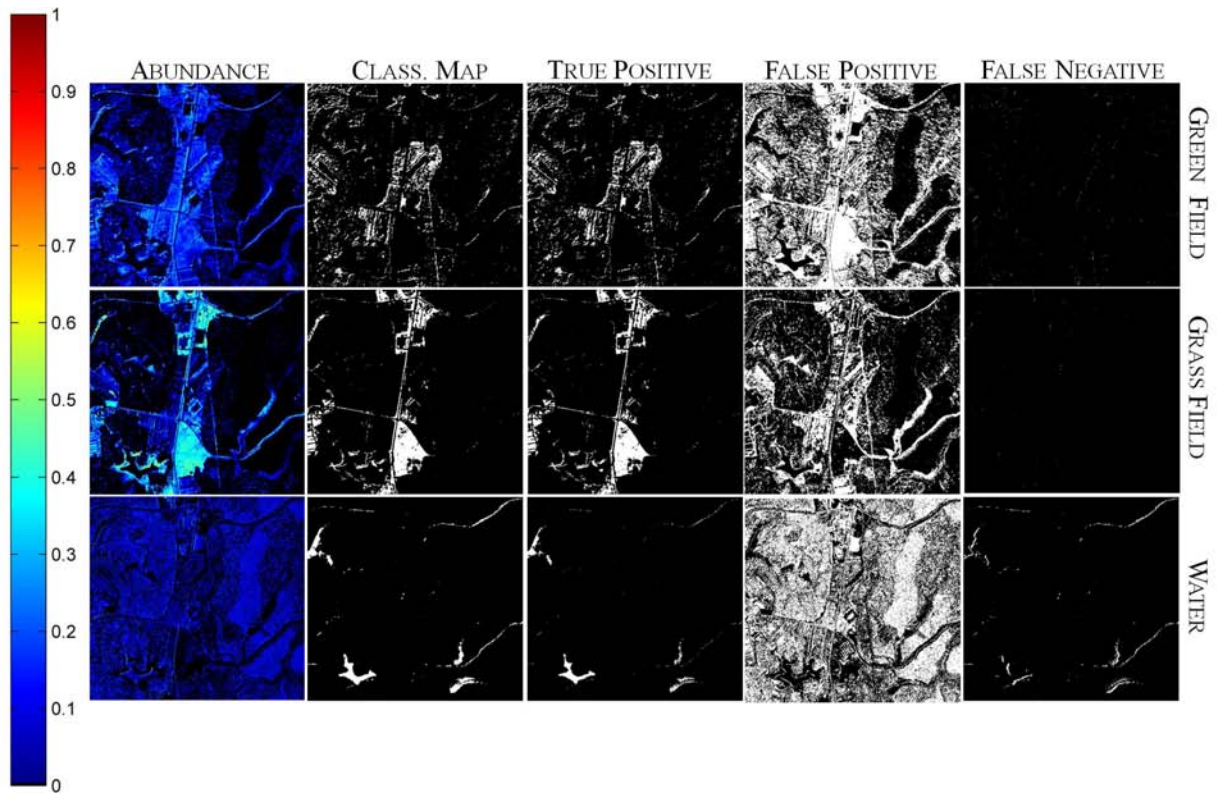


Figure 7.10: Comparison among abundances, classification map, and true positives, false positives, and false negatives of *green field*, *grass field*, and *water* classes extracted using SMACC.

Table 7.2: True positive, false positive, and false negative rates for A.P. Hill classes extracted using SMACC.

ID	Class	True Positive			False Positive			False Negative
		%	Abundance		%	Abundance		
			Mean	σ		Mean	σ	
A	<i>loblolly pine</i>	97.98	0.21	0.09	53.74	0.25	0.17	2.01
B	<i>sum. deciduous</i>	99.63	0.55	0.16	88.35	0.45	0.21	0.23
C	<i>soil</i>	99.98	0.38	0.15	58.10	0.03	0.05	0.02
D	<i>shaded Veg.</i>	13.80	0.15	0.13	16.86	0.08	0.08	86.20
E	<i>green field</i>	96.91	0.19	0.09	48.07	0.09	0.08	3.06
F	<i>grass field</i>	99.57	0.34	0.09	26.39	0.12	0.11	0.43
G	<i>autumn decid.</i>	~	~	~	~	~	~	100
H	<i>water</i>	57.22	0.004	0.04	56.63	0.07	0.05	42.78

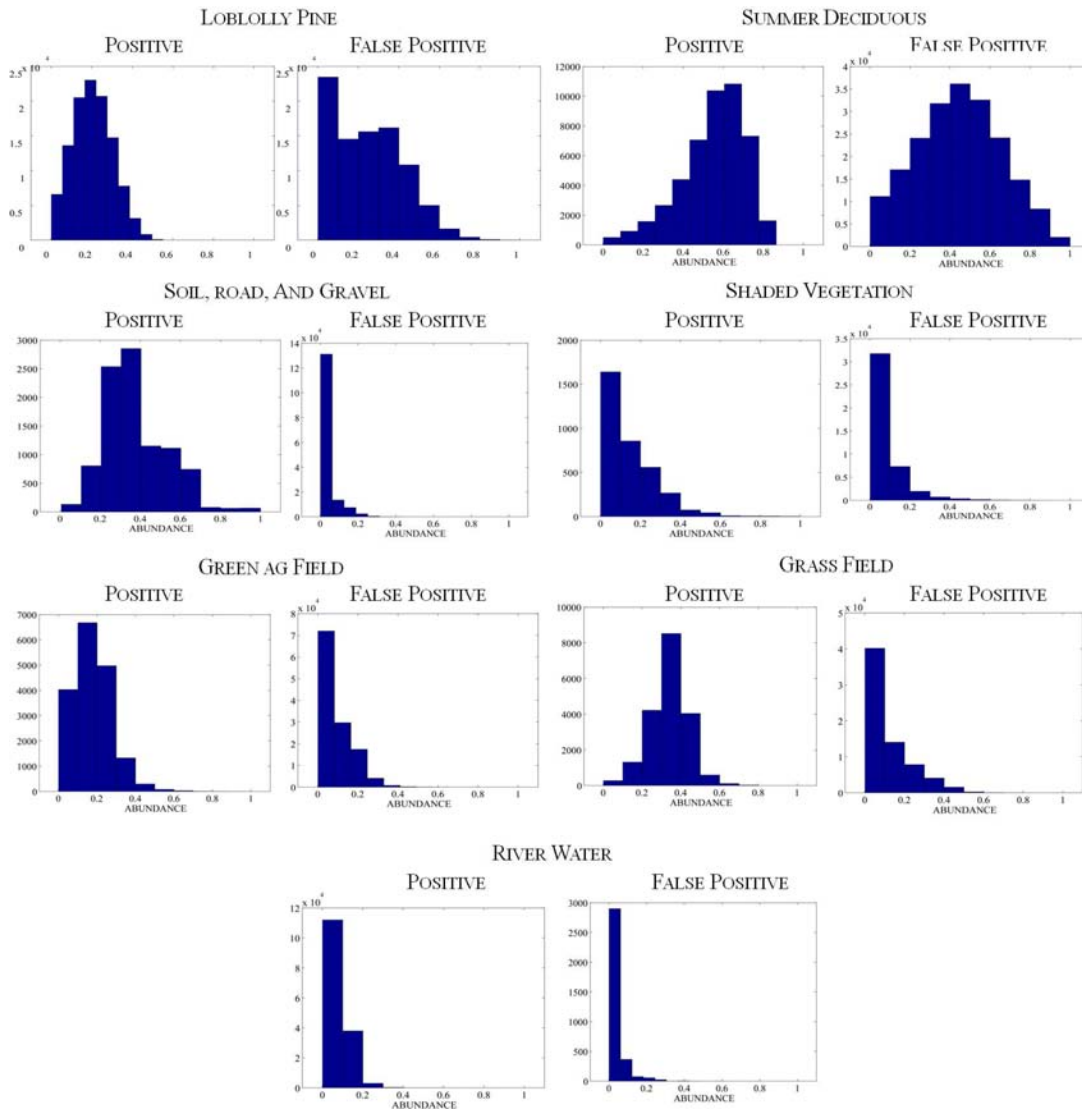


Figure 7.11: Histogram for the abundances of true positive and false positive pixels of A.P. Hill classes extracted using SMACC.

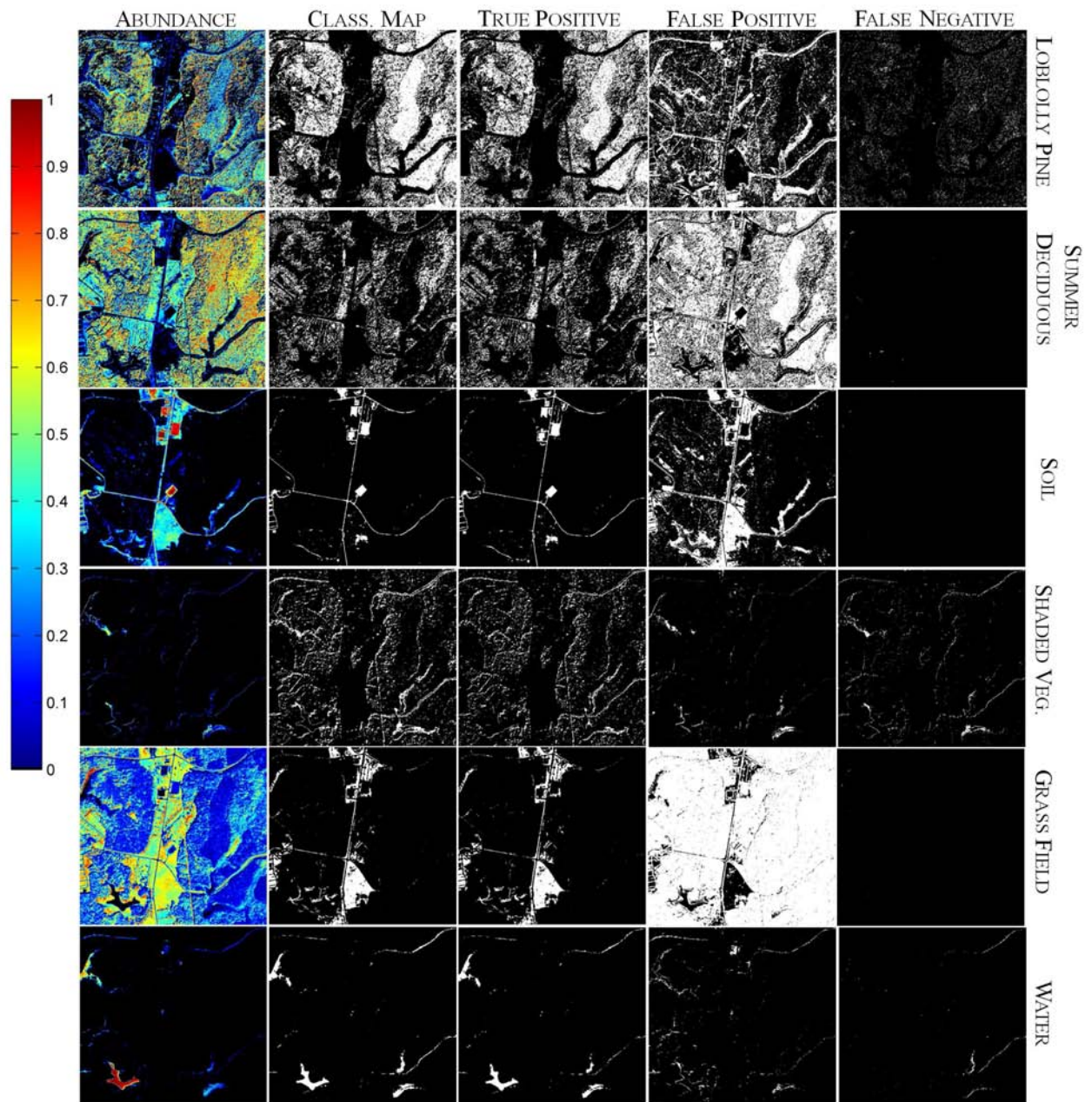


Figure 7.12: Comparison among abundances, classification map, and true positives, false positives, and false negatives of *loblolly pine*, *summer deciduous*, *soil*, *shaded vegetation*, *grass field*, and *water* classes extracted using RBSPP.

Table 7.3: True positive, false positive, and false negative rates for A.P. Hill classes extracted using RBSPP.

ID	Class	True Positive			False Positive			False Negative
		%	Abundance		%	Abundance		
			Mean	σ		Mean	σ	
A	<i>loblolly pine</i>	89.01	0.38	0.22	42.35	0.39	0.28	10.99
B	<i>sum. deciduous</i>	100	0.60	0.09	74.69	0.42	0.24	0
C	<i>soil</i>	99.80	0.65	0.15	17.12	0.20	0.16	0.20
D	<i>shaded veg.</i>	18.47	0.21	0.19	1.20	0.11	0.12	81.53
E	<i>green field</i>	~	~	~	~	~	~	100
F	<i>grass field</i>	100	0.63	0.09	97.50	0.27	0.19	0
G	<i>autumn decid.</i>	~	~	~	~	~	~	100
H	<i>water</i>	87.08	0.49	0.34	1.42	0.14	0.13	12.92

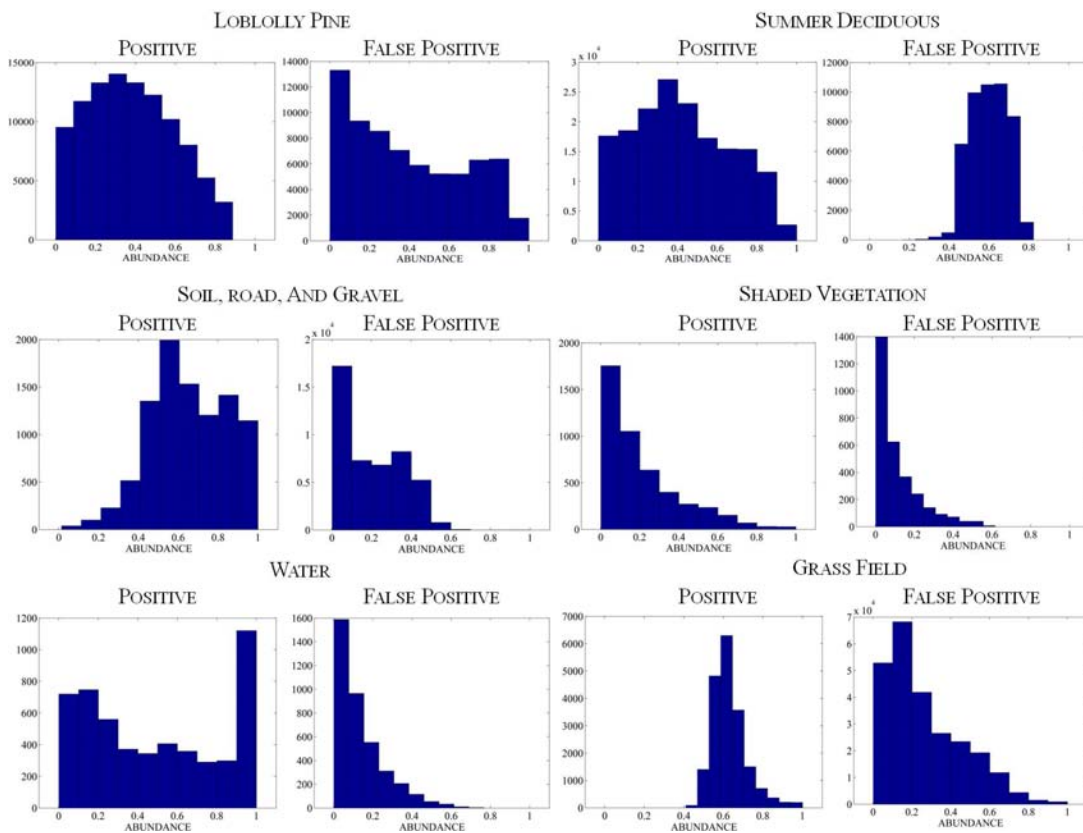


Figure 7.13: Histogram for the abundances of true positive and false positive pixels of A.P. Hill classes extracted using RBSPP.

obtained for the *summer deciduous* class. *Loblolly pine*, *soil*, and *green field* obtained false positive rates between 48% and 58%. *Grass field* was the best detected class by SMACC with 99.57% of true positive rate, and 26.39% of false positive rates. Note that the abundances obtained for *shaded vegetation*, *green field*, *grass field*, and *water* (Figures 7.9 and 7.10) are small for both true positive and false positive pixels. Instead, *summer deciduous* obtained high abundances for both true positive and false positive pixels with averages equal to 0.55 and 0.45 respectively. It is expected that the estimated abundances of true positive pixels become larger than the estimated abundances of false positive pixels. However, some classes extracted using SMACC obtained similar abundances for both true positive and false positive pixels (e.g. *summer deciduous* and *loblolly pine* classes in Table 7.2).

Green field and *autumn deciduous* classes are not extracted by RBSPP algorithm. On the other hand, most of the classes detected by RBSPP obtained high true positive rates. For instance, *summer deciduous* and *grass field* obtained true positive rates as higher as 100%. And *loblolly pine*, *soil*, and *water* classes obtained true positive rates higher than 87%. The lowest true positive rate was obtained for *shaded vegetation* class (18%). Despite the high true positive rates for *summer deciduous* and *grass field* classes, their false positive rates are also high with values equal to 74% and 97% respectively. In addition, the estimated abundances for false positive pixels of *summer deciduous* are close to the values obtained for the true positives. Similarly, *loblolly pine* class has a 42.35% false positive rate with an abundance mean of 0.39 for the false negatives pixels compared to 0.38 for the true positives. The best detected class by RBSPP was *water* with 87% true positive rate and a false positive rate of 1.42%.

Table 7.4 presents a comparison between the true positive and false positive rates obtained from the unmixing results of the proposed approach (Section 6.3.3.2), SMACC and RBSPP. *Loblolly pine*, *summer deciduous*, *soil*, and *grass field* were the classes with highest number of true positive pixels for all three algorithms with rates higher than 89%. On the other hand, true positive rate for *shaded vegetation* class extracted using

Table 7.4: Comparison of true positive and false positive rates for A.P. Hill classes extracted using the proposed approach, SMACC, and RBSPP.

Class	True Positive Rate (%)			False Positive Rate (%)		
	Proposed Approach	SMACC	RBSPP	Proposed Approach	SMACC	RBSPP
<i>Loblolly Pine</i>	89.9	97.9	89.0	37.7	53.7	42.4
<i>Sum. Deciduous</i>	91.8	99.6	100	67.3	88.3	74.7
<i>Soil</i>	98.9	99.9	99.8	22.3	58.1	17.1
<i>Shaded Veg.</i>	86.4	13.8	18.5	39.7	16.8	1.2
<i>Green Field</i>	68.3	96.9	~	52.9	48.1	~
<i>Grass Field</i>	97.6	99.6	100	14.1	26.4	97.5
<i>Autumn</i>	74.8	~	~	20.8	~	~
<i>Water</i>	97.3	57.2	87.1	19.1	56.6	1.4

the proposed approach was 86% which outperform the extraction of this class obtained using SMACC (13%) and RBSPP (18%). *Green field* is not detected by RBSPP. But, SMACC extracted this class with a 96.9% true positive rate, and the proposed approach obtained 68.3% true positive rate. *Autumn deciduous* is only detected with the proposed approach with a 74.8% true positive rate. In addition, *Water* class is best extracted by the proposed approach. Despite the high true positive rates for *loblolly pine* and *summer deciduous* classes for all algorithms, the false positive rates of these classes are also high with values between 37% and 88%. However, the lowest false positive rates for *loblolly pine* and *summer deciduous* classes were obtained by the proposed approach. In addition, *soil* is better extracted using RBSPP and the unmixing approach based on multiscale representation than with SMACC. *Grass field* is better extracted by the proposed approach with a false positive rate of 14.1%. *Grass field* classes extracted by SMACC and RBSPP obtained 26.4% and 97.5% of false positive rates respectively. *Water* class obtained good false positive rates for the proposed approach (19.1%) and RBSPP (1.4%).

Table 7.5: Agreement matrix between reference map and generated classification map from unmixing results of A.P. Hill using SMACC.

	A	B	C	D	E	F	G	H	TOTAL	BETWEEN CLASS AGREEMENT (%)
<i>Loblolly Pine</i>	23112	88832	0	919	76	2	0	332	113273	20.40
<i>Summer Deciduous</i>	8811	38800	0	67	112	2	0	9	47801	81.17
<i>Soil ag field, generic road, gravel</i>	0	179	7448	32	14	1797	0	75	9545	78.03
<i>Shaded Vegetation</i>	757	21675	216	1106	60	313	0	974	25101	4.41
<i>Green ag field</i>	6783	10577	0	0	614	4	0	3	17981	3.41
<i>Grass field</i>	1	3084	224	1	1612	14251	0	5	19178	74.31
<i>Autumn deciduous</i>	12	31542	565	82	1036	4268	0	105	37610	0
<i>River water</i>	17	2327	1304	310	0	28	0	2005	5991	33.47
TOTAL	39493	197016	9757	2517	3524	20665	0	3508		
ASSIGNMENT CLASS AGREEMENT (%)	58.52	19.69	76.33	43.94	17.42	68.96	0	57.16	OVERALL CLASS AGREEMENT (%)	31.51

7.1.2.3 Agreement Assessment of Classification Maps

Classification maps were generated from the estimated abundances from SMACC, and RBSPP endmembers. These classification maps are compared with the published classification map using agreement matrices. Then, the between class agreements, the assignment class agreements, and the overall agreement are used to compare the unmixing results from the proposed approach, SMACC, and RBSPP. Figures 7.14(c) and 7.14(d) show the classification maps for A.P Hill obtained using SMACC and RBSPP results respectively. Figure 7.14(a) shows the published classification map (Figure 6.1(b)) merging some classes such as in Section 6.3.3.3. Tables 7.5 and 7.6 present the agreement matrices for both SMACC and RBSPP classification maps. In addition, Figure 7.14(b) includes the classification map obtained with the proposed approach.

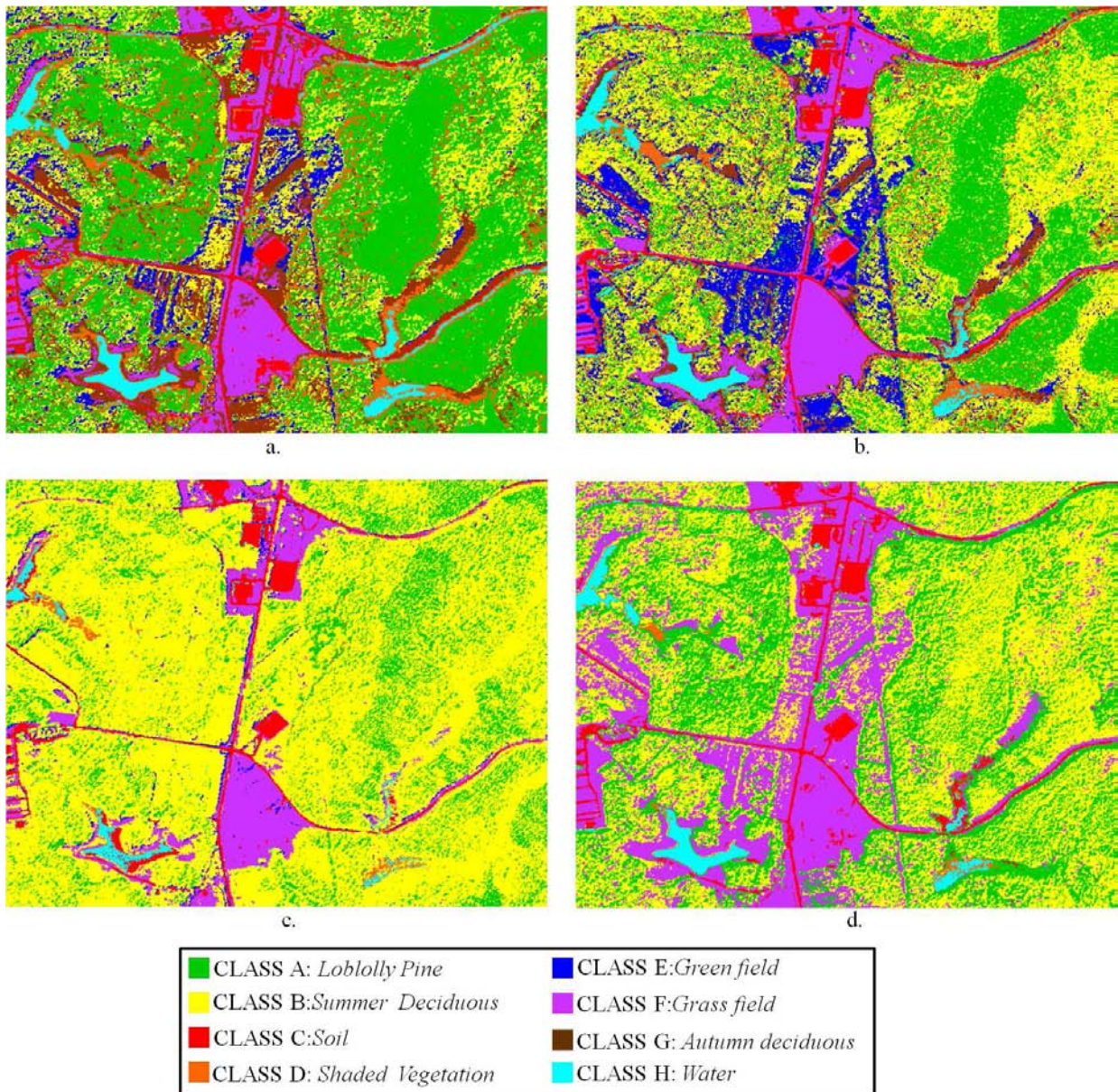


Figure 7.14: Classification maps from unmixing results of A.P. Hill. (a) Reference map, (b) Proposed Approach, (c) SMACC, (d) RBSPP.

Table 7.6: Agreement matrix between reference map and generated classification map from unmixing results of A.P. Hill using RBSPP.

	A	B	C	D	E	F	G	H	TOTAL	BETWEEN CLASS AGREEMENT (%)
<i>Loblolly Pine</i>	40686	72473	0	114	0	0	0	0	113273	35.92
<i>Summer Deciduous</i>	0	40535	0	0	0	7266	0	0	47801	84.80
<i>Soil ag field, generic road, gravel</i>	47	8	8381	5	0	1082	0	22	9545	87.81
<i>Shaded Vegetation</i>	22096	143	849	1219	0	308	0	486	25101	4.86
<i>Green ag field</i>	0	0	0	0	0	17981	0	0	17981	0
<i>Grass field</i>	0	0	182	0	0	18996	0	0	19178	99.05
<i>Autumn deciduous</i>	12138	4111	1832	10	0	19512	0	7	37610	0
<i>River water</i>	1384	1	157	185	0	121	0	4143	5991	69.15
TOTAL	76351	117271	11401	1533	0	65266	0	4658		
ASSIGNMENT CLASS AGREEMENT (%)	53.29	34.57	73.51	79.52	0	29.11	0	88.94	OVERALL CLASS AGREEMENT (%)	41.22

For SMACC results, *Summer deciduous*, *soil*, and *grass field* were the classes with the best between-class agreements with respect to the published classification map. These classes obtained between-class agreements higher than 74%. The remainder classes obtained small between-class agreements with values lower than 33%. *Soil* and *grass field* classes also obtained good assignment-class agreements (76% and 68% respectively). But, the assignment-class agreement of *summer deciduous* was small (19%). Many pixels are assigned to *summer deciduous* class although these are identified with other classes in the published classification map. Most of the pixels labeled as *loblolly pine*, *shaded vegetation*, *green field*, *autumn deciduous* and *water* are assigned to *summer deciduous*. The overall agreement between the classification map obtained using SMACC results and the published classification map was of 31.51%.

The classification map obtained using RBSPP results also presents the best between-class agreements for *summer deciduous*, *soil*, and *grass field* classes. In addition, *water*

class obtained a between-class agreement equal to 68%. *Loblolly pine* and *shaded vegetation* obtained 35% and 4% of between-class agreements. *Soil* and *water* classes also presented a good assignment-class agreement (73% and 88% respectively). *Summer deciduous* and *grass field* have assignment-class agreements lower than 34%. Similar to the result obtained using SMACC, many pixels of *loblolly pine* are assigned to *summer deciduous*. And many pixels of different classes are assigned to *grass field* class. The overall agreement between the classification map of RBSPP and the published classification map was 41.22%.

Table 7.7 presents a comparison among the between-class agreements and assignment-class agreements of the classification maps obtained from the unmixing results of the proposed approach, SMACC and RBSPP. Although the proposed unmixing approach is the only algorithm that detects the *autumn deciduous* classes, it only obtained a between-class agreement of 24.9%. *Green field* was also difficult to detect. RBSPP did not extract this class, and the proposed approach and SMACC did detect *green field* but the between-class agreement was lower than 31%. *Loblolly pine* and *water* classes obtained using the proposed approach present better between-class agreements than the obtained using SMACC and RBSPP results. On the other hand, *summer deciduous*, *soil*, and *grass field* classes obtained using RBSPP present a better agreement with the published classification map than the obtained using the proposed approach and SMACC. The proposed approach was the best in terms of overall agreement. In Figure 7.14, it can be noted that many pixels are assigned to summer deciduous class using the three algorithms. The agreement between the classification map obtained by the proposed approach (Figure 7.14(b)) and the published classification map (Figure 7.14(a)) is better than the classification maps of SMACC and RBSPP.

Table 7.7: Comparison agreement analysis among classification maps obtained from the proposed approach, SMACC, and RBSPP.

Class	Between class agreement(%)			Assignment class agreement (%)		
	Proposed Approach	SMACC	RBSPP	Proposed Approach	SMACC	RBSPP
<i>loblolly pine</i>	51.2	20.4	35.9	76.5	58.5	53.3
<i>sum. deciduous</i>	57.0	81.1	84.8	30.5	19.7	34.6
<i>soil</i>	74.9	78.0	87.8	79.8	76.3	73.5
<i>shaded veg.</i>	45.6	4.4	4.8	48.9	43.9	79.5
<i>green field</i>	31.2	3.4	0	15.2	17.4	0
<i>grass giield</i>	84.6	74.3	99.0	69.5	68.9	29.1
<i>autumn deciduous</i>	24.9	0	0	76.6	0	0
<i>water</i>	73.3	33.5	69.2	68.9	57.1	88.9
Overall Aggrement (%)	Proposed Approach	50.5	SMACC	31.5	RBSPP	41.2

7.2 UNMIXING ANALYSIS OF CUPRITE

Unmixing results for Cuprite using SMACC, VCA, and RBSPP were also evaluated using the methodology described in Section 6.2. For this image, VCA obtains results comparable to the obtained using SMACC and RBSPP. Thus, VCA is taken into account in the quantitative assessment. Section 7.2.1 presents the unmixing results, and the assessment is performed in Section 7.2.2.

7.2.1 Unmixing using SMACC, VCA, and RBSPP for Cuprite

The number of endmembers was set to 17 for SMACC, VCA, and RBSPP algorithms. This is the number of spectral endmember classes estimated by the proposed unmixing approach. NNSLO was used to estimate the abundances for the three algorithms. Figures 7.15, 7.17, and 7.19 present the spectral signatures of endmembers extracted

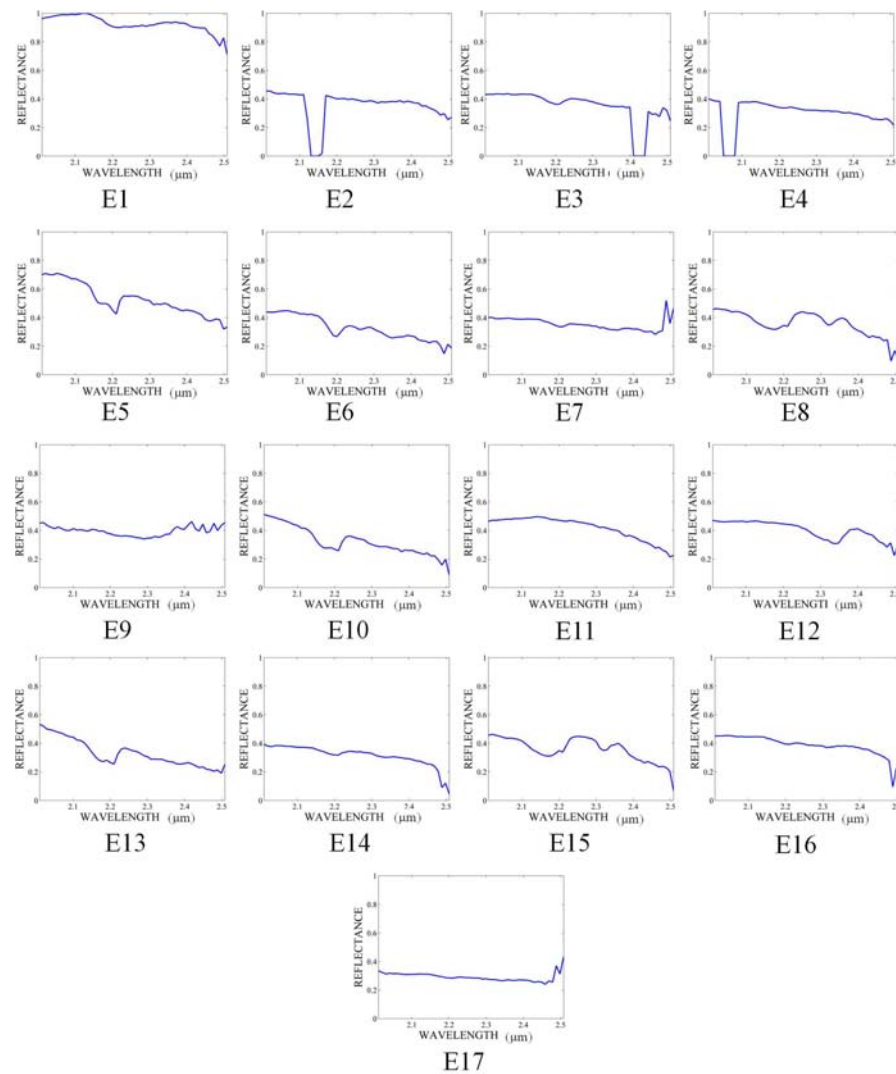


Figure 7.15: Extracted endmembers from Cuprite image using SMACC.

using SMACC, VCA, and RBSPP respectively. Figures 7.16, 7.18, and 7.20 show the estimated abundances using NNSLO.

7.2.2 Assessment of Unmixing Results

The first part of the assessment shows the qualitative comparison between the extracted endmember and the information within the classification map and spectral library of Cuprite. The signature of materials present in the scene can be found in the USGS spectral library (see Section 6.1). Thus, the spectral angle can be used

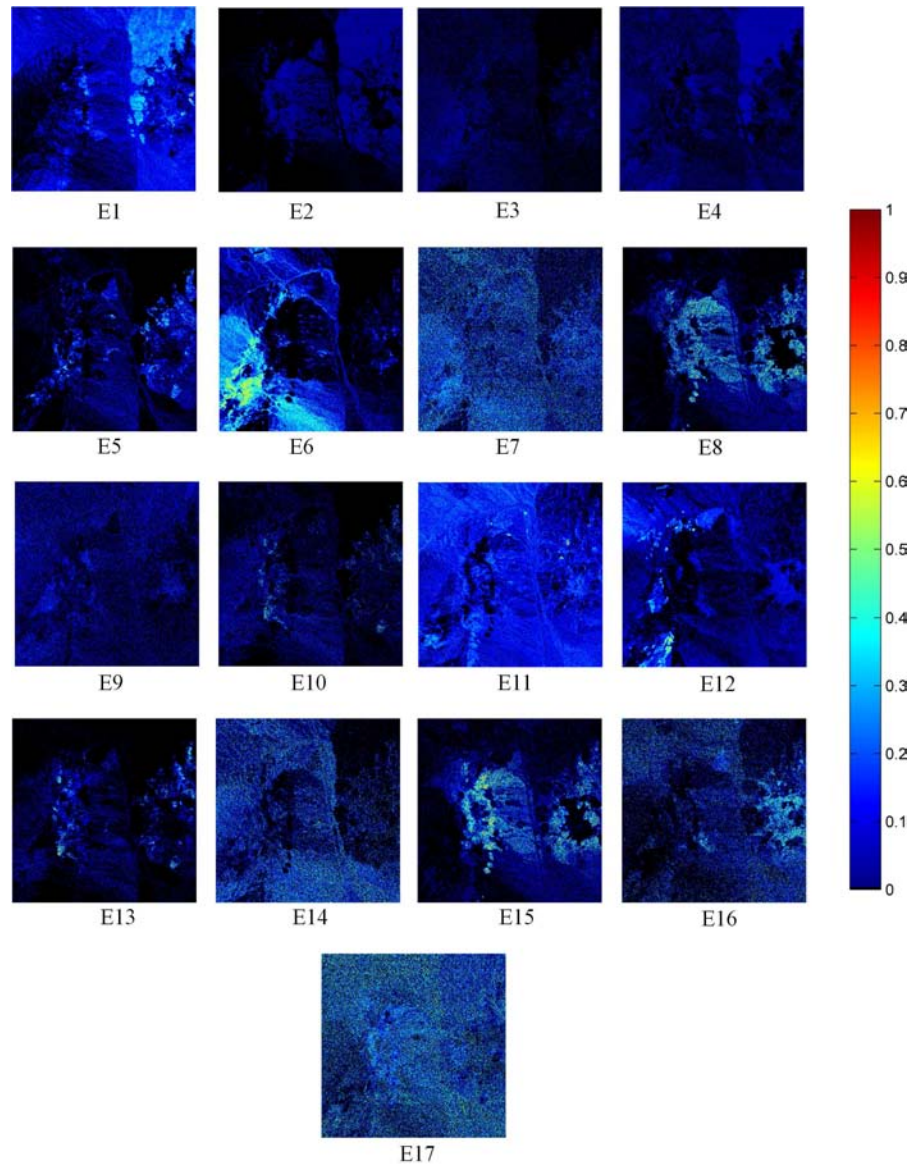


Figure 7.16: Abundances for extracted endmembers from Cuprite using SMACC.

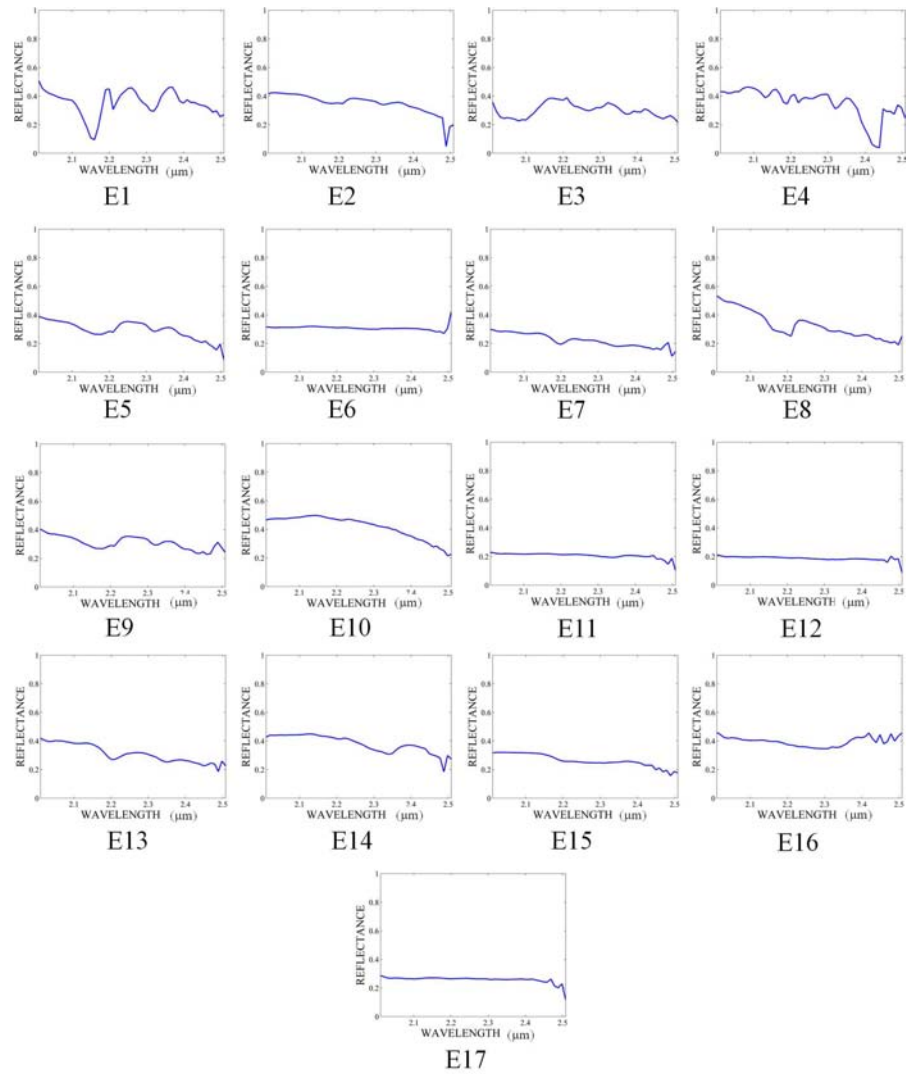


Figure 7.17: Extracted endmembers from Cuprite image using VCA.

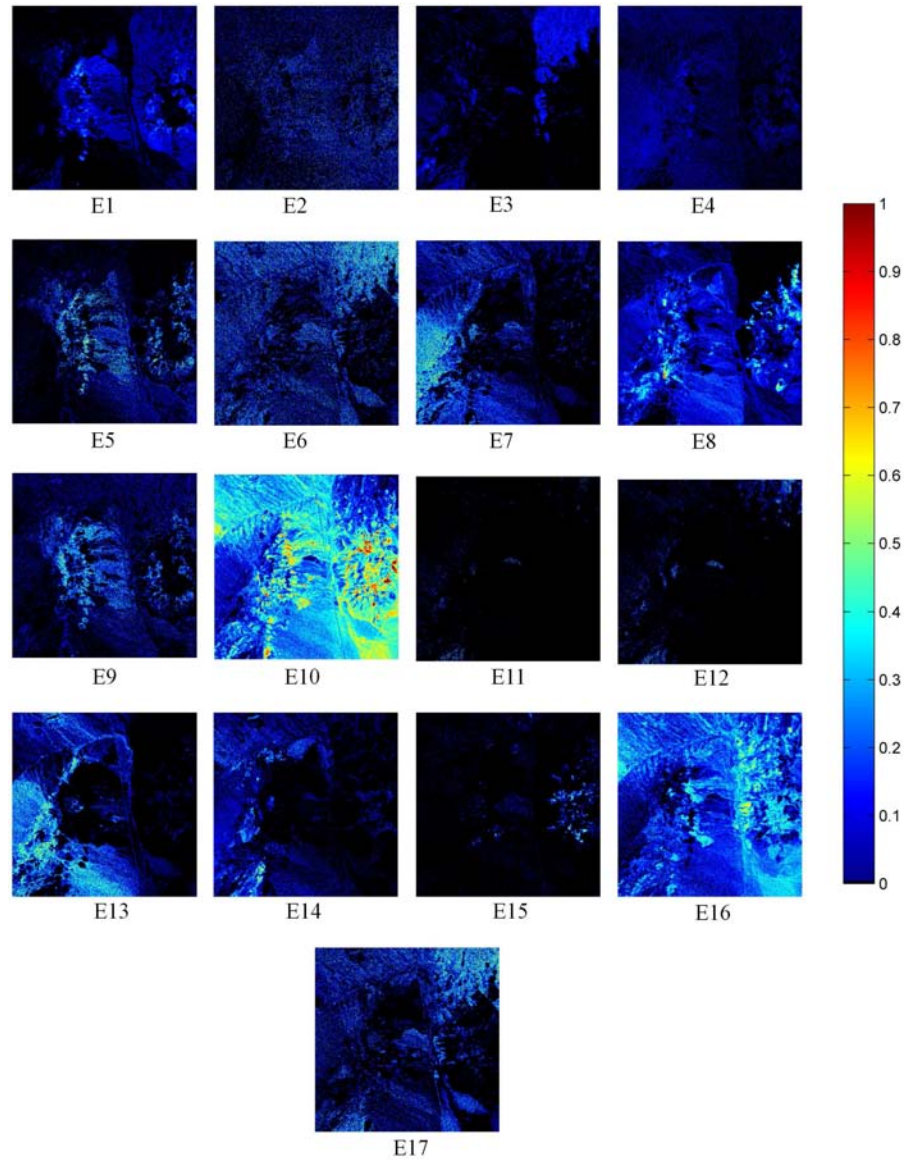


Figure 7.18: Abundances for extracted endmembers from Cuprite using VCA.

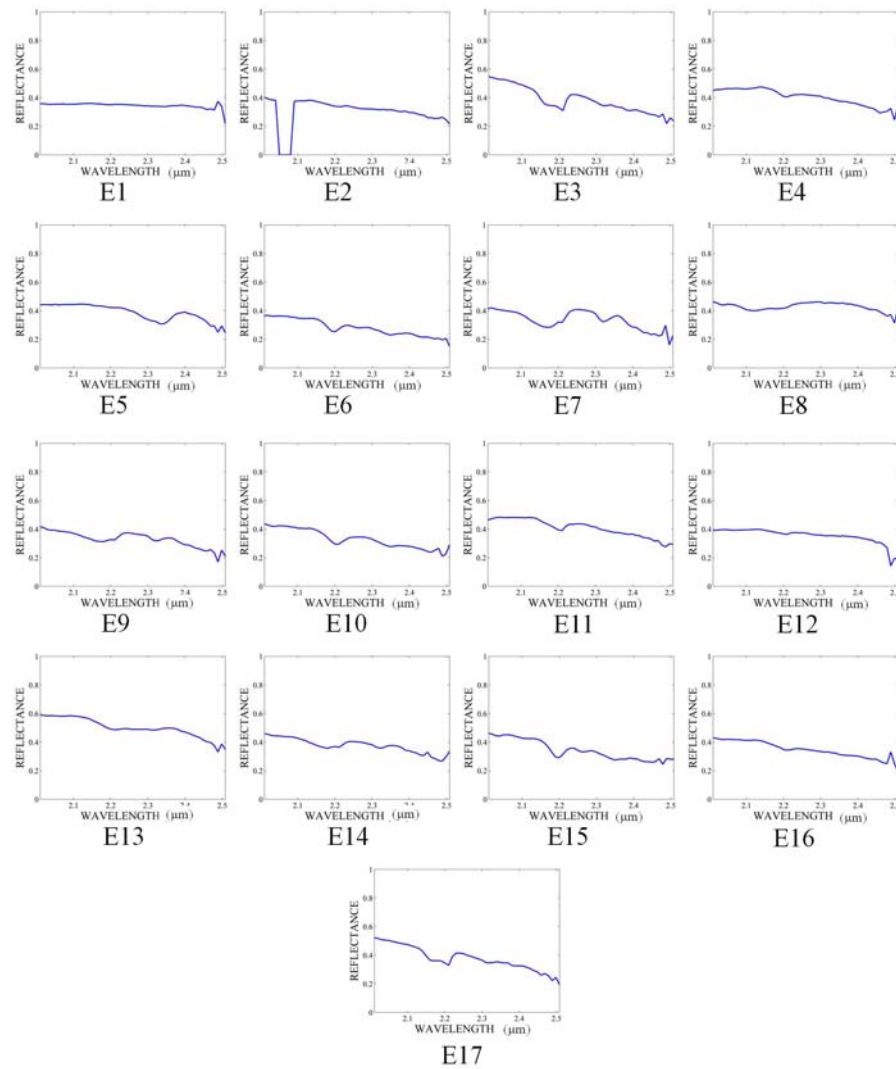


Figure 7.19: Extracted endmembers from Cuprite image using RBSPP combined with VCA.

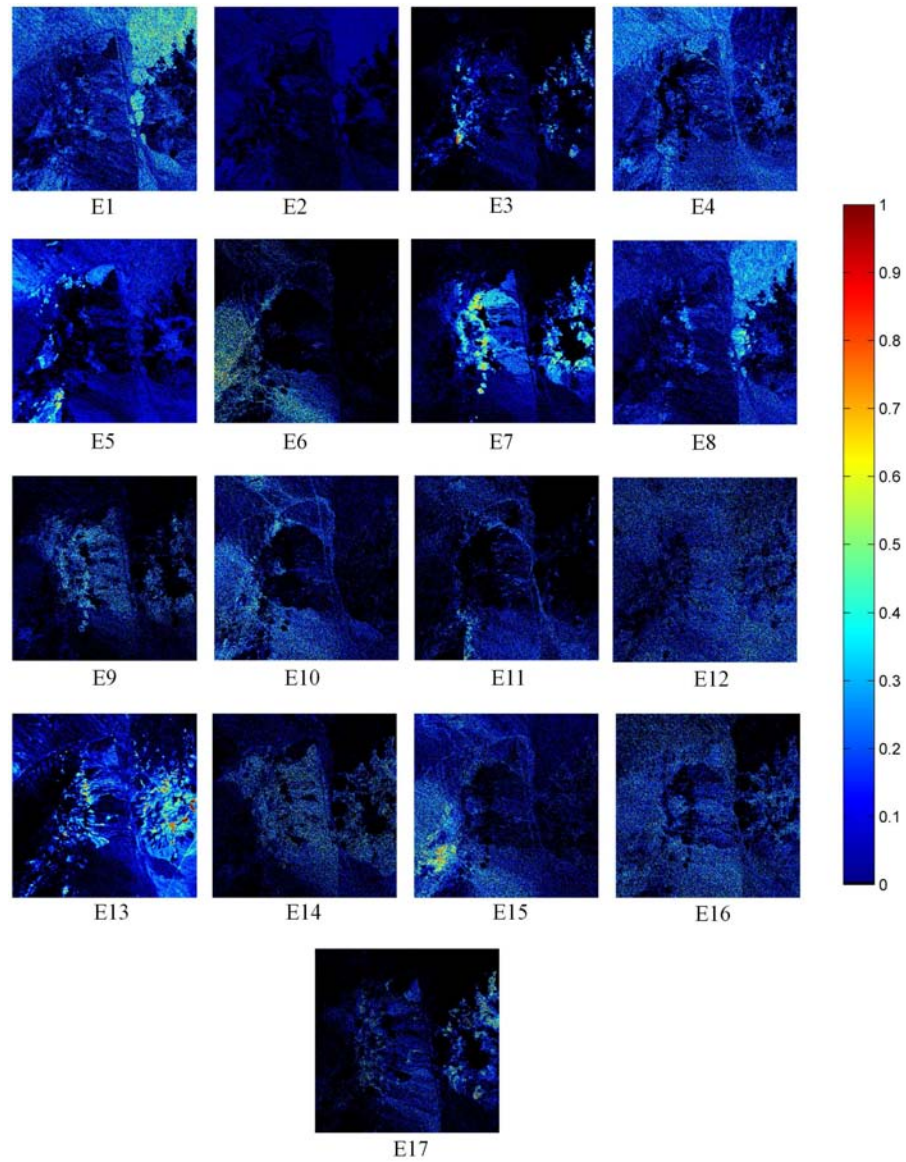


Figure 7.20: Abundances for extracted endmembers from Cuprite using RBSPP combined with VCA.

to assess the extracted endmembers. However, it is important to note that the extracted endmember correspond with image-derived spectra, and some features can vary with respect to the laboratory spectra contained in the USGS spectral library. Once the information classes and endmembers are related, the quantitative analysis of unmixing results using the true positive, false positive and false negative rates as well as the agreement analysis among classification maps is performed.

7.2.2.1 Qualitative Evaluation

The endmembers related to *kaolinite*, *chalcedony*, *calcite*, *muscovite*, *kaolinite+smectite*, and *alunite* are identified in the unmixing results. Endmembers E5, E10, and E13 from SMACC correspond with *kaolinite* as well as endmember E8 from VCA. RB-SPP also extracted *kaolinite* in endmembers E3 and E17. Endmembers E16, E15, and E13, from SMACC, VCA, and RBSPP respectively, represent *chalcedony*. *Calcite* is identified in the endmember E12 from SMACC, E14 from VCA, and E5 from RBSPP. In addition, SMACC extracts *muscovite* and *kaolinite+smectite* (E6 and E14 in Figure 7.16 respectively), and two endmembers related to *alunite* (E8 and E15 in Figure 7.16). The endmembers E13 and E7 from VCA are related to *muscovite* and *kaolinite+smectite*, and both E5 and E9 represent *alunite*. RBSPP extracted two endmembers related to *muscovite* (E6 and E15 in Figure 7.20), one endmember that represent *kaolinite+smectite* (E10 in Figure 7.20), and an endmember of *alunite* (E7 in Figure 7.20). Table 7.8 summarize the relation among extracted endmembers and information classes.

Figure 7.21 shows a comparison of endmembers related to *kaolinite* and *alunite* classes including spectral endmember classes extracted by the proposed approach. Figures 7.21(a)-(d) present the estimated abundances corresponding with *kaolinite* endmembers: E13 from SMACC, E8 from VCA, E17 from RBSPP, and EC2 from the proposed unmixing approach. The spectral signatures are shown in Figures 7.21(e)-(h). Abundance maps from VCA and the proposed approach present a more

Table 7.8: Relation between endmembers extracted by SMACC, VCA, and RBSPP, and information classes for Cuprite.

Group Name	SMACC Endmembers	VCA Endmembers	RBSPP Endmembers
<i>Kaolinite</i>	E5, E10, E13	E8	E3, E17
<i>Chalcedony</i>	E16	E15	E13
<i>Calcite</i>	E12	E14	E5
<i>Muscovite</i>	E6	E13	E6, E15
<i>Kaolinite+Smectite</i>	E14	E7	E10
<i>Alunite</i>	E8, E15	E5, E9	E7

consistent distribution of this material with that of the classification map. Small regions with abundances higher than 40% of *kaolinite* are estimated by VCA, RBSPP combined with VCA, and the proposed approach. SMACC estimates abundances less than 40% of this material in the image. Figures 7.21(i)-(l) present the estimated abundance from endmembers related to *alunite*: E15 from SMACC, E9 from VCA, E7 from RBSPP, and EC9 from the proposed unmixing approach. Figure 7.21 (m)-(p) show the signatures for these endmembers. For this material, RBSPP and the proposed approach present the best distributions when compared to the information in the classification map.

The spectral angles among extracted endmembers and signatures within the spectral library of cuprite are presented in Table 7.9. Table 7.9 compares the spectral angle obtained for the unmixing results of the proposed approach, SMACC, VCA, and RBSPP. The smallest spectral angles for *kaolinite*, *chalcedony*, *calcite*, *muscovite*, and *alunite* are obtained for RBSPP with values between 0.0007 and 0.0029. The spectral endmember classes corresponding to *kaolinite+smectite* of the proposed approach obtained the lowest spectra angle when comparing with SMACC, VCA and RBSPP results. The proposed approach obtained a spectral endmember class of *kaoli-*

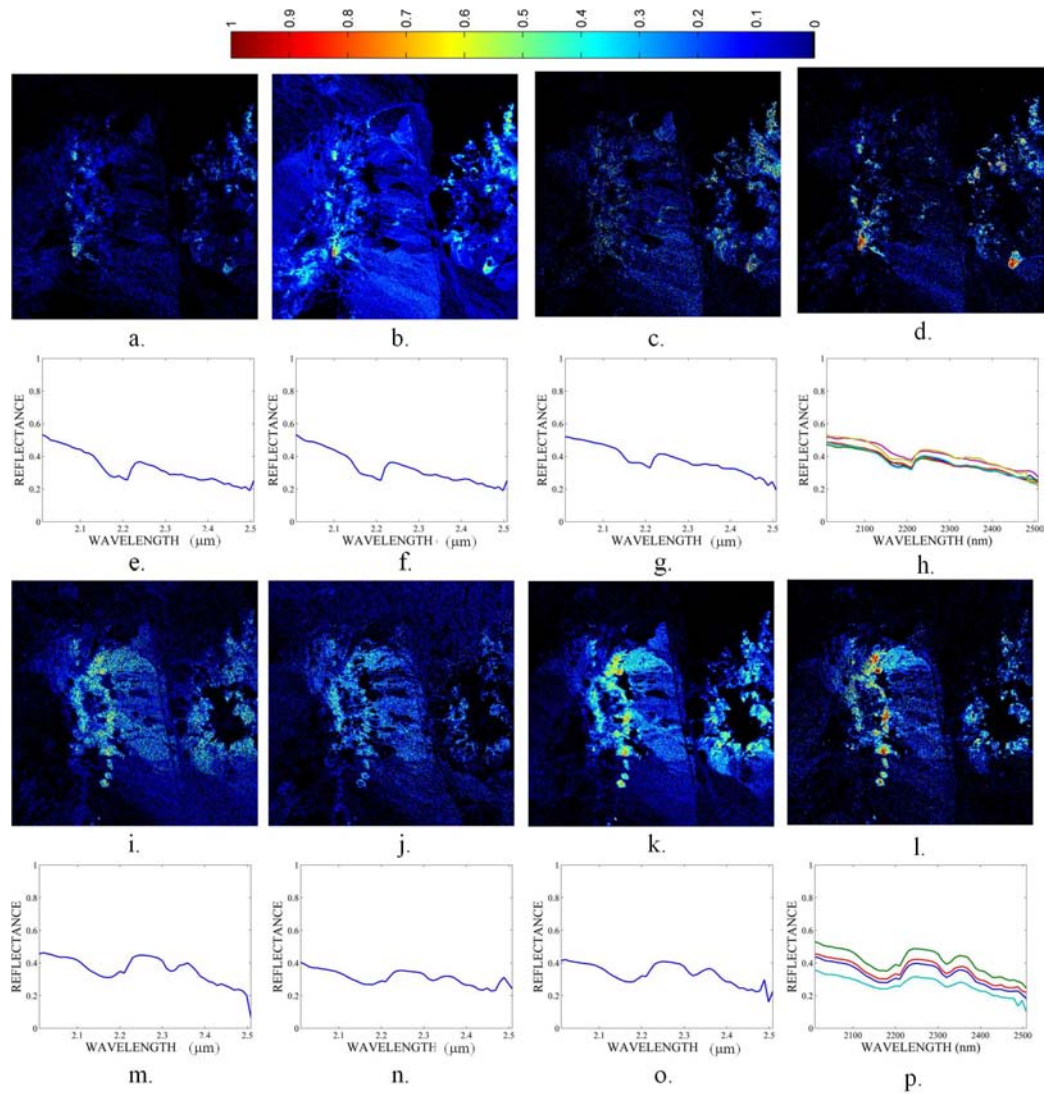


Figure 7.21: Comparison of *kaolinite* and *alunite* endmembers. Abundances and endmembers for *kaolinite* (a)-(h) and *alunite* (i)-(p) extracted using SMACC, VCA, RBSPP combined with VCA, and the proposed approach.

Table 7.9: Spectral angle between extracted endmembers by SMACC, VCA, RBSPP, proposed approach, and reference spectra.

	SMACC	VCA	RBSPP	Proposed Approach
<i>Kaolinite</i>	0.0037	0.0028	0.0007	0.0017
<i>Chalcedony</i>	0.0060	0.0016	0.0007	0.0014
<i>Calcite</i>	0.0008	0.0018	0.0007	0.0044
<i>Muscovite</i>	0.0039	0.0023	0.0029	0.0036
<i>Kaolinite+Smectite</i>	0.0068	0.0048	0.0034	0.0009
<i>Alunite</i>	0.0039	0.0030	0.0015	0.0017

nite+smectite with a spectral angle of 0.0009 with respect to the signatures in the USGS spectral library. The other spectral endmember classes obtained using the proposed approach have spectral angles comparable to the spectral angles of RBSPP.

The reconstruction errors from the unmixing results of SMACC, VCA, RBSPP and the proposed approach were calculated. These are presented in the Figure 7.22. All algorithms obtained reconstruction errors quite small. The proposed approach obtained errors close to 5%. Unlike the poor results obtained with VCA for A.P. Hill, unmixing of Cuprite with this algorithm results in endmembers and abundances comparable with the other algorithms. Next part in the assessment methodology performs the quantitative analysis and comparison of the unmixing results from SMACC, VCA, RBSPP, and the proposed unmixing approach.

7.2.2.2 Quantitative Assessment of Detected Classes

True positive, false positive, and false negative rates are calculated by comparing the estimated abundances from the three algorithms (i.e. SMACC, VCA, and RBSPP) and the mask generated for each information class. Figures 7.23, 7.25, and 7.27 show these comparison for SMACC, VCA, and RBSPP results respectively. The first column in Figures 7.23, 7.25, and 7.27 presents the estimated abundances, and the second column in these figures shows the mask generated from the classification

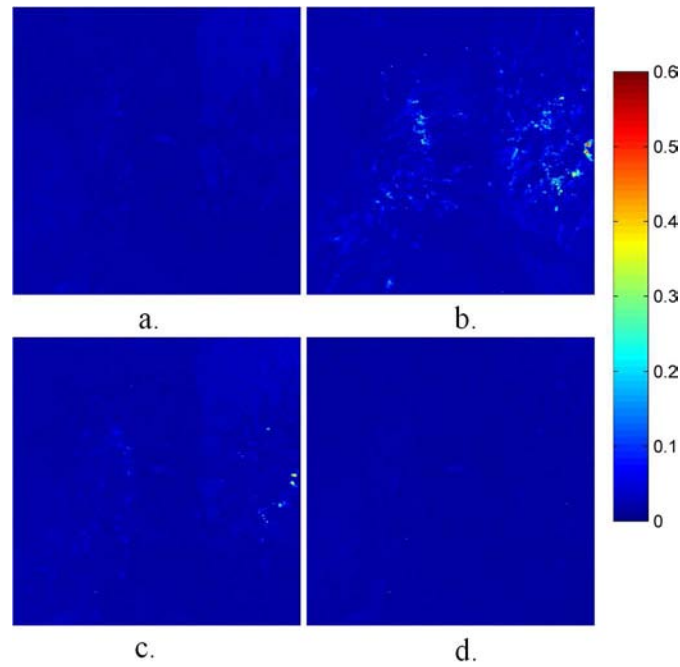


Figure 7.22: Reconstruction error from unmixing results of Cuprite. (a) SMACC, (b) VCA, (c) RBSPP combined with VCA, and (d) proposed approach based on mutliscale representation.

map. The masks that identified the true positive, false positive, and false negative pixels for Cuprite classes are shown from the third to the fifth columns. Tables 7.10, 7.11 and 7.12 summarize the true positive rates, false positive rates, and false negative rates for each information class. Figures 7.24, 7.26 and 7.28 show the histograms for the estimated abundances corresponding to true positive and false positive pixels obtained from SMACC, VCA, and RBSPP respectively.

Tables 7.13 and 7.14 present the comparison among the true positive and false negative rates obtained from SMACC, VCA, RBSPP and the proposed approach results. The true positive rates and false negative rates for the proposed approach were obtained in Section 6.3.3.2.

True positive rates for *kaolinite* class were 90%, 86%, and 72% from SMACC, VCA, and RBSPP respectively. The estimated abundances for these true positive pixels have means smaller than 0.19. The false positive rates obtained using SMACC and VCA are as high as 57% and 63% with abundance means of 0.008 and 0.009 respectively.

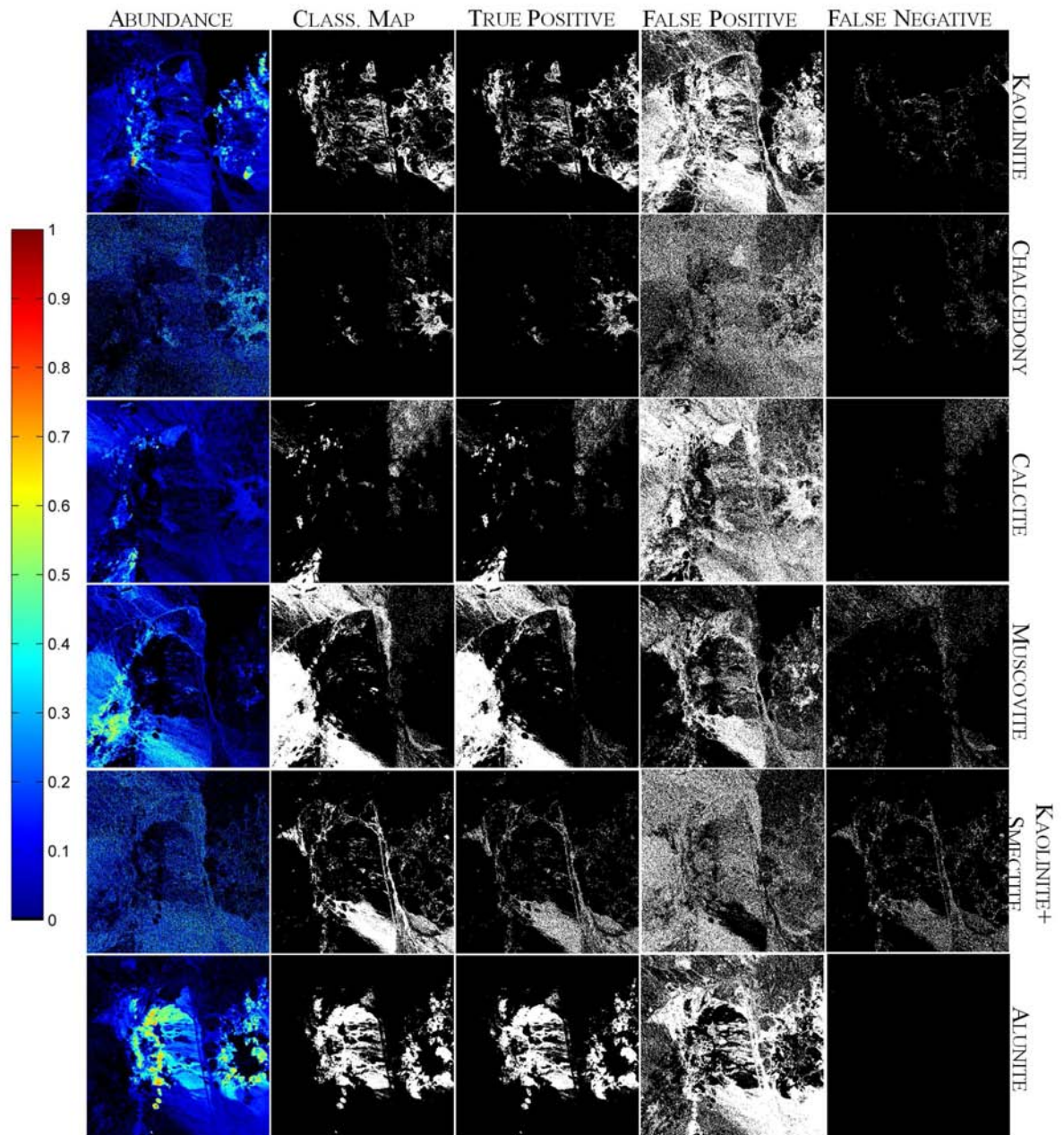


Figure 7.23: Comparison among abundances, classification map, and true positives, false positives, and false negatives of Cuprite classes extracted using SMACC.

Table 7.10: True positive, false positive, and false negative rates for Cuprite classes extracted using SMACC.

ID	Class	True Positive			False Positive			False Negative
		%	Abundance		%	Abundance		
			Mean	σ		Mean	σ	
A	<i>Kaolinite</i>	90.69	0.17	0.14	57.67	0.08	0.07	9.31
B	<i>Chalcedony</i>	69.98	0.27	0.15	37.25	0.15	0.11	30.02
C	<i>Calcite</i>	76.13	0.15	0.13	60.95	0.06	0.05	23.87
D	<i>Muscovite</i>	87.39	0.23	0.14	34.93	0.09	0.08	12.61
E	<i>Kaolinite+Smectite</i>	60.84	0.20	0.13	42.09	0.16	0.11	39.16
F	<i>Alunite</i>	100	0.39	0.13	55.93	0.08	0.08	0

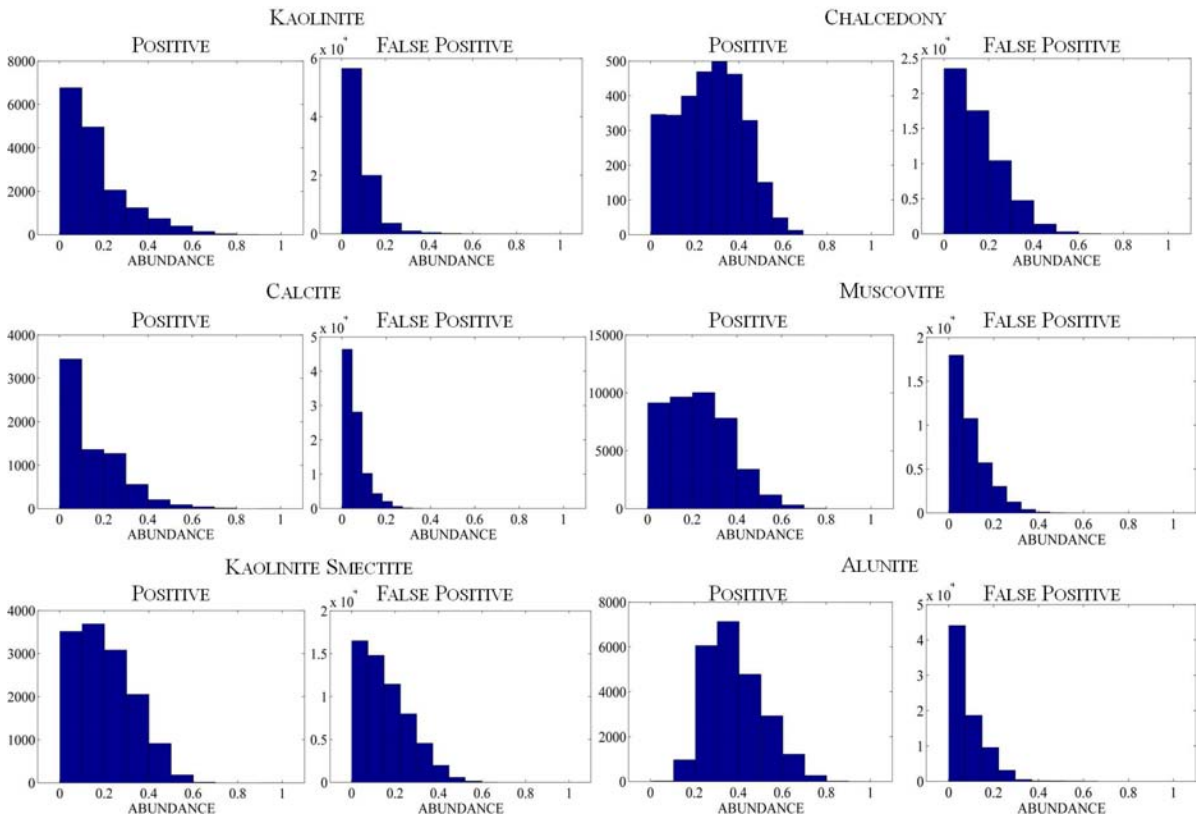


Figure 7.24: Histogram for the abundances of true positive and false positive pixels of Cuprite classes extracted using SMACC.

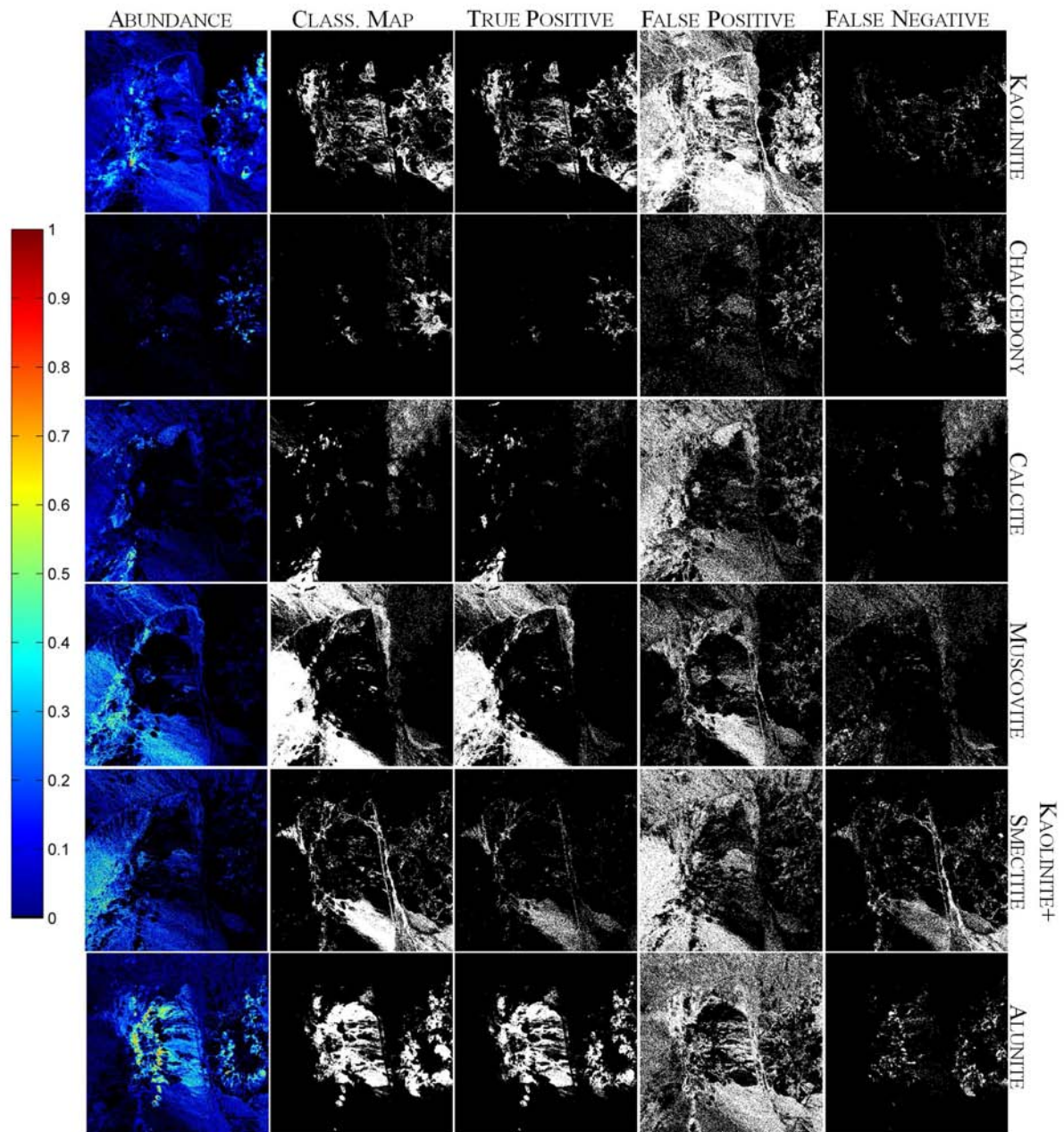


Figure 7.25: Comparison among abundances, classification map, and true positives, false positives, and false negatives of Cuprite classes extracted using VCA.

Table 7.11: True positive, false positive, and false negative rates for Cuprite classes extracted using VCA.

ID	Class	True Positive			False Positive			False Negative
		%	Abundance		%	Abundance		
			Mean	σ		Mean	σ	
A	<i>Kaolinite</i>	86.85	0.16	0.12	63.44	0.09	0.08	13.15
B	<i>Chalcedony</i>	33.23	0.17	0.13	6.14	0.06	0.06	66.77
C	<i>Calcite</i>	46.65	0.19	0.15	30.19	0.08	0.06	53.35
D	<i>Muscovite</i>	80.82	0.22	0.13	22.63	0.11	0.09	19.18
E	<i>Kaolinite+Smectite</i>	33.42	0.09	0.07	38.54	0.15	0.12	66.58
F	<i>Alunite</i>	82.99	0.29	0.17	46.74	0.09	0.08	17.01

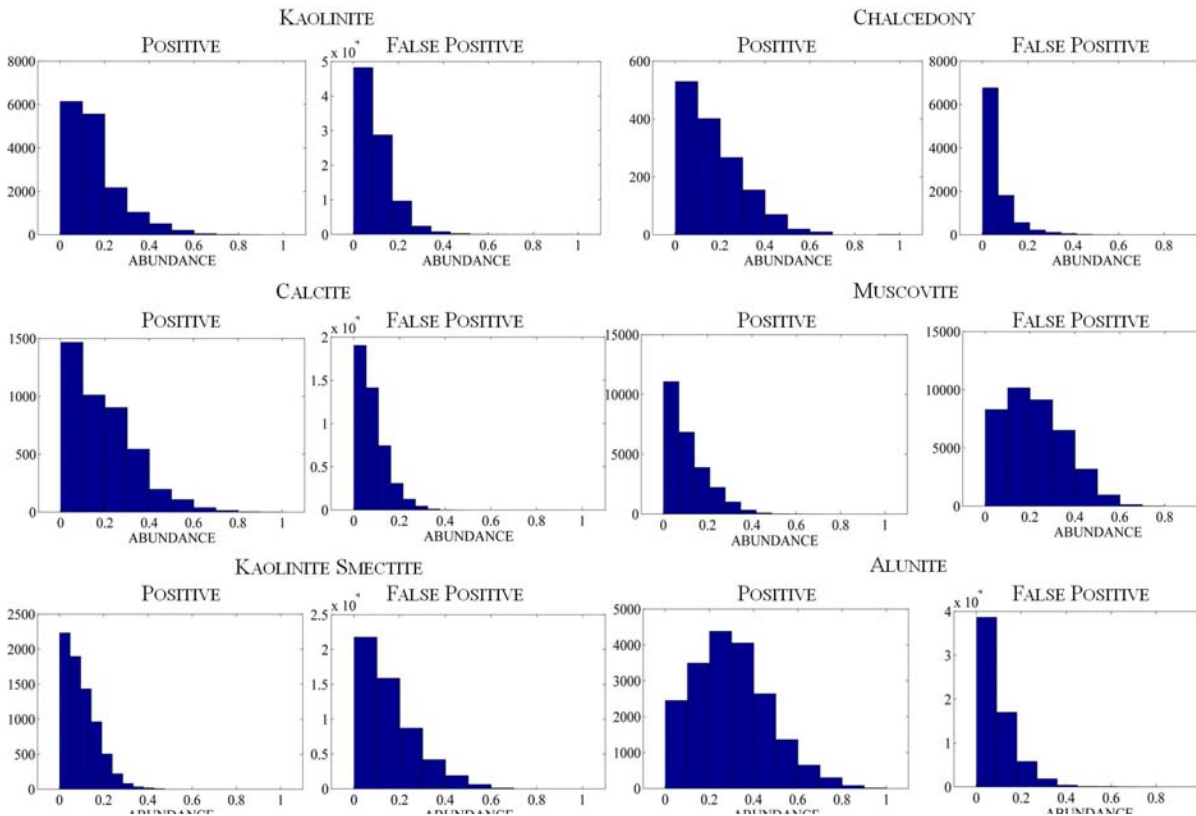


Figure 7.26: Histogram for the abundances of true positive and false positive pixels of Cuprite classes extracted using VCA.

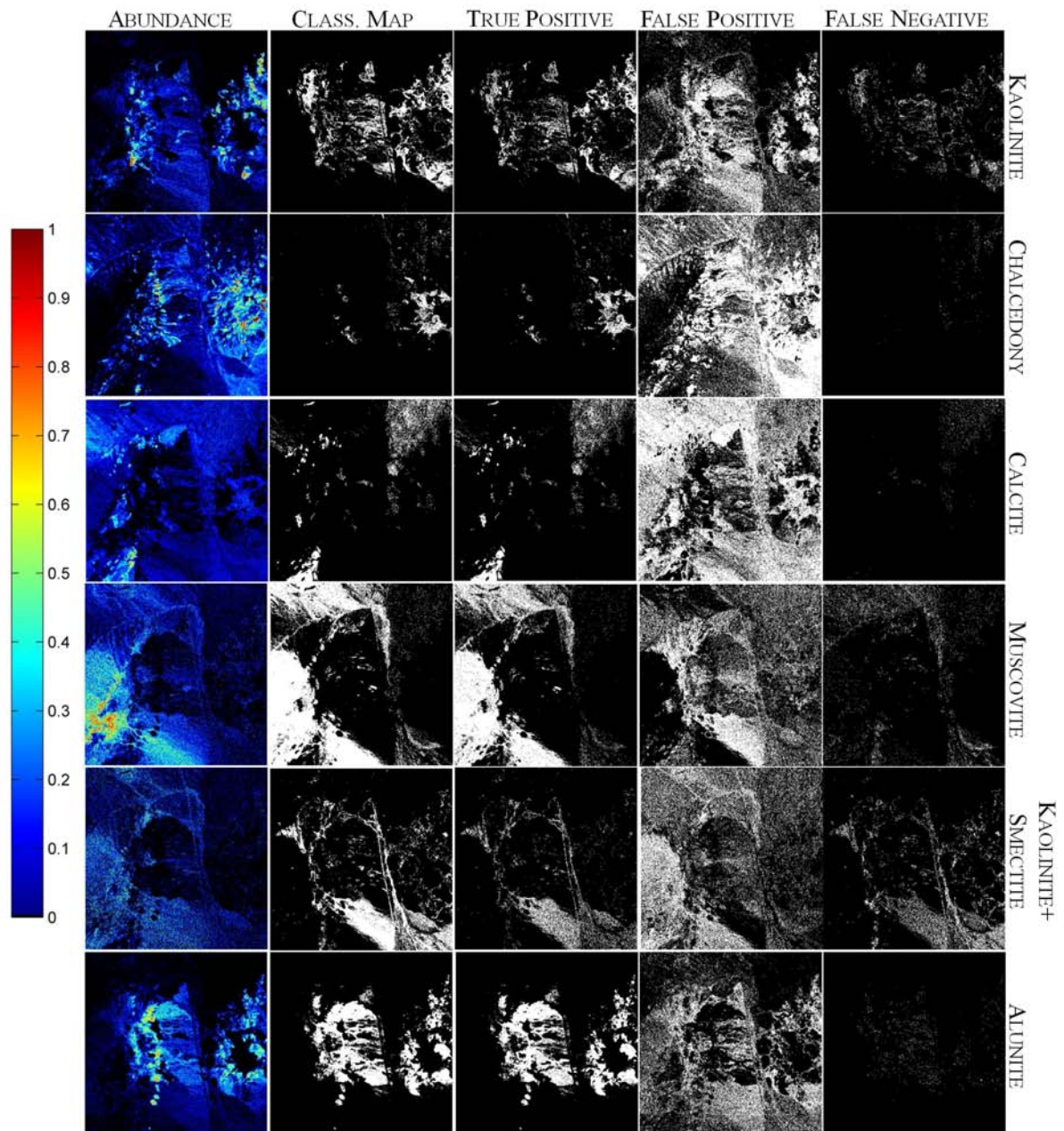


Figure 7.27: Comparison among abundances, classification map, and true positives, false positives, and false negatives of Cuprite classes extracted using RBSPP.

Table 7.12: True positive, false positive, and false negative rates for Cuprite classes extracted using RBSPP.

ID	Class	True Positive			False Positive			False Negative
		%	Abundance		%	Abundance		
			Mean	σ		Mean	σ	
A	<i>Kaolinite</i>	72.87	0.19	0.18	31.54	0.11	0.11	27.13
B	<i>Chalcedony</i>	92.04	0.35	0.21	52.65	0.15	0.14	7.96
C	<i>Calcite</i>	89.59	0.20	0.14	60.32	0.08	0.07	10.41
D	<i>Muscovite</i>	85.79	0.27	0.18	42.30	0.11	0.09	14.21
E	<i>Kaolinite+Smectite</i>	48.90	0.15	0.11	35.82	0.15	0.13	51.14
F	<i>Alunite</i>	95.72	0.28	0.15	29.94	0.08	0.07	4.28

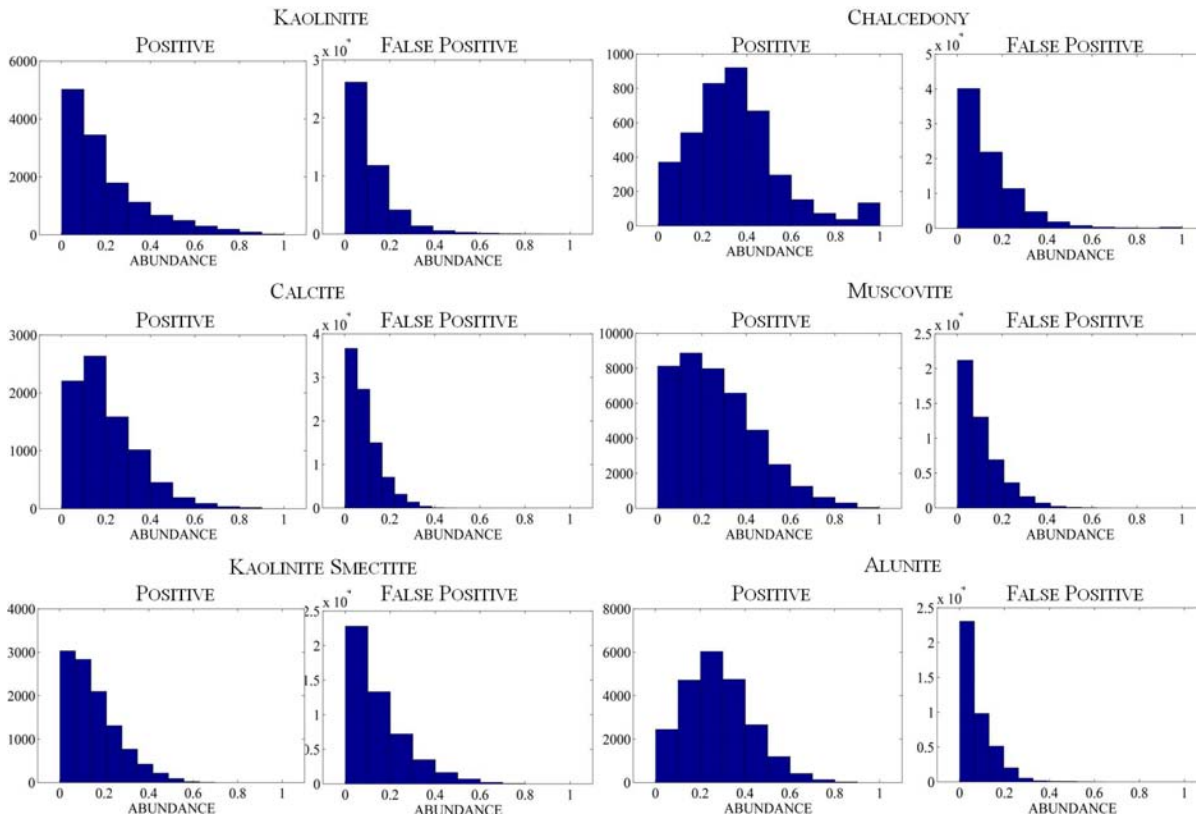


Figure 7.28: Histogram for the abundances of true positive and false positive pixels of Cuprite classes extracted using RBSPP.

Table 7.13: Comparison of true positive rates for A.P. Hill classes extracted using the proposed approach, SMACC, and RBSPP.

Class	True Positive Rate (%)			
	Proposed Approach	SMACC	VCA	RBSPP
<i>Kaolinite</i>	62.42	90.69	86.85	72.87
<i>Chalcedony</i>	87.45	69.98	33.23	92.04
<i>Calcite</i>	75.94	76.13	46.65	89.59
<i>Muscovite</i>	76.09	87.39	80.82	85.79
<i>Kaolinite+Smectite</i>	88.70	60.84	33.42	48.90
<i>Alunite</i>	91.83	100	82.99	95.72

Table 7.14: Comparison of false positive rates for A.P. Hill classes extracted using the proposed approach, SMACC, and RBSPP.

Class	False Positive Rate (%)			
	Proposed Approach	SMACC	VCA	RBSPP
<i>Kaolinite</i>	29.99	57.67	63.44	31.54
<i>Chalcedony</i>	68.39	37.25	6.14	52.65
<i>Calcite</i>	55.64	60.95	30.19	60.32
<i>Muscovite</i>	43.22	34.93	22.63	42.30
<i>Kaolinite+Smectite</i>	65.21	42.09	38.54	35.82
<i>Alunite</i>	36.87	55.93	46.74	29.94

Note in Figures 7.23 and 7.25 that it is very difficult to distinguish the true positive and false positive pixels in the estimated abundance for *kaolinite* by SMACC and VCA since many true positive pixels appear to have similar abundances than the false positive pixels. In addition, the histograms for *kaolinite* obtained from SMACC and VCA results (Figure 7.24 and 7.26) show that most of the true positive pixels have smaller abundances (less than 0.2) that are similar to the abundance distribution obtained for the false positive pixels. RBSPP obtained the lowest false positive rate for *kaolinite* when comparing with SMACC and VCA. The false positive rate obtained using RBSPP was equal to 31% with an abundance mean of 0.11. Some regions of *kaolinite* are estimated with high abundances by RBSPP, these can be seen in the abundance map in Figure 7.27. The proposed approach based on multiscale representation obtained a true positive rate of 62% and a false positive rate of 29% for *kaolinite* (see comparison in Tables 7.13 and 7.14). Despite that the proposed approach obtained a lower positive rate than RBSPP, the false positive rate is similar to that obtained using RBSPP (Table 7.14). In addition, the true positive pixels are estimated with higher abundances than the false positive pixels for the proposed approach as seen in Section 6.3.3.2.

Chalcedony obtained true positive rates as high as 92% with RBSPP. True positive rates obtained from SMACC and VCA are 69% and 33% respectively. The mean abundance for *chalcedony* true positive pixels are between 0.17 and 0.35 for SMACC, VCA, and RBSPP. RBSPP obtained a false positive rate of 52% with an abundance mean equal to 0.15. The histograms for *chalcedony* from RBSPP results (Figure 7.28) show that most of true positive pixels have abundances between 0.2 and 0.5 and the false positive pixels have abundances lower than 0.2. The proposed approach based on multiscale representation obtained a true positive rate equal to 87% and false positive rate equal to 68% for *chalcedony* (Tables 7.13 and 7.14). Despite that the proposed approach obtained a higher false positive rate than RBSPP for *chalcedony* class, the estimated abundances distribution of *chalcedony* (Figure 6.23) shows a better

correspondence with *chalcedony* class within the published classification map since most of the *chalcedony* pixels are estimated with high abundances. Note that RBSPP and the proposed approach obtained similar true positive rates (Table 7.13) for *chalcedony*. But, the estimated abundances for this class by the proposed approach are higher than the estimated abundance using RBSPP as can be seen when comparing the histograms in Figures 6.24 and 7.28.

Calcite presents good true positive rates for SMACC and RBSPP algorithms with values higher than 76%. But, VCA only detects 46% of the pixels of *calcite*. *Calcite* was also detected with small abundances with averages less than 0.20 for both SMACC and RBSPP. *Calcite* false positive rates were close to 60% for both SMACC and RBSPP, and the abundance mean of false positive pixels was 0.06 for SMACC and 0.08 for RBSPP. It can be noted in estimated abundances (Figures 7.23 and 7.27) and histograms (Figures 7.24 and 7.28) that true positive pixels and false positive pixels have similar abundances for *calcite* according to SMACC and RBSPP. The proposed approach obtained a 75% true positive rate and a 55% false positive rate. Despite that *calcite* true positive rate obtained with the proposed approach is lower than the true positive rates for SMACC and RBSPP, the estimated abundances for true positive pixels with the proposed approach have higher values achieving a mean 0.41, and false positive pixels have only an abundance mean of 0.16 (Table 6.8).

Muscovite is estimated with true positive rates between 80% and 87% for the three algorithms and with abundance means between 0.22 and 0.27. The *muscovite* false positive rates were 34%, 22% and 42% for SMACC, VCA, and RBSPP respectively. The abundance mean for the false positive pixels was 0.09 for SMACC and 0.11 for both VCA and RBSPP. The proposed approach obtained a true positive rate equal to 76% and a false positive rate equal to 43% for *muscovite* class with abundance mean of 0.23 and 0.09 for true positive and false positive pixels respectively. Note that estimated *muscovite* abundances of SMACC and VCA are very similar (Figures 7.23 and 7.25). RBSPP and the proposed unmixing approach also present similar

abundances (Figures 7.27 and Figures 6.23) with higher values than the estimated using SMACC and VCA.

SMACC obtained the best true positive rate for *kaolinite+smectite* when compared with VCA and RBSPP results. The true positive rate for *kaolinite+smectite* was 60% with an abundance mean of 0.20. *kaolinite+smectite* false positive rate was 42% for SMACC and the false positive pixels have an abundance mean equal to 0.16. The proposed approach achieves a better true positive rate (88%, see Table 7.13) than SMACC. Although, the *kaolinite+smectite* false positive rate of the proposed approach was 65%.

SMACC obtained 100% of pixels that correspond to *alunite* with an abundance mean of 0.39. VCA and RBSPP also obtained good true positive rates for *alunite* with values between 82% and 95%. The lowest false positive rates for *alunite* are obtained using RBSPP. SMACC and VCA false positive rates are 55% and 46% respectively. True positive pixels from SMACC have an abundance mean equal to 0.39 and the false positive pixels have an abundance mean equal to 0.08. Similar abundance means for the true positive and false positive pixels are obtained for RBSPP and VCA: close to 0.29 for true positive pixels and 0.09 for the false positive pixels. Comparable results were also obtained for *alunite* with the proposed unmixing approach. *Alunite* true positive rate was 91% and the false positive rate was 36% for the proposed approach. The true positive rates have an abundance mean of 0.36 and the false positive pixels have an abundance mean equal to 0.06.

Note in Tables 7.13 and 7.14 that the proposed unmixing approach obtained true positive and false positive rates comparable with SMACC and RBSPP results. However, the estimated abundances from the spectral endmember classes has higher values than the obtained from SMACC and RBSPP.

Table 7.15: Agreement matrix between reference map and generated classification map from unmixing results of Cuprite using SMACC.

	A	B	C	D	E	F	TOTAL	BETWEEN CLASS AGREEMENT (%)
<i>Kaolinite</i>	4968	3109	112	61	2452	7377	18079	27.48
<i>Chalcedony</i>	102	2622	585	234	704	126	4373	59.96
<i>Calcite</i>	101	2190	5623	325	552	397	9188	61.20
<i>Muscovite</i>	426	5321	2448	26261	12844	240	47540	55.24
<i>Kaolite+Smectite</i>	1956	4213	131	5746	8521	1535	22102	38.55
<i>Alunite</i>	849	523	1	1	551	21464	23389	91.77
TOTAL	8402	17978	8900	32628	25624	31139	OVERALL CLASS AGREEMENT (%)	55.71
ASSIGNMENT CLASS AGREEMENT (%)	59.13	14.58	63.18	80.49	33.25	68.93		

7.2.2.3 Agreement Assessment of Classification Maps

Classification maps generated from the estimated abundances with SMACC, VCA and RBSPP are shown in Figure 7.29. These classification maps are compared with the published classification map using agreement matrices. Figure 7.29(c) shows the classification maps for Cuprite obtained using SMACC. Figures 7.29(d) and 7.29(e) shows the classification maps obtained from VCA and RBSPP respectively. In addition, Figure 7.29 includes the classification map (Figure 7.29(a)) obtained from the published classification map merging some classes as described in Section 6.3.3.1 and the classification map obtained from the proposed unmixing approach (Figure 7.29(b)). The between-class agreements, the assignment class-agreements, and the overall agreement are used to compare the unmixing results from the proposed approach, SMACC, and RBSPP similarly to the analysis performed for A.P. Hill. Tables 7.15, 7.16, and 7.17 present the agreement matrices for SMACC, VCA and RBSPP classification maps respectively.

Alunite was the class with the best between-class agreement from SMACC results (91%). *Calcite*, *chalcedony*, and *muscovite* classes obtained between-class agreements

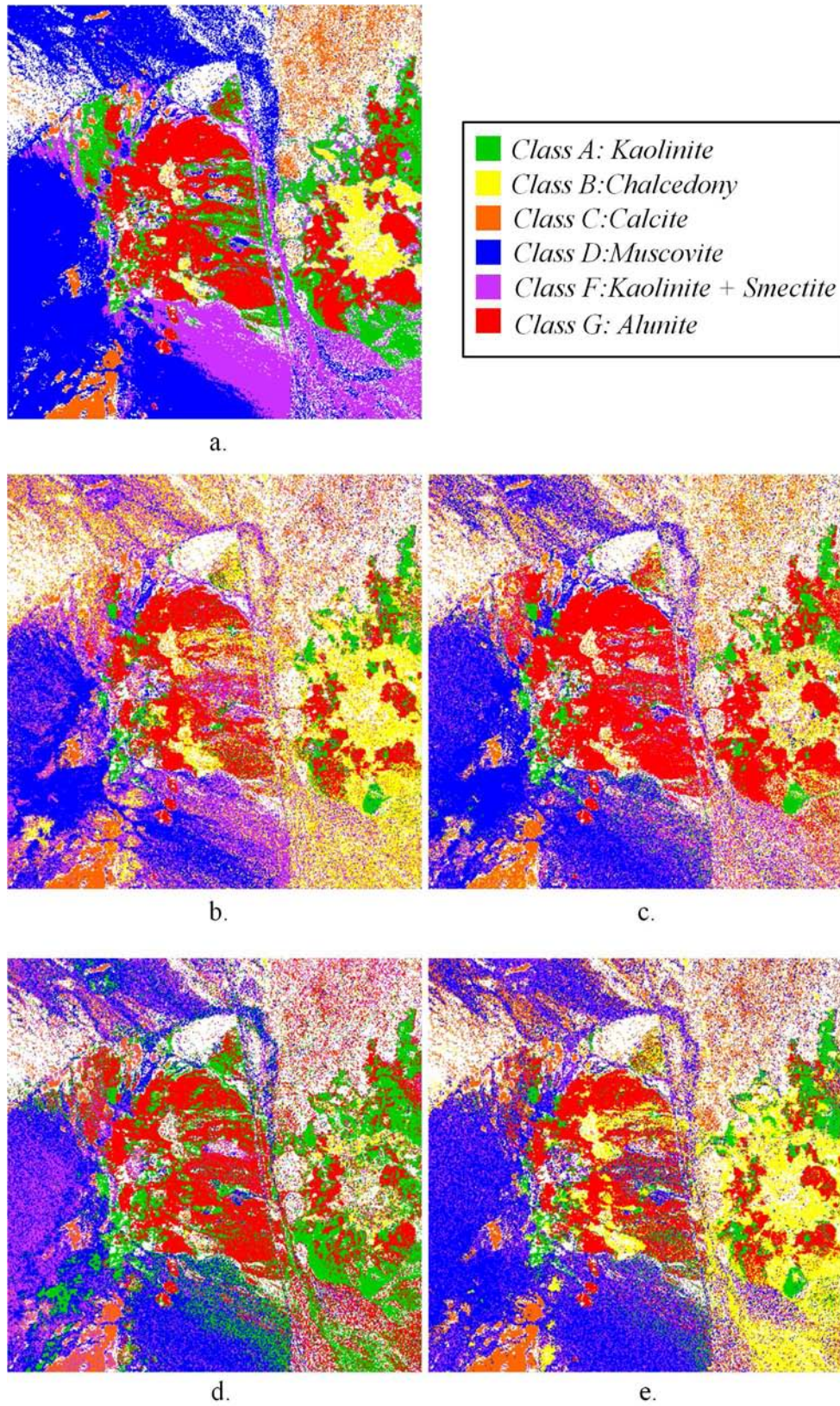


Figure 7.29: Classification maps from unmixing results of Cuprite image. (a) Reference map, (b) Proposed Approach, (c) SMACC, (d) VCA, (e) RBSPP.

Table 7.16: Agreement matrix between reference map and generated classification map from unmixing results of Cuprite using VCA.

	A	B	C	D	E	F	TOTAL	BETWEEN CLASS AGREEMENT (%)
<i>Kaolinite</i>	9463	391	284	143	944	6854	18079	52.34
<i>Chalcedony</i>	1031	1368	610	270	400	694	4373	31.28
<i>Calcite</i>	537	497	3461	349	2200	2145	9189	37.66
<i>Muscovite</i>	4662	300	2632	22927	15181	1838	47540	48.23
<i>Kaolite+Smectite</i>	8967	438	384	5040	1871	5402	22101	8.47
<i>Alunite</i>	6747	190	147	75	304	15926	23389	68.09
TOTAL	31407	3184	7518	28804	20900	32859	OVERALL CLASS AGREEMENT (%)	44.13
ASSIGNMENT CLASS AGREEMENT (%)	30.13	42.96	46.04	79.60	8.95	48.47		

Table 7.17: Agreement matrix between reference map and generated classification map from unmixing results of Cuprite using RBSPP.

	A	B	C	D	E	F	TOTAL	BETWEEN CLASS AGREEMENT (%)
<i>Kaolinite</i>	5504	6015	732	1977	1178	2673	18079	30.44
<i>Chalcedony</i>	18	3650	334	284	82	5	4373	83.47
<i>Calcite</i>	31	464	7358	1110	179	46	9188	80.08
<i>Muscovite</i>	205	2587	6552	27417	10549	230	47540	57.67
<i>Kaolite+Smectite</i>	1951	6554	814	6992	4888	903	22102	22.12
<i>Alunite</i>	3349	3275	104	619	538	15504	23389	66.29
TOTAL	11058	22545	15894	38399	17414	19361	OVERALL CLASS AGREEMENT (%)	51.59
ASSIGNMENT CLASS AGREEMENT (%)	49.77	16.19	46.29	71.40	28.07	80.08		

between 55% and 61% from SMACC. The worst between-class agreements were obtained by *kaolinite* and *kaolinite+smectite* with values smaller than 38%. *Muscovite* class extracted using SMACC have an assignment-class agreement equal to 80%. Assignment-class agreements for *kaolinite*, *calcite*, and *alunite* were between 59% and 68%. *Chalcedony* only has 14% of pixels correctly assigned when compared with the published classification map. *Kaolinite+smectite* class from SMACC obtained 33% for assignment-class agreement. The overall class agreement achieved using SMACC was 55.71 % with the published classification map.

Similar to SMACC, *alunite* class from VCA obtained the best between-class agreement, however, it is equal to 68%. *Kaolinite* and *muscovite* between-class agreements were 52% and 48%. *Calcite*, *chalcedony*, and *kaolinite+smectite* have between-class agreements smaller than 37%. The assignment-class agreements for VCA results also present low percentages between 8% and 48% for most of the classes. *Muscovite* was the only class from VCA that obtained an assignment-class agreement higher than 79%. The overall class agreement achieved using VCA was 44.13 % with the published classification map.

From RBSPP, *chalcedony* and *calcite* were the class with the highest between-class agreements when compared with the published classification map. The between-class agreement for these classes were higher than 80%. *Muscovite* and *alunite* have between-class agreement equal to 57% and 66% respectively. Similar to the results obtained from SMACC, *kaolinite* and *kaolinite+smectite* classes have the lowest between-class agreements with values smaller than 30%. *Muscovite* and *alunite* obtained the highest number of correctly assigned pixels with percentages higher than 71%. *Kaolinite*, *chalcedony*, *calcite*, and *kaolinite+smectite* from RBSPP obtained assignment-class agreements smaller than 49%. The overall class agreement for the classification map obtained using RBSPP was 51.59% with the published classification map.

Tables 7.18 and 7.19 present the comparison among the between-class agreements and assignment-class agreements of the classification maps obtained from the unmix-

Table 7.18: Comparison of between-class agreement of classification maps obtained from the proposed approach, SMACC, VCA, and RBSPP.

Class	Between class agreement(%)			
	Proposed Approach	SMACC	VCA	RBSPP
<i>Kaolinite</i>	22.54	27.48	52.34	30.44
<i>Chalcedony</i>	78.88	59.96	31.28	83.47
<i>Calcite</i>	69.65	61.20	37.66	80.08
<i>Muscovite</i>	39.36	55.24	48.23	57.67
<i>Kaolinite+Smectite</i>	43.55	38.55	8.47	22.12
<i>Alunite</i>	66.08	91.77	68.09	66.29

ing results for the proposed approach, SMACC, VCA and RBSPP. In addition, Table 7.20 shows the overall agreements obtained from the different classification maps when compared with the published classification map. RBSPP algorithm obtains the best between-class agreement for *kaolinite*, *chalcedony*, *calcite*, and *muscovite*. The percentage of between-class agreement obtained using the proposed approach for *chalcedony* and *calcite* classes are comparable with those obtained by RBSPP (Table 7.18). The proposed approach has the best between-class agreement for *kaolinite+smectite*, and SMACC obtains the best between-class agreement for *alunite*. In terms of the assignment-class agreement, the proposed approach presents comparable results to SMACC and RBSPP (Table 7.19). The best overall agreement was obtained by SMACC followed by RBSPP and the proposed approach as shown in Table 7.20.

7.3 FURTHER ANALYSIS

Comparing the information classes for A.P. Hill and the unmixing results obtained with SMACC, VCA, RBSPP, and the proposed approach (Tables 6.5 and 7.1), it can be seen that the best results were obtained by the proposed approach since these extracted endmembers classes related with all information classes within the pub-

Table 7.19: Comparison of assignment-class agreement of classification maps obtained from the proposed approach, SMACC, VCA, and RBSPP.

Class	Assignment class agreement (%)			
	Proposed Approach	SMACC	VCA	RBSPP
<i>Kaolinite</i>	54.28	59.13	30.13	49.77
<i>Chalcedony</i>	11.13	14.58	42.96	16.19
<i>Calcite</i>	40.52	63.18	46.04	46.29
<i>Muscovite</i>	79.18	80.49	79.60	71.40
<i>Kaolinite+Smectite</i>	31.23	33.25	8.95	28.07
<i>Alunite</i>	89.20	68.93	48.47	80.08

Table 7.20: Comparison of overall agreement of classification maps obtained from the proposed approach, SMACC, and RBSPP.

	Overall Agreement (%)
Proposed Approach	46.12
SMACC	55.71
VCA	44.13
RBSPP	51.59

lished classification map. SMACC did not identify one class (*autumn deciduous*) and RBSPP did not identified two classes (*autumn deciduous* and *green field*). On the other hand, VCA presented the worst results for A.P. Hill. Most of the extracted endmembers by VCA correspond to water and no vegetation endmember was found. The spectral endmember classes extracted by the proposed approach are consistent with the classification map and their spectral endmembers are very similar to the spectral library.

Unmixing results from Cuprite using the four algorithms present comparable results. In this case, VCA extracted several endmembers related with the materials described by the classification maps. In terms of the reconstruction error, the four algorithms obtained low error. Cuprite is a complex image with several small spectrally uniform regions. However, the proposed approach detected the different materials and obtained results comparable with the other methods. Abundances from extracted endmember spectral classes were more consistent with the distribution of materials in the classification map than the other methods (see Figure 7.21). Although the best results in terms of true positive rates were obtained by RBSPP and SMACC, the proposed approach obtains comparable true positive rates while the estimated abundance of true positive pixels are higher than abundance of false positive pixels.

An implementation of the unmixing approach based on multiscale representation was developed using the MATLAB platform. This implementation allows the unsupervised processing of hyperspectral images. The automation of the spectral endmember extraction allows to analyze scenes without the need to develop expertise in computing. The implementation takes a family of smoothed images $\{\mathbf{Y}_1, \mathbf{Y}_2, \dots, \mathbf{Y}_{T_F}\}$ and the maximum number of spectral endmember classes c_{\max} as the inputs. The output provides spectral endmember classes $C_{\hat{c}}$ and their corresponding abundance maps \mathbf{A}_C . Figure 8.1 presents a block diagram for the computing system. The next section describes in detail the implementation of each block, and the complexity analysis is presented in Section 8.2.

8.1 IMPLEMENTATION DESCRIPTION

The implementation of the unmixing approach based on multiscale representation takes a set of smoothed images as input. The multiscale representations for the experiments included in this document were obtained with Duarte's algorithm presented in [26]. However, there are several methods for nonlinear diffusion such as those reviewed by Duarte et al. in [74] and *tensor anisotropic diffusion* presented by Marin-Quintero in [106]. These methods can be combined with the proposed unmixing algorithm for the analysis of hyperspectral images.

The computational system for the unsupervised unmixing analysis is divided in 7 steps: scale selection, spectral endmember extraction, abundance estimation, pair-

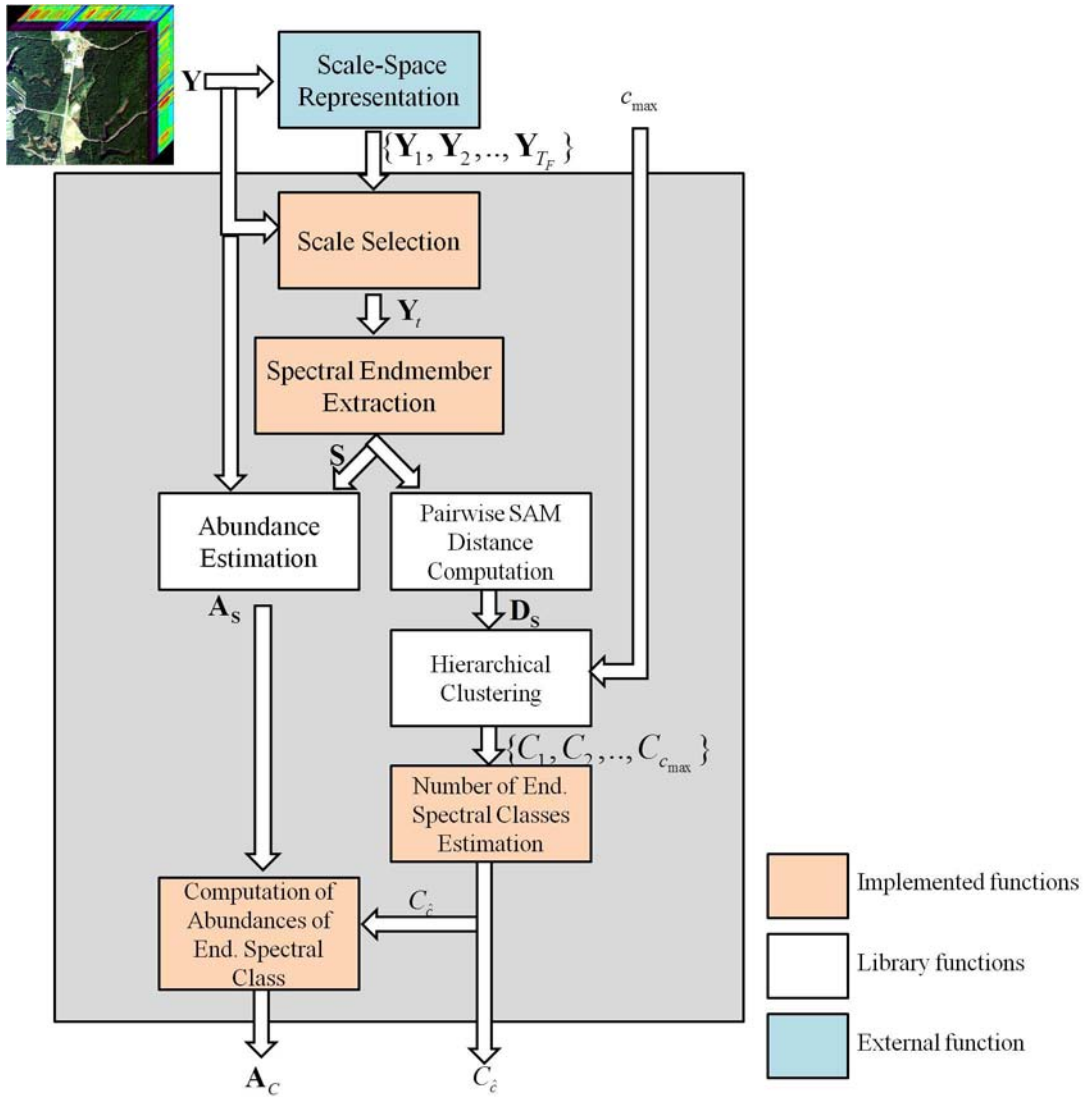


Figure 8.1: Computational system for unsupervised unmixing analysis.

Table 8.1: Algorithm for scale selection.

Inputs: \mathbf{Y}_0 and $\{\mathbf{Y}_1, \mathbf{Y}_2, \dots, \mathbf{Y}_{T_f}\}$
Repeat for $i = 1$ to T_f :
Compute $\mathbf{Y}_D(i, j, k) = \frac{ \mathbf{Y}_t(i, j, k) - \mathbf{Y}_0(i, j, k) }{\mathbf{Y}_0(i, j, k)}$
Calculate the entropy $E(i)$ for \mathbf{Y}_D
Compute the entropy changes $\delta E(i) = E(i) - E(i - 1)$ for $i = 2 \dots T_f$
Select T such that $\delta E(i) < 0.01$
Output: Smoothed image \mathbf{Y}_T

wise SAM (spectral angle measure) distance computation, hierarchical clustering, estimation of the number of spectral endmember classes, and abundance computation (see Figure 8.1). Some of these steps use existing MATLAB functions (white boxes in Figure 8.1) and others were implemented as part of this work (pink boxes in Figure 8.1). The description of each step is included below.

First, the entropy change criterion developed in Section 3.2.1.5 is used for automatic scale selection. The entropy of image $\mathbf{Y}_D(i, j, k)$ (see Equation 3.21) is calculated to select the optimal stopping time. The entropy change criterion employs the average of the entropy for each band of image \mathbf{Y}_D . The optimal scale is selected as the end of the break point of the L-curve formed by the entropy change. A threshold of 0.01 is used to determine the end of the break point. Results presented in Chapters 3 and 6 show that this threshold works very well for different types of image. The inputs for the function *scaleSelection* are the original image \mathbf{Y}_0 , the path of the directory that contains the family of smoothed images (\mathbf{Y}_t), and the number of smoothing iteration T_f where $0 < t < T_f$. This function selects a single smoothed image and returns the smoothed image in the optimal scale T (see algorithm in Table 8.1).

The spectral endmembers are extracted using the multigrid representation as described in Section 3.1. The multigrid structure is a set of graphs where each graph is a layer of the multigrid and the graphs are connected between themselves. An object oriented programming (OOP) approach was used for the implementation of

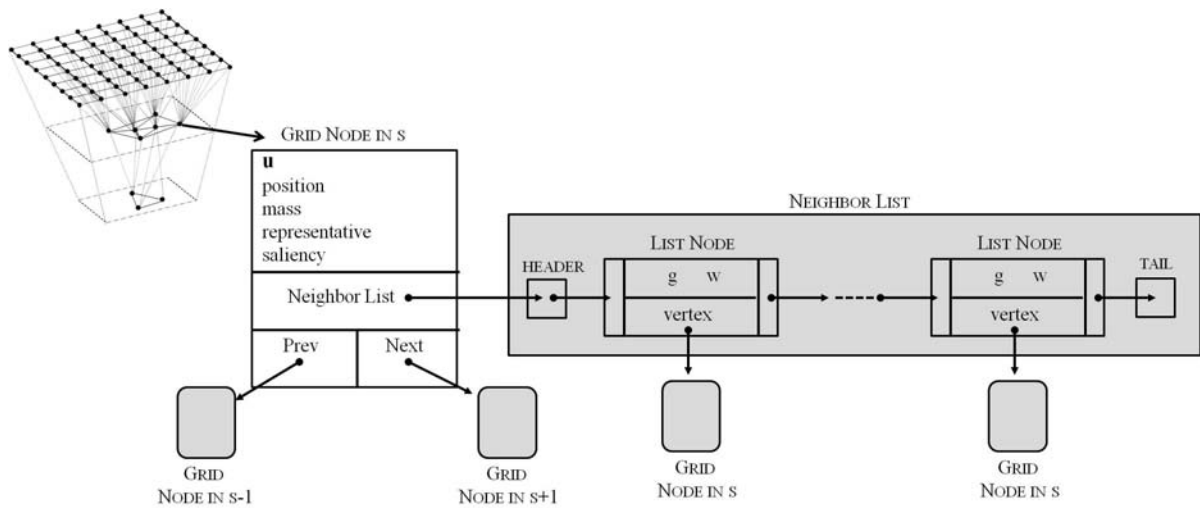


Figure 8.2: Data structures for multigrid.

the multigrid structure in MATLAB. Other implementation can be done using the adjacency matrix. However, most of the graphs are represented by large sparse matrices making necessary the use of sparse representations such as the MATLAB sparse storage organization¹. Although most of the algebra is optimized for sparse matrix in MATLAB, the searching and indexing algorithms were very slow for this problem. Using OOP in MATLAB, the multigrid was built as a data structure where each vertex was represented by a *Grid Node* object. The grid nodes keep most of the information necessary for the construction of the multigrid such as the signature \mathbf{u} (Equation 3.8), the position of the vertex with respect to the original image, the mass (Equation 3.7), the saliency (Equation 3.10), and a Boolean variable that indicates if the vertex is selected as a representative. Furthermore, the grid node in layer s keeps the connection with their list of neighbors and two pointers to itself in the previous ($s - 1$) layer and in the next layer ($s + 1$) of the multigrid. If the vertex is not a representative, then the next pointer is empty. The list of neighbors is a single link list where each node has the information about the weights w (Equation 3.6), the similarity g (Equation 3.9), and a pointer to the next node in the list and its associated *Grid Node*. Figure 8.2 presents the structures used to build the multigrid. The steps for

¹ <http://www.mathworks.com/help/matlab/ref/sparse.html>

Table 8.2: Algorithm for spectral endmember extraction using multigrid structure.

Inputs: \mathbf{Y}_o and α

Initialization: $\mathbf{U}^0 = \mathbf{Y}_o$, $V^0 = \{\mathbf{u}_1^0, \mathbf{u}_2^0, \dots, \mathbf{u}_M^0\}$
and for each vertex V_i , initialize:
 $neighborList(V_i^0) = \{(g_{ij}, j) \mid j \text{ is a neighbor of } i\}$
 $mass(V_i) = g_{ij}$
and $Representative = false$.

Repeat until convergence:
 sort masses into a *List*
 $V^{s+1} = V^{s+1} \cup \mathbf{u}_i^s$ $i = \text{first vertex in } List$
 For remaining vertex in *List*:
 if V_i^s holds condition in 3.5 then $V^{s+1} = V^{s+1} \cup \mathbf{u}_i^s$
 For each vertex in s
 Compute w_{ij} using 3.6
 For each vertex in $s + 1$
 Actualize *masses* by 3.7
 Actualize \mathbf{u}^{s+1} by 3.8
 Connect new grid $s + 1$ using 3.9
 For each vertex in $s + 1$
 Compute *saliency* by 3.10
 For each vertex in last grid:
 $index = getPosition(V_i)$
 $\mathbf{S} = \mathbf{S} \cup \mathbf{Y}_o(index)$

Output: Spectral endmember matrix \mathbf{S}

the spectral endmember extraction correspond to the construction of the multigrid (Equations 3.5 to 3.10) but the masses are initialized equal to g (see Section 3.2). A pseudo-code for spectral endmember extraction using the multigrid data structure is presented in Table 8.2.

Once the spectral endmembers are extracted, the abundances are computed using either constrained least square methods or sparse regression. If the number of spectral endmembers is less than or equal to the number of bands then the function NNSLO [37] is used for abundance estimation. This function is part of the HIAT toolbox developed at the UPRM Laboratory for Applied Remote Sensing and Im-

age Processing [107]. The complete toolbox is available online ². Another function used to estimate the abundances is SUNSAL [62] that solves sparse regression in the case that the number of spectral endmembers exceeds the number of bands. The algorithm is found in [62] and a MATLAB implementation is available online ³.

The MATLAB function *clusterdata* was used to perform the clustering of the spectral endmember classes. The function *clusterdata* uses hierarchical clustering techniques with different types of linkages and distances. Experiments in Section 4.3.2 showed that hierarchical clustering using complete linkage and spectral angle distance obtained the best results for spectral endmember class extraction. Thus, complete linkage and SAM are used as default for spectral endmember class extraction. The number of clusters is varied between 2 and c_{max} where c_{max} is set by the user.

The number of spectral endmember classes is estimated using the Davies and Bouldin validity index [95]. The function *ValidityIndexDaviesBouldien* is responsible to select the optimal number of clusters. The input for this function is the set of spectral endmembers \mathbf{S} , and the clustering results obtained from the *clusterdata* function and organized in a matrix where each column is a clustering result. The spectral angle measure is used to compute the dispersion measure and the distance between clusters (see Section 4.1.3.2). The function selects the optimal number of clusters and returns a vector with the values of the validity index for 2 to c_{max} (see algorithm in Table 8.3). Finally, the abundances for the spectral endmember classes are computed as the sum of abundances for spectral endmembers belonging to the same class. The outputs for the implementation are the set of spectral endmembers clustered into spectral endmember classes $C_{\hat{c}}$, and their abundances \mathbf{A}_C .

The spectral endmembers are extracted automatically and grouped based on the spectral similarity. However, the assignment of labels that related the spectral endmember classes with known materials requires the interpretation and analysis of

² <http://www.censsis.neu.edu/software/hyperspectral/hyperspectral.html>

³ <http://www.lx.it.pt/biucas/publications.html>

Table 8.3: Algorithm for the Davies and Bouldin validity index computation.

Inputs: $C_1 \dots C_{max_c}$ and the set of spectral endmembers \mathbf{S}

Repeat for $i = 1$ to max_c :

Compute the similarity between clusters: $R_{ij} = \frac{d_i + d_j}{M_{ij}}$

where $d_i = \frac{1}{m_i} \sum_{j=1}^{m_i} dist(\mathbf{s}_j, \mu_i)$

and $M_{ij} = dist(\mu_i, \mu_j)$

Compute the Davies and Bouldin index: $DB(k) = \frac{1}{k} \sum_{i=1}^k R_i$

Select the number of spectral endmember class such that $\hat{c} = \min DB(k)$ for $k = 2 \dots c_{max}$

Output: Endmember spectra classes C_i

experts. The developed unsupervised unmixing approach is a tool for information extraction, and these results require of interpretation of experts to bring the information to a higher abstraction level.

8.2 COMPLEXITY ANALYSIS

Scale selection requires computing the entropy for each one of the n spectral bands and its complexity is linear in the number of pixels m . The entropy is calculated N_s times, where N_s is the maximum number of smoothing iterations, or the number of images in the scale space representation. Thus, the running time of scale selection is $N_s n m = O(nm)$, where n is the number of bands and m is the number of pixels.

Spectral endmember extraction depends on the construction of the multigrid, which consists of several operations over the vertices of each layer [26]. Thus, the running time of the spectral endmember extraction algorithm is:

$$\sum_s \tau n v_s \leq \tau n \sum_s (1/2)^s m < 2\tau n m = O(nm)$$

where τ is a constant representing the number of operation per vertex (Equations 3.5 to 3.10), s is the number of layers, and v_s is the number of vertex in each layer where $v_s < (1/2)v_{s-1}$ and $v_0 = m$ [26].

The computation of the pairwise distance takes $O(nm^2)$ and the hierarchical clustering algorithm has complexity of $O(m^2)$ [30].

Finally, SUnSAL [62] and NNSLO [37] algorithms for abundance estimation take $O(nmp)$ time per each iteration until the stopping criteria are satisfied. The abundance estimation is the most expensive step of the system since it requires to solve an optimization problem for each pixel in the image.

8.3 SUMMARY

The proposed approach allowed the implementation of a full unsupervised application for the unmixing analysis of hyperspectral imagery which uses only the information within the image. The implementation of the proposed approach described in Figure 1.4 consists of seven steps: scale selection, spectral endmember extraction, abundance estimation, pairwise SAM distance computation, hierarchical clustering, estimation of the number of spectral endmember classes, and abundance computation. Important parameters such as the scale and the number of spectral endmember classes are automatically determined using the criteria proposed in Sections 3.2.1.5 and 4.1.3.2 respectively. The most time consuming operation in the unmixing analysis is the abundance estimation since it requires solving an optimization problem per pixel. However in the future, it can be parallelized to improve performance.

ETHICAL CONSIDERATIONS ABOUT REMOTE SENSING IMAGING

The launch of Landsat 1 in 1972 started a new era for remote sensing. Although some remote sensing systems existed before Landsat, this satellite was the first attempt for monitoring the Earth surface from the space ¹. Since then, a large number of government and commercial remote sensing systems have been developed capturing images each time with higher spatial resolutions and in a large variety of spectral ranges. Applications of remote sensing technology include environmental monitoring, climate change studies, agriculture, mineral exploration, archeology, meteorology, military application, and others [1]. This wide range of applications and the increasing availability of sensors pose the need of regulation and ethical guidelines regarding to the acquisition, processing, and interpretation of remote sensing imagery [108].

Initially, remote sensing systems were run by governments, and therefore, their activities were regulated by the laws of each estate. However, the emergence of commercial remote sensing systems opened several inquiries about national security, sovereignty, and privacy. The United Nations Committee on the Peaceful Uses of Outer Space (COPUOS) has made a great effort to establish treaties and laws concerning space activities. In 1986, COPUOS declared 15 principles regarding remote sensing of the Earth from the space ². These principles have established general guidelines for information sharing and technology cooperation among countries that practice remote sensing activities. One of the principles say explicitly that re-

¹ <http://landsat.gsfc.nasa.gov/about/landsat1.html>

² <http://www.oosa.unvienna.org/oosa/en/SpaceLaw/treaties.html>

remote sensing activities cannot affect the sovereignty of other estates. The principles established that products obtained from data collected over other states should be available at a “reasonable cost” for the sensed territory. These principles are an effort to establish international cooperation for Earth monitoring and study. These principles are limited to activities in outer space leaving a gap for the regulation of remote sensing activities using aircrafts and do not take into account individual privacy.

Privacy is, maybe, the aspect more discussed about remote sensing imagery. The increasing incorporation of this technology in law enforcement activities [109, 110] and the emergence of high spatial resolution imagery systems with information available for everyone pose the question how far the use of these technologies respects the privacy of individuals. For instance, Canada is allowing the use of infrared multispectral sensors for the detection of heat loss from buildings that is a common indicator of marijuana growing [109]. In UK, remote sensors are employed for the monitoring of farms to verify the incompliance with environmental regulations [110]. Although these activities are regulated for governments, people who do not know this technology and how it is being used may feel they are violating their privacy. The availability of satellite images through the Internet poses another problem of privacy. For example, Google Earth ³ and Google Maps ⁴ are products for pc and mobile navigation that allows you to view satellite imagery all over the world. Most of these images have very high spatial resolution allowing the observation in great details of buildings, homes and cars exposing places belonging to private individual.

The increased use of products derived from remote sensing data also posse the need of regulations for the processing and analysis of this information. The American Society for Photogrammetry and Remote Sensing in their ethical code rejects remote sensing activities that involve “deception through data alteration” ⁵. Cromey

³ <http://www.google.com/earth/index.html>

⁴ <https://maps.google.com/>

⁵ <http://www.asprs.org/About-Us/Code-of-Ethics-of-the-American-Society-for-Photogrammetry-and-Remote-Sensing.html>

[111] described several ethical guidelines for the processing of scientific imagery. While this guide is focused on biological image processing, most of these guidelines should be followed by remote sensing scientists. The twelve guidelines [111] describe the adequate manipulation and presentation of images. Cromey said that always a copy of the unprocessed image must be kept. Comparison between images or results should be performed only when the original images were acquired in the same conditions. Cropping and adjustments such as contrast or histogram stretch can be used and a complete description about the image transformation should be included with the presentation of the results. Cloning and copying an object into an image is not recommendable. The final product should be saved in an uncompressed format. For example, JPEG is not recommended since it is a lossy compression format that introduces elements in the image which can lead to the misinterpretation of the results. TIFF is the more commonly recommended format for scientific images [111]. Other guidelines and their importance for image processing can be found in [111].

Although there are few regulations for the processing of remote sensing images, it is important that researchers and scientists using these images develop an ethical consciousness of the capabilities of this technology. Remote sensing technology is advancing rapidly. To create regulations that control the different problems that may arise due to the use of these technologies is very complicated. So, it is very important that scientists, researchers, and even ordinary people develop awareness of this technology, its uses, and capabilities.

CONCLUSIONS AND FUTURE WORK

10.1 CONCLUSIONS

Unmixing analysis of hyperspectral imagery is usually performed by spectral techniques which do not employ the spatial information of the images. Recently, spatial-spectral algorithms have been developed. Most of these algorithms incorporate the spatial information in the unmixing analysis by using spatial kernels. However, this introduces dependence on the size of neighborhood. Martin and Plaza [17] proposed a spatial-spectral algorithm that avoid the use of spatial kernels using unsupervised clustering techniques to look for spectrally uniform regions. However, this technique is only a pre-processing step that requires the use of standard spectral-only techniques for the final endmember extraction. In addition, it requires the estimation of the number of endmembers like most of the existing unmixing algorithms.

This work developed a new spatial-spectral approach for unmixing analysis using multiscale representation and multigrid methods for unsupervised endmember extraction. Multiscale representation using nonlinear diffusion allows to generate a family of images where fine details are iteratively removed decreasing the local spectral variability. The proposed approach selected one of the smoothed images by using entropy to measure the information removed by the smoothing operation. The entropy change criterion obtained consistent results for different types of images. This criterion tends to select scales in the first few iterations of the nonlinear diffusion avoiding mixed pixels at later stages.

Once a scale is selected, spectral endmember extraction was performed by the construction of a multigrid structure where the vertices in the coarsest grid represent the spectral features of the image and these are selected as the spectral endmembers. Results showed that spectral endmember extraction using the multigrid effectively extracts the image components as well as preserve the spectral variability.

Spectral endmembers were grouped into spectral endmember classes using clustering techniques. Hierarchical, partitional, and spectral clustering were studied for spectral endmember class extraction. Hierarchical algorithms with complete and average linkage outperforms partitional and spectral clustering results. The most commonly used distance metrics for spectral data were also compared. Euclidian distance, spectral angle, spectral correlation, and spectral information divergence were employed to build the pairwise distance required in the clustering process obtaining the best results with the spectral angle measure. Validity indexes were studied for the estimation of the number of spectral endmember classes. Dunn, Davies and Bouldin, Kim, SD and CH indexes were used. The best results were obtained using the Davies and Bouldin index with complete linkage and spectral angle measure.

A full evaluation of the unsupervised unmixing approach was conducted using synthetic data and real hyperpectral images. Synthetic data allows the quantitative assessment of the proposed approach under a controlled environment. However, it is very important to recognize the difficulties to simulate image with controlled condition. Real images are affected by several factors such as the spectral variability of the materials, topographic and atmospheric effects, and noise. In addition, hyperspectral images do not only have spectral information, these images keep information about the spatial distribution of materials. Two synthetic data sets were used for the quantitative assessment of the proposed approach. The first data set has a simple spatial distribution that allows the evaluation of the proposed approach with different noise levels. The results showed that the nonlinear diffusion filtering used in the first step of the proposed approach helps to reduce the noise effects. The second data

set simulated a known spatial distribution by using extracted abundances from real hyperspectral images. The results from this data set showed larger errors for some of the endmembers that were due to the difference of amplitude between the original endmembers (i.e. endmembers used to generate the image) and the extracted spectra.

Futhermore, hyperspectral imagery from mining and forest scenarios were employed for a quantitative evaluation of the proposed unmixing technique. It is important to recognize that there are great limitations to perform quantitative assessment of unmixing results. Most of the time, only classification maps and spectral libraries are available for hyperspectral dataset. Even the spectral libraries are usually laboratory spectra. Thus, a new assessment methodology was developed to use published classification maps for a quantitative evaluation of the proposed unmixing approach. First, the assessment methodology uses a qualitative comparison between the estimated abundances and the information classes on the scene. It is assumed that the classification maps provide information about the distribution of materials, and one or more spectral endmember classes can be related to the information classes within the classification map. Unmixing results for A.P.Hill and Cuprite were related to several materials in the reference classification maps showing consistency among spectral endmember and reference spectra. Once the relation between spectral endmember classes and information classes was established, the quantitative assessment is performed using three statistics inspired by detection theory: true positive rate, false positive rate, and false negative rate. The proposed unmixing approach obtained good true positive rates for most of the A.P. Hill and Cuprite classes. The false positive rate were high. But, the study of the estimated abundance of false positive pixels showed that these were smaller than the abundance estimated for the true positive pixels. In addition, the assessment methodology generates a classification map using the estimated abundances and a majority vote criterion. The classification maps obtained for A.P. Hill and Cuprite show good correspondence with the

published classification maps. The between-class agreement and assignment-class agreement were used to compare the generated classification map and the published ones.

The proposed approach was compared with SMACC, VCA and RBSPP combined with VCA. SMACC and VCA are selected since these are widely used geometrical approaches that only require the number of endmembers. Instead, RBSPP is a spatial-spectral pre-processing step that does not use kernels like the proposed approach. The three algorithms assume that endmembers are pixels in the image. Although the developed algorithm uses only information contained in the image and has few free parameters such as the diffusion parameter and the maximum number of clusters, the obtained results were excellent for A.P. Hill. For Cuprite, the results obtained from the four unmixing algorithms are comparable. The unmixing results for the A.P. Hill image significantly outperform results obtained with other unmixing techniques. The consistency among spectral endmember classes and the classification map showed the capabilities of the proposed approach for applications where little a priori information about the basic spectral components is available.

The proposed approach allowed the implementation of a computing system for full unsupervised unmixing analysis of hyperspectral imagery. Important parameters such as the scale and the number of spectral endmember classes are automatically determined using the proposed entropy change criterion and the Davies and Bouldin validity index respectively.

The main contribution of this work was the integration of multiscale representation, multigrid, and clustering for the development of a new approach for the unmixing analysis of hyperspectral imagery. Many of these techniques are widely used in image processing. But, there is no previous work that uses multiscale representation and multigrid techniques for the unmixing analysis. Multiscale representation and the multigrid allow the integration of spatial information in the unmixing analysis without using spatial windows. In addition, the multigrid structure allows the spec-

tral endmember extraction without the estimation of the number of endmembers. The proposed unmixing approach provides useful information (spectral endmember classes and abundances) but these products still require further interpretation and analysis by experts.

10.2 FUTURE WORK

The developed computational system used as input a family of smoothed images obtained from the Duarte's algorithm for multiscale representation of hyperspectral imagery using nonlinear diffusion [26]. However, there are several methods that can produce a family of smoothed images such as those reviewed by Duarte et al. [74] and tensor anisotropic diffusion [106]. A study about the influence of the diffusion method over the extracted endmembers should be addressed in the future. The nonlinear diffusion step is a very important component inside the proposed approach. An interesting question to address in the future is how different methods change the number of extracted endmembers and their shapes using the proposed methodology.

Sometimes, spectral endmember class extraction using clustering produced clusters with mixed components such as the generated for the False Leaf image shown in Section 4.3.3.2. Feature selection and extraction techniques can be studied in the future to improve the clustering results. Methods such as Fisher discriminant analysis [112], principal components [2], SVDSS [113], and information divergence projection pursuit [114] could be used to reduce the number of features, and improve the spectral endmember classes.

On the other hand, the developed unmixing approach uses image-derived endmembers. It means that images collected in different conditions can result in differ-

ent spectral endmembers. In the future, it can be study how the spectral endmembers compare with the extracted from images collected in different conditions.

During the assessment of the proposed approach, it was noted the difficulties to perform quantitative validation of spatial-spectral unmixing algorithms. This work used both synthetic data and real imagery for the quantitative assessment. However, the synthetic data do not reach the complexity found in real images. Furthermore, the quantitative analysis used actual data is limited to classification maps and spectral libraries. There are no images with detailed abundance maps that allow a direct quantitative assessment. Although a quantitative methodology was developed, it is important to continue studying quantitative methodologies and generation of synthetic data in the future that allow a direct and complete assessment of unmixing results.

BIBLIOGRAPHY

- [1] R. A. Schowengerdt, *Remote Sensing: Methods and Models for Image Processing*. Academic Press (Elsevier), 2007.
- [2] J. Richards and X. Jia, *Remote Sensing Digital Image Analysis*. Springer, 2006.
- [3] N. Keshava and J. F. Mustard, "Spectral unmixing," *IEEE Signal Processing Magazine*, vol. 19, no. 1, pp. 44–57, 2002.
- [4] J. Adams and A. Gillespie, *Remote Sensing of Landscapes with Spectral Images: A physical Modeling Approach*. Cambridge University Press, 2006.
- [5] J. W. Boardman, "Automating spectral unmixing of aviris data using convex geometry concepts," *Summaries 4th Annual JPL Airborne Geoscience Workshop*, vol. 1, pp. 11–14, 1993.
- [6] T. Blaschke, "Object based image analysis for remote sensing," *Journal of Photogrammetry and Remote Sensing*, vol. 65, pp. 2–16, 2010.
- [7] T. Blaschke and J. Strobl, "What's wrong with pixels? some recent developments interfacing remote sensing and gis," *Zeitschrift fur Geoinformationssysteme*, vol. 14, pp. 12–17, 2001.
- [8] A. Plaza, J. Benediktsson, J. Boardman, J. Brazile, L. Bruzzone, G. Camps-Valls, J. Chanussot, M. Fauvel, P. Gamba, A. Gualtieri, M. Marconcini, J. Tilton, and G. Trianni, "Recent advances in techniques for hyperspectral image processing," *Remote Sensing of Environment*, vol. 113, pp. s110–s122, 2009.

- [9] A. Plaza, P. Martinez, R. Perez, and J. Plaza, "Spatial/spectral endmember extraction by multidimensional morphological operations," *IEEE Transactions on Geosciences and Remote Sensing*, vol. 40, no. 9, pp. 2025–2041, 2002.
- [10] L. Jimenez, J. Rivera-Medina, E. Rodriguez-Diaz, E. Arzuaga-Cruz, and M. Ramirez-Velez, "Integration of spatial and spectral information by means of unsupervised extraction and classification for homogeneous objects applied to multispectral and hyperspectral data," *IEEE Transactions on Geoscience and Remote Sensing*, vol. 43, no. 4, pp. 844–851, 2005.
- [11] V. Walter, "Object-based classification of remote sensing data for change detection," *Journal of Photogrammetry and Remote Sensing*, vol. 58, pp. 225–238, 2004.
- [12] Q. Yu, P. Gong, N. Chinton, G. Biging, M. Kelly, and D. Schirokauer, "Object-based detailed vegetation classification with airborne high spatial resolution remote sensing imagery," *Photogrammetric Engineering and Remote Sensing*, vol. 72, pp. 799–811, 2006.
- [13] M. Baatz, U. Benz, S. Dehghani, M. Heynen, A. Hölzje, P. Hofmann, I. Lingenfelder, M. Mimler, M. Sohlbach, and G. W. Weber, "ecognition user guide," *Definiens Imaging GmbH*, 2001.
- [14] D. M. Rogge, B. Rivard, J. Zhang, A. Sanchez, J. Harris, and J. Feng, "Integration of spatial-spectral information for the improved extraction of endmembers," *Remote Sensing of Environment*, vol. 110, no. 3, pp. 287–303, 2007.
- [15] M. Zortea and A. Plaza, "Spatial preprocessing for endmember extraction," *IEEE Transactions on Geoscience and Remote Sensing*, vol. 47, no. 8, pp. 2679 – 2693, aug. 2009.

- [16] K. Canham, A. Schlamm, A. Ziemann, B. Basener, and D. Messinger, "Spatially adaptive hyperspectral unmixing," *IEEE Transactions on Geoscience and Remote Sensing*, vol. 49, no. 11, pp. 4248–4262, 2011.
- [17] G. Martin and A. Plaza, "Region-based spatial preprocessing for endmember extraction and spectral unmixing," *IEEE Geoscience and Remote Sensing Letters*, vol. 8, no. 4, pp. 745–749, 2011.
- [18] A. Zare and P. Gader, "Piece-wise convex spatial-spectral unmixing of hyperspectral imagery using possibilistic and fuzzy clustering," *IEEE International Conference on Fuzzy Systems (FUZZ)*, pp. 741–746, 2011.
- [19] J. Liu, J. Zhang, Y. Gao, C. C. Zhang, and Z. Li, "Enhancing spectral unmixing by local neighborhood weights," *IEEE Journal of Selected Topics in Applied Earth Observations and Remote Sensing*, vol. 5, no. 5, pp. 1545–1552, 2012.
- [20] D. A. Roberts, M. Gardner, R. Church, S. Ustin, G. Scheer, and R. O. Green, "Mapping chaparral in the santa monica mountains using multiple endmember spectral mixture models," *Remote Sensing of Environment*, vol. 65, pp. 267–279, 1998.
- [21] A. Zare and P. D. Gader, "Pce: Piece-wise convex endmember detection," *IEEE Transactions on Geosciences and Remote Sensing*, vol. 48, no. 6, pp. 2620–2632, 2010.
- [22] A. Zare and P. Gader, "Endmember detection using the dirichlet process," *Proc. of IEEE 19th International conference on Pattern Recognition*, pp. 1–4, 2008.
- [23] B. Somers, M. Zorteza, A. Plaza, and G. Asner, "Automated extraction of image-based endmember bundles for improved spectral unmixing," *IEEE Journal of Selected Topics in Applied Earth Observations and Remote Sensing*, vol. 5, no. 2, pp. 396–408, april 2012.

- [24] T. Lindeberg, *Scale-space Theory in Computer Vision*. Kluwer Academic Publisher, 1994.
- [25] G. Sapiro, *Geometric Partial Differential Equations and Image Analysis*. Cambridge University Press, 2001.
- [26] J. M. Duarte, G. Sapiro, M. Velez, and P. Castilo, "Multiscale representation and segmentation of hyperspectral imagery using geometric partial differential equations and algebraic multigrid methods," *IEEE Transactions on Geosciences and Remote Sensing.*, vol. 46, no. 8, pp. 1303–1314, 2008.
- [27] R. D. Falgout, "An introduction to algebraic multigrid," *Computing in Science and Engineering*, vol. 8, no. 6, pp. 24–33, 2006.
- [28] A. K. Jain and R. C. Dubes, *Algorithms for Clustering Data*. Prentice Hall, 1988.
- [29] A. K. Jain, M. N. Murty, and P. Flynn, "Data clustering: a review," *ACM computing surveys*, vol. 31, no. 3, pp. 264–323, 1999.
- [30] R. Xu and D. Wunsch, "Survey of clustering algorithms," *IEEE Transactions on Neural Network*, vol. 16, pp. 645–678, 2005.
- [31] D. J. Kim, Y. W. Park, and D. J. Park, "A novel validity index for determination of the optimal number of clusters," *IEICE Transactions on information and systems*, vol. E84, no. 2, pp. 281–285, 2001.
- [32] U. Maulik and S. Bandyopadhyay, "Performance evaluation of some clustering algorithms and validity indices," *IEEE Transactions on Pattern Analysis and Machine Intelligence*, vol. 24, no. 12, pp. 1650–1654, 2002.
- [33] J. Gruninger, A. J. Ratkowski, and M. L. Hoke, "The sequential maximum angle convex cone (smacc) endmember model." *Proc. SPIE - Algorithms and Technologies for Multispectral, Hyperspectral, and Ultraspectral Imagery X*, vol. 5425, pp. 1–14, 2004.

- [34] J. M. Nacimient and J. M. Bioucas, "Vertex component analysis: a fast algorithm to unmix hyperspectral data," *IEEE Transactions on Geosciences and Remote Sensing*, vol. 43, no. 3, pp. 898–914, 2005.
- [35] J. Seguel and D. Rodriguez, "The doctoral program in computing and information sciences and engineering of the university of puerto rico," *Future Generation Computer Systems*, vol. 19, pp. 1293–1298, 2003.
- [36] R. Basedow, W. Aldrich, J. Colwell, and W. Kinder, "Hydice system performance: an update," *Proc. SPIE - Hyperspectral Remote Sensing and Applications*, vol. 2821, pp. 76–84, 1996.
- [37] S. Rosario-Torres and M. Velez-Reyes, "An algorithm for fully constrained abundance estimation in hyperspectral unmixing," *Proc. SPIE - Algorithms and Technologies for Multispectral, Hyperspectral, and Ultraspectral Imagery XI*, vol. 5806, pp. 711–719, 2005.
- [38] A. Ifarraguerri and C. Chang, "Multispectral and hyperspectral image analysis with convex cones," *IEEE Transactions on Geosciences and Remote Sensing*, vol. 37, no. 2, pp. 756–770, 1999.
- [39] J. W. Boardman, F. Kruse, and R. Green, "Mapping target signatures via partial unmixing of aviris data," *Summaries JPL Airborne Earth Science Workshop*, 1995.
- [40] M. E. Winter, "N-findr: An algorithm for fast autonomous spectral endmember determination in hyperspectral data," *Proc. SPIE - Imaging Spectrometry V*, vol. 3753, pp. 265–275, 1999.
- [41] —, "Fast autonomous spectral endmember determination in hyperspectral data," *International Conference on Applied Geologic Remote Sensing Vancouver British Columbia Canada*, vol. 3753, pp. 337–344, 1999.

- [42] C. W. C. Chang, W. Liu, and Y. Ouyang, "A new growing method for simplex-based endmember extraction algorithm," *IEEE Transactions on Geoscience and Remote Sensing*, vol. 44, no. 10, pp. 2804–2819, 2006.
- [43] D. Donoho and V. Stodden, "When does non-negative matrix factorization give a correct decomposition into parts?" *Advances in Neural Information Processing Systems*, vol. 16, pp. 1141–1148, 2004.
- [44] J. W. Boardman, "Geometric mixture analysis of imaging spectrometry data," *Proc. IEEE International Geoscience and Remote sensing Symposium*, vol. 4, pp. 2369–2371, 1994.
- [45] A. Geen, M. Berman, P. Switzer, and M. Craig, "A transformation for ordering multispectral data in terms of image quality with implications for noise removal," *IEEE Transactions on Geosciences and Remote Sensing*, vol. 26, no. 1, pp. 65–74, 1988.
- [46] D. Lee and S. Seung, "Learning the parts of objects by non-negative matrix factorization." *Nature*, vol. 401, pp. 788–791, 1999.
- [47] C. Y. Liou and K. D. O. Yang, "Unsupervised classification of remote sensing imagery with non-negative matrix factorization," *Proc. Twelfth International Conference on Neural Inf. Proc.*, pp. 280–285, 2005.
- [48] L. Miao and H. Qi, "Endmember extraction from highly mixed data using minimum volume constrained nonnegative matrix factorization," *IEEE Transactions on Geosciences and Remote Sensing*, vol. 45, no. 3, pp. 765–777, 2007.
- [49] S. Jia and Y. Qian, "Constrained nonnegative matrix factorization for hyperspectral unmixing." *IEEE Transactions on Geosciences and Remote Sensing*, vol. 47, no. 1, pp. 161–173, 2009.

- [50] Y. Masalmah and M. Velez-Reyes, "A full algorithm to compute the constrained positive matrix factorization and its application in unsupervised unmixing of hyperspectral imagery," *Proc. SPIE - Algorithms and technologies for multispectral, hyperspectral, and ultraspectral imagery XIV*, vol. 6966, pp. 1–12, 2008.
- [51] A. D. Stocker and P. Schaum, "Application of stochastic mixing models to hyperspectral detection problems," *Proc. SPIE - Algorithms for Multispectral and Hyperspectral Imagery III*, vol. 3071, pp. 22–23, 1997.
- [52] J. Nascimento and J. Bioucas, "Hyperspectral unmixing algorithm via dependent component analysis," *Proc. IEEE Geoscience and Remote Sensing Symposium*, pp. 4033–4036, 2007.
- [53] O. Eches, N. Dobigeon, and J. Tourneret, "Estimating the number of endmembers in hyperspectral images using the normal compositional model and a hierarchical bayesian algorithm," *IEEE Journal on Selected Topics in Signal Processing*, vol. 4, no. 3, pp. 582–591, 2010.
- [54] K. Lee, *A subpixel scale target detection algorithm for hyperspectral imagery*. Ph.D. Dissertation, Rochester Institute of Technology, Center for Imaging Science, 2003.
- [55] J. Bioucas-Dias and J. Nascimento, "Hyperspectral subspace identification," *IEEE Transactions on Geoscience and Remote Sensing*, vol. 46, no. 8, pp. 2435 – 2445, 2008.
- [56] M. Velez-Reyes and S. Rosario-Torres, "Solving abundance estimation in hyperspectral unmixing as a least distance problem," *Proc. IEEE International Geoscience and Remote Sensing Symposium*, vol. 5, pp. 3276–3278, 2004.

- [57] A. Castrodad, Z. Xing, J. Greer, E. Bosch, L. Carin, and G. Sapiro, "Discriminative sparse representation in hyperspectral imagery," *Proc. IEEE International Conference on Image Processing*, pp. 1313–1316, 2010.
- [58] Y. Chen, N. M. Nasrabadi, and T. D. Tran, "Sparse representation for target detection in hyperspectral imagery," *IEEE Journal of Selected Topics in Signal Processing*, vol. 5, no. 3, pp. 629–640, 2011.
- [59] Y. Chen, N. Nasrabadi, and T. Tran, "Hyperspectral image classification using dictionary-based sparse representation," *IEEE Transactions on Geoscience and Remote Sensing*, vol. 49, no. 10, pp. 3973–3985, 2011.
- [60] M. Iordache, J. Bioucas, and A. Plaza, "Sparse unmixing of hyperspectral data," *IEEE Transactions on Geosciences and Remote Sensing*, vol. 49, no. 6, pp. 2014–2039, 2011.
- [61] A. Charles, B. Olshausen, and C. Rozell, "Learning sparse codes for hyperspectral imagery," *IEEE Journal of Selected Topics in Signal Processing*, vol. 5, no. 5, pp. 1–27, 2011.
- [62] J. M. Bioucas-Dias, "Alternating direction algorithm for constrained sparse regression: application to hyperspectral imaging," *IEEE GRSS Workshop on Hyperspectral Image and Signal Processing WHISPERS 2010*, pp. 1–4, 2010.
- [63] C. Chang and Q. Du, "Estimation of number of spectrally distinct signal sources in hyperspectral imagery," *IEEE Transactions on Geoscience and Remote Sensing*, vol. 42, no. 3, pp. 608–619, 2004.
- [64] H. Akaike, "Information theory and an extension of the maximum likelihood principle," *Proc. International Symposium on Information Theory*, pp. 267–281, 1973.

- [65] J. Rissanen, "Modeling by shortest data description," *Automatica*, vol. 43, no. 9, pp. 465–471, 1978.
- [66] M. Wax and T. Kailath, "Detection of signals by information theoretic criteria," *IEEE Transactions on Acoustics, Speech and Signal Processing*, vol. 33, no. 2, pp. 387–392, 1985.
- [67] C. C. Wu, W. Liu, and C. Chang, "Exploration of methods for estimation of number of endmembers in hyperspectral imagery," *Proc. SPIE - Chemical and Biological Sensors for Industrial and Environmental Monitoring II*, vol. 6378, p. 63781C, 2006.
- [68] A. Santos, *Understanding the Effect of Spatial Resolution on Unmixing Algorithms for Hyperspectral Imagery*. Master Thesis, University of Puerto Rico, Mayaguez, 2010.
- [69] P. Bajorski, "Does virtual dimensionality work in hyperspectral images?" *Proc. SPIE - Algorithms and Technologies for Multispectral, Hyperspectral, and Ultraspectral Imagery XV*, vol. 7334, p. 73341J, 2009.
- [70] J. M. V. D. Hof, "Realization of positive linear systems," *Linear Algebra and its Applications*, vol. 256, pp. 287–308, 1994.
- [71] L. Alvarez, F. Guichard, P. L. Lions, and J. M. Morel, "Axioms and fundamental equations of image processing," *Archives of Rational Mechanics and Analysis*, vol. 123, no. 3, pp. 199–257, 1993.
- [72] P. Perona and J. Malik, "Scale-space and edge detection using anisotropic diffusion," *IEEE Transactions on Pattern Analysis and Machine Intelligence*, vol. 12, no. 7, pp. 629–639, 1990.

- [73] J. Weickert, B. Romenu, and M. Viergever, "Efficient and reliable schemes for nonlinear diffusion filtering," *IEEE Transactions on Image Processing*, vol. 7, no. 3, pp. 398–410, 1998.
- [74] J. M. Duarte, P. Castillo, and M. Velez-Reyes, "Comparative study of semi-implicit schemes for nonlinear diffusion in hyperspectral imagery," *IEEE Transactions on Image Processing*, vol. 16, no. 5, pp. 1303–1314, 2007.
- [75] E. Sharon, A. Brandt, and R. Basri, "Fast multiscale image segmentation," *Proc. IEEE Conference on Computer Vision and Pattern Recognition CVPR 2000*, vol. 1, pp. 70–77, 2000.
- [76] J. Weickert, "Coherence enhancing diffusion of color images," *Image and Vision Computing*, vol. 17, pp. 201–212, 1999.
- [77] P. Mrazek and M. Navarra, "Selection of optimal stopping time for nonlinear diffusion filtering," *International Journal of Computer Vision*, vol. 52, pp. 189–203, 2003.
- [78] J. Sporring and J. Weickert, "Information measures in scale spaces," *IEEE Transactions on Information Theory*, vol. 45, pp. 1051–1058, 1999.
- [79] I. Vanhamel, C. Mihai, H. Sahli, A. Katartzis, and I. Pratikakis, "Scale selection for compact scale-space representation of \hat{A} vector-valued images," *International Journal of Computer Vision*, vol. 84, pp. 194–204, 2009.
- [80] Y. Jiabin and L. Guizhong, "A novel anisotropic diffusion time estimation method," *Congress on Image and Signal Processing*, vol. 3, pp. 241–244, 2008.
- [81] G. Camps-Valls, T. V. Bandos, and D. Zhou, "Semi-supervised graph-based hyperspectral image classification," *IEEE Transactions on Geoscience and Remote Sensing*, vol. 45, no. 10, pp. 3044–3054, 2007.

- [82] D. T. Anderson and A. Zare, "Spectral unmixing cluster validity index for multiple sets of endmembers," *IEEE Journal of Selected Topics in Applied Earth Observations and Remote Sensing*, vol. 5, no. 4, pp. 1282–1295, 2012.
- [83] R. A. Mercovich, J. Albano, and D. Messinger, "Techniques for the graph representation of spectral imagery," *3rd Workshop on Hyperspectral Image and Signal Processing: Evolution in Remote Sensing (WHISPERS)*, pp. 1–4, 2011.
- [84] Y. Tarabalka, J. Benediktsson, and J. Chanussot, "Spectral-spatial classification of hyperspectral imagery based on partitional clustering techniques," *IEEE Transactions on Geoscience and Remote Sensing*, vol. 47, no. 8, pp. 2973–2987, 2009.
- [85] F. A. Kruse, A. B. Lefkoff, J. W. Boardman, K. B. Heidebrecht, A. T. Shapiro, P. J. Barloon, and A. F. H. Goetz, "The spectral image processing system (sips) interactive visualization and analysis of imaging spectrometer data," *Remote Sensing of Environment*, vol. 44, pp. 145–163, 1993.
- [86] F. V. der Meer and W. Bakker, "Cross correlogram spectral matching (ccsm): application to surface mineralogical mapping using aviris data from cuprite, nevada," *Remote Sensing of Environment*, vol. 61, no. 3, pp. 371–382, 1997.
- [87] C. I. Chang, "An information theoretic-based approach to spectral variability, similarity and discriminability for hyperspectral image analysis," *IEEE Transactions on Information Theory*, vol. 46, no. 5, pp. 1927–1932, 2000.
- [88] U. Luxburg, "A tutorial on spectral clustering," *Statistics and Computing*, vol. 17, no. 4, pp. 395–416, 2007.
- [89] F. Chung, "Spectral graph theory," *CBMS Regional Conference Series in Mathematics*, vol. 92, 1997.

- [90] A. Ng, M. Jordan, and Y. Weiss, "On spectral clustering: analysis and an algorithm," *Advances in Neural Information Processing Systems*, T. Dietterich, S. Becker, and Z. Ghahramani (Eds.), vol. 14, pp. 849 – 856, 2002.
- [91] J. Shi and J. Malik, "Normalized cuts and image segmentation," *IEEE Transactions on Pattern Analysis and Machine Intelligence*, vol. 22, no. 8, pp. 888 – 905, 2000.
- [92] F. Kovacs, C. Legany, and A. Babos, "Cluster validity measurement techniques," *Proc. International Conference on Artificial Intelligence, Knowledge Engineering and Data Bases*, pp. 388–393, 2006.
- [93] B. Basener, A. Castrodad, D. Messinger, J. Mahle, and P. Prue, "A dynamical systems algorithm for clustering in hyperspectral imagery," *Proc. SPIE- Algorithms and Technologies for Multispectral, Hyperspectral, and Ultraspectral Imagery XII*, vol. 6966, 2008.
- [94] J. Dunn, "Well separated clusters and optimal fuzzy partitions," *Journal of Cybernetica*, vol. 4, pp. 95–104, 1974.
- [95] D. Davies and D. Bouldin, "A cluster separation measure," *IEEE Transactions on Pattern Analysis and Machine Intelligence*, vol. 1, no. 2, pp. 224–227, 1979.
- [96] M. Kim and R. Ramakrishna, "New indices for cluster validity assessment," *Pattern Recognition Letters*, vol. 26, no. 15, pp. 2353–2363, 2005.
- [97] M. Halkidi, M. Vazirgiannis, and Y. Batistakis, "Quality scheme assessment in the clustering process," *Proc. European Conference on Principles of Data Mining and Knowledge Discovery*, pp. 265–276, 2000.
- [98] R. Calinski and J. Harabasz, "A dendrite method for cluster analysis," *Communications in Statistics-theory and Methods*, vol. 3, no. 1, pp. 1–27, 1974.

- [99] G. Martin, J. Plaza, and A. Plaza, "On the incorporation of spatial information to endmember identification algorithms without the pure pixel assumption," *IEEE GRSS Workshop on Hyperspectral Image and Signal Processing WHISPERS 2011*, pp. 1–4, 2011.
- [100] J. J. Cipar, R. Lockwood, T. Cooley, and P. Grigsby, "Background spectral library for fort a.p. hill, virginia," *Proc. SPIE - Remote Sensing and Modeling of Ecosystems for Sustainability*, vol. 5544, pp. 35–46, 2004.
- [101] T. Cooley, J. Cipar, and R. Lockwood, "Terrain categorization using a background spectral library," *Proc. IEEE International Geoscience and Remote sensing Symposium*, vol. 2, pp. 1029–1031, 2003.
- [102] J. Goodman, "2007 puerto rico hyperspectral mission: Image acquisition and field data collection, november 28 - december 21, 2007," University of Puerto Rico at Mayagüez, Tech. Rep., 2009.
- [103] A. Plaza, P. Martínez, R. Perez, and J. Plaza, "A comparative analysis of end-member extraction algorithms using aviris hyperspectral imagery," *In Summaries of the 11th JPL Airborne Earth Science Workshop*, 2002.
- [104] L. Ludeman, *Random Processes: Filtering, Estimation, and Detection*,. John Wiley & Sons, 2003.
- [105] J. C. Harsanyi and C.-I. Chang, "Hyperspectral image classification and dimensionality reduction: An orthogonal subspace projection," *IEEE Transactions on Geoscience and Remote Sensing*, vol. 32, no. 4, pp. 779–785, 1994.
- [106] M. J. Marin-Quintero, *An adaptive spectrally weighted structure tensor applied to tensor anisotropic nonlinear diffusion for hyperspectral images*. Ph.D Dissertation, University of Puerto Rico, Mayaguez, 2012.

- [107] S. D. H. S. Rosario-Torres, M. Velez-Reyes and L. O. Jimenez, "New developments and application of the uprm matlab hyperspectral image analysis toolbox," *Proc. SPIE Algorithms and Technologies for Multispectral, Hyperspectral, and Ultraspectral Imagery XIII*, vol. 6565, pp. 10–1117, 2007.
- [108] E. T. Slonecker, D. Shaw, and T. Lillesand, "Emerging legal and ethical issues in advanced remote sensing technology," *Photogrammetric Engineering and Remote Sensing*, vol. 64, no. 6, pp. 589–595, 1998.
- [109] S. McKee, "Remote sensing issues at the supreme court of canada," *Bulletin-association of Canadian map libraries and archives*, vol. 123, pp. 3–6, 2005.
- [110] R. Purdy, "Attitudes of uk and australian farmers towards monitoring activity with satellite technologies: Lessons to be learnt," *Space Policy*, vol. 27, no. 4, pp. 202–212, 2011.
- [111] D. Cromey, "Avoiding twisted pixels: Ethical guidelines for the appropriate use and manipulation of scientific digital images," *Science and Engineering Ethics*, vol. 16, pp. 639–667, 2010.
- [112] L. Jiménez-Rodríguez, E. Arzuaga-Cruz, and M. Vélez-Reyes, "Unsupervised linear feature-extraction methods and their effects in the classification of high-dimensional data," *IEEE Transactions on Geoscience and Remote Sensing*, vol. 45, no. 2, pp. 469–483, 2007.
- [113] E. Arzuaga-Cruz, L. O. Jimenez-Rodriguez, and M. Vélez-Reyes, "Unsupervised feature extraction and band subset selection techniques based on relative entropy criteria for hyperspectral data analysis," *Proc. SPIE - Algorithms and Technologies for Multispectral, Hyperspectral, and Ultraspectral Imagery IX*, vol. 5093, pp. 462 – 473, 2003.

- [114] A. Ifarraguerri and C. Chang, "Unsupervised hyperspectral image analysis with projection pursuit," *IEEE Transactions on Geoscience and Remote Sensing*, vol. 38, no. 6, pp. 2529–2538, 2000.